UNIVERSITY OF TASMANIA

Influence of Inlet Flow Configuration on the Flow Field Within and Around a Fan-Shaped Film Cooling Hole

by

James S Porter, BEng (Hons)

A thesis submitted in fulfillment of the requirements
for the degree of Doctor of Philosophy

in the
Faculty of Science, Engineering and Technology
School of Engineering

November 2010

Declaration of Authorship

I, James S. Porter, declare that this thesis titled, 'Influence of Inlet Flow Configuration on the Flow Field Within and Around a Fan-Shaped Film Cooling Hole' and the work presented in it are my own. I confirm that:

- This work was done wholly or mainly while in candidature for a research degree at this University.
- Where any part of this thesis has previously been submitted for a degree or any other qualification at this University or any other institution, this has been clearly stated.
- Where I have consulted the published work of others, this is always clearly attributed.
- Where I have quoted from the work of others, the source is always given. With the exception of such quotations, this thesis is entirely my own work.
- I have acknowledged all main sources of help.
- Where the thesis is based on work done by myself jointly with others, I have made clear exactly what was done by others and what I have contributed myself.

- This thesis may be made available for loan and limited copying in accordance with the Copyright Act 1968.

Signed: 

Date: 25-11-2010

UNIVERSITY OF TASMANIA

Abstract

Faculty of Science, Engineering and Technology
School of Engineering

Doctor of Philosophy

by James S Porter

This thesis examines the internal flow dynamics of a typical fan-shaped film cooling hole, as found in gas-turbine aero-engines. As design turbine entry temperatures continue to rise in search of greater engine efficiency, effective cooling is required to maintain turbine components at acceptable temperatures and prevent failure.

Literature regarding shaped cooling hole investigations, particularly the influence of inlet conditions on cooling hole flows, is reviewed. A general failure to fully quantify inlet conditions and an inconsistent terminology for describing them is noted. This thesis argues for use of an inlet velocity ratio (IVR) defined as the ratio of the coolant passage velocity to the jet velocity, together with additional parameters required to define the velocity distribution in the coolant supply passage.

A unique facility has been designed and constructed to conduct large scale testing of film cooling hole geometries. This facility enables independent control of cooling passage velocity and orientation, coolant flow rate, and external cross-flow. Experimental investigations of the internal flow field for a laterally expanded 50 times scale fan-shaped hole are presented. Hot-wire anemometry and pneumatic measurements reveal the extent of separation at the cooling hole inlet and its variation with IVR and coolant passage orientation. Inlet lip separation causes a jetting effect that extends throughout the length of the cooling hole. The exit velocity profiles and turbulence distributions are highly dependent on the IVR. In addition, the effect of blowing ratio between coolant and external cross-flow is investigated through flow field measurements at the hole exit.

Computational simulations of limited flow configurations, together with discharge coefficient and axial pressure distribution measurements, enable a complete description of the internal flow dynamics and provide important data for use in cooling system design and validation of numerical simulations.

Acknowledgements

I certainly wouldn't be writing acknowledgements for a PhD thesis without the expertise and support of my supervisors, Dr Jane Sargison, Dr Greg Walker, and Dr Alan Henderson, who individually and together have prompted me to think, offered solutions, and encouraged me to stay motivated. I have been very lucky to slip in amongst such great minds and I can only hope that some of their wisdom has rubbed off onto the pages of this thesis. My time at UTas Engineering has been punctuated by interaction with so many great people with varied expertise whom I have called upon numerous times, often in desperation! Thank you to Steve, Glenn, John, Bernie, Russell, Ray, Nathan, Andrew, Mary and Judy for so willingly and expertly rendering your assistance, and know that your varied contributions are subtly contained within these pages.

I'm also very thankful for friendships that developed during many hours spent in the workshop and the lab which, without doubt, gave me a wonderful sense of normality and encouragement during the crazier times of impending deadlines and things just generally not working! So a big thank you to Pete and Dave for providing hours of banter, inappropriate emails, bike talk, and general thoughts on the price of hay. I also very much appreciate the 'competitive advantage' I was afforded in the workshop through your loyalty, and the wonderful shop skills you displayed in building my rig, and added to my rookie abilities. I will get you those mugs one day I promise... To my fellow postgrads, thank you for sharing your tales of woe and making me feel somewhat more 'normal'.

I have also been lucky enough to have a group of friends who, while not really caring to know more than that I play with turbines and a wind tunnel in the 'bat-cave', managed to coax me out into the real world now and then despite protests of being 'too busy', and dispensed an adequate level of light-hearted abuse and ridicule to keep me in check. Jacko, Steve, Milf, Wil, Boof, and many others - thank you. To my parents, for continuing to support me, feed me, wash my clothes, and generally make my life pretty easy outside of work and study, despite having to endure a grumpy and reclusive son for much of the time! I certainly wouldn't be where I am without you; thank you. And finally to my beautiful Erin Lee, whose own battle with thesisising has made for a very studious household! Throughout it all, your support and love and counselling has kept me on track, and for that I am truly thankful.

The author gratefully acknowledges the support of Rolls-Royce UK for financial assistance. The author was the recipient of an Australian Postgraduate Award during candidature.

Contents

List of Figures

List of Tables

Abbreviations

CAD	Computer Aided Design
CFD	Computational Fluid Dynamics
CNC	Computer Numerically Controlled
CRVP	Counter-Rotating Vortex Pair
CTA	Constant Temperature Anemometer
DNS	Direct Numerical Simulation
DPMS	Dynamic Pressure Measurement System
HP	High Pressure
ICVR	Inlet Cross-flow Velocity Ratio
IFVR	Inlet Friction Velocity Ratio
IVR	Inlet Velocity Ratio
LDV	Laser Doppler Velocimetry
LES	Large Eddy Simulation
RANS	Reynolds Averaged Navier-Stokes
TET	Turbine Entry Temperature
TFI	Turbulent Flow Instrumentation
VI	Virtual Instrument

Symbols

A	flow area	m^2
C_d	discharge coefficient	
c_p	fluid specific heat	kJ $kg^{-1}K^{-1}$
D	hole diameter	mm
H	coolant passage height	mm
h_f	heat transfer coefficient	W $m^{-2}K^{-1}$
I	momentum flux ratio	
k	turbulent kinetic energy	m^2 s^{-2}
L	hole length	mm
$\dot{m}$	mass flow rate	kg s^{-1}
M	mass flux (blowing) ratio	
Ma	Mach number	
P	pressure	Pa
$\dot{q}$	heat transfer rate	J s^{-1}
Re	Reynolds number	
T	temperature	°C
Tu	turbulence intensity	%
U	velocity	m s^{-1}
u^*	wall friction velocity ($\sqrt{\tau_w/\rho}$)	m s^{-1}
y^+	non-dimensional wall distance	
α	hole inclination angle	°
β	coolant passage orientation angle	°
δ	boundary layer thickness	mm
η	film effectiveness	

γ	diffuser half-angle	°
μ	fluid viscosity	kg $m^{-1}s^{-1}$
ω	turbulent frequency	1/s
ρ	fluid density	kg m^{-3}

Subscripts

aw	adiabatic wall
c	coolant
e	exit
g	gas
j	cooling hole flow
h	cooling hole
m	exit cross-flow
s	supply
t	throat
w	wall
0	total

Chapter 1

Introduction

1.1 The Case for Film Cooling

Gas turbines have become an integral part of daily operations in the developed world; they are relied upon to power aircraft, large naval ships, and to generate electrical power on land. There are 3 essential components in the typical gas-turbine (Fig. 1.1): compressor; combustion chamber; and turbine. In the compressor, air passes through a series of blade rows, or stages, and is heavily compressed, with typical compression ratios in the order of 30:1 [1]. After the last stage of compression, high pressure air continues on to the combustion chamber where fuel is injected, and the mixture ignited, to generate even higher temperature combustion gases. Temperatures at the exit of the combustor are commonly over 1900° C [1], which is significantly above the melting point of most modern alloys.

The turbine section of the engine takes advantage of these highly energised gases by absorbing some energy as they rush past to reach lower downstream pressures. The flow of gas is directed by nozzle guide vanes onto rows of turbine blades which are aerodynamically designed to extract mechanical energy from the flow. The hot gas pushes on the turbine blades which in turn rotates the turbine disc and central shaft, connecting the turbine to the compressor. In an aero engine, the combustion gases are further accelerated through the exhaust nozzle to generate thrust for the aircraft. The turbofan shown in Fig. 1.1 is typical of that used on commercial aircraft where a large fan is located at the front of the engine. Part of the air drawn in by the fan flows through the core, but the remainder flows through the bypass duct to produce thrust. The bypass ratio describes the relationship between the bypass duct flow and the core engine flow.

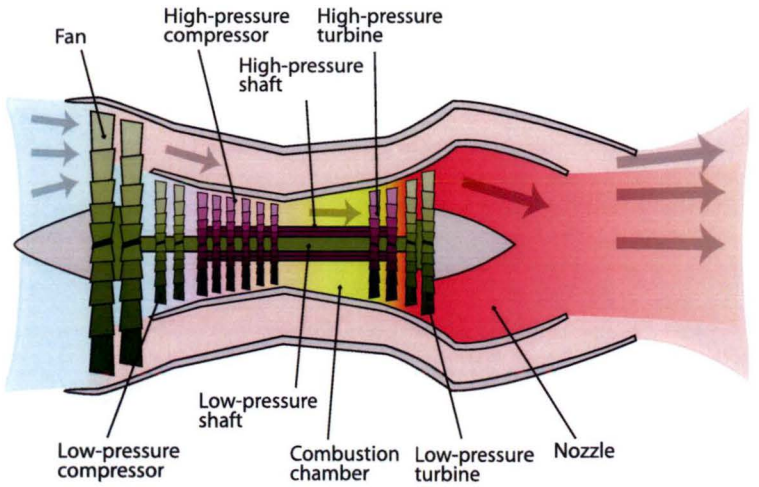

FIGURE 1.1: Cut-away view of a typical gas-turbine aero-engine (from Aainsqatsi [2])

The efficiency of a gas turbine engine is largely dependent on the temperature achievable in the combustor. Higher temperature means that the combustion gases have more energy to transfer as they expand through the turbine sections, and the energy transfer process approaches that of the ideal cycle where efficiency is governed by pressure ratio alone (Fig. 1.2). Higher temperature in itself is not the primary cause for efficiency gains, as higher temperatures require higher fuel burn. The improvement comes in a reduction of specific fuel consumption, which becomes of significant importance for a turbofan as it means the relative size of the core can be reduced to increase the bypass ratio and thus the propulsive efficiency.

The use of film cooling techniques to control the operating temperature of gas turbine components continues to be one of the most important contributors to the overall performance of a gas turbine jet engine. It can be shown that even small increases in turbine entry temperature (TET) result in large increases in engine thrust. Elevated temperatures have been made possible partly by improvements in materials technology, including surface coatings, but to a greater extent through improved aerodynamics as well as internal and film cooling design [3]. Effective cooling not only enables higher temperatures to be reached, but also allows cheaper materials to be used at the same operating conditions as un-cooled, higher quality metals, and provides longer service life components.

1.1.1 Film Cooling Technology

The application of effective film cooling techniques provides the first line of defence for hot gas path surfaces against extreme heat fluxes, serving to directly reduce the incident

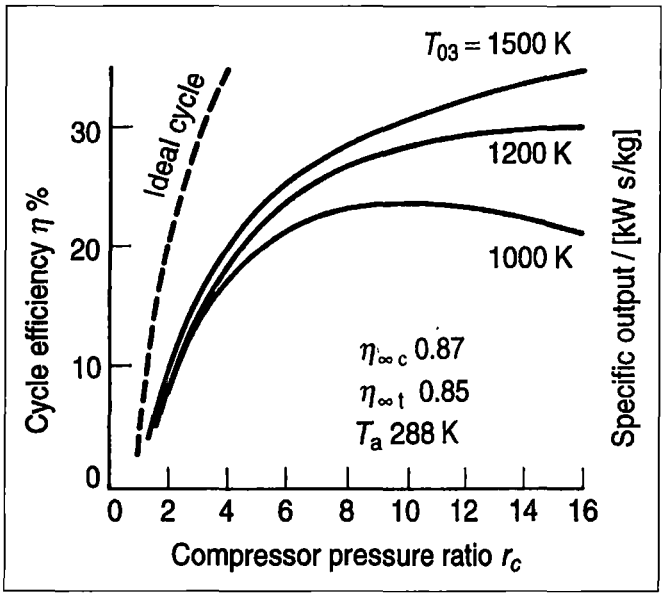

FIGURE 1.2: Influence of turbine entry temperature on gas turbine cycle efficiency (from Cohen et al. [1])

convective heat flux on the surface [4]. Film cooling involves bleeding a small percentage of cooler air from the high pressure (HP) compressor, bypassing the combustion chamber, and feeding directly to the turbine vanes and blades as well as to the end walls of the turbine passages. The coolant path through a typical cooled turbine blade (Fig. 1.3) follows a series of 'serpentine' passages that carry the coolant up and down the inside of the blade from root to tip. At strategic locations, rows of holes are drilled from the external surface to meet these passages and provide a path for the coolant to exit. The resulting coolant 'jets' of air leave the holes and interact with the hot-gas flowing over the blade surface, as well as with adjacent cooling jets. These jets optimally coalesce to form an insulating film of air between the hot mainstream gases (from the combustor), and the blade material.

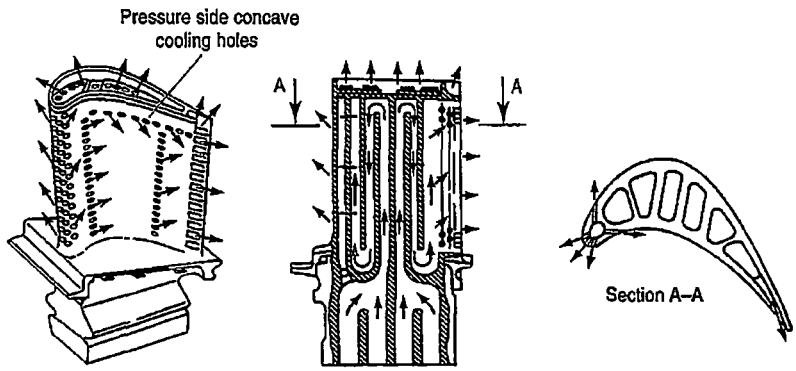

FIGURE 1.3: Typical coolant path through a high pressure turbine blade (from Cohen et al. [1])

Film cooling holes are drilled either by laser or electro-discharge machining to create a surface pattern that provides the best film coverage. Typically, these holes are either cylindrical (round) or fan-shaped (expanded exit). The angle of the hole axis relative to the passage and external hot-gas flows is varied and depends on the location of the hole both internally and on the blade surface. In addition, the surface outline of the hole will vary with hole angle, and with hole geometry. In all cases, it is the goal of discrete geometry film cooling to approach the formation of an ideal tangential slot injection, leading to a continuous layer of coolant film over the surface [4].

The coolant performs a second duty on its way to the external surface film by providing cooling for the internal passages. Heat transfer to the coolant is enhanced by the addition of ribs and pedestals in the passages which increase turbulence levels and promote better convective cooling. The introduction of these obstructions, however, brings higher aerodynamic penalties which ultimately lead to lower engine efficiency. It should also be realised that coolant bled from the compressor is unavailable for combustion and, furthermore, the process of mixing the coolant with the mainstream air after ejection leads to a reduction in aerodynamic efficiency. Consequently, the successful implementation of a turbine cooling system requires careful design in order to achieve effective cooling without compromising the engine performance and efficiency.

1.2 Motivation

The aerodynamic component of cooling hole performance is often seen as secondary in importance to that of the heat transfer and cooling effectiveness. Indeed, preventing the blade from thermally induced failure is a primary aim, and thus concentration on thermal performance is understandable. However, as indicated in Sec. 1.1, the important value of overall engine efficiency has a strong dependence on the performance of the turbine section. This means that optimising the coolant flow path to reduce aerodynamic losses while maintaining a sufficient level of cooling is a very worthwhile exercise.

As cylindrical, or round, cooling holes were the first to be used in the film cooling technique, the majority of available literature discusses the performance of these types of hole. It has only been in more recent years that shaped film cooling holes have become more prevalent in cooling designs. Most experimental work with fan shaped holes has examined the effects of various parameters on centreline and laterally averaged film cooling effectiveness, or the effect on discharge coefficients (which measure aerodynamic loss). While these quantitative results are important for evaluating a configuration's downstream performance, they are the end result of a complex three-dimensional flow path through the cooling system; a more detailed understanding of the flow field is,

therefore, essential for improvements in cooling hole design to be realised. Focus on the internal flow configuration has been lacking in studies up to this point, despite its importance in defining the flow field downstream. In particular, this thesis examines the effect that different hole inlet conditions have on the coolant flow as it enters, moves through, and exits a fan-shaped cooling hole.

Several computational studies have predicted the in-hole and downstream flows for a limited number of configurations in recent years, and indeed, the design engineer is increasingly dependent on computational fluid dynamics (CFD) as a design tool. With computing becoming ever cheaper and more powerful, CFD can be used to test a wider variety of designs in much reduced time. Iterative schemes and multiple-pass design techniques can therefore be employed, leading to the 'optimisation' of designs for a wide range of parameters. The increase in functionality of CFD might, therefore, be thought to signal the beginning of the end for experimental work. However, CFD codes need to be validated and modified on the basis of experimental data. At the same time, experimentalists will increasingly find the direction of their research dictated by the demands of CFD. Future developments will be achieved through the interaction between CFD, which suggests promising possibilities, and experiment, which provides validating test cases [5].

1.3 Definition of Flow Parameters

In the discussion of film cooling in this thesis, there are several parameters important in describing the flow configurations. These will be discussed further in following chapters but are defined here for reference. Figure 1.4 shows a schematic of a typical cooling hole from a side elevation and also a plan view of the hole and coolant passage. The cooling hole inclination angle α is that between the axis of the cooling hole and the mainstream surface at exit. The coolant passage orientation angle is defined by the relationship between the mean velocity in the coolant passage, U_c, and the component of coolant passage velocity in the plane of the cooling hole axis $U_{c,0}$.

Commonly used in film cooling investigations is the mass flux ratio, or blowing ratio, between the coolant jet and the mainstream cross-flow at exit. Referring to Fig. 1.4, this ratio is defined as

$$M = \frac{\rho_j U_j}{\rho_m U_m} \tag{1.1}$$

and enables density (ρ) effects to be included in the ratio of flows. If the coolant and mainstream have the same density (as in the current investigation), this ratio reduces

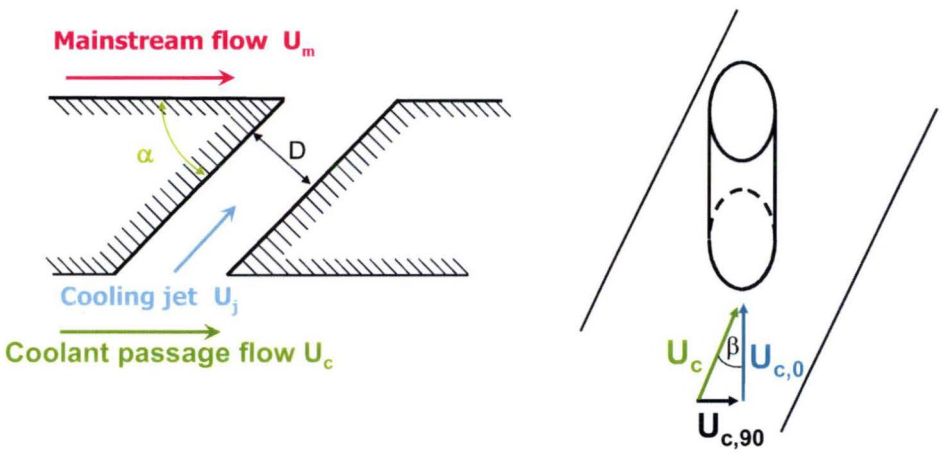

FIGURE 1.4: Diagram of typical cooling hole and associated flows

to the velocity ratio:

$$VR = \frac{U_j}{U_m} \tag{1.2}$$

Related to, and an extension of the blowing ratio is the momentum flux ratio, I. As the name suggests, this ratio defines the relationship between the momentum of the two flows and is defined as

$$I = \frac{\rho_j U_j^2}{\rho_m U_m^2} \tag{1.3}$$

The inlet velocity ratio (IVR) will be defined here as the ratio of the coolant passage mean velocity component in the plane of the cooling hole centreline to the mean velocity in the cooling hole throat:

$$IVR = \frac{U_{c,0_{MEAN}}}{U_{j_{MEAN}}} \tag{1.4}$$

It is logical to define cross-flow as the velocity component normal to the cooling hole centreplane. This study will use the term "cross-flow" in this sense. Pure cross-flow is then the case where the coolant passage orientation is perpendicular to the cooling hole centreline. The inlet flow situation may vary from co-flowing (0° cross-flow angle, $U_{c,0}$), through pure cross-flow (90°, $U_{c,90}$), to counter-flow (180°).

The inlet cross-flow velocity ratio ICVR, can be defined as the ratio of the component of coolant passage mean velocity normal to the cooling hole centre-plane to the cooling hole throat velocity,

$$ICVR = \frac{U_{c,90_{MEAN}}}{U_{j_{MEAN}}} \tag{1.5}$$

The coolant passage flow direction or cross-flow angle, β (Fig. 1.4), is therefore given by

$$\beta = \arctan(\frac{ICVR}{IVR}) \tag{1.6}$$

The IVR alone is not enough to fully specify the approach flow conditions at inlet to the cooling hole. An inlet friction velocity ratio (IFVR) has also been defined as the ratio of wall friction velocity u^* on the hole inlet wall of the coolant passage to the mean velocity in the cooling hole throat

$$IFVR = \frac{u^*}{U_{JMEAN}} \tag{1.7}$$

Of course, if the coolant supply passage flow were fully developed, the channel Reynolds number would suffice to determine the time-mean velocity distribution and wall shear of the approaching flow.

1.4 Thesis Overview

Literature pertaining to film cooling is vast and spans more than 40 years of research. Chapter 2 reviews those works that have looked at shaped film cooling holes and highlights known performance characteristics under various operating conditions. The quantity of research into shaped holes is revealed as low compared to that of the round hole, and a general lack of information on the effects of hole inlet conditions is identified.

Chapter 3 looks at the requirements to achieve similarity between engine and laboratory conditions. A dimensional analysis sets out the parameters in the present investigation that are matched to engine conditions, and the implications of those that are not.

The test facility used for experimental measurements was custom built for this investigation. Chapter 4 details work involved in the design, construction, and commissioning of the wind tunnel and instrumentation. This work was required to produce a unique facility for large scale model testing that provides flexibility in flow parameter variation, and generates high quality data. Further detail on investigations of unsteady flow are presented in App. A.

Chapter 5 begins the presentation of experimental data with flow field measurements from within the cooling hole model. The information here provides a unique look at the distribution of coolant in the throat and its progression through the fan-shaped diffuser portion of the hole. The effects of changing the IVR are clearly shown, as is the minimal influence of blowing ratio.

The behaviour of the coolant once it has left the cooling hole defines the level of cooling effectiveness for a given configuration. Chapter 6 presents data from four measurement planes at the cooling hole exit and downstream. This information extends the internal flow field description and adds the influence of the external cross-flow on the downstream coolant distribution. From these findings, some inference can be made as to the cooling effectiveness of different configurations.

While flow field data provides a picture of the behaviour of coolant through the cooling hole, an additional useful quantity is that of the discharge coefficient, C_d, which helps to quantify the aerodynamic losses of a geometry and flow conditions. C_d is frequently used by the turbine designer to size cooling holes and design the intricacies of the cooling system. Chapter 7 describes the variation in C_d for the tested configurations, and goes some way towards understanding the sources of loss within the cooling hole.

Chapter 8 turns to computational fluid dynamics to provide a simulated description of the coolant flow for several of the experimentally tested configurations. CFD is increasingly being used in design, and here it serves as a useful tool to augment the knowledge gained from experimental data. Conversely, the results from CFD are validated against experimental data to provide confidence in the solution.

Chapter 9 draws the information from previous chapters together to provide a solid description of the coolant flow distribution through the shaped film cooling hole and at exit. Chapter 10 draws conclusions on the effect of inlet flow configuration and provides some recommendations.

Chapter 2

Literature Review

The catalogue of film cooling literature available in the public domain has grown steadily in recent years, with film cooling data gathered by numerous researchers examining the effects of a range of physical phenomena and geometric configurations. A recent review by Bunker [4] cited an unpublished bibliography of film cooling studies that listed nearly 2700 publications, the majority of which have appeared within the last 30 years. Almost all aspects of film cooling have been explored to various extents; however, the inherently complex nature of the film cooling problem has meant that there are many areas that are yet to be sufficiently explored. As mentioned in Ch. 1, the most significant advancement in film cooling technology has been the transition from round film holes to shaped film holes. This shift has occurred only in the last 10-15 years; consequently the majority of shaped hole investigations have occurred in a similar period, though they are still vastly outnumbered by round hole investigations. This chapter outlines the current state of film cooling technology, and demonstrates the need for further experimental data on the flow field for shaped film cooling holes, both for understanding cooling performance results, and for validating computational predictions.

2.1 Measures of Film Cooling Thermal Performance

The main concerns of film cooling are to provide uniform and effective cooling to a component surface, and to prevent thermal fatigue and premature failure. As a result, film cooling studies are largely concerned with measures of film effectiveness, η, and heat transfer coefficient, h_f. These quantities will be defined here.

Film cooling is dominated by three temperatures (Fig. 2.1): the temperature of the hot gas T_g, the temperature of the coolant T_c, and the temperature of the subsequently

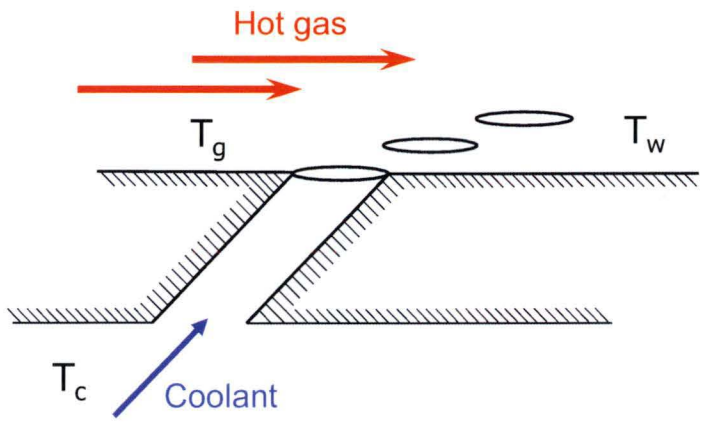

FIGURE 2.1: Film cooling temperatures used in determining heat transfer and cooling effectiveness

cooled wall T_w. The heat transfer to a film cooled surface, $\dot{q}_w$, is commonly given by

$$\dot{q}_w = h_f(T_{aw} - T_w) \tag{2.1}$$

with the adiabatic wall temperature T_{aw} used as a reference temperature. The adiabatic wall temperature is that which would exist in the absence of heat transfer, and is typically described by the non-dimensional adiabatic film effectiveness:

$$\eta = \frac{T_g - T_{aw}}{T_g - T_c} \tag{2.2}$$

Thus the adiabatic cooling effectiveness describes the cooling potential of the coolant film without heat flux into the wall.

The heat transfer coefficient h_f gives information about the influence of the coolant injection on the heat transfer process due to changes in the boundary layer flow field, and effects of advection to the edge of the boundary layer caused by changes in mixing and turbulence levels.

Although these measures of cooling performance are obviously important in quantifying the success of a particular configuration, they do not provide information on the aerodynamic performance. Further gains in film cooling performance will only be achieved by better understanding of the underlying flow physics that drive the eventual cooling effect.

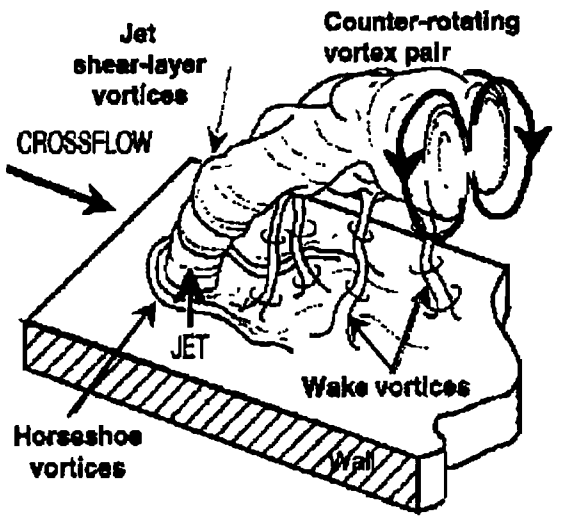

FIGURE 2.2: Structure of a round jet in cross-flow (from Peterson [6])

2.2 General Trends in Film Cooling Performance

2.2.1 Cylindrical Holes

The cooling performance and flow dynamics of the cylindrical (round) jet in cross-flow have been investigated extensively in both film cooling and wider literature, and a number of characteristic behaviours of the complex three-dimensional flow field have been identified. A round jet issuing into a cross-flow will bend in the streamwise direction; as the jet bends, mainstream fluid is entrained and vortices in both the issuing jet and free stream stretch and align to form four dominant flow structures (see Fig. 2.2). Peterson [6] lists these as:

- ring vortices found on the upstream shear layer of the jet, which are produced by a Kelvin-Helmholtz instability in the shear layer
- a system of horseshoe vortices in the boundary layer upstream of the jet, similar to those produced by a cylinder in a cross-flow
- a pair of counter-rotating vortices embedded in the jet
- a system of wake vortices oriented in roughly the same direction as the original jet

Flow visualisations produced by Kelso et al. [7], Haven & Kurosaka [8], and Smith & Mungal [9] clearly show these features of the interaction. The most significant of these is the counter-rotating 'kidney' vortex pair (CRVP). It has been shown that these primary vortices formed at injection tend to drag the hot mainstream fluid to the surface and

even under the cooling jet, thereby leading to potentially severe degradation of film effectiveness. The mechanism for creation of this vortex is still under debate, though theories from Andreopoulos & Rodi [10], Fric & Roshko [11], and Moussa et al. [12] give some explanation. Several numerical studies have attempted to define the link between in-hole vortices and the CRVP, with simulations by Leylek & Zerkle [13], Kohli & Thole [14], and Leedom & Acharya [15] all demonstrating a vortex pair within the cooling hole itself. However, in all cases the CRVP developed downstream of the exit, indicating that in-hole vorticity may not be the causal quantity.

The cooling performance of the cylindrical jet and the influence of the flow structure on this performance has been documented by many studies, including those by Hale et al. [16, 17] and Sinha et al. [18]. A significant limitation of cylindrical cooling holes is the occurrence of jet 'lift-off' or 'blow-off' at higher blowing rates. Here, the ejected coolant jet has high momentum compared to the cross-flow and penetrates far enough into this flow to actually separate from the surface before re-attaching at some distance downstream. This phenomenon, in conjunction with effects of the CRVP, increases the ability of the hot gas cross-flow to be entrained under the jet, and is the cause for poor cooling performance in the near hole region at higher blowing ratios, as seen in Goldstein et al. [19].

2.2.2 Shaped Holes

The work of Goldstein et al. [19] is acknowledged as the first published study to identify the film cooling effects of shaped holes. They tested a row of axially aligned fan-shaped holes of a geometry entailing a one diameter length cylindrical throat and a 10° lateral expansion on either side. Goldstein et al. hypothesised that the increase in exit area would improve film cooling effectiveness by two mechanisms. First, the penetration of the jet into the mainstream would decrease as a result of the reduced momentum flux at the exit. Second, it was expected that the shaping would produce a Coanda effect to keep the coolant jet closer to the surface. Flow visualisations and effectiveness measurements downstream of both the shaped holes and a row of cylindrical holes for three values of blowing ratio, proved both of these postulations to be true. Indeed, this finding has formed the basis for use of the fan-shaped cooling hole to the present day.

Following the work of Goldstein et al. [19], Bunker [4] made three main observations that generally hold true throughout film cooling studies relating to the performance of shaped holes:

i) Shaped hole cooling effectiveness shows little variation with blowing ratio, and tends to sit at the higher end of round hole cooling effectiveness for the same mass flow.

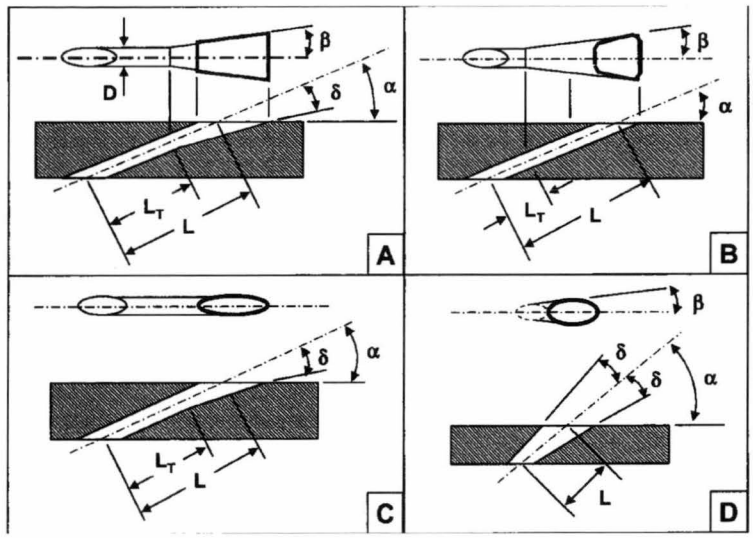

FIGURE 2.3: Geometries for four types of shaped film cooling holes (from Bunker [4])

ii) The overall magnitude of shaped cooling effectiveness approaches that of two-dimensional slot cooling.

iii) The far field effectiveness from shaped holes tends to decay at the same non-dimensional downstream distance as for round cooling holes.

Four main types of cooling hole geometries are commonly used in film cooling investigations, and they are classified by Bunker [4] as shown in Fig. 2.3. Type A consists of both a lateral, fan-shaped expansion, and an expansion into the surface, commonly referred to as 'laidback' or 'forward-diffused'. Type B has only a fan-shaped lateral expansion, and type C has only a laidback expansion. Type D is a conical hole that expands uniformly from inlet to outlet on all sides. Type A is the most commonly applied form, due mostly to manufacturing methods failing to produce a pure single direction expansion, such as type B and C. Type D holes are not widely used and there are limited data available for the performance of this hole shape. Type A and B geometries are most commonly examined by film cooling researchers, and are typically compared with results for the traditional round cooling hole.

A study by Gritsch et al. [20] examined the cooling performance of a cylindrical, fan-shaped (type B), and laidback fan-shaped (type A) hole for blowing ratios of 0.5, 1.0, and 1.5. Comparing these geometries, they found that the type B hole provided a high centreline effectiveness, but that the effectiveness decreased rapidly off-centreline. For the type A hole, the effectiveness magnitude was lower compared to type B, but the lateral spread of the coolant was improved. Measurements of laterally averaged effectiveness clearly showed the superiority of the type A holes in terms of coolant spread in this configuration, particularly at high (> 1.5) blowing ratios. Dittmar et al. [21]

presented data for type B holes in agreement with [20], and also presented heat transfer coefficient results for several hole configurations. These results showed higher levels of h_f in the surface region immediately downstream of the hole exit when compared to a round hole, which was attributed to higher turbulence levels in the jet due to the expansion within the diffuser. Gritsch et al. [22] also presented h_f measurements for type A and B holes; but, in contrast to Dittmar et al., they reported significantly lower h_f values just downstream of exit when compared to cylindrical holes at higher blowing ratios. These conflicting results could be explained by the difference in exit cross-flow velocity between the two studies, or some effect of the hole inlet configuration. Despite this disagreement, the conclusions of Gritsch et al. [22] further demonstrate the superiority of fan-shaped holes in terms of cooling effectiveness at higher blowing ratios, and lower lateral heat transfer coefficients.

Several other studies have looked at the cooling effectiveness for type A and type B holes. Lutum et al. [23] examined rows of each of these hole types and reported that the type A holes performed slightly worse; they attributed this behaviour to local flow separation within or just downstream of these laid back fan-shaped holes. Kohli and Bogard [24] compared two type A holes but with different forward-diffusion angles of 15 and 25 degrees. The hole with the larger diffusion angle was expected to keep the coolant jet closer to the surface and thus provide better cooling performance. Results showed, however, that the effectiveness of this larger diffusion angle geometry were lower due to increased flow separation in the diffuser, aligning with the findings of [23]. Further studies by Reiss & Bölcs [25], Colban and Thole [26], and Saumweber & Schulz [27, 28, 29], also demonstrate the superiority of the shaped cooling hole in terms of cooling effectiveness magnitude and lateral coolant spread on the surface downstream.

Zuniga et al. [15] presented measurement data on 3 conical (type D) hole geometries with expansion angles of 6° and 4°, as well as a 2° hole with a cylindrical entry length. All holes were inclined at 35° to the surface and axially aligned with the mainstream flow. Results for blowing ratios of 0.5-1.5 were compared to Gritsch et al. [30] for fan shaped holes of similar expansion angles and demonstrated that for the configurations tested, the conical holes were very similar in performance to the fan-shapes, being a little better at low blowing ratios and a little worse at higher blowing ratios in the near field. Cooling effectiveness showed less variation with downstream distance and extended further than the fans at higher blowing ratios. It was noted that mainstream turbulence levels were not taken into account in this study. A cylindrical entry length prior to the conical section appeared to further improve performance at high blowing ratios.

2.2.3 Novel Geometries

It is worth noting that several novel cooling hole geometries have been investigated to explore the possibilities for improved cooling performance or reduced aerodynamic loss. An interesting investigation by Nakamata et al. [31] presented a novel cooling hole geometry designed to improve lateral spreading of the coolant fluid, and reduce coolant blow-off. This new arrow head shaped hole (ASH) geometry was designed to allow greater spacing between holes, thus reducing the amount of coolant required, and to minimise the risk of hot gas back-flow by permitting high pressure ratios without blow-off. The ASH demonstrated a continually increasing effectiveness with blowing ratio as the tendency to lift-off was suppressed. Numerical solutions indicated that this was due to the development of counter-rotating vortices from the sides of the ASH, with a direction such that mutual downforce is induced on the jet flow, as opposed to the typical lift created by the CRVP.

The converging slot hole, or CONSOLE, design was introduced by Sargison et al. [32, 33] as a film-cooling system with the mechanical stability of discrete holes, but with a high film-cooling effectiveness, uniform lateral cooling, and low aerodynamic loss. The geometry transitions from a circular inlet to a slot at outlet, with convergence in the axial direction and divergence laterally, so that the exit area of adjacent holes intersect to mimic a continuous slot. There is a reduction in area to slightly accelerate the flow and reduce jet turbulence, but not necessarily to a choked condition. Comparisons with fan shaped holes showed equivalent or better effectiveness and heat transfer coefficient, but with lower aerodynamic loss.

2.2.4 Shaped Hole Flow Field

In many of the above-mentioned studies of film cooling effectiveness, the authors attempt to explain the observed changes in flow distribution by making assumptions about the underlying flow dynamics. It is clear, however, that these assumptions will not be confirmed without information on the complex three-dimensional flow field that drives the cooling performance of any cooling system configuration. In contrast to cylindrical holes, there are only a handful of studies to date that have at least partially examined the flow field for shaped cooling holes, despite the first recognition of shaped hole cooling benefits over 30 years ago. A 1998 paper by Thole et al. [34] used laser Doppler velocimetry (LDV) to obtain mean velocity vectors, turbulence intensity, and turbulent shear stress distributions in the exit region and slightly inside the holes for cylindrical, type A, and type B shaped holes with a blowing ratio of 1.0. Their results indicated that, compared to the round hole, the flow field for the shaped holes showed a marked reduction in jet

penetration and near field velocity gradients. Thole et al. observed that peak turbulence for the fan shaped holes was located at the exit of the cooling hole due to the expansion angle being too great, while for the round hole it was located downstream of the hole exit where velocity gradients were very large. This reduction in turbulence for the shaped holes leads to less shear-driven mixing of the injected cooling jet with the mainstream. In addition, both shaped holes showed a much higher degree of lateral spreading, supporting the thermal results of Goldstein et al. [19] and Gritsch et al. [20]. This increased lateral spreading means that for a given hole spacing in a row of film holes, a continuous film is formed at a shorter distance downstream.

The lateral expansion of the shaped hole also tends to create a positive effect on the development of vortex structures, as previously discussed for cylindrical holes. First, the lateral spreading helps to separate the branches of the counter-rotating kidney vortex pair, which in turn reduces the tendency for jet blow-off. Second, measurements made by Haven & Kurosaka [8] and Haven et el. [35] have demonstrated an 'anti-kidney' flow structure with vortices developing in the opposite sense to that typically associated with the round jet, thus reducing the strength of this vortex. Type A shaped holes tend to demonstrate this to a greater extent than type B shaped holes. Although the above general trends have been identified, the complex vortical structure at the exit of these holes is still not fully understood: especially the flow within the cooling hole itself, and the effects that variations in both geometry and flow parameters have on the internal flow field.

2.3 Influence of Geometry Variations

Compared to a standard cylindrical hole, it is obvious that for shaped cooling holes, the number of geometric parameters defining the hole shape are significantly increased. Along with the parameters that define the cylindrical hole, such as hole diameter, hole length, and the orientation of the hole axis relative to the surface (inclination and compound angles) and hole spacing, there are further parameters that describe the diffuser portion of the hole. These include the starting point of the diffuser, as well as the angles of expansion in both the lateral and streamwise directions. These parameters then fix quantities such as the area ratio of the hole and the surface coverage. Variations in hole geometry frequently occur due to imperfections in manufacturing techniques, and a computed parametric study by Bunker [36] showed significant changes in effectiveness for seemingly small adjustments in geometry. There are only a few studies that try to identify the influence of these geometric parameters on film cooling, and a summary of these is presented in the following section.

2.3.1 Influence of Length-to-Diameter Ratio

Typical hole lengths in film cooling applications are in the length-to-diameter (L/D) range of $2 \leq L/D \leq 10$. The primary influence of changes in hole length are related to distributions of velocity and turbulence at the hole exit. Relatively longer hole lengths, such as those used by Crabb et al. [37] and Andreopoulos and Rodi [10], allow the in-hole flow to develop significantly and recover from any inlet separation effects that may occur long before the exit plane is reached. For short holes, however, the influence of inlet flow disturbances create non-symmetric flow distributions at the exit, which tend to impact negatively on cooling performance. Burd et al. [38] revealed fundamental differences in velocity profiles at the hole exit between cylindrical holes with L/D of 2.3 and 7.0. Lutum and Johnson [39] found for cylindrical holes that the hole length-to-diameter ratio had basically no effect for $L/D > 5$, and decreased effectiveness as L/D was reduced below 5. Gritsch et al. [30] extended these results to type B fan-shaped holes, finding no appreciable difference in cooling effectiveness for $7.5 \leq L/D \leq 11.5$. A more recent study by Saumweber and Schulz [28] tested the effect of changing the length of the cylindrical entry portion of a shaped hole ($L/D = 2$, 6), but keeping the diffuser section the same. From effectiveness results some comments on the possible changes in internal hole flow were made. They found that the elongated ($L/D = 6$) fan-shaped hole tended to concentrate coolant in the centreline area, giving increased lateral temperature gradients, and surmised that a separation 'bubble' on the wall of the diffuser is suppressed by the extra length of the cylindrical portion of the hole. Further discussion from Saumweber and Schulz [28] shows that the effect of L/D on cooling performance is strongly governed by the internal flow development.

2.3.2 Influence of Inclination Angle and Diffuser Expansion Angle

The inclination angle, α (defined in Fig. 1.4), should in practice be as shallow as possible to reduce the component of velocity normal to the surface and minimise penetration of the coolant into the hot-gas cross-flow. At high blowing ratios, however, studies have shown that steeply inclined cylindrical holes can provide improved cooling [24]. The increased penetration into the hot-gas cross-flow leads to an intensified interaction that enhances mixing in both lateral and vertical directions. This improves spreading of the coolant, and also sees the jet re-attach at shorter distances downstream, although the effectiveness along the centreline deteriorates sooner. Saumweber and Schulz [28] investigated the effectiveness distribution downstream of a type B shaped hole for inclination angles of $\alpha = 30°$, 45°, and 60°. Their results showed minimal influence of inclination angle at low blowing ratios, but a significant decrease in performance at high blowing ratios and steeper inclination angles.

The expansion angle of the fan has trended towards wider diffusers in search of increased lateral spread of the coolant and a greater reduction in coolant momentum to prevent jet lift-off. Saumweber and Schulz [28] presented effectiveness distributions downstream of type B fan-shaped holes with diffuser half-angles of 6°, 10°, and 14°. Their results showed that the widest diffuser gave the highest laterally averaged cooling effectiveness across all tested blowing ratios. In addition, the sensitivity of effectiveness to diffuser angle at high blowing ratios increased, with over 50% improvement from a 6° to 14° expansion at a blowing ratio of 2.5. Zuniga et al. [40] showed similar trends for conical type C holes, with a higher expansion angle showing improved lateral spreading and a reduced rate of decay of effectiveness with downstream distance.

2.4 Influence of Flow Parameter Variation

2.4.1 Blowing Ratio

The effect of blowing ratio has already been discussed in Sec. 2.2.1, with marked decreases in effectiveness at higher blowing ratios due to jet lift-off. Typical values of blowing ratio in industrial applications are in the order of $0.5 - 2$. The study by Gritsch et al. [20] shows the typical trend for shaped cooling holes, measuring effectiveness distributions downstream of type A and B holes for blowing ratios of $0.5 - 1.5$. Type B holes demonstrate higher centreline and laterally averaged effectiveness at low to moderate blowing ratios, and perform well at higher blowing ratios. The type A holes show no real signs of reaching a maximum effectiveness over the tested range, increasing continuously with blowing ratio to perform better than type B shaped holes for blowing ratios > 1.4. Data from Sargison et al. [41] is in agreement with Gritsch et al. [20].

2.4.2 Density Ratio

In aero-engine applications the density ratio between cool and hot air flows is approximately $1.8 - 2$. However, due to the difficulties of replicating this ratio in laboratory environments, most studies are performed at density ratios closer to 1.0. Because density ratio is linked to blowing and momentum flux ratio, both cannot be simultaneously held constant while density ratio is varied, making it difficult to ascertain the effects of density ratio alone. Sinha et al. [18] investigated cylindrical holes and found that the effect of variable density ratio could not be scaled with blowing ratio, velocity ratio, or momentum flux ratio alone. At low blowing rates the centreline effectiveness scaled with blowing ratio; at higher blowing rates where jet detachment was present, effectiveness scaled with the momentum flux ratio. The lateral spread of the jets was also found to

be somewhat dependent on the density ratio. Pietrzyk et al. [42] presented flow field measurements in the exit region of a cylindrical hole and found differences in penetration between density ratios of 1 and 2, with the denser jet staying closer to the wall. In this case, however, the velocity ratio of the denser jet was lower, suggesting that the effect was at least partially governed by the velocity ratio. A general opinion is that the momentum ratio tends to be more important near the hole exit where a total pressure fight occurs between the coolant and mainstream gas. The denser jets remaining closer to the wall is likely a result of reduced momentum for the same value of $\rho \times U$. To the author's knowledge, there are no publicly available studies of density ratio for shaped cooling holes.

2.4.3 Freestream Turbulence

Turbulence levels exiting the combustor preceding the high pressure turbine section of a gas-turbine engine can range from 7% to 20% depending on the combustor design. The majority of film cooling studies employ low freestream turbulence intensities, generally in the order of 4%. Research into the effects of freestream turbulence on round hole film effectiveness has shown that elevated intensity levels can quite severely reduce effectiveness [4]. Kohli and Bogard [43] used a high frequency response temperature sensor to study the dispersion of coolant jets for two different turbulence levels of 0.5% and 20%. Their results showed that the process of coolant dispersion is distinctly different for the low and high free-stream turbulence flows. For low mainstream turbulence levels the shear layer between mainstream and coolant jet generates strong intermittent flow structures that cause mixing of the coolant and mainstream flows. In the case of high freestream turbulence, the mainstream fluid penetrates through the core of the coolant jet towards the wall, causing rapid mixing of coolant and mainstream and a pronounced degradation of the jet. Saumweber et al. [44] looked at type A and B shaped holes at elevated freestream turbulence from 3% to 11%. They showed that the effect of freestream turbulence was most pronounced at lower blowing ratios, giving a reduction in effectiveness of 10-20%. At higher blowing ratios, the effect of turbulence intensity is much less pronounced as the jet strength and turbulence levels dominate. Another paper by Saumweber and Schulz [29] investigated freestream turbulence in conjunction with several other parameters, and concluded that although elevated turbulence levels can result in improvements in effectiveness for cylindrical holes at medium to high blowing rates, the effect on shaped cooling hole effectiveness is always detrimental.

2.5 Influence of Hole Inlet Conditions

In recent years, it has been recognised that a plenum feed to film cooling holes does not necessarily represent the true configuration for film cooled aerofoils. Coolant supply passages within the blade are narrow: mainly for structural integrity, but also to promote increased passage velocities and thus higher heat transfer coefficients on the passage walls. In addition, the orientation of the supply passage flow relative to the cooling hole axis (or cross-flow angle) may vary, depending on the location within the blade, from 0° up to 180°. Over this range of inlet flow conditions there is a correspondingly large variation of the in-hole flow structure that cannot be overlooked as part of the overall film cooling design. Studies from as early as 1969, such as those by Rohde et al. [45] and Hay et al. [46], have documented the effects of coolant passage cross-flow on the pressure loss, or discharge coefficient, for cylindrical holes. Thole et al. [47], in their 1997 paper, were the first to present flow-field data for cylindrical cooling holes using an experimental set-up that included a variable coolant cross-flow. A text by Miller [48] presents loss coefficient data versus internal flow ratio and area ratio for a range of configurations including dividing junctions and manifolds. Interest in the effects of internal coolant cross-flow has grown significantly in recent years and more studies have been published covering discharge coefficients, coolant flow-field, and cooling performance results for different inlet configurations. One parameter which to this point has not been explicitly investigated for film cooling flows, however, is that of the inlet velocity ratio (IVR), as defined in eq. (1.4).

2.5.1 Previous Studies with Specific Treatment of Inlet Conditions

A 1998 review by Hay and Lampard [49] examined published literature on discharge coefficients of film cooling holes and compiled an extensive list of investigations up to that time. The authors noted that the majority of work completed was experimental, with several including internal cross-flow effects, but little attention had been paid to shaped cooling holes. More recently, the review paper by Bunker [4] also observed that relatively little attention had been given to the effects of the internal coolant passage flow.

Previous studies of cooling hole inlet effects have employed parameters such as the coolant passage to jet 'velocity head ratio' $(P_{0c} - P_j)/(P_{0c} - P_c)$ used to correlate discharge coefficient data by Rohde et al. [45], and the internal 'jet-to-crossflow' momentum flux ratio $\rho_j U_j^2/\rho_c U_c^2$ used by Gritsch et al. [50]. For isothermal incompressible flows the latter reduces to the inverse square of the IVR used in the present investigation. Hay et al. [46] stated that the 'velocity head ratio' was difficult to use with cross-flows on either

side of the hole. Indeed, it seems the 'standard' parameter for correlating discharge coefficient data among researchers is the pressure ratio P_{0c}/P_m.

Hay et al. [46] published one of the first studies of the effects of cross-flows at inlet and exit of a cooling hole. They used a row of cylindrical holes ($L/D = 6$, $D = 10$ mm) supplied by a co-flow and a cross-flow coolant passage. The coolant passage Mach number was set and a general range of coolant Reynolds number provided. No coolant passage boundary layer information was included. Another paper by Hay & Lampard [51] examined discharge coefficients for fan shaped cooling holes with a co-flow coolant passage, but again specified only the coolant passage Mach number and pressure ratio across the hole.

Although not dealing specifically with film cooling holes, a paper by Lloyd and Brown [52] examined the velocity and turbulence fields at the entry to a long ($L/D = 21$) cylindrical pipe mounted perpendicular to an entrance cross-flow. Radial profiles taken at several axial locations revealed that the velocity characteristics within the pipe were significantly influenced by the ratio of the cross-flow to pipe velocities. The results also indicated that the distribution at the inlet was highly skewed, with a jetting of fluid towards the downstream inlet lip.

Byerley [53] carried out a study of cylindrical film cooling holes fed from a passage with $H/D = 3$. Investigations were centred around heat transfer and flow field measurements downstream of the cooling hole inlet, and demonstrated enhanced heat transfer in this region. The study also presented discharge coefficient data and a discussion of inlet separation. A related study by Gillespie et al. [54] showed that heat transfer enhancement just inside the cooling hole was highest when the inlet lip separation was reduced.

A study by Thole et al. [47] was the first in open literature to look specifically at the effect of a co-flowing coolant passage on the exit flow field of a cylindrical cooling hole. The coolant passage Mach number was varied for fixed blowing ratio and fixed exit cross-flow Mach number, for a round hole with $L/D = 6$ and 30° inclination angle. Velocity measurements at the exit showed a progressive movement of the peak exit velocity location from the upstream edge of the hole for low coolant passage Ma towards the downstream wall at higher coolant passage Ma. The authors surmised that at higher coolant passage Ma the separation region inside the hole moved from the downstream to the upstream walls of the hole. The authors provided comprehensive details on the coolant passage flow, with Mach number, mean velocity, Reynolds number, and upstream boundary layer thickness being specified. Although not stated, the provided information enabled the tested IVRs to be calculated as 0, 1.2, and 2.0. The most uniform exit profile and lowest turbulence levels found by these authors corresponds to the IVR = 1.2 case.

The condition of the coolant passage boundary layer was not given, and the wall shear at the hole entry was not defined.

Kohli and Thole [14] performed a computational investigation for a type A cooling hole with a plenum inlet, as well as coolant passage orientations of 0, 90 and 180° for a blowing ratio of $M = 1.0$. Results revealed a large separation region on the downstream side of the diffuser for all cases. This is not so surprising given the large 15° forward expansion angle of the hole. Results also showed separation within the throat section for all cases, with the minimum separation for the co-flowing case. The location of maximum turbulence intensity was found to coincide with a shear layer between the separated region and the high-speed jetting fluid. Although not stated explicitly, an IVR of 0.7 can be deduced for test cases where a coolant passage velocity existed at the hole inlet. Further work from Kohli and Thole [55] used CFD to investigate the effect of coolant passage Reynolds number and orientation for the same type A shaped hole geometry. The effect of coolant passage Reynolds number was investigated only for a 90° cross-flow and a blowing ratio of $M = 2$. They found the co-flowing coolant passage orientation to give the highest laterally averaged cooling effectiveness, while the 90° cross-flow case was consistently the poorest performing. Here again, the inlet velocity ratio was undefined and only the inlet wall boundary layer thickness was provided.

A series of papers by Gritsch et al. [20, 22, 56] examined discharge coefficients for both shaped and cylindrical cooling holes with a co- or cross-flowing coolant passage. The same test facility was used for these studies with parameters such as coolant passage Mach number, Reynolds number and turbulence intensity being specified. These studies make use of the internal momentum flux ratio, which is related to the IVR, giving a tested IVR range of $0 - 3$. A later paper from Gritsch et al. [57] looked at the effect of coolant passage Mach number on downstream cooling effectiveness, specifying the same parameters as in previous studies. In this case the internal momentum flux ratio was not used, so the range of tested IVRs cannot be determined. They investigated a cylindrical and two fan-shaped geometries for various blowing ratios at a coolant passage orientation of 90°. Cooling effectiveness distributions showed a strong influence of coolant passage Mach number, with laterally and spatially averaged effectiveness values giving a marked drop in performance at higher coolant passage Mach numbers. These distributions also showed a distinct skewing of the exit flow to one side of the hole. Despite focussing on coolant passage Mach number, none of these studies by Gritsch et al. gave information on the coolant passage boundary layer.

Adami et al. [58] presented a numerical study of the in-hole flow field for cylindrical, type A, and type B holes with a 90° cross-flow at inlet. They examined the flow-field for one test configuration and specified only an external blowing ratio. Kissel et al. [59]

introduced ribs to a cross-flowing coolant passage and examined passage and main-flow Reynolds number effects on downstream surface cooling performance. The passage Reynolds number and hole pressure ratio were specified, but there were no details on the passage boundary layer (which would certainly have been influenced by the wall ribs) and insufficient data to determine the tested IVRs.

The most recent study that includes the effects of the coolant passage flow is that by Saumweber and Schulz [27]. This investigation looked at a cross-flowing coolant passage, and offered data for a range of coolant passage Mach numbers and blowing ratios for a fixed exit cross-flow Mach number. Again, the IVR was not quantified, but could be calculated from data provided. These tests covered a range from IVR $= 0 - 3.5$ at the highest coolant passage Mach number of 0.59 and for a blowing ratio of 1.0.

2.5.2 Description of Internal Flow Dynamics

In reviewing this literature it becomes apparent that there has been a distinct lack of consistency in terminology and specification of the coolant passage flow conditions. The majority of studies specify a coolant passage Mach number or Reynolds number, and a handful of studies provide a wall boundary layer thickness at a distance upstream of the hole inlet. However, none of these studies explicitly provide details on the IVR and the incoming boundary layer condition at the cooling hole entrance. In contrast, the flow conditions at hole exit have been well defined and specified in the majority of papers, with the commonly accepted blowing or mass flux ratio M being used in conjunction with exit cross-flow Mach number and wall boundary layer information. What is lacking for the coolant passage flow is information about the relationship between coolant and jet flows, through the IVR, and importantly, details on the velocity distribution on the inlet-side passage wall. The latter is critical to the development of the in-hole flow, as the relative thickness of the coolant passage boundary layer and wall velocity gradients will, within limits, determine the condition of the hole inlet flow. Although the lack of this information complicates the direct comparison of results from different researchers, several common key points regarding the inlet flow have been identified.

The most prominent inlet flow phenomenon is that of separation from the inlet edge of the cooling hole. As discussed by Hay et al. [46], the typical 30° inclination angle of cooling holes creates significantly different inlet conditions to those of a sudden contraction or orifice type flow. Work by Pietrzyk et al. [60] presented exit velocity and turbulence information for an inclined cylindrical hole fed by a plenum inlet. The skewed exit profile of the jet led to the conclusion that a separated region must exist on the downstream side of the cooling tube as a result of the large turning angle. A numerical

study by Leylek and Zerkle [13], replicating the work of Pietrzyk et al., predicted the existence of this separated region and associated jetting of fluid towards the upstream side of the exit. Further works of Thole et al. [47], Kohli and Thole [14, 55], Gritsch et al. [22], Kissel et al. [59], and Saumweber and Schulz [27], have all discussed this inlet separation and implied from exit data or numerical predictions that such a separation exists. Heat transfer contours on the cooling passage wall by Gillespie et al. [54] confirmed the existence of a separation region at the hole inlet for a 90° and 150° inclined hole. There has so far been no full flow field experimental data presented from within the hole to complement this finding.

2.5.3 Inlet Stagnation Point Location

The location of the stagnation point at the hole entrance is critical in defining the location and extent of the separated region. Hay et al. [49] noted this in relation to understanding the variation of discharge coefficients, stating that as the coolant passage mean velocity (in the present terminology) increases, the stagnation point moves upwind to the downstream inlet edge, and then into the hole at still higher cross-flow velocities. This is in line with a study by Brandner and Walker [61] who experimentally investigated a flush mounted water jet propulsor inlet, commonly used in high speed ferries. Brandner and Walker found that incidence angle on the inlet lip has a significant effect on non-uniformity at the duct exit, with large velocity gradients for low and high IVRs. As IVR was increased from 0 to 3, the stagnation point, measured by lip static tappings, progressed from outside to inside the duct. In addition, the DC60 parameter, used to quantify distortion at the duct outlet, showed an almost linear variation with IVR over the range from $1 - 2$, with minimum distortion at an IVR of 1. Byerley [53] also discussed inlet lip separation in the context of discharge coefficient results, finding that the discharge coefficient was reduced for the case of a 150° inclined hole because of the large areas of separated flow at the inlet induced by the sharp turning angle into the hole. Indeed, all studies incorporating coolant passage cross-flow have noted a significant alteration of exit flow-field, cooling performance, or discharge coefficients with varying coolant passage Mach number or Reynolds number, and hence IVR.

2.5.4 Inlet Velocity Ratio

The inlet velocity ratio has not been previously defined in published literature for film cooling flows, despite its importance in defining the in-hole flow. Several studies, such as Saumweber and Schulz [27], Thole et al. [47] and Gritsch et al. [56] have hinted at the implications of such a ratio, but have not characterized the flow in terms of IVR. An

important point to note is that experiments conducted by increasing the blowing ratio for a fixed exit flow and fluid density must produce associated changes in the IVR: thus the results obtained must depend on the combined effects of blowing ratio and IVR, and it is therefore incorrect to attribute the observed changes to the influence of blowing ratio alone.

2.6 Discharge Coefficients for Shaped Holes

2.6.1 Definition of the Discharge Coefficient

The discharge coefficient of a hole, C_d, is the ratio of the actual mass flow through the hole, $\dot{m}_{actual}$, to the theoretical or ideal mass flow through the hole which neglects friction and separation effects, $\dot{m}_{ideal}$:

$$C_d = \frac{\dot{m}_{actual}}{\dot{m}_{ideal}} = \frac{(\rho.U.A)_{actual}}{(\rho.U.A)_{ideal}} \tag{2.3}$$

where ρ is the density, U is the velocity, and A is the reference cross-sectional area of flow. The discharge coefficient gives a measure of the overall aerodynamic penalty occurring due to separation and frictional losses within the hole.

2.6.2 Studies of Discharge Coefficient

A 1998 paper by Hay and Lampard [49] reviewed the state of discharge coefficient literature up to that time. Hay and Lampard noted that the majority of studies were experimental and that analytical predictions of C_d (thus making the design process simpler) covered only limited cases. Furthermore, data for shaped hole C_d values had been measured in only a few experimental sets. Besides the cooling effectiveness benefits shaped cooling holes give over cylindrical holes, the addition of an expanding section also enhances C_d. This is due to the fan-shaped portion acting as a crude diffuser, recovering pressure and leading to an enhanced actual mass flow for a given pressure ratio across the cooling hole. A potential disadvantage of the fan-shaped hole is that the resulting deceleration of fluid at the exit may enlarge the velocity difference between the coolant and mainstream flows such that mixing losses are increased. This can work in favour of the shaped hole, however, in regions of the blade where mainstream fluid is slower. Tailoring of internal component pressure losses can help achieve the appropriate coolant exit velocity to maximise cooling effectiveness.

Hay and Lampard [51] conducted a thorough investigation into the behaviour of fan-shaped holes, with both normal (90°) and 30° inclined holes. They discovered that

fan-shaped holes have discharge coefficients up to 15% higher than cylindrical holes when based on the throat cross-sectional area, with particular improvement in the lower pressure ratio range. These authors also concluded that the length of the cylindrical section prior to the flare should be at least two hole diameters in length (and preferably four) in order to allow reattachment of the flow to the hole walls before entering the flare, thereby ensuring the maximum diffusing action of the fanned section. Gritsch et al. [62] compared the discharge coefficients of cylindrical and fan-shaped holes for pressure ratios of up to 2. With no internal or external crossflow, they found that the fan-shape geometry increased C_d by up to 10%, with the effect again being more pronounced at lower pressure ratios. As highlighted by Hay et al. [46], the complexity of the cooling hole flow situation makes numerical prediction schemes difficult to implement, and the need for more information on the internal flow structure and specific sources of loss is evident.

2.7 Computational Simulations

An extensive computational investigation into the flow field of round and shaped film cooling holes is described in a series of papers co-authored by J.H. Leylek that used a systematic computational methodology, and looked at both round and shaped holes. Hyams and Leylek [63] produced one in a series of four papers looking at the physics of film cooling for round and shaped cooling holes. These authors examined four different shaped hole configurations, including the traditional laterally expanded fan shaped hole (type B), and identified this configuration as having the best overall cooling performance of all those tested. They presented velocity field data in the exit region and provided an analysis using components of vorticity, based on a proposition by Moussa et al. [12]. This approach was used to explain the sources of the well-documented counter-rotating vortex pair for the round hole; it demonstrated that the laterally and forward diffused holes significantly reduce the axial aligned vorticity, thus discouraging mainstream ingestion downstream. Kohli and Thole [14] examined the flow field of a round and fan shaped hole inclined at 35°. They concentrated on the effects of inlet cross-flows, finding that for the cases considered, a large separation region occurred within the expanded portion of the fan. This study also found that the shaped hole produced no counter-rotating vortices at exit, and had a maximum in turbulence intensity at the leeward edge of the hole. Due to the flexibility of computational fluid dynamics, these studies and others have provided useful information on the flow field for shaped holes in conjunction with cooling performance data; however, the need for experimental validation of such computational studies remains high.

2.8 Summary

Shaped hole film cooling has become standard in the highly cooled turbine components of modern gas-turbine engines. The performance of cooling hole configurations is conventionally described by the cooling effectiveness and heat transfer coefficient. In comparison to cylindrical cooling holes, shaped geometries have received relatively little attention in film cooling literature. The studies that have dealt with shaped holes have shown that a lateral or fan-shaped expansion from a cylindrical entry portion demonstrates significantly improved cooling effectiveness in most configurations, particularly at higher blowing ratios. Flow field investigations indicate that the vortical structure at the hole exit is significantly altered from that of a cylindrical hole, and contributes to the greater lateral spreading of coolant and a resistance to jet lift-off. The shaped hole introduces additional geometric parameters which can significantly influence the internal and exit flow and subsequent cooling performance. The inlet conditions to the hole have been shown to significantly alter the flow distribution at exit of the hole for both cylindrical and shaped holes, due to separation and internal jetting. More recent studies have acknowledged the influence that inlet geometry and flow conditions can have on the development of flow through a cooling hole and the subsequent interaction with the mainstream. Computational studies have provided some assistance in understanding the complex flow fields within shaped cooling holes, but there is a clear lack of detailed experimental information on this internal flow that can validate simulations and allow the technology to progress.

Chapter 3

Similarity Parameters

3.1 Dimensional Analysis

In order for model test results to provide meaningful correlations to real world conditions, it is essential that the parameters determining the flow are properly identified. The principle of dimensional analysis provides a means of ascertaining the forms of physical equations from knowledge of relevant variables and their dimensions [64]. The dimensionless groups established from this method can be used in conjunction with the laws of similarity to translate model results to engine conditions.

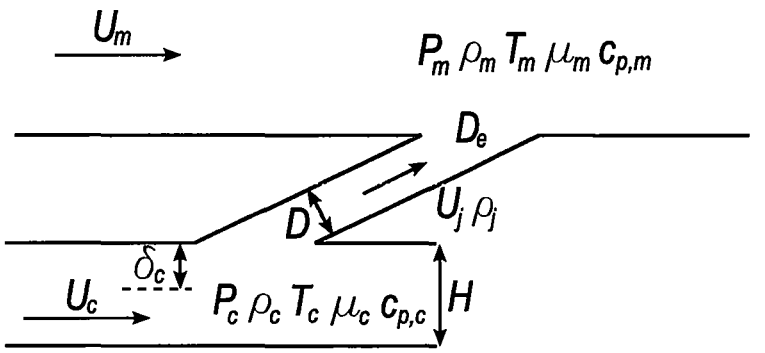

FIGURE 3.1: Schematic of typical film cooling configuration and variables

Figure 3.1 depicts the typical film cooling situation with both internal and external cross-flows present. The current investigation uncouples these two flows with the aim of examining the representative external flow with variations of internal parameters. The variables determining the internal flow configuration could be chosen as:

D	hole diameter
H	coolant passage height
δ_c	coolant passage boundary layer thickness
U_c	coolant passage mean velocity
D_e	hole exit equivalent diameter
P_{0_c}	coolant total pressure
ΔP	pressure differential across the cooling hole
T_{0_c}	coolant total temperature
ρ_{0_c}	coolant density
μ_c	coolant viscosity
$c_{p,c}$	coolant specific heat

Here there are 11 interrelated variables, involving four fundamental units: mass, length, time, and temperature. Application of Buckingham's Π theorem gives $(11 - 4) = 7$ independent dimensionless groups. These can be chosen as:

$$\frac{\rho_{0_c} D U_c}{\mu_c}, \frac{D_e}{D}, \frac{D}{H}, \frac{\delta_c}{D}, \frac{P_{0_c}}{\rho_{0_c} U_c^2}, \frac{U_c^2}{c_p T_{0_c}}, \frac{\Delta P}{\rho_{0_c} U_c^2}$$

From these, more common and meaningful dimensionless groups can be formed, as listed below.

$\frac{A_e}{A_t} = f_n(\frac{D_e}{D})$	area ratio of fan expansion
$\frac{\delta_c}{D}$	ratio of passage boundary layer thickness to hole diameter
$\frac{D}{H}$	ratio of hole diameter to coolant passage height
$Re_{c,D} = \frac{\rho_{0_c} D U_c}{\mu_c}$	coolant Reynolds number based on hole diameter
$Re_{c,H} = f_n(\frac{D}{H}, Re_{c,D})$	coolant Reynolds number based on passage height
$\frac{U_c}{U_j} = f_n(\frac{\Delta p}{\rho_c U_c^2}, \frac{D}{H}, Re)$	inlet velocity ratio (IVR)
$Ma_c = f_n(\frac{U_c^2}{c_p T_{0_c}})$	coolant Mach number

These dimensionless quantities define the important fluid dynamic relationships at the inlet to a film cooling hole. If we also include the flow conditions of the external cross-flow, a number of other dimensionless groups emerge, as demonstrated by Rowbury [5]. These include:

$Ma_m = f_n(U_m)$	mainstream Mach number
$Re_{m,D} = \frac{\rho_{0_m} D U_m}{\mu_m}$	mainstream Reynolds number based on hole diameter
$M = \frac{\rho_j U_j}{\rho_m U_m}$	coolant jet to mainstream mass flux (blowing) ratio
$I = \frac{\rho_j U_j^2}{\rho_m U_m^2}$	coolant jet to mainstream momentum flux ratio

3.2 Matching Engine Conditions

The current investigation is focussed on the internal cooling hole flow and the influence hole inlet conditions have on this flow field. The flow dynamics in these low speed tests are largely determined by the Reynolds number, as this dimensionless parameter gives the ratio of inertial forces to viscous forces in the fluid flow. Previous studies, such as [65] and [55], have used coolant passage Reynolds numbers based on passage height, H, in the order of $Re_{c,H} = 60,000$. The design of the current facility, as outlined in Ch. 4, achieves Reynolds similarity to engine conditions by matching the coolant passage Reynolds number $Re_{c,H} = f_n(D/H, Re_{c,D}) = 35,000$. In addition, the mainstream Reynolds number, $Re_{m,D}$, is matched to engine conditions; thus the dynamics of the flow at model scale can be transferred to engine conditions.

From the dimensional analysis another parameter, defined by this study as the inlet velocity ratio (IVR), is defined as $\frac{U_{c,0}}{U_j} = f_n(\frac{\Delta p}{\rho_c U_c^2}, geometry, Re)$. Similarly, we could choose the mean velocity component perpendicular to the cooling hole centre-plane, $U_{c,90}$, and dimensional analysis would give a inlet cross-flow velocity ratio as $ICVR = U_{c,90}/U_j$. The IVR (or ICVR) provides important information about the relationship between coolant passage and cooling hole jet flows, which will be shown to have a significant influence on the internal flow distribution within the cooling hole.

The cooling passage flow regime falls between the limiting cases of inviscid flow, and fully developed passage flow. For the former case the passage flow can be fully defined by the IVR for incompressible flow, or a momentum ratio for compressible flow. For the latter case the velocity distribution near the wall can be solely determined from knowledge of the passage Reynolds number or wall friction velocity ratio. In the general case, the coolant passage flow will not be fully developed and a boundary layer will be present on the passage wall preceding the hole inlet. Full specification of the flow condition approaching the inlet will then require knowledge of both the boundary layer thickness, δ_c and passage Reynolds number. Where the boundary layer thickness is comparable with the hole diameter the ratio of these two lengths, δ_c/D, also becomes relevant, and the velocity distribution of the whole boundary layer region needs to be defined. This is critical to the development of the in-hole flow, as the size of the coolant passage boundary layer and wall velocity gradients will, within limits, determine the condition of the hole inlet flow.

Neglecting compressibility effects at the hole entrance, the density of the coolant in both the passage and the cooling hole are the same, meaning that the inlet momentum flux ratio, $I = \frac{\rho_j}{\rho_c}.(\frac{1}{IVR})^2$, is solely a function of IVR. Geometric similarity is achieved

through a scale model of a typical fan-shaped cooling hole geometry and coolant passage height, hence D_e/D and D/H are matched to engine conditions.

3.3 Low Speed Limitations

The limitations of a low speed wind tunnel facility in terms of modelling a high speed flow occur through an inability to match Mach numbers, and difficulty in matching temperature and density ratios. In previous studies, the density ratio has been successfully matched to engine conditions through use of a dense foreign gas as the coolant. For aerodynamic problems, the temperature ratio of the hole is then considered to have little effect. In the present investigation, it is impractical to use a foreign gas due to the open circuit design of the wind tunnel; the large film cooling hole and long measurement times would require a large amount of gas to be used during testing.

As the density ratio between coolant and hot gas streams cannot be matched to engine conditions in the current investigation, the momentum flux ratio, blowing ratio, and velocity ratio cannot be simultaneously matched. With a unit density ratio, however, the blowing ratio collapses to the velocity ratio, while the momentum flux ratio reduces to the square of the velocity ratio. The parameter most commonly used in other research is the blowing ratio, M. The current investigation uses M to analyse the effects of the exit region interaction between the coolant and mainstream flows.

The low speed facility obviously cannot replicate compressibility effects such as shock waves, choking, and the resulting variations in flow properties. Coolant passage Mach numbers are often less than 0.6 in tests by other workers, and thus the presence of shock waves is unlikely in the internal flow regions. Through the cooling hole, however, the flow can accelerate significantly and may reach choked conditions in the throat of the hole. Such a situation brings about significant differences in the pressure distribution through the hole, determined by the area expansion of the fan-shaped diffuser (A_e/A_t). Further discussion of this effect is included in Ch. 7.

3.4 Summary

In the discussion of similarity to engine conditions for the current investigation, it is evident that certain non-dimensional parameters that influence the film cooling flow are not matched to the engine conditions. The low speed facility prevents matching of flow Mach numbers, and coolant to mainstream temperature and density ratios which prevents the external blowing and momentum flux ratios being simultaneously matched.

Similarity to the engine is drawn from a scaled geometry, and matching of coolant and mainstream Reynolds numbers. Full specification of the approaching coolant passage flow is obtained through additional information of the boundary layer thickness, and inlet velocity ratio.

Although there are some limitations imposed by the low speed modelling, it is important to highlight the goal of the current investigation. The current study aims to provide an extensive database of high resolution internal flow measurements for a typical fan-shaped film cooling hole. This database can then be used as validation data for more detailed computational simulations of film cooling flows. As such, the provision of complete engine representative conditions is not critical to gaining an understanding of the internal flow dynamics under different internal conditions, nor to generating data sets for validation of numerical techniques.

Chapter 4

Test Facility

Experimental work was carried out on the film cooling rig in the School of Engineering Aerodynamics Laboratory at the University of Tasmania. The film cooling rig is part of a more extensive research facility that includes a fully instrumented 1.5 stage axial compressor, a large recirculating tunnel, and several smaller multi-use wind tunnels. As detailed in the following sections, the pre-existing film-cooling facility required substantial modification to enable the flexibility required in representing engine conditions, as well as providing access within the cooling hole. The design, construction, and commissioning of the wind tunnel by the author formed a considerable portion of the research program, with many custom fabricated components required. In addition, the data acquisition system was installed onto a 'naked' wind tunnel, requiring significant set-up time. The end result is a flexible, capable, and high-quality film cooling research facility.

4.1 Pre-Existing Facility

The pre-existing wind tunnel selected for modification (as described in [66]) was an open circuit design using an axial flow fan to draw air through the working section. A previous alteration to the facility installed a 1 meter long working section with 225 $\times$ 225 mm cross-section, preceded by a smooth two-dimensional contraction (Fig. 4.1), as detailed in Sargison et al. [67] and Rossi [68]. The 6th degree polynomial wall profile resulted in mainstream turbulence intensity of 0.6%, flow direction uniform to within $\pm 0.5°$, and velocity uniform to within $\pm 2\%$. The boundary layer was tripped 200 mm upstream of the working section inlet to ensure a fully developed turbulent boundary layer, and the maximum mainstream velocity was 20 m/s. These features of the tunnel were retained in the updated design. The working section was configured so that an entire side could be removed to facilitate interchanging of model geometries. A cylindrical and a type B

FIGURE 4.1: Pre-existing film cooling research facility

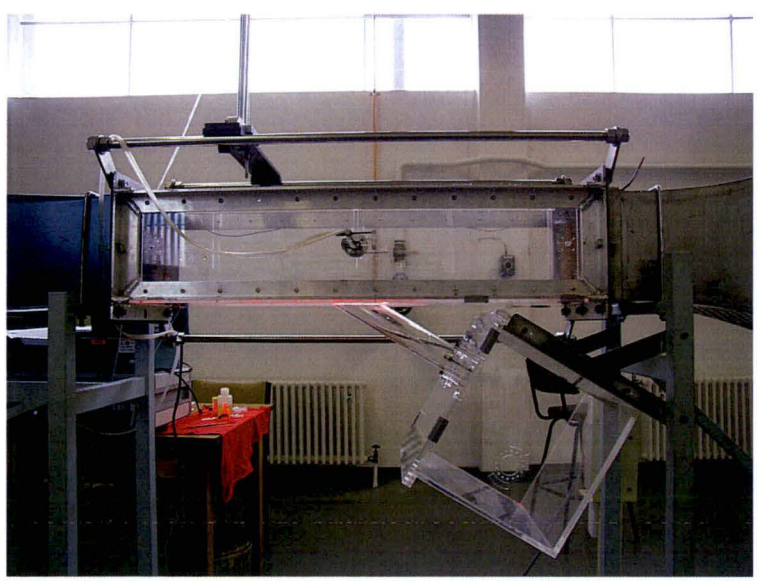

FIGURE 4.2: Plenum inlet to cooling hole model in pre-existing facility

fan-shaped cooling hole model could be fitted to the working section for testing. Cooling hole flow was supplied from a plenum, with the inlet plane perpendicular to the hole axis as shown in Fig. 4.2. Flow measurement was achieved via a bell-mouth nozzle fitted upstream of the plenum which drew air from atmosphere. The cooling hole mass flow was governed by the pressure differential across the hole created by the drop in static pressure relative to atmosphere of the mainstream cross-flow at the cooling hole exit. Flow metering involved insertion of uniform mesh screens at the plenum entry to achieve the required pressure differential. Mass flux ratios of up to $M = 0.76$ could be achieved in the pre-existing configuration.

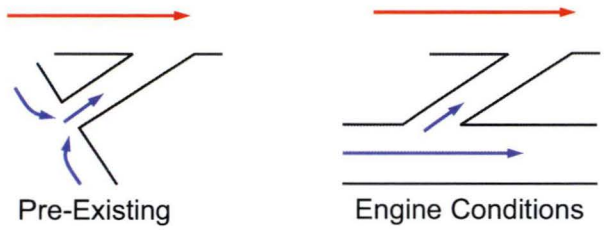

FIGURE 4.3: Comparison of pre-existing and typical engine conditions at the hole inlet

4.1.1 Limitations of the Pre-existing Facility

There are two primary reasons why the pre-existing wind tunnel facility was unsuitable for the current investigation. Firstly, the inlet configuration was not representative of engine conditions; and secondly, the achievable blowing ratios did not cover the span of typical engine values. In addition, the cooling hole models available were limited to a cylindrical hole and a type B shaped hole (refer Ch. 2) with 28° included angle, and had no provision for varying coolant passage orientation.

In a typical high pressure turbine blade, the coolant air is fed through a series of passages to be ejected out of rows of cooling holes. These internal passages are aligned radially with respect to the engine axis, from root to tip of the blade, whereas the hot-gas flow over the external surface of the blade is axial. To minimise mixing between coolant and hot-gas, film cooling holes are typically oriented so that the ejected coolant is aligned with the external cross-flow direction. This means that in the majority of locations around a cooled blade, the cooling hole axis is at an angle of approximately 90° to the internal coolant supply passage. The reality of the internal passage orientation means that the pre-existing configuration, with a plenum inlet, is not representative of the actual situation at engine conditions, as shown in Fig. 4.3.

4.2 New Facility Design

Table 4.1 lists a range of values comparing typical engine specifications with the capabilities of the newly designed facility. The design required greater flexibility in setting flow parameters such as the IVR and blowing ratio, covering values either side of unity. In addition, a focal point of this study is the effect of internal coolant passage orientation on the flow development within the cooling hole. To achieve this, the coolant supply passage configuration needed to have the ability to rotate relative to the plane of the cooling hole axis by at least 90° to achieve similarity to engine conditions. These requirements led to design of a coolant supply loop to sit below the existing wind tunnel

Parameter	Engine (Typical*)	Test Facility
D (hole diameter)	$0.7 - 1.2$ mm	50 mm
α (inclination angle)	$20 - 60°$	$30°$
L/D	$3 - 6$	5
Fan expansion angle	$14 - 32°$	$30°$
DR (density ratio)	$1.5 - 2$	1
VR (ext velocity ratio)	$0.5 - 2$	$0.5 - 1.9$
M	$0.8 - 4$	$0.5 - 1.9$
I	$0.9 - 2$	$0.25 - 3.61$
Re_{D_j}	$1 - 3 \times 10^4$	3×10^4

*Ref. [5, 14]

TABLE 4.1: Comparison of engine and experimental parameters for current study

and feed air from an external blower to the cooling hole. This supply loop incorporates a coolant passage to give internal cross-flow at the hole entrance, and an in-line fan to control the cross-flow velocity.

It should be noted that although the supply loop air is referred to as 'coolant', the temperature ratio between the two flows is not modelled. This is due to the difficulties in heating or cooling the large volumes of air required, and also the undesirable thermal effects on hot-wire measurements in the mixing region of the coolant and mainstream flows if they were at different temperatures. Hence the word 'coolant' is used more generally to describe the air passing through the supply loop and cooling hole model. There is scope, however, for experiments with different density ratios in future work by using a foreign gas with appropriate density as the coolant.

4.3 Coolant Supply Loop

Design of the coolant supply loop necessitated consideration of a range of constraints and requirements, such as flow rate, Reynolds number, pressure loss, flow condition, and physical geometry. A schematic of the basic set-up is shown in Fig. 4.4 and outlines the configuration of a flow loop with air supplied from an external blower, two 180° bends, an in-line axial flow fan, transition pieces, and a supply passage at the cooling hole inlet. The design of the facility enables independent control of flow conditions in the coolant passage, cooling hole, and mainstream, in a similar fashion to the facility described by Wittig et al. [69]. The coolant loop has a recirculating mass of air driven by the in-line axial fan. This controls the coolant flow rate in the coolant supply passage and thus the cross-flow velocity at the cooling hole inlet. The supply loop is sealed against leakage and closed apart from one inlet, connected to a metered air source, and one exit, the

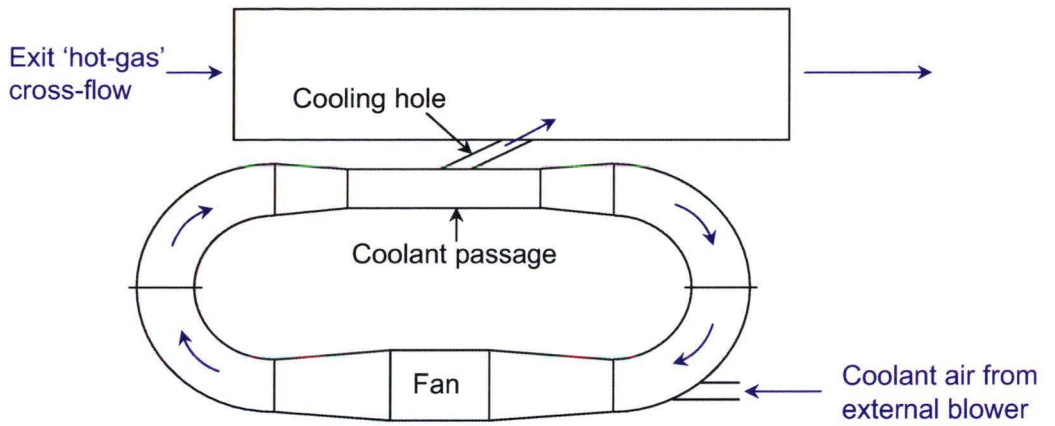

FIGURE 4.4: Schematic diagram of the re-designed film cooling facility

film cooling hole. In this way, at steady state, the mass flow of air that enters the supply loop is equivalent to the mass flow exiting through the cooling hole.

4.3.1 Coolant Supply Passage Configuration

To model the internal flow conditions of a typical turbine blade internal passage, a coolant supply passage was designed to condition the incoming coolant flow to the hole inlet. This passage has a rectangular cross-section and is constructed from clear acrylic sheet for optical transparency and low thermal and electrical conductivity. The supply passage dimensions were guided by the geometry and passage Reynolds number required to be representative of engine conditions, having a range of $7,000 < Re_{c,H} < 90,000$ [65], where H is the height of the coolant passage. Kohli and Thole [14] used a value of $Re_{c,H} = 30,000$ in their CFD study, while Hay et al. [46] list a value of $Re_{c,H} = 60,000$ as typical for engine conditions. The passage dimensions for the current study were chosen at a height of 100 mm (2D) and width of 180 mm (3.4D), with 6 diameters of uniform passage upstream and 4 diameters downstream of the hole inlet centre, as shown in Fig. 4.5. For a mean flow velocity of 7.5 ms^{-1} these dimensions give a passage Reynolds number of $Re_{c,H} = 5.1 \times 10^4$. These dimensions also provide a nearly constant cross-sectional area transition from the round cross-section duct work upstream of the passage.

To better represent the internal configuration of an actual blade, the coolant supply loop was designed to be able to rotate to a range of angles in the plane of the cooling hole inlet, thereby permitting investigation of the effects of internal coolant passage orientation on film cooling aerodynamics. To achieve this, the coupling between the cooling hole model and the supply passage consisted of a large 3.2D diameter round

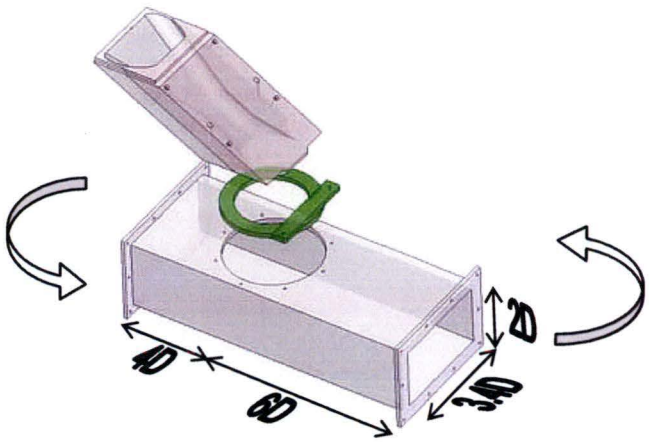

FIGURE 4.5: Coolant supply passage, interface flange, and cooling hole model exploded view

hole and a custom interface flange on each cooling hole model geometry to be inserted. The round hole permits rotation of the supply loop about the hole inlet centre, as shown in Fig. 4.5.

4.3.2 Transitional Pieces

The coolant supply passage is connected to the in-line fan and make-up air inlet through a series of connecting pieces and two 180° bends. At the design stage, dimensions were limited by the need to fit the supply loop underneath the existing wind tunnel, accommodation of the in-line fan and supply passage dimensions, a consideration of losses due to turning and flow separation, and the availability of suitable components. The in-line fan for controlling the passage velocity was sourced from Fantech based on expected head loss through the supply loop, and the required velocity head to achieve the design passage velocity of 7.5 ms^{-1}. The specifications of the Fantech TD-800/200 Hi are presented in App. B. The shroud diameter is 198 mm at the connecting flange and the fan is 302 mm in overall length. These dimensions together with those of the supply passage were fixed, and all connecting pipework needed to accommodate this.

For the 180° bends, research into plumbing products revealed a standard size PVC '90° bend' at a 150 mm inside diameter, and a radius of curvature of approximately 250 mm. Thus, two of these bends butted together resulted in a large radius 180° bend, which reduced aerodynamic turning losses. After discussion with the supplier, it became apparent that the bends were in fact 88° to provide slope in typical plumbing applications. A solution was to manufacture PVC flanges and extensions to correct the 2° offset and create a true 180° bend. A drawing of the flange and the finished product is shown in Fig. 4.6. To accommodate an inlet for the 'make-up' coolant fluid from the external

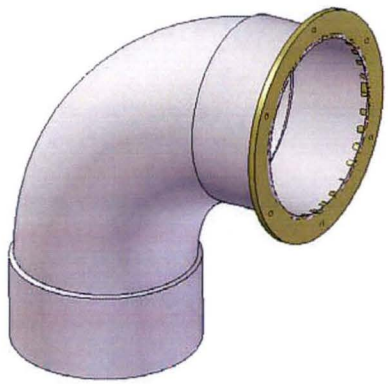

FIGURE 4.6: Coolant supply loop bend with 2° flange

supply, a piece of 40 mm PVC pipe was inserted into the lower bend upstream of the in-line fan, and shaped to match the contour of the bend wall. At the inlet to this pipe section was fitted a threaded collar and rubber o-ring coupling to secure to the coolant supply pipe work.

To change from the round cross-section bends to the rectangular cross-section supply passage, a transitional piece was designed to connect the two components. The dimensions of the transition are from a 150 mm diameter circle, to a 180×100 mm rectangle. This results in an area change of 328 mm^2, and requires a contraction in the vertical direction, and an expansion laterally. It was desired to keep the angle of expansion within 7° to minimise pressure loss from flow separation. The length of the transition was therefore described to stay within this maximum angle constraint. Similarly, two round-round transitional pieces were required to join the 150 mm pipe bends to the in-line fan (one diffuser and one contraction) restricted by the same maximum expansion angle of 7°. The length of these transitional pieces ultimately determines the overall length of the coolant supply loop. Therefore, there was an added geometric constraint brought about by the physical limitations of the main wind tunnel framework under which the supply loop had to fit.

With the dimensions of the transition pieces finalised after numerous measurements and calculations, design drawings were sent to a sheet metal fabricator for construction. 20 mm flanges were included in the design to permit fastening of the transitions to adjacent components. The finished transitions were painted and inside surfaces cleared of any irregularities to reduce frictional losses and flow non-uniformities. In addition, an epoxy filler was applied to the joins between components to eliminate any turbulence-inducing 'step' at the interfaces. All joints were sealed with a silicone gasket and tape where required.

4.3.3 Framework

Extensive measurements of the existing framework and components enabled a three-dimensional CAD model of the wind tunnel assembly to be constructed. A significant design challenge was to incorporate the supply loop within the confines of this framework, while still achieving the geometry to satisfy flow requirements. In addition, the coolant supply loop needed to rotate relative to the cooling hole centre-plane in order to change the coolant passage orientation. This required the supply loop framework to be mobile and also adjustable in height to permit disconnection from the main tunnel and re-orientation of the loop, and to correct for any variations in level of the laboratory floor. Three-dimensional drawings of all supply loop components were constructed in modelling software by the author as part of the design process, and these were assembled together with the existing framework to ascertain the areas where the new components would interfere with the existing tunnel. From this, it was decided to modify some of the horizontal members of the existing tunnel framework in order to provide clearance for the supply loop bends. The existing tunnel was disassembled and the modifications to the framework carried out by the School of Engineering workshop, including a fresh coat of paint.

The supply loop frame was designed in an 'H' shape with horizontal cross-members to support the top and bottom sections of the loop. Four castor wheels fitted to the bottom of each of four legs made the frame mobile, with a threaded T-bar providing manual height adjustment at each corner once the framework was in the desired position beneath the main tunnel. The completed supply loop and framework is shown in Fig. 4.7, and installed beneath the main working section in Fig. 4.8.

4.3.4 Coolant Air Flow Control

In the original coolant delivery design, a large compressed air storage tank on the roof of the aerodynamics laboratory was to be used to provide coolant during short duration testing. Calculations of tank capacity and discharge rate for the desired coolant mass flow rate through the cooling hole revealed that steady flow at the highest mass flow rate required would only be provided for approximately 10 minutes. As the majority of tests would require constant flow conditions for more than 30 minutes in many cases, an alternative was needed. Continuing with compressed air, a screw-type industrial compressor had been used to charge the storage tank and a direct outlet was available near the facility. This compressor was capable of delivering approximately 0.6 kgs^{-1} of air, which was well above the 0.072 kgs^{-1} required for the highest coolant flow case. A

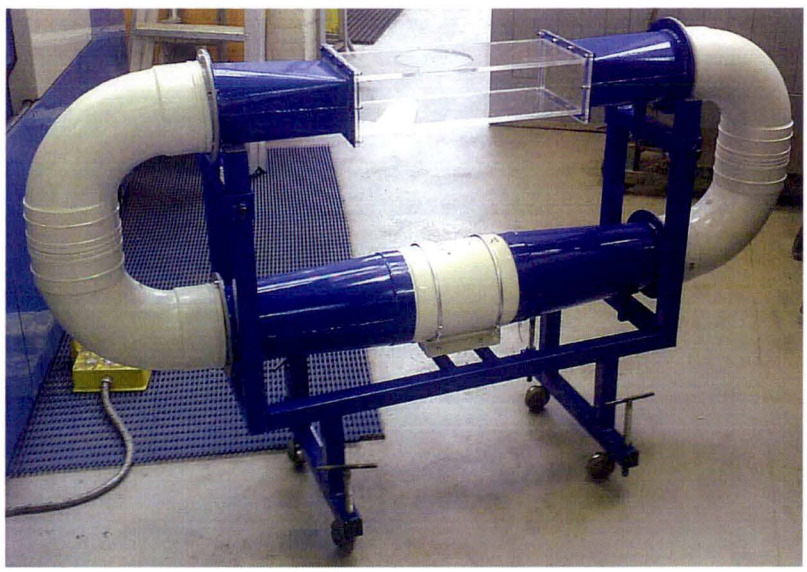

FIGURE 4.7: Assembled coolant supply loop and framework

FIGURE 4.8: Coolant supply loop installed into film cooling facility

mass flow metering system was installed at the compressed air wall outlet, which consisted of a pressure regulator, needle valve, digital flow rate meter, pressure transducer, and thermocouple. Measuring the volumetric flow rate from the meter, together with the pressure and temperature of the air, enabled the mass flow rate to be calculated. Initial tests with the screw compressor as the coolant source proved acceptable for low mass flow rates. However, during calibration at higher rates, the flow rate was found to fluctuate unacceptably due to compressor switching as the pressure in the receiver tank dropped below the set pressure. This fluctuation had a long period of approximately 3 minutes with an amplitude variation of 5-10% of the mean value. The set pressure on the compressor could not be varied as the air supply was used for other applications within the workshop.

With these results, attention was turned to the possibility of connecting a radial flow blower to supply the coolant loop inlet. An existing blower in the laboratory was tested for capacity in terms of head and pressure and found to be acceptable. This solution was advantageous for two reasons; the blower could be controlled remotely to maintain a set flow rate, and the flow rate was easily measured via a bellmouth nozzle and thermocouple on the intake of the blower. A Richardson VB $2\frac{1}{2}$ unit (App. B) was brought out of storage and refurbished for use with the film cooling facility. Once installed, a large radius bend and contraction piece was fitted to permit connection to the inlet coupling on the supply loop.

The in-line fan to control passage velocity is a 0.14 kW in-line mixed flow single phase fan made by Fantech, commonly used in air-conditioning applications. It is capable of delivering 200 Pa of head at a flow rate of 0.2 m^3s^{-1}. A Powerform Controls RC110B variable speed drive, with 0-10 V input, was coupled to the fan to adjust speed remotely via computer.

4.4 Cooling Hole Geometry

A novel aspect of this investigation is the use of a large scale film cooling hole model which permits the insertion of measurement probes to obtain detailed information on the internal flow characteristics. The cooling hole model geometry is at a scale of 50:1 as compared with film cooling holes in engine applications. This gives a cylindrical throat diameter of 50 mm.

The geometry was based around typical designs used in Rolls-Royce turbine blades [70]. The throat or metering section diameter of the hole was selected based on the maximum achievable mainstream velocity, and matching the hole Reynolds number to engine-like

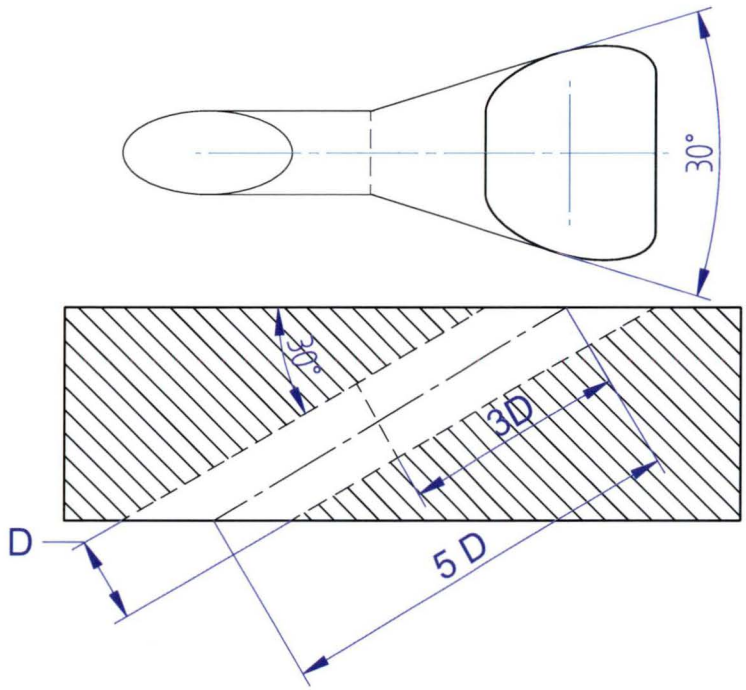

FIGURE 4.9: Cooling hole model dimensions

values in the order of $Re_{j,D} = 3 \times 10^4$. The hole length is $5D$ with a throat length of $2D$. A lateral expansion with an included angle of 30° completes the hole.

The hole model was cut from clear acrylic block on a computer numerically controlled (CNC) machine, and finished by hand to achieve a smooth, optically clear finish. A schematic of the geometry is presented in Fig. 4.9, and the final manufactured hole is shown in Fig. 4.10.

4.5 Instrumentation

For any type of experimental investigation, it is the instrumentation that provides the link between a physical quantity and a numerical representation of that quantity. Appropriate selection of instrumentation that satisfies the requirements of accuracy, precision, time response, and output type, requires due consideration prior to embarking on any type of measurement activity.

4.5.1 Traverse System

Positioning of probes within the measurement domain with good precision is essential in providing confidence in the spatial resolution of experimental data sets. To facilitate

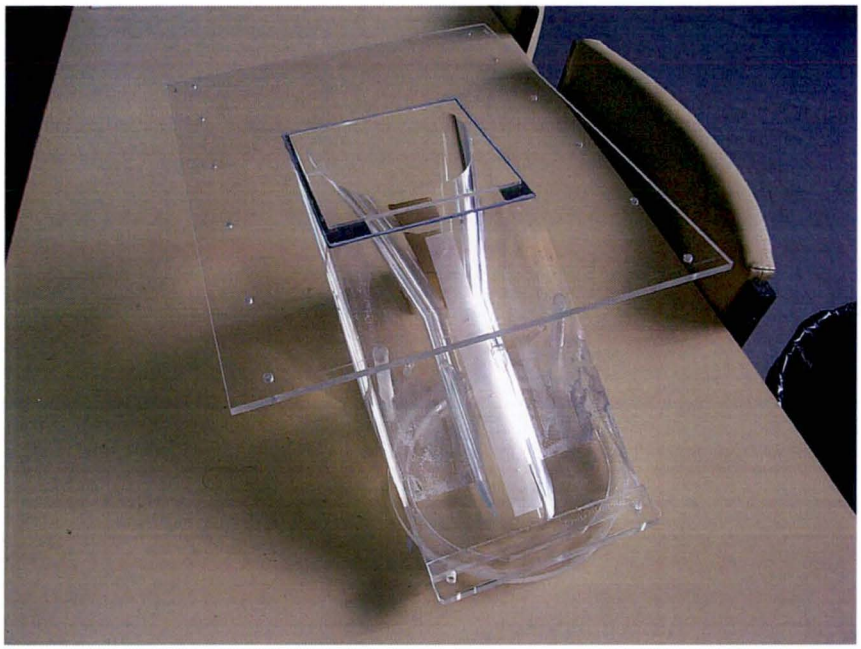

FIGURE 4.10: Example of completed cooling hole model

precise movement within the working section of the film cooling facility, a 3-axis traverse system was designed and installed. The traverse has manual control in the longitudinal and lateral directions, and has an automated, step-driven system for the vertical direction. This automated system has a resolution of 0.005 mm and is controlled via computer using custom programming. The longitudinal traverse utilises linear shaft bearings to provide smooth travel, and a metric scale with 0.5 mm resolution. The lateral traverse is accomplished via a specially designed mechanism, involving a threaded drive shaft that moves a carriage along two machined guide rails. The position of the carriage is monitored via an electronic vernier with 0.01 mm resolution.

In addition, the automated traverse can be mounted such that the probe axis is in line with the plane of the cooling hole axis, at 30° to horizontal. This configuration permits the probe to be traversed within the cooling hole, extending into the coolant passage if desired. Special probe extensions were manufactured to facilitate this. The traverse system thus enables almost the entire cooling hole and exit cross-flow domains to be investigated. The traverse is shown in Fig. 4.11.

4.5.2 Coordinate System

The coordinate systems for the measurement domain are shown in Fig. 4.12. Each of the coolant supply passage (s), cooling hole (h), and exit cross-flow have a local origin and system of coordinates to make specification of spatial position simpler. The origins

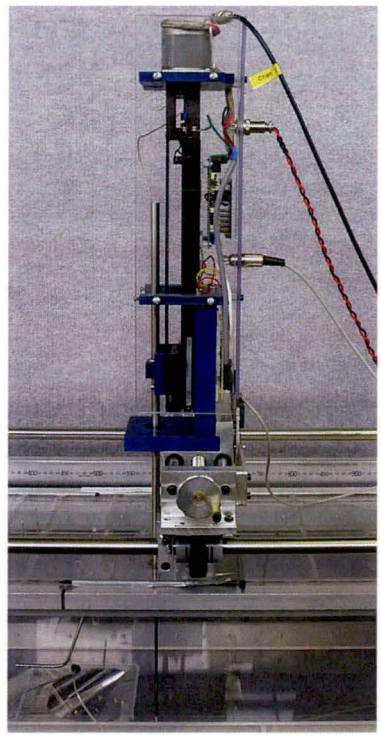

FIGURE 4.11: Stepper motor traverse installed over working section

of these coordinates are placed at the centre of either the cooling hole inlet or outlet plane, and aligned such that the X-axis is parallel with the bulk flow direction. The coordinates assume the right-hand configuration, such that the positive Z-axis is out of the page for all coordinate systems, with $Z = 0$ lying on the cooling hole centreplane.

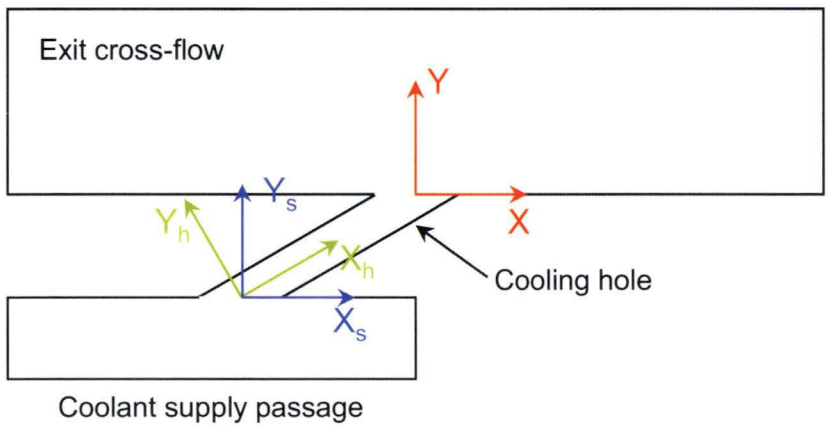

FIGURE 4.12: Coordinate system origins and X-Y coordinate axes

4.5.3 Pressure Measurement

Despite advances in alternative technologies, the measurement of pressures in fluid dynamics research has remained very important in quantifying flow behaviour. In this investigation, wall pressure tappings were used to monitor static pressures at various locations. These include the static pressure differential of the tunnel contraction, used to measure the flow velocity in the exit cross-flow, and the static pressure at the hole exit to determine discharge coefficients. Other steady pressure measurements include those for the Pitot-static probe, which was used to measure free-stream velocities in both the coolant supply passage and exit cross-flow. The Pitot-static probe enables the local total, P_{tot} and static, P_{stat} pressures of the flow to be measured simultaneously. The difference between these two pressures represents the dynamic pressure $P_{dyn} = P_{tot} - P_{stat}$, from which a velocity can be calculated based on the Bernoulli principle as

$$P_{dyn} = \frac{1}{2}\rho.U^2.C \tag{4.1}$$

where ρ is the fluid density, U is the flow velocity parallel to the Pitot-static head, and C is the coefficient of the probe. The Pitot-static probes used in this investigation were 4 mm diameter Airflow Dynamics probes. These probes have a coefficient of very close to unity, with minimal error for yaw angles less than $\pm 5°$. Hence, in practice, a value of $C = 1.0$ was used.

Static pressure measurements were made predominantly with two micromanometers from Furness, an FCO12 and FCO14. These are pressure transducers with a 0-5 volt output for acquisition. The FCO12 has a digital display and a range of 199.9 mm H_2O, and the FCO14 has an analogue gauge and range of 100 mm H_2O. A Furness FCS421 pressure scanner was used to easily connect multiple pressure measurement locations to the one transducer. This scanner could be controlled via an RS-232 serial connection to computer.

4.5.3.1 Unsteady Pressures

The time-dependent behaviour of a fluid flow can reveal much about the underlying processes that drive that behaviour. When working with air, the maximum frequency at which a measurement system can accurately follow pressure fluctuations is governed by a number of factors, but primarily by the response characteristics of the sensing element and the connecting tubing. Higher frequency response is obtained with smaller diameter tubing and thus lower volume of air between the measurement location and the sensor. It is possible, however, to calculate the response characteristics of a particular

system, or even to experimentally calibrate a system by using a set of known excitation frequencies.

For the current investigation a Dynamic Pressure Measurement System (DPMS) manufactured by Turbulent Flow Instrumentation (TFI) was installed to monitor the transient wall pressures along the axis of the cooling hole model. The system provides eight temperature compensated pressure transducers with a range of 2.5 kPa, optimised for ±1 kPa, housed in two 4-transducer units. These transducers were experimentally calibrated by TFI using a set length of tubing. The best system response of approximately 7 kHz was achieved with a 0.65 mm inside diameter tube at 65 mm length. This configuration was used in the experimental results presented in Ch. 7. A photo of a transducer module installed on the wind tunnel is shown in Fig. 4.13.

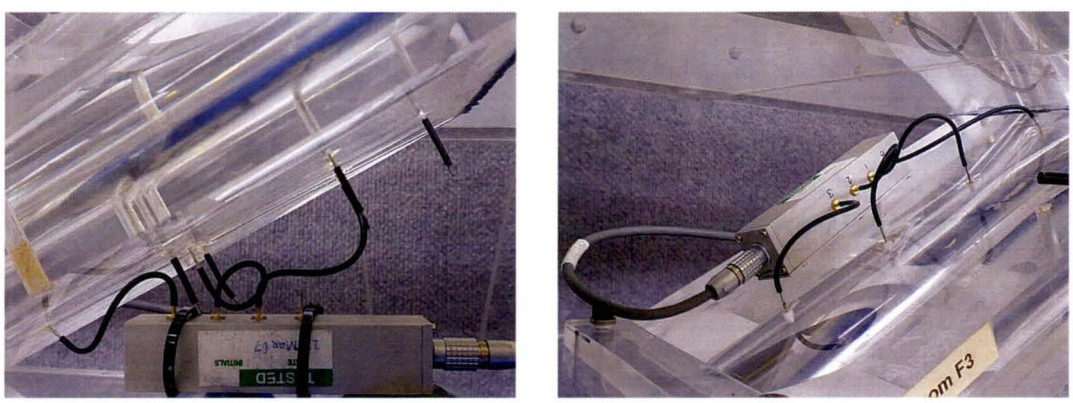

FIGURE 4.13: Dynamic Pressure Measurement System installed on cooling hole throat

4.5.3.2 Calibration

A Beltz precision differential liquid manometer was used as a calibration laboratory standard to gain an estimate of bias error in the manometers, and reduce this error through a calibration curve. The Beltz manometer has a resolution of ±1 Pa. The precision error was estimated from a series of measurements over several minutes with the Beltz manometer held at a fixed pressure reading. Results indicated precision uncertainties of 0.115 Pa for an individual measurement. The combined overall uncertainty was ±1.01 Pa. The determined calibration curve (Fig. 4.14) was applied to all measurements from the Furness manometers.

4.5.4 Hot-wire Anemometry

Measurements of velocity and turbulence intensity in this investigation were made using hot-wire anemometry. This technique is well-established, accurate and reliable, and

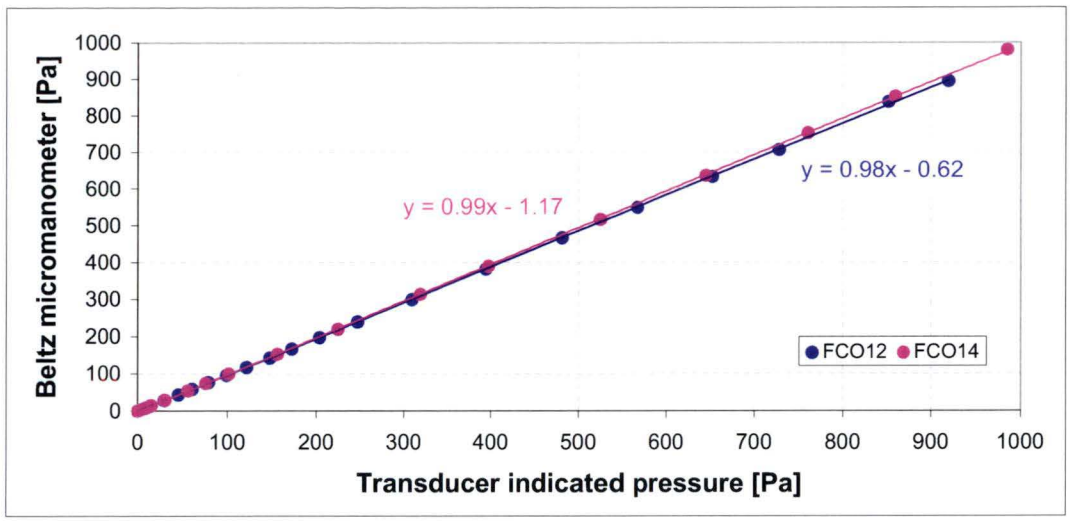

FIGURE 4.14: Calibration of Furness transducers against Beltz laboratory standard manometer

when appropriately tuned, provides a high frequency response. The constant temperature anemometer (CTA) works on the basis of convective heat transfer from a heated sensor to the surrounding fluid; the heat transfer being related primarily to the fluid velocity. The rate of heat loss depends on the excess temperature of the sensing element, its physical properties and geometrical configuration, and the properties of the moving fluid [71].

Single axis probes were used in the current investigation due to their robustness, ease of calibration and use, and relatively low cost. The probes selected were 55P11 miniature wire probes manufactured by Dantec Dynamics, and fitted to an assortment of probe supports from the same manufacturer. The 55P11 have a 5 μm diameter, 1.25 mm long platinum-plated tungsten wire sensor welded directly to the prongs, with the entire wire length acting as the sensor. The probe body is a 1.9 mm diameter ceramic tube, equipped with gold-plated connector pins that connect to the probe supports by means of a plug and socket arrangement (Fig. 4.15).

The hot-wire probes were connected to a two-channel TSI IFA100 constant temperature anemometer. This has an output voltage of 0-12 V, maximum bridge current of 1.2 A, and an amplifier gain of greater than 1×10^6.

4.5.4.1 Signal Conditioning

Signal conditioning was performed by a model 157 signal conditioner contained within the IFA100 cabinet. This has the ability of providing a 0-9 V offset and gain of between 1-900, with a frequency response of 400kHz at a gain of 10. A low-pass filter provides

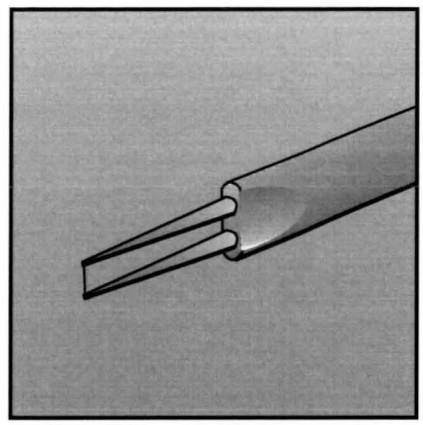

FIGURE 4.15: Dantec 55P11 hot-wire probe, 5μm diameter, 1.25 mm long sensing element

18dB/octave roll-off at frequencies between 1Hz-500kHz. Typical settings were an offset of 1 and gain of 10. Output from the signal conditioner was passed directly to the data acquisition board.

4.5.4.2 Calibration

Hot-wire calibration followed a standard procedure as outlined in the TSI manual [72] and in the Dantec guide [71]. Probe and cable resistances were measured using the IFA100 to within 0.003 ohms. The hot-wire sensor was calibrated in-situ against a Pitot-static probe in the uniform and one-dimensional free stream of the exit cross-flow. An automated procedure stepped through tunnel velocities up to 20 ms^{-1} and recorded the necessary data. A MATLAB routine processed the raw data to determine the dimensionless relationship between the flow velocity and wire heat transfer. Temperature variations are compensated for through the heat transfer equation. A typical calibration curve is shown in Fig. 4.16. Typical uncertainties in a velocity measurement following this calibration method are 3% with a 95% confidence interval.

The use of a single axis probe in a highly three-dimensional flow does, however, bring with it errors in measured values due to the insensitivity to flow direction of the probe. In the case of a wire with a finite length, the temperature is not constant over the length of the wire and aerodynamic perturbations are created by the prongs. These are taken into account by arguing that the component of velocity that is parallel to the axis of the wire now contributes to the cooling effect [73]. The plot in Fig. 4.18 demonstrates the effect of yaw angle on the effective velocity, as defined in Fig. 4.17.

There are also effects of probe stem orientation relative to the flow direction, with studies showing up to 20% variation in measured velocity as the stem is rotated about

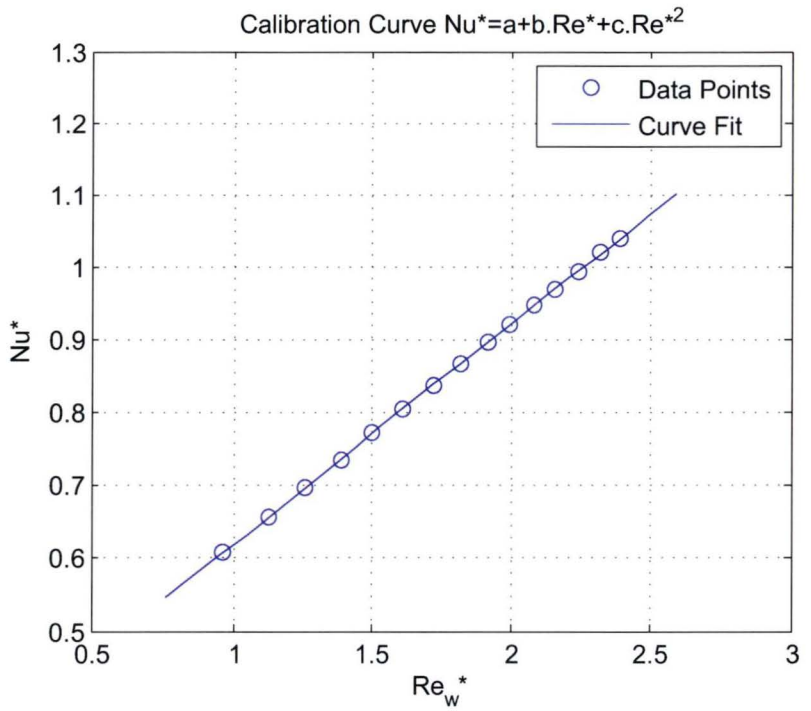

FIGURE 4.16: Typical non-dimensional calibration of hot-wire

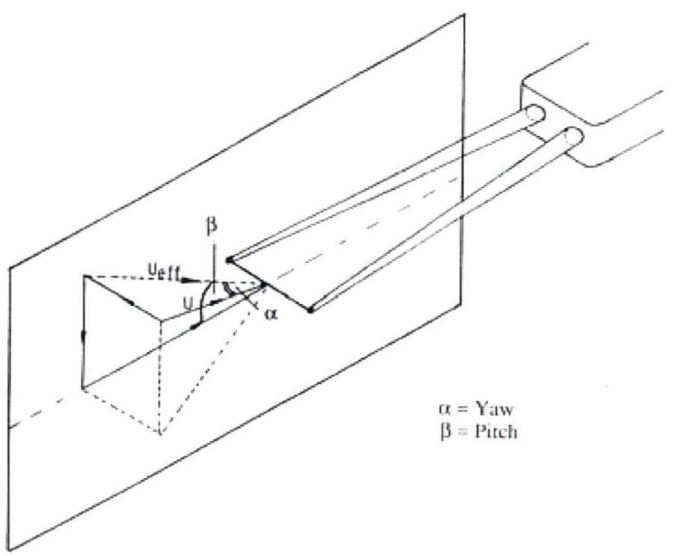

FIGURE 4.17: Definition of yaw and pitch angles relative to the hot-wire sensor

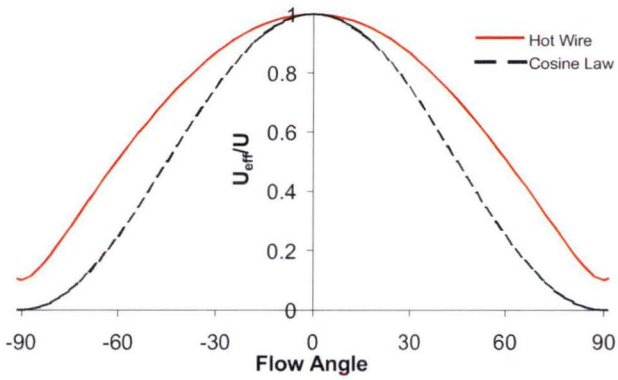

FIGURE 4.18: Effect of flow yaw angle on response of hot-wire sensor

the sensing element from $\beta = 0°$ to $\beta = 90°$ [74]. In the current investigation, the probe stem was aligned parallel to the mean flow direction, reducing blocking effects and vortex shedding from the sensor prongs.

It should be noted, however, that the measured velocity from anemometry presented in subsequent chapters will, in most cases, represent an effective velocity that contains a component at some angle to the probe axis. In the case of yaw, the effect is small. In the case of pitch, variations have been minimised by aligning the probe support with the bulk flow direction.

4.5.5 Thermocouples

Temperature measurements were made using type-K chromel-alumel thermocouples. Calibration was performed using a standardised controlled temperature bath and a zero degree ice bath as a reference. The calibration characteristics were integrated into the acquisition system.

4.6 Control and Data Acquisition System

National Instruments (NI) manufacture a large variety of PC-based data acquisition and control hardware that provide excellent flexibility and cost-effective solutions for laboratory environments. The acquisition boards used in this study were a NI PCI-6221 multifunction DAQ card for high speed acquisition and general input/output, a NI USB-6008 for additional input/output, and an NI 4351 logger and TBX-68T terminal block for acquiring thermocouple temperatures. NI also design and distribute software that provides a reasonably convenient programming interface. LabVIEW is a graphical

programming environment from NI used to develop sophisticated measurement, test, and control systems using graphical icons and wires that resemble a flowchart.

Various system components required control via computer interface to facilitate semi-automated operation of data acquisition routines. All three flow control fans were operated remotely via a 0-5V output to the speed controllers. On the larger 2-phase fans controlling the exit cross-flow and cooling hole flows, Xtravert model X707 and X709 controllers were used, while on the smaller in-line coolant supply loop fan, a Powerform Controls RC110B was utilised. In addition to the fans, the stepper motor traverse was controlled via computer as part of an extensive interface between instrumentation and the laboratory computer using custom LabVIEW routines.

Control of the film cooling facility was implemented via a complex, unique set of LabVIEW virtual instruments (VIs). The created program was structured such that the top-level VI, which incorporated the user interface, called on a number of nested or sub-VIs. This structure, typical of most function-based computer programming, reduced the complexity of any individual VI but also added increased flexibility in the operation of the final program. An image of a section of the front panel of the main user-controlled VI is shown in Fig. 4.19, and a section of the associated block diagram is shown in Fig. 4.20. As can be seen from these images, the user interface provides direct control of most system parameters and important feedback on measured signals and flow conditions. By selecting appropriate combinations of front panel buttons, the user is able to switch between several 'modes' of operation, toggling between calibration and measurement, manual and automated probe positioning and acquisition, as well as displaying the acquired information from different sources in close to real time. The small section of the corresponding block diagram gives insight into the complexity of the 'back-end' of the created virtual instrument.

This level of functionality was essential to provide a system that was able to adapt to different measurement plans, but also to be robust and reliable. It is difficult to convey the level of effort that was put into creating and tuning the LabVIEW interface so that the data acquisition process was as straight-forward as possible. Needless to say it was many hours and a significant portion of the facility set-up time. The end result, however, is a system that provides an excellent level of control and a multitude of data acquisition options.

4.6.1 Data Analysis

Processing of recorded data was performed largely with a suite of custom MATLAB functions and scripts. Data was output in a standard form by the LabVIEW interface

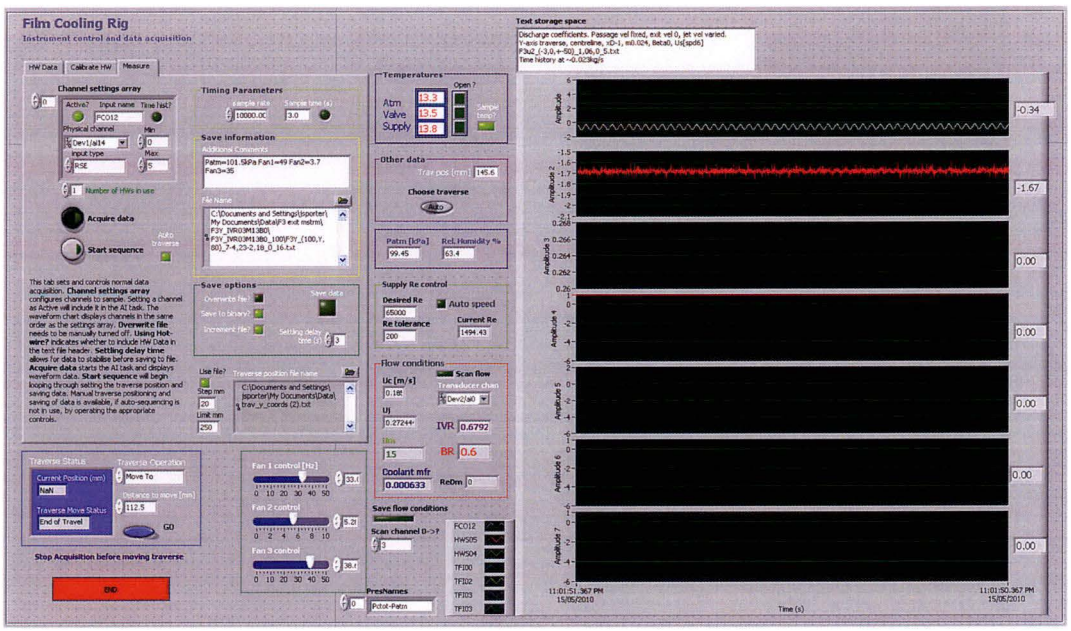

FIGURE 4.19: User interface (front panel) of LabVIEW control and acquisition virtual instrument

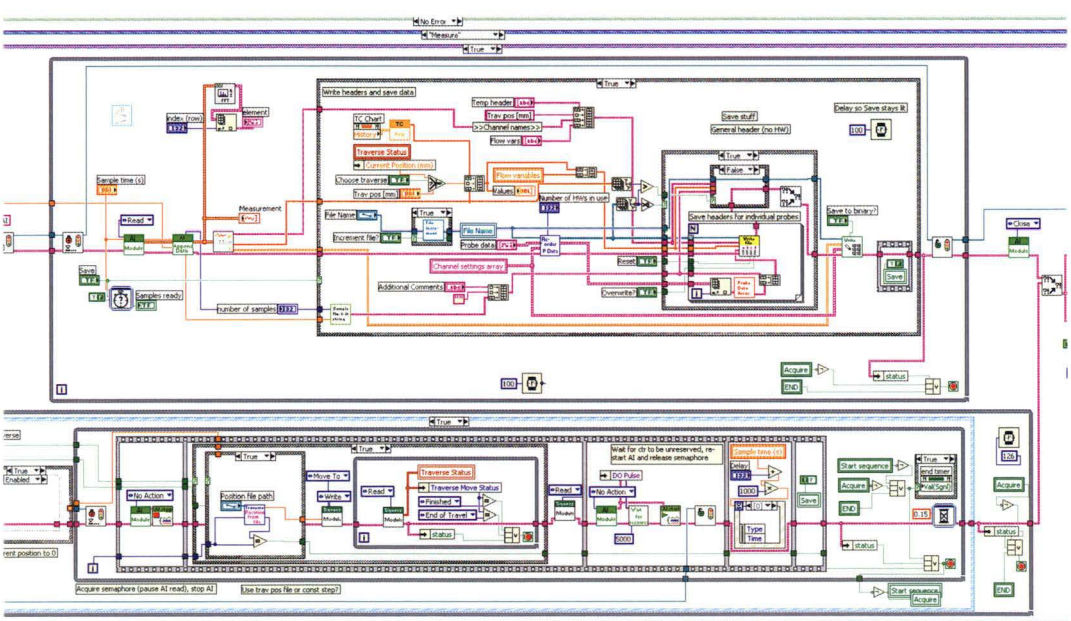

FIGURE 4.20: Section of LabVIEW block diagram

and was read into MATLAB to be processed in a number of ways. By utilising the strength of MATLAB's vector-based architecture, large data files could be read and processed swiftly, to do such things as determine velocity and turbulence information from hot-wire signals, compile and sort multi-dimensional arrays of data, analyse time-dependent signals, and display results in graphical form. As with the LabVIEW coding, much time and effort was put into generating robust, reliable, and efficient MATLAB codes so that any changes in the measurement approach could be easily incorporated.

4.7 Facility Commissioning

When taking any type of reading, regardless of the application, there are often numerous points in the measurement system where errors or irregularities can be introduced, and it is only through identification and understanding of these error sources that confidence in experimental data can be found. This paradigm is also applicable to the experimental apparatus itself, as events during construction and the imperfect nature of real world components combine to produce a piece of equipment that has its own unique characteristics.

The newly designed coolant supply loop required calibration to ensure confidence in the system's performance. The mass flow rate of air entering the supply loop needed to be accurately known in conjunction with the leakage characteristics of the loop to determine the mass flow of air through the cooling hole model and thus the mean throat velocity and blowing ratio. In addition, the coolant passage velocity at the hole inlet needed to be defined in terms of velocity magnitude distribution, flow direction, and turbulence level.

4.7.1 Exit Cross-flow

The mainstream exit cross-flow is measured via static wall tappings at either end of a calibrated two-dimensional contraction. Calibration of the contraction was repeated using the current measurement system and a Pitot-static tube to confirm the relationship between static pressure differential across the contraction and the velocity in the working section. The calibration curve is shown in Fig. 4.21.

4.7.2 Coolant Air Metering

In order to calculate the velocity of coolant through the metering section of the cooling hole geometries (required for determining the IVR and M) the mass flow rate of the

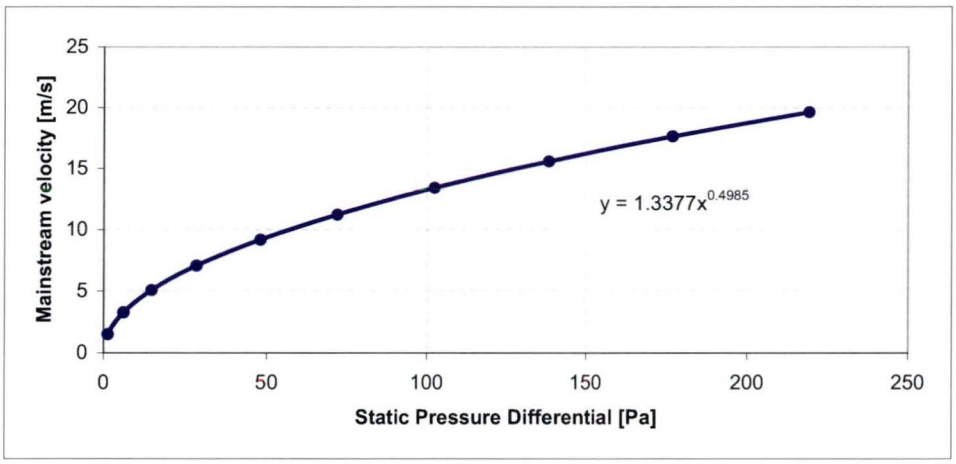

FIGURE 4.21: Exit cross-flow contraction calibration curve

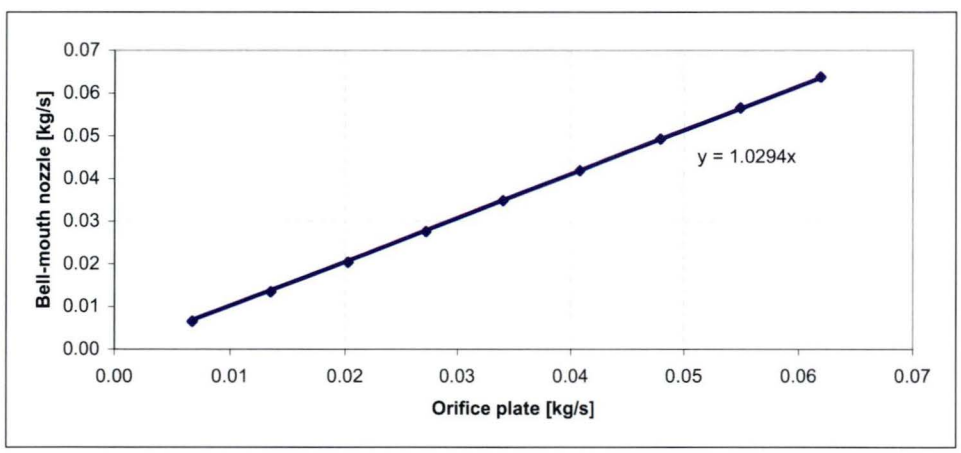

FIGURE 4.22: Calibration of coolant mass flow rate against standard orifice

coolant needs to be known. The design of the supply loop means that the mass flow of air entering the loop is equivalent to that leaving the loop through the cooling hole. Therefore, accurate measurement of the mass flow through the cooling hole is essential in calculating the velocity through the metering section. As described in Sec. 4.3.4, a bell-mouth nozzle is used in conjunction with the Furness FC012 pressure transducer to measure the coolant flow rate. This configuration was calibrated against a standard orifice plate. The plate was fitted within a length of pipe at a location conforming to the guidelines in BS 1042: Part 2A. The pipe transitioned to flexible tubing upstream with a matching connection to the outlet of the blower. The mass flow rate from the system was set to a range of values that created a calibration curve for the flow measurement system. Figure 4.22 shows the resulting plot and fitted polynomial regression. The combined total uncertainty in mass flow values is less than 3% of a reading.

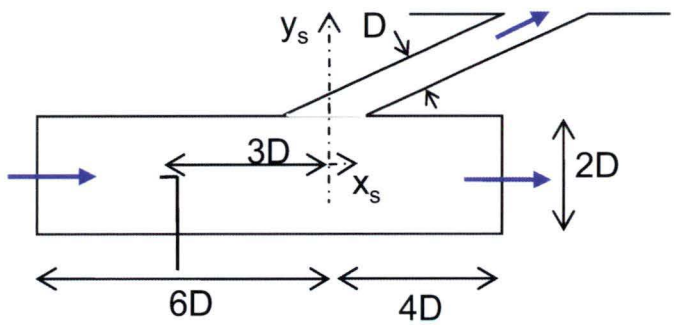

FIGURE 4.23: Measurement probe insertion points in coolant supply passage

4.7.3 Supply Passage Uniformity

4.7.3.1 Mean velocity

Measurements of flow velocity, direction, and turbulence were made in the coolant supply passage upstream of the cooling hole inlet. Probe insertion points were created on the supply passage mid-planes to allow both a vertical and horizontal traverse, as indicated in Fig 4.23. A 4 mm Airflow Developments Ltd Pitot-static tube was used to make time-averaged velocity measurements in each traverse direction to determine the uniformity of flow in the passage. Initially, no flow conditioning was installed in the supply loop between the blower and supply passage. The vertical Pitot traverse revealed significant non-uniformity in the flow due to a combination of flow turning through the bends, and a residual effect of the fan. Progressive levels of conditioning, consisting of 2 mm square nylon mesh screens, were inserted into the loop at flanged connections between the transitions and 180 degree bends upstream of the passage. The process was incremental, starting with a single layer of mesh at the upper flange, and adding up to two layers of non-aligned mesh at the upper and lower flanges. A section of honeycomb straightener (cell length 5x cell diameter) was also positioned in the round-rectangular transition just upstream of the passage start.

The resulting profiles from various configurations of mesh (Tab. 4.2) are shown in Fig. 4.24. It is interesting to compare the vertical profiles with those from a horizontal traverse, as shown in Fig. 4.25. It can be immediately seen that the horizontal profiles exhibit far less variation than their vertical profile counterparts. This led to the conclusion that the large peaks in the vertical profiles near the walls and significant variation through the interior could not be due to the blower, as some radial consistency in the profiles would be expected in that case. Attention was subsequently drawn to

	Mesh at bend start	Mesh at bend end	Honey-comb	Mesh over honeycomb
A				
B		•		
C	•	•	•	
D	•	•	•	•

TABLE 4.2: Test configurations for coolant passage flow control

the positioning of the honeycomb in the end of the round-rectangular transition. It was possible, due to the convergent angle of the transition upper and lower walls, that some coolant may have been ejected from around the honeycomb at an angle to the passage axis. This fluid would also be slightly accelerated as it passed through the reducing flow area between the angled wall and axially aligned honeycomb exterior, and would not be subjected to pressure losses from entering and passing through the honeycomb cells. This would explain the regions of higher velocity fluid near the walls. As a result, it was decided to move the honeycomb into the rectangular supply passage to try and eliminate this feature.

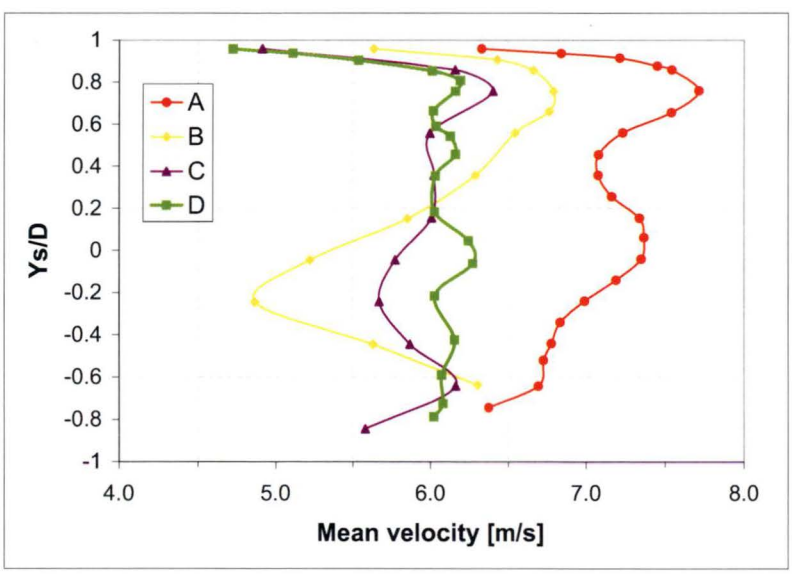

FIGURE 4.24: Vertical centreline mean velocity profiles in coolant supply passage

Placing a layer of nylon mesh across the downstream end of the honeycomb had a significant impact on the uniformity of the velocity profile in the supply passage. This is due to the smaller mesh cell size breaking up the wakes from the honeycomb cells and thus reducing the length scale of the turbulent eddies. Smaller eddies take less downstream distance to dissipate and create a more uniform flow more quickly. There is still some variation across the passage, however the profile is quite flat through the central region with flow uniformity to within 1.5%.

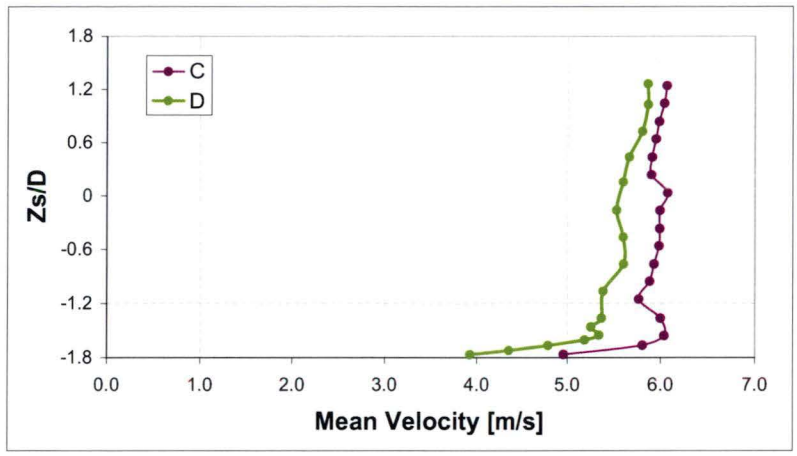

FIGURE 4.25: Lateral centreline mean velocity profiles in coolant supply passage

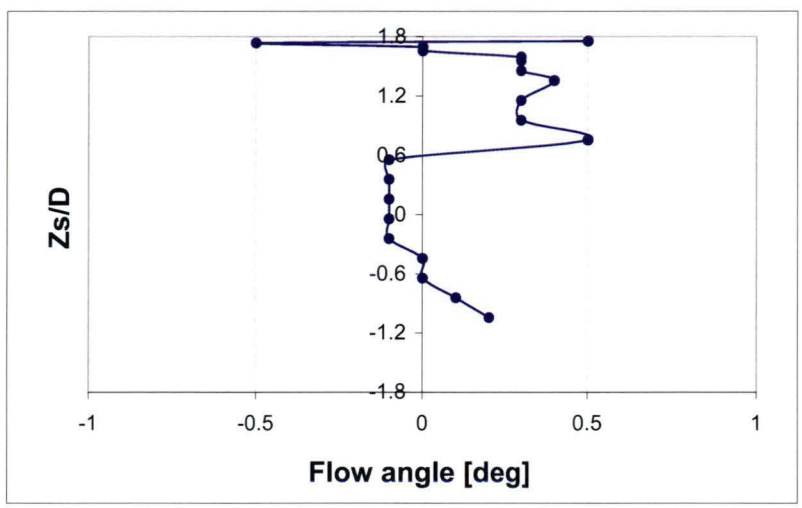

FIGURE 4.26: Vertical centreline mean flow angle in coolant supply passage

It should be noted that in an actual turbine blade passage, the flow would be expected to be somewhat non-uniform due to the presence of turbulating ribs, passage bends, and flow effects from preceding holes. So although we wish to have a consistent and defined velocity profile upstream of the hole inlet, the creation of a typical profile for fully developed flow is not essential.

4.7.3.2 Flow direction

A 3-hole wedge probe was used to assess the flow direction in the mid planes of the supply passage. The results, shown in Fig. 4.26, indicate that the honeycomb flow straightener works well. Flow direction is parallel to the passage walls to within $\pm 0.5°$.

4.7.3.3 Turbulence intensity

A single axis hot-wire probe provided measurements of average velocity and turbulence intensity in the supply passage. Measurements revealed good agreement with velocity profiles from the Pitot-static traverse. Turbulence intensity values of about 2% were measured through the central region of the passage flow, increasing toward the walls through the boundary layer region. The effect of the mesh on the downstream side of the honeycomb flow straightener can be seen in the uniformity of the turbulence intensity through this central region in Fig. 4.27.

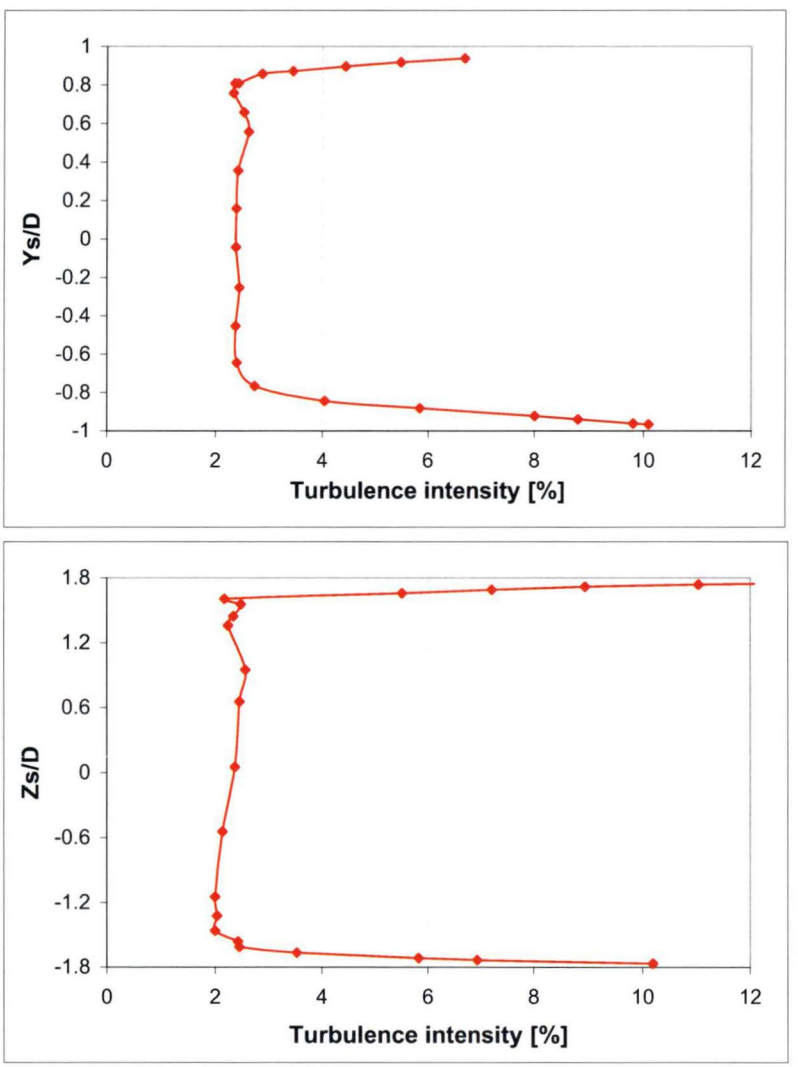

FIGURE 4.27: Vertical (a) and lateral (b) centreline turbulence in coolant supply passage

4.7.3.4 Passage boundary layer condition

Coolant passage boundary layer data is presented in Tab. 4.3. The boundary layer thickness varies only slightly across the three test cases, between 14% and 16% of the inlet diameter. The wall friction velocity upstream of the hole inlet shows a much greater variation with Reynolds number. For experimental results presented in the following chapters, the coolant passage Reynolds number $Re_{c,D}$ is held steady at about 2.3×10^{-4}.

	δ/D	IFVR	$\mathbf{Re_{c,D}(\times10^{-4})}$
$IVR = 0.3$	0.143	0.026	0.9
$IVR = 0.6$	0.157	0.103	1.8
$IVR = 0.9$	0.161	0.178	2.5

TABLE 4.3: Coolant passage boundary layer condition at inlet

4.7.4 Measurement Uncertainties

Uncertainty analysis is an important component of the presentation of measured data. A comprehensive review of error sources and the propagation of those errors through the measurement system and subsequent data reduction allows a defined level of confidence to be established in the reported values. Instrumentation of the wind tunnel included calibration and uncertainty estimation for the various measurement devices in use. The procedure followed was based on the approach of [75] and similarly from [76] and [77]. All combined uncertainties are expressed at 95% confidence and result from appropriate propagation of uncertainties through the measurement and data reduction system. Typical uncertainty estimates for key variables are described in Tab. 4.4.

Measurand	Uncert. (95%)	Typ. value	Typ. error
Hot-wire velocity U	3.2%	19.2 ms^{-1}	0.61 ms^{-1}
Passage velocity U_m	3.6%	7.5 ms^{-1}	0.26 ms^{-1}
Mass flow rate $\dot{m}$	4.5%	1.75×10^{-2} kgs^{-1}	7.87×10^{-4} kgs^{-1}
Discharge coefficient C_d	5.1%	0.98	0.05

TABLE 4.4: Uncertainty estimates for measured quantities

4.7.5 Unsteady Flow and System Resonant Frequencies

The large expansion angle of the diffuser used in the current study is greater than that typically required for the flow to remain attached to the sidewalls. It is expected, therefore, that flow separation will occur to some extent in the diffuser, and regions of stalled fluid will be present. The inherently unsteady nature of these areas of stall may

give rise to periodic flow phenomena, such as a 'flapping' of fluid from side to side as recirculating eddys are shed from the walls. In addition, natural resonant frequencies of the tunnel may give rise to periodic components in the hot-wire signal. An investigation of these effects did not reveal any strongly dominant frequencies, nor the existence of any side-to-side periodicity within the diffuser. Further details can be found in App. A.

4.8 Summary

Construction of a dedicated facility for large scale testing of film cooling geometries has been accomplished by the author in the UTas School of Engineering Aerodynamics Laboratory. The wind tunnel provides flexibility in setting the conditions at the hole inlet including the coolant supply passage orientation and inlet velocity ratio. There is scope for different cooling hole geometries to be installed. The facility includes instrumentation to enable flow control and monitoring of flow conditions within the working sections. Measurement of mean velocity and turbulence intensity is conducted using hot-wire anemometry, and a high accuracy three-axis traverse system with capability for in-hole measurements. The completed facility enables the acquisition of high-quality flow field data for the detailed examination of film cooling configurations.

Chapter 5

Internal Flow Measurements

5.1 Overview

The experimental measurement programme using hot wire anemometry forms the basis of this investigation into the internal flow field of a fan shaped film cooling hole. Extensive measurements have been taken of the flow field in two axially aligned centre-planes for a range of flow and geometry configurations. All measurements presented here were made using the Dantec P11 hot-wire probe and associated componentry described in Ch. 4. The following sections describe the measured velocity U and turbulence intensity $Tu = (u'/U)^2$ profiles in detail for all tested flow cases. These profiles are further interpreted and the influence of inlet velocity ratio, coolant cross-flow orientation, and exit blowing ratio are examined and discussed. Further, the uniformity of exit plane profiles for the different cases is considered, and precedes a summary of findings for this chapter.

5.1.1 Test Cases

As discussed in Ch. 3, there are several parameters that are key to defining the flow dynamics within a film cooling hole. Of these, the inlet velocity ratio (IVR), internal coolant passage orientation β, and the exit blowing ratio M, are the focus of the current investigation. Table. 5.1 shows the matrix of test cases used to investigate the influence of these parameters on the internal flow distribution within the fan-shaped film cooling hole. All combinations of geometric and flow parameters were tested.

IVR	**0.3**	**0.8**	**1.0**	**1.2**	**1.6**
$\beta = 0°$	•	•	•	•	•
$\beta = 90°$	•	•	•	•	•
$M = \infty$	•	•	•	•	•
$M = 1.3$	•		•		•

TABLE 5.1: Test cases for hot-wire anemometry

5.1.2 Measurement Locations

The hot-wire probe was traversed in two planes to take measurements of velocity and turbulence intensity within the cooling hole. In terms of coordinates, these are the X_h - Y_h plane at $Z_h = 0$, and the X_h - Z_h plane at $Y_h = 0$. The measured profiles are therefore in either the Y_h or Z_h directions at different X_h locations along the hole axis. Figure 5.1 shows the locations of measured profiles within the cooling hole, and also highlights the two chosen planes of measurement along the centrelines of the hole.

5.1.3 Presentation of Data

The measurements of mean velocity and turbulence intensity obtained with the hot-wire probe are presented in a format unique to the current investigation. The following paragraph explains the layout of these charts and how to interpret them. A sample chart for the presentation of data in the Y_h measurement plane is presented in Fig. 5.2.

The measured Y_h profiles are viewed from the side of the hole (toward -Z_h), and the Z_h profiles are viewed from the top (toward -Y_h). An outline of the cooling hole model is overlaid on the chart to provide context of location, and a three-dimensional depiction of the measurement plane is provided in the top right corner. The inlet, throat, and exit planes are also marked on these charts with text and solid black lines, and an arrow indicates the direction of the coolant passage mean flow, U_c, at inlet.

The charts are arranged so that the vertical dashed line corresponds to both the physical location of the measured profile, and the zero value of $U/U_{j_{mean}}$ for that profile. For example, the first profile (coloured orange) is measured at a location of $X_h/D = 0.4$ as indicated in the legend to the right of the chart. $U_{j_{mean}}$ is determined from the cooling hole mass flow rate and the cross-sectional area of the throat. The horizontal scale at the bottom of the chart represents values of $U/U_{j_{mean}}$ with the tick marks being separated by intervals of 0.2. These intervals are marked for the first profile up to a value of

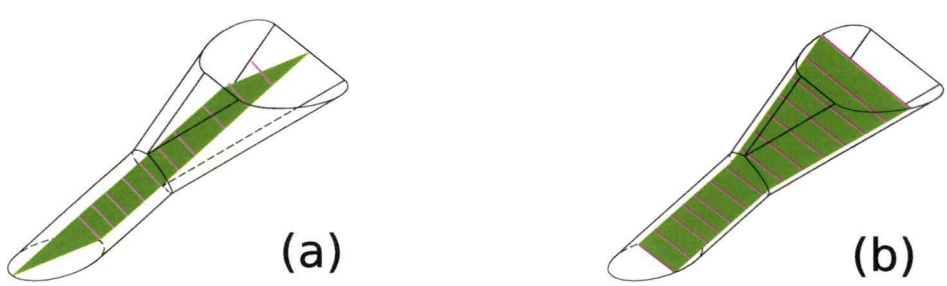

FIGURE 5.1: Y_h (a) and Z_h (b) profile measurement locations (pink lines)

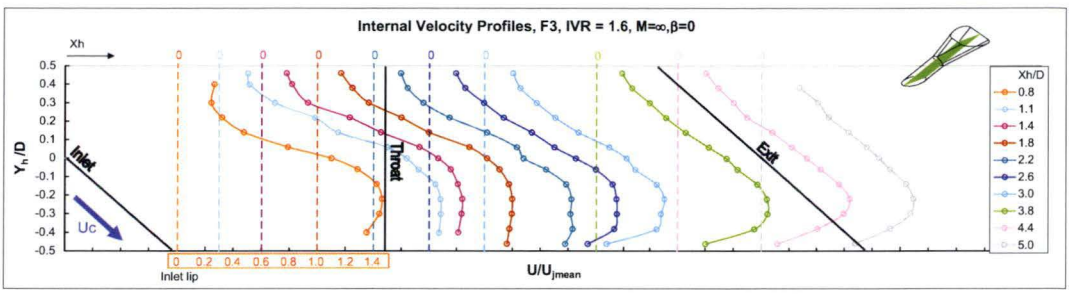

FIGURE 5.2: Sample chart of Y_h profiles

$U/U_{jmean} = 1.4$. This scale can then 'slide' along to any profile so that the '0' marker aligns with the colour-coded dashed vertical line for any profile.

A more conventional presentation of the measured profiles is shown in Fig. 5.3, where each profile is overlaid on a common origin. While this view of the data enables more direct comparison of relative flow changes between profiles, it is difficult to relate the measurements back to their locations within the hole. As a result of the unique presentation style used in the current investigation, the profiles are displayed in a manner that enables visualisation of the flow development along the length of the cooling hole.

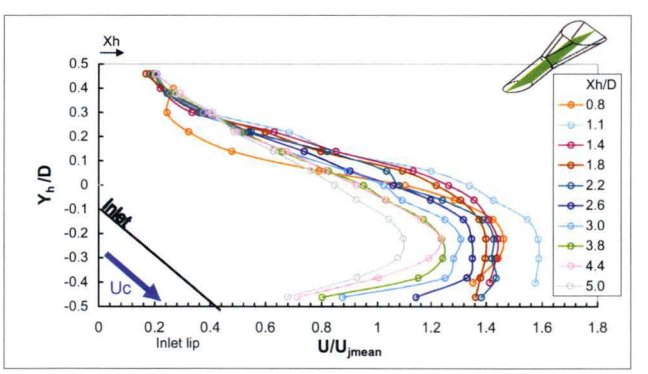

FIGURE 5.3: Conventional presentation of Y_h profiles

5.2 Internal Flow Distribution for M = ∞, $\beta = 0°$

Measurements are presented in Figs. 5.4 - 5.6 for IVRs of 0.3, 1.0 and 1.6, plotting normalised mean velocity and turbulence intensity profiles. For this set of results, there is no external cross-flow ($M = \infty$) and the coolant passage orientation is co-flowing ($\beta = 0°$).

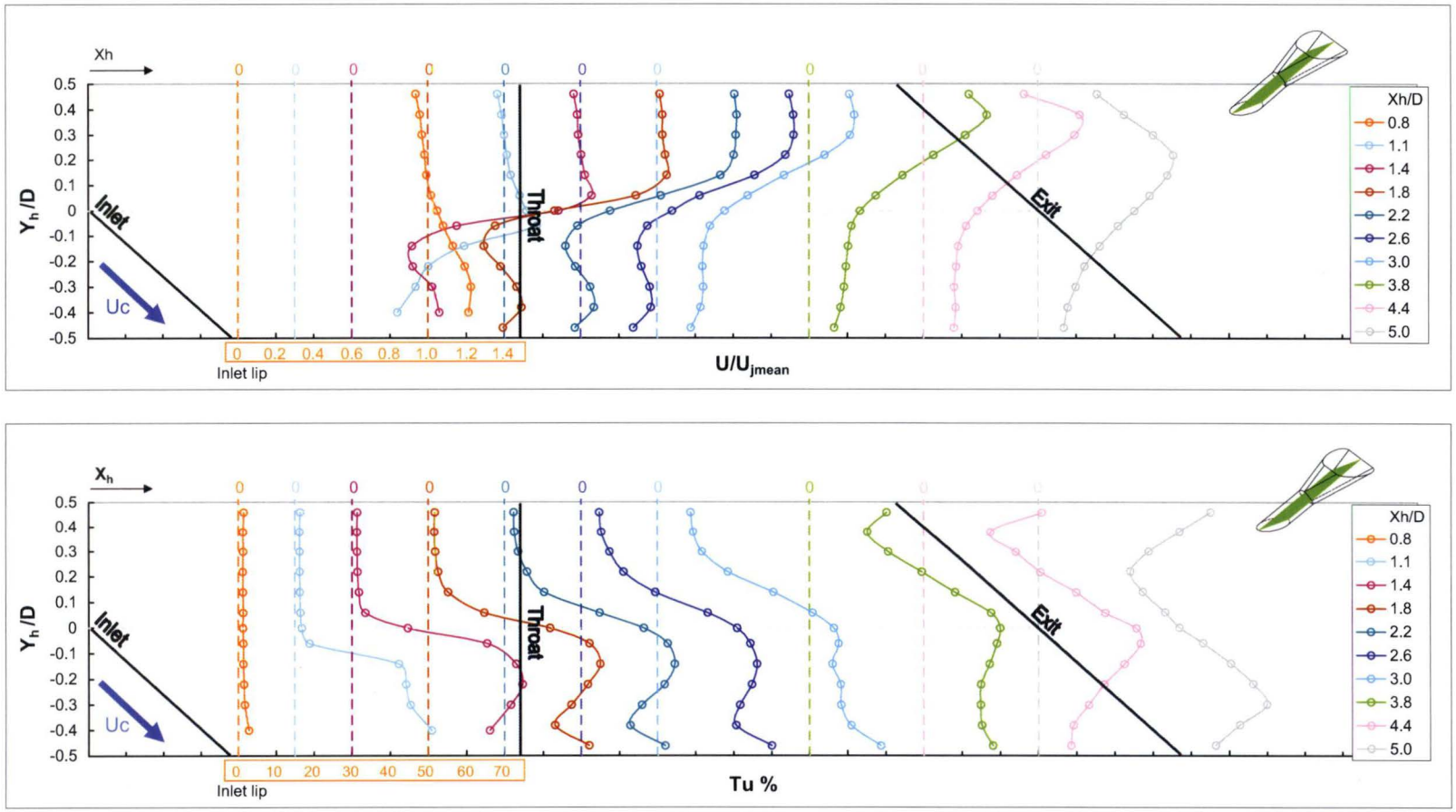

FIGURE 5.4: Y_h velocity and turbulence profiles for IVR = 0.3, $M = \infty$, $\beta = 0°$

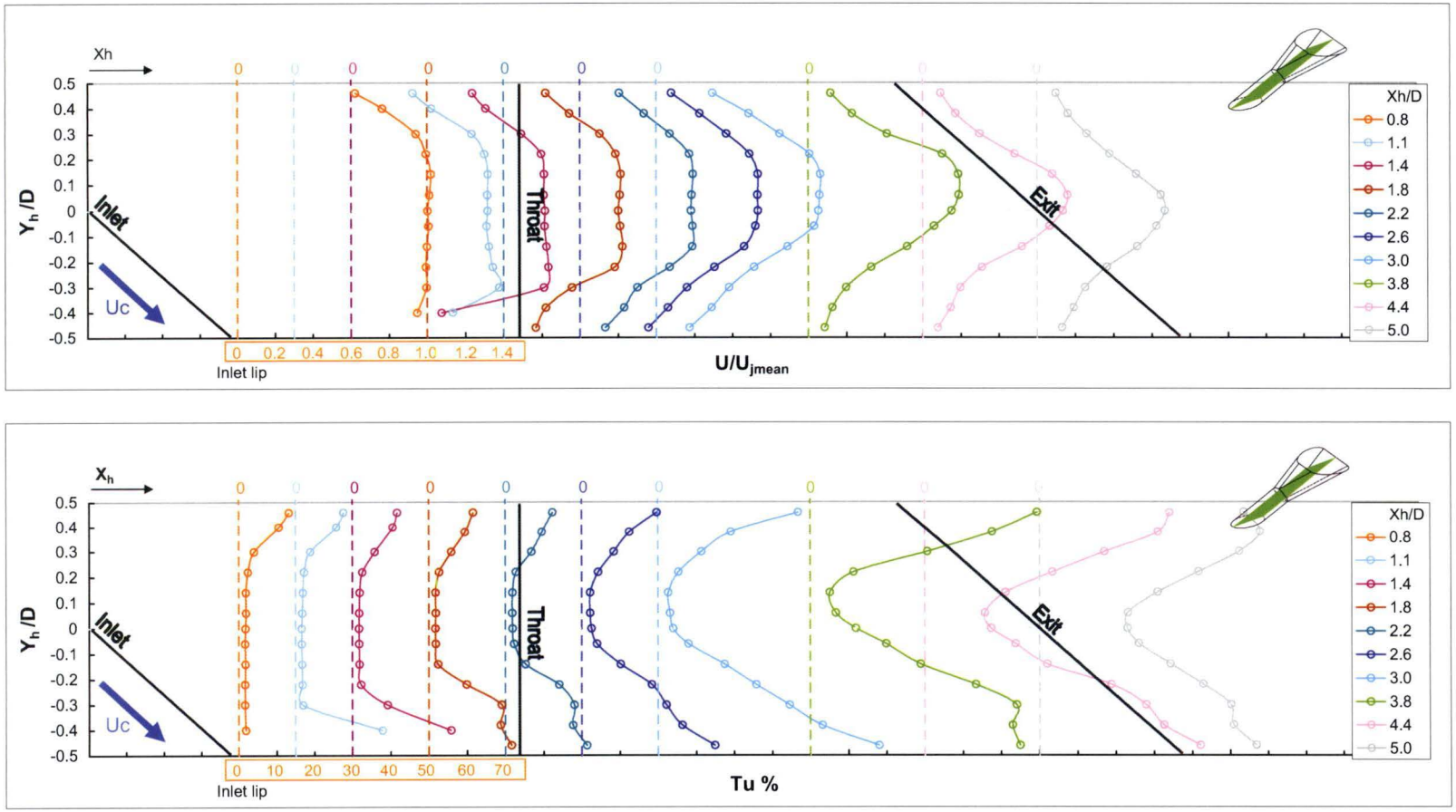

FIGURE 5.5: Y_h velocity and turbulence profiles for IVR = 1.0, $M = \infty$, $\beta = 0°$

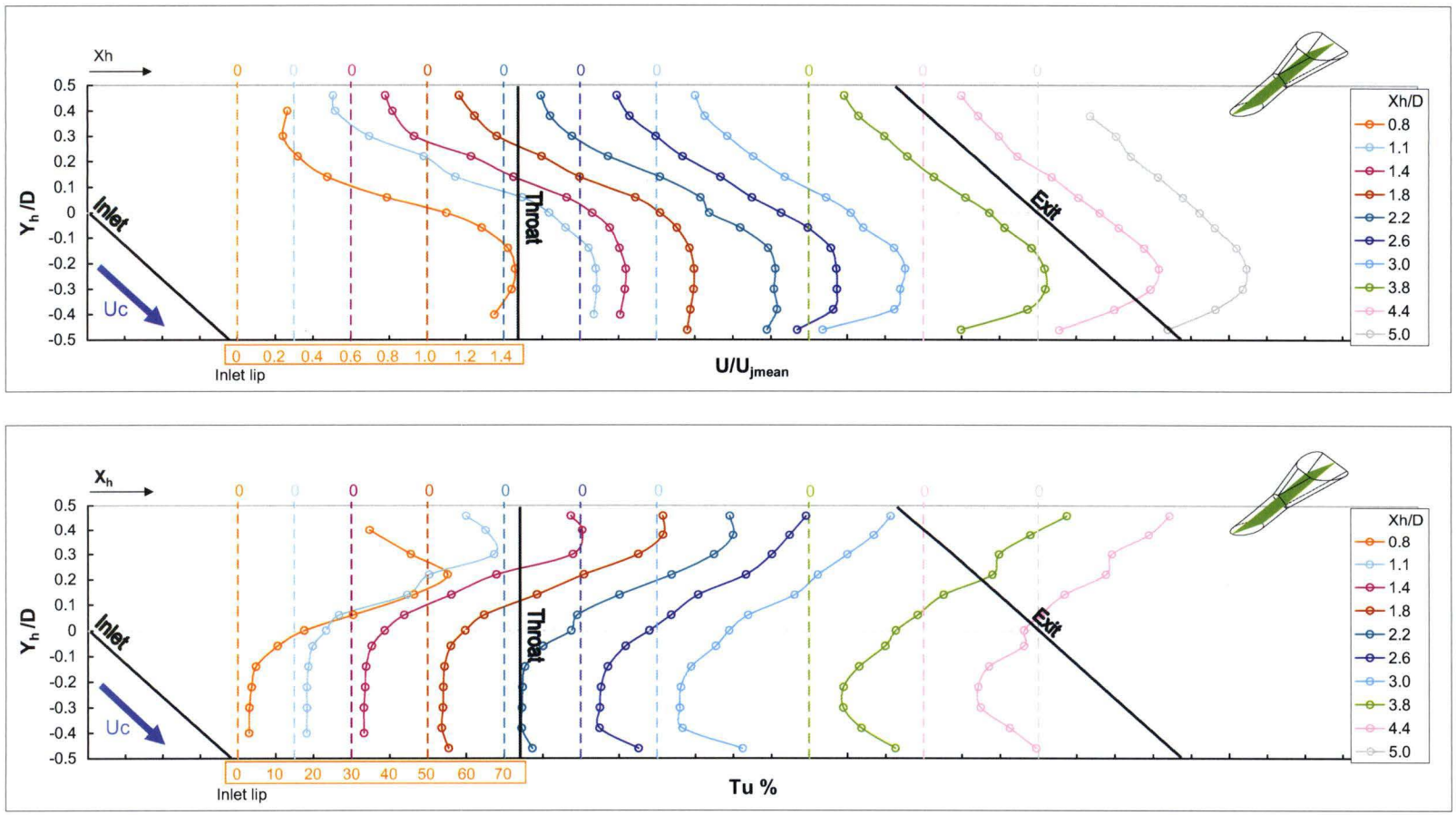

FIGURE 5.6: Y_h velocity and turbulence profiles for IVR = 1.6, $M = \infty$, $\beta = 0°$

5.2.1 Description of Y_h Profile Data

Looking at the Y_h profiles of normalised mean velocity for an IVR of 0.3 (Fig. 5.4), the profile near the inlet lip ($X_h/D = 0.8$) is flat in the upper part at a value of $U/U_{Jmean} = 1.0$ and increases in the lower half of the hole. However, by the next measurement location, the flow in the lower half of the hole is reduced significantly near the wall and increases with Y_h to a peak value of $U/U_{Jmean} = 1.3$ near the centreline. This profile shape continues for the remainder of the measurement locations downstream. Near the lower wall, for profiles at $X_h/D = 1.4 - 3.0$, a second peak in velocity can be seen. As the flow enters the diffuser section, the extent of the high velocity region at the upper wall reduces, forming a sharper peak, but does not increase in magnitude. Similarly, the lower wall peak reduces and then flattens to a low value spanning the lower half of the hole. This reduction in mean velocity is expected due to the area expansion of the diffuser section.

Increasing the IVR to a value of 1.0 tends to shift the high velocity region towards the centreline of the hole, with the velocity profiles now resembling that typically seen in turbulent pipe flow. As seen in the IVR = 0.3 case, the profile at the inlet lip shows higher velocities near the lower wall that produces a slight asymmetry. However, a high velocity region is established along the centreline within 2 diameters of the inlet. The development of this region with axial distance is similar to that seen in the IVR = 0.3 case, with the velocity peak becoming sharper and the flow near the walls decreasing in magnitude. The corresponding turbulence intensity profiles reveal slightly more information about the flow near the lower wall. The turbulence level near the centreline is low where there is high velocity uniform flow, but moving toward the lower wall the profiles from $X_h/D = 1.1$ and downstream show a steep rise before flattening and then rising again closer to the wall. This is in contrast to the flow along the upper wall, which has a fairly constant profile shape throughout the hole. These profiles suggest that there is perhaps a small region of separated fluid on the lower wall that grows as the central 'jet' establishes itself.

Increasing the IVR further to a value of 1.6 creates a velocity distribution within the hole that has an elevated velocity region near the lower wall persisting from the inlet plane right through to the exit plane. This is the opposite to the distribution seen in the IVR = 0.3 case where the core flow sits adjacent to the upper wall. This is representative of classical shearing free jet flow, as investigated by other workers such as Kline [78], with high Tu% at the edge of the jet due to entrainment. In the present case, the development of the high velocity region along the length of the hole is the now familiar sharpening of the peak and reduction of the mean velocity through the diffuser.

The flow near the upper wall remains essentially unchanged throughout the length of the hole.

5.2.2 Description of Z_h Profile Data

The profiles taken in the Z_h direction expand on the story presented by the Y_h profile measurements. At an IVR of 0.3, the Z_h velocity profiles reveal a velocity deficit in the central region of the throat. This deficit becomes more pronounced as the flow enters the diffuser and the side peaks become more defined. The flow spreads laterally to fill the diffuser and maintains a symmetrical distribution with a fairly wide and flat low velocity region in the central portion. The corresponding turbulence profiles show very low intensities through the mean flow up to $X_h/D = 1.1$. Further downstream, however, there is a marked peak in the centre of the profiles which becomes broader as the flow moves through the diffuser and spreads. Near to the side walls, the turbulence intensity can be seen to increase as the hot-wire probe enters the boundary layer region.

At an IVR of 1.0 there is a considerable change in the internal flow pattern and, much like the Y_h profiles, the most immediately noticeable change is the flattening of the mean velocity through the central region of the hole. The profiles within the throat section are quite developed, and show a slightly elevated velocity near the side-walls which develops into a very weak double peak by $X_h/D = 2.2$, suggesting a vortex pair rolling up from the inlet lip and being carried through the hole. In the diffuser, the profile remains flat through the middle but widens downstream as the flow spreads and decelerates. The exit profile is fairly uniform across the mid section, and drops steadily towards the wall through the boundary layer. The turbulence intensity plots are similarly flat through the central region but increase considerably near the wall.

With the IVR increased to 1.6, the flow pattern in the $Y_h = 0$, X_h - Z_h plane changes quite significantly again, as shown in Fig. 5.9. Here, the normalised velocity profiles are reasonably flat through the central region, but the peak is narrower, and significantly higher in magnitude; approaching $U/U_{jmean} = 1.4$. This turbulent pipe flow profile in the throat persists into the diffuser where the profiles develop into a V-shape spanning the diffuser. The corresponding turbulence intensity profiles show moderate levels through the central region and are elevated towards the walls. The measurements here do not represent a smooth curve, indicating that while the turbulence intensity is high, there are significant variations in magnitude in this flow region near the wall.

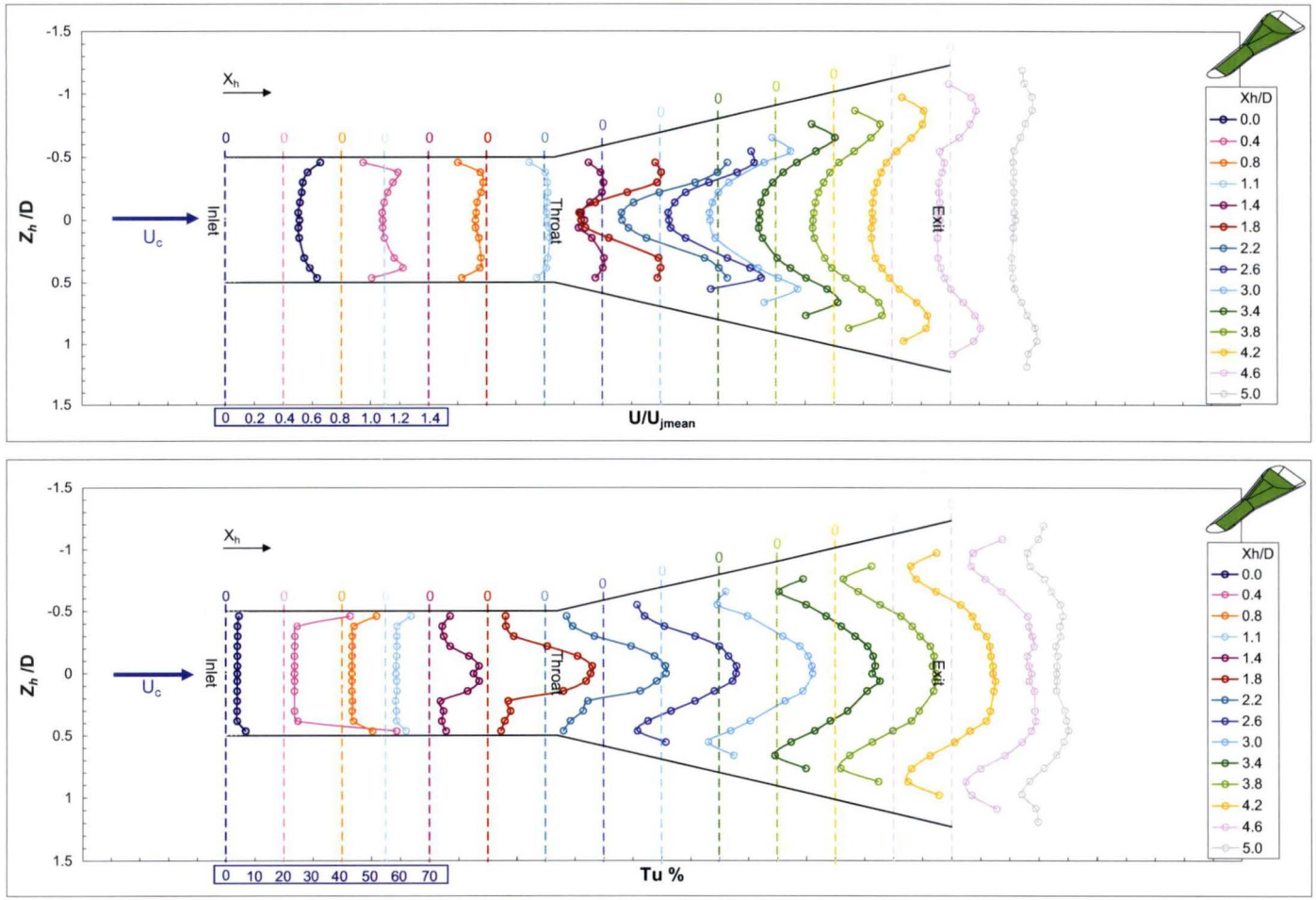

FIGURE 5.7: Z_h velocity and turbulence profiles for IVR = 0.3, $M = \infty$, $\beta = 0°$

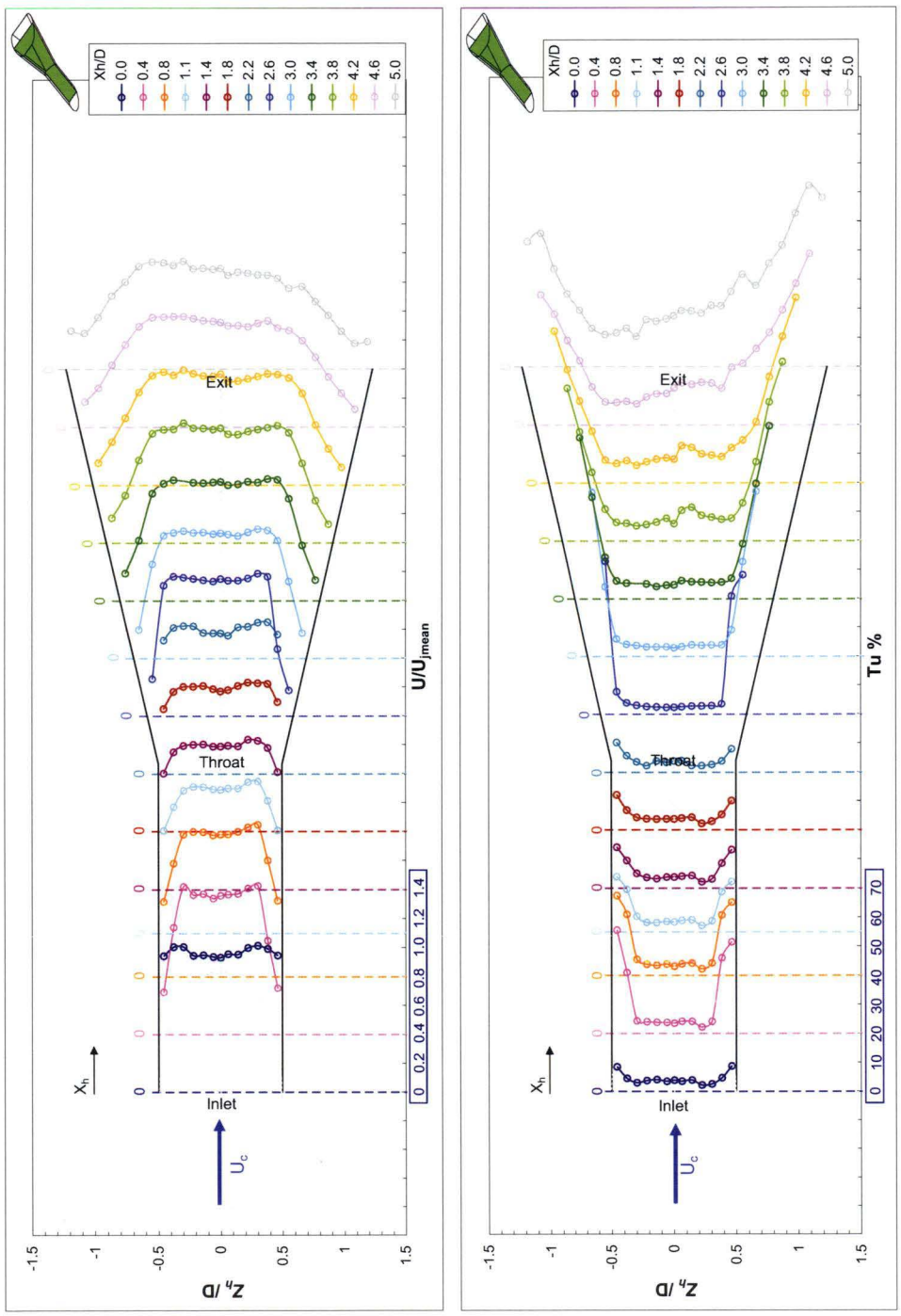

FIGURE 5.8: Z_h velocity and turbulence profiles for IVR = 1.0, $M = \infty$, $\beta = 0°$

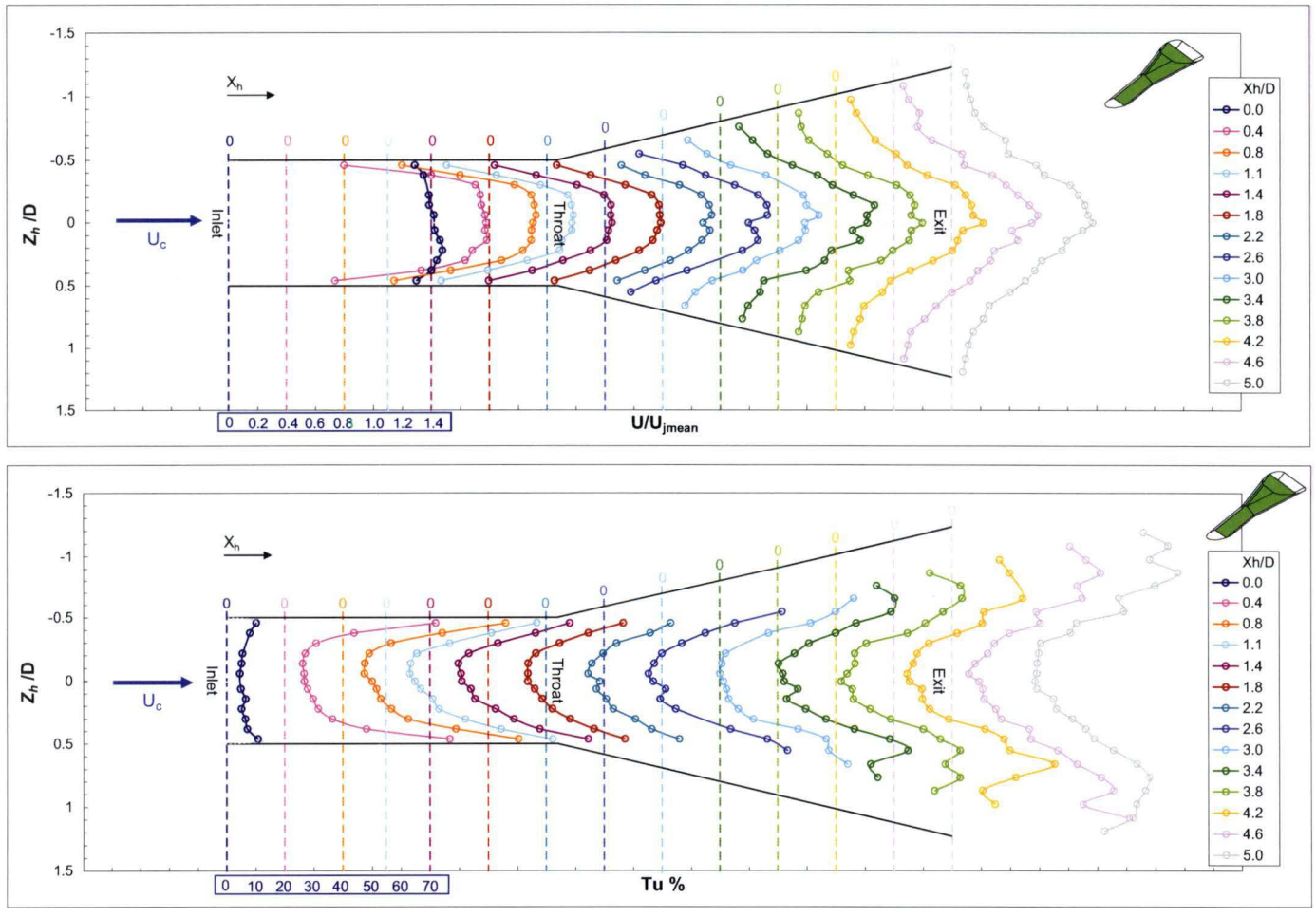

FIGURE 5.9: Z_h velocity and turbulence profiles for IVR = 1.6, $M = \infty$, $\beta = 0°$

5.3 Internal Flow Distribution for M = ∞, $\beta = 90°$

The orientation angle of the internal cross-flow is a parameter that varies with position of the cooling hole on the blade, and is largely a consequence of manufacturing requirements. As a result, many cooling holes have a supply of coolant fluid that passes the hole entry at an orientation other than 0° . A common orientation angle encountered in high pressure turbine blades is 90°, which is the configuration modelled in this study. With the coolant supply passage of the UTas Film Cooling Rig rotated to achieve an orientation of 90° to the plane of the cooling hole centreline (pure cross-flow), hot-wire measurements were taken in the Y_h and Z_h planes for IVRs of 0.4, 1.0, and 1.6. Resulting measurements are presented in Figs. 5.10 - 5.15 and discussed in the following sections.

5.3.1 Description of Y_h Profile Data, $\beta = 90°$

Charts of Y_h velocity profiles for the IVR cases of 0.4, 1.0, and 1.6 are presented in Figs. 5.10 - 5.12. At an IVR of 0.4 (Fig. 5.10) the velocity profile at the first measurement location ($X_h/D = 0.8$) shows a clear peak near the lower wall of the hole, reaching a value of $U/U_{Jmean} = 1.65$, and decays towards the upper wall. At the next measurement location, however, just 0.3D downstream, the velocity profile is almost the complete opposite, with a low ($U/U_{Jmean} = 0.4$) velocity near the lower wall, rising to a value of 1.3 near the mid plane, before reducing slightly and flattening toward the upper wall. This profile shape persists through the remainder of the throat and the first half of the diffuser, though the velocity gradient between the lower and upper walls becomes less. Between $X_h/D = 1.4$ and 3.0, there is a clear 'dip' or velocity deficit in the lower half of the hole. This deficit spreads upward and weakens with axial distance to reach a profile shape at $X_h/D = 3.8$ that has a very shallow dip spanning the majority of the diameter. The mean velocity here is much reduced as the bulk flow velocity decreases due to the area expansion of the geometry. The turbulence intensity plots for the same IVR = 0.4 case show a fairly typical variation with low turbulence intensity in high velocity regions, and high turbulence in low velocity regions. Hence the curves show quite low turbulence intensity (2-3%) in the upper half of the hole, and increase significantly towards the lower wall, peaking at about 50% at a location that corresponds to the dip in the velocity profile already discussed. An interesting feature of the turbulence chart is the very low and uniform profile at $X_h/D = 0.8$. The level of turbulence is 2-3% across the whole passage with a slight rise near the lower wall to about 4%. This could indicate that the fluid passing this measurement location is drawn primarily from the low turbulence intensity coolant freestream.

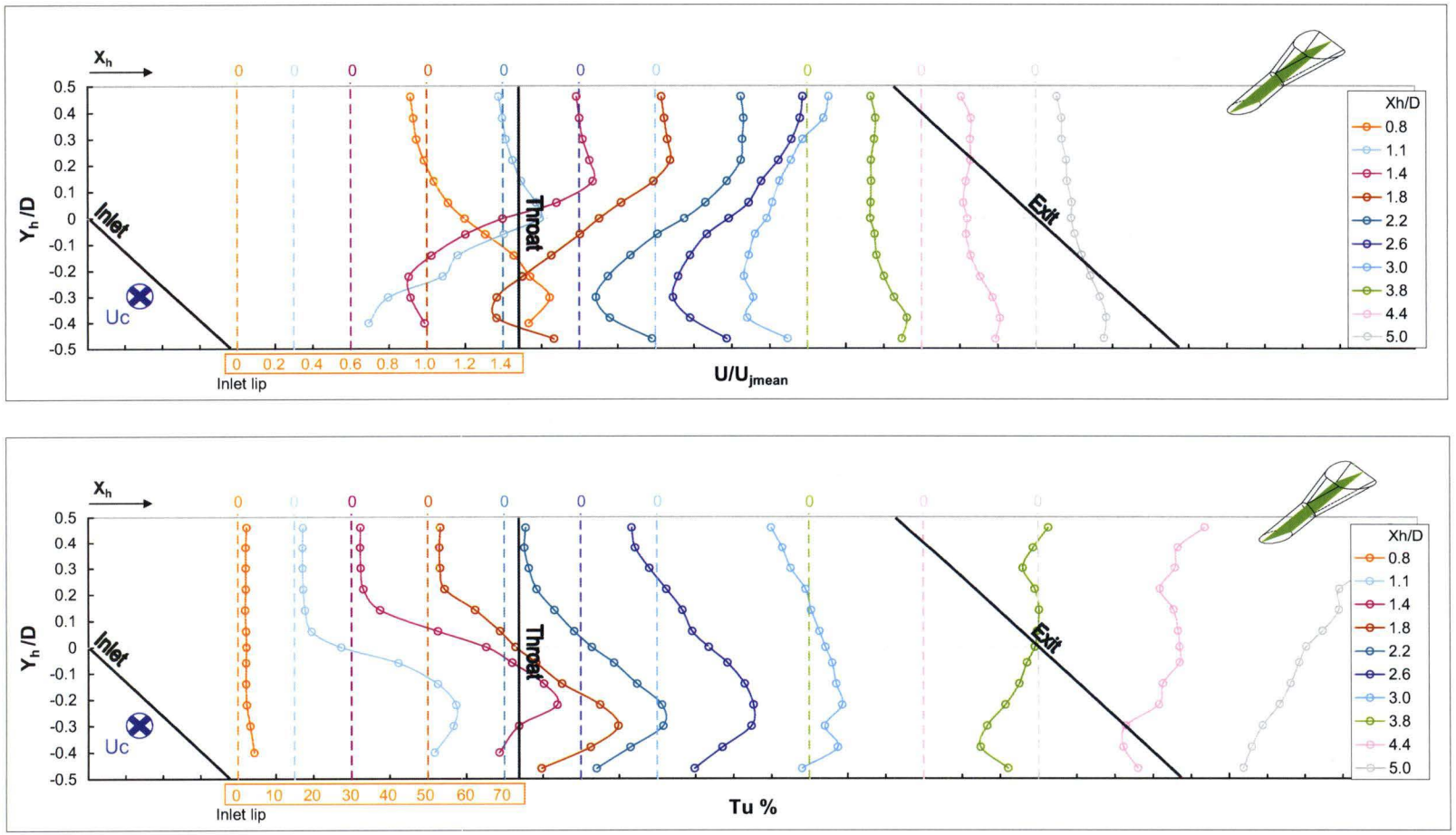

FIGURE 5.10: Y_h velocity and turbulence profiles for IVR = 0.4, $M = \infty$, $\beta = 90°$

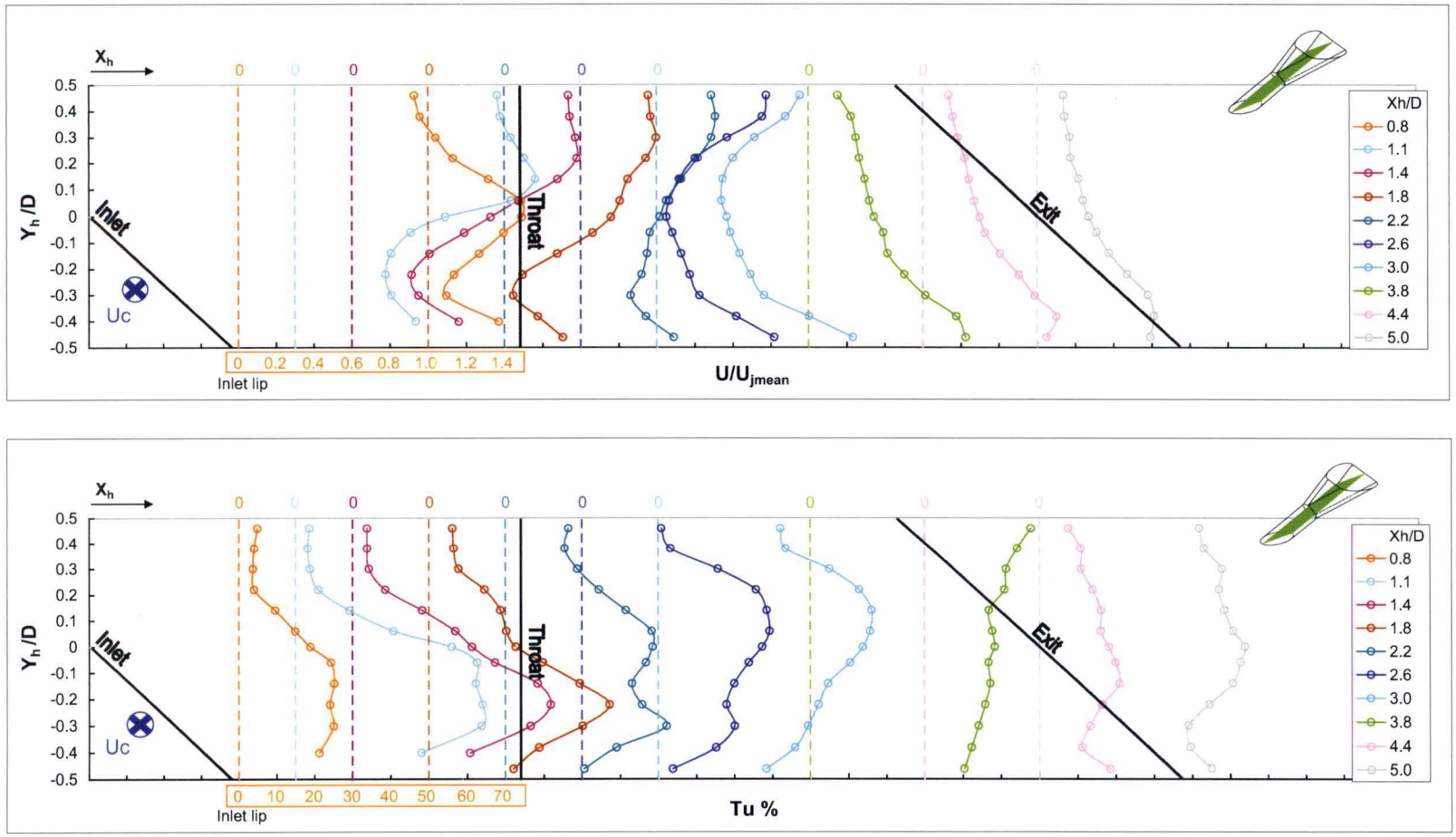

FIGURE 5.11: Y_h velocity and turbulence profiles for IVR = 1.0, $M = \infty$, $\beta = 90°$

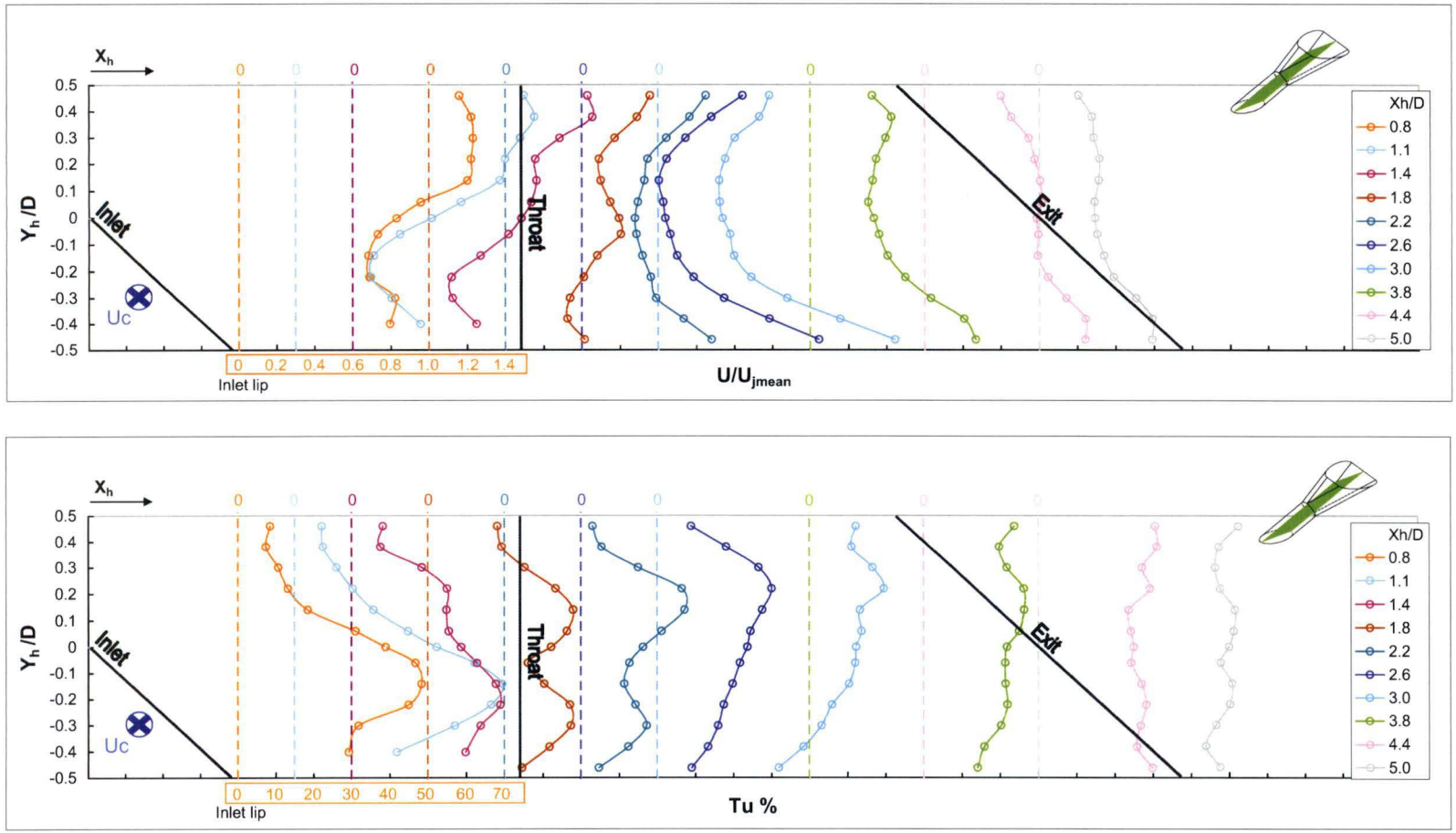

FIGURE 5.12: Y_h velocity and turbulence profiles for IVR = 1.6, $M = \infty$, $\beta = 90°$

At an IVR of 1.0 (Fig. 5.11), the internal Y_h profiles are quite different to those at 0.4. Most noticeable is the broader and flatter velocity deficit highlighted in the $X_h/D = 2.6$ and 3.0 profiles. At the hole entry, there is a sharp peak in velocity of $U/U_{jmean} = 1.5$ at the hole centreline which decreases toward 0.9 near the upper wall. Near the lower wall, there is a dip in the velocity profile, which continues to be present in profiles further downstream. The velocity at the low point in this dip, however, is at a value of $U/U_{jmean} = 1.1$, indicating that the fluid here is significantly accelerated due to turning at the hole inlet. The corresponding turbulence intensity profile shows a broad region of elevated turbulence in the lower half of the hole, but decreases markedly toward a region of uniform, low turbulence flow near the upper wall. Downstream at $X_h/D = 1.1$, the flow velocity near the upper wall remains high, but decreases in the lower half of the hole, showing a broader deficit in this region down to velocity values of $U/U_{jmean} = 0.5$. The profiles are similar at the next two measurement locations, but the minimum of the deficit moves closer to the lower wall and reduces in magnitude to $U/U_{jmean} = 0.3$ at $X_h/D = 1.4$, before increasing to and stabilising at $U/U_{jmean} = 0.6$ further downstream. The turbulence profiles here show a sharpening peak and shift of the peak value towards the lower wall, matching the shift in corresponding velocity profiles. At $X_h/D = 2.2$ there is a double peak in turbulence, with the flow in the middle region of the hole showing a significant increase in intensity compared with the profiles upstream. At $X_h/D = 2.6$ there is a marked shift in the flow distribution. This location corresponds to a position just downstream of the start of the diffuser. A much broader velocity deficit occupies the majority of the hole, and a similar broadening of the turbulence peak is evident from the chart. There is also a bias of the flow toward lower velocity, higher turbulence fluid in the upper half of the hole. At $X_h/D = 3.8$ the Y_h profile is markedly different again, with the velocity near the upper wall significantly reduced to a value of about $U/U_{jmean} = 0.2$ and an increasing velocity towards the lower wall, peaking closer to the wall at a value of $U/U_{jmean} = 0.8$. This trend remains for the last two measurement locations. The turbulence profiles flatten considerably toward the exit and show high values of $40 - 50\%$. These significant flow developments over a short distance indicate that there are strong secondary flow patterns present.

For the IVR = 1.6 case (Fig. 5.12), the flow pattern shows similar progression to the IVR = 1.0 case, but there are several key differences. The inlet lip profile at $X_h/D = 0.8$ shows a region of uniform, faster moving fluid near the upper wall, and the characteristic dip in velocity in the lower half of the hole. This lower velocity region is cause for the high values of turbulence intensity near the lower wall. The next profile downstream is similar, although the velocity dip is smaller and lower in the hole, and the start of a second dip developing near the upper wall can be seen. At $X_h/D = 1.4$ this second velocity deficit starts to emerge, and at the next measurement location 0.4D further

downstream, there is a clear 'W' shape to the profile with a small peak along the midline. The dual dip profile is more clearly seen in the turbulence profiles, except here the profiles are a double peak, or 'M' shape, with the low velocity fluid showing higher turbulence intensity. As the flow enters the diffuser, however, this 'W' shape is not visible, replaced by a broad, flat velocity deficit occupying over half the hole diameter. This profile shape continues right through to $X_h/D = 3.8$, but all profiles show higher velocity near the lower wall. By the final two profiles this deficit region is much shallower, and the final velocity profile is fuller and more uniform, though still with a bias towards high velocity fluid near the lower wall. The turbulence intensity here is higher still than the IVR = 1.0 case, with the flattened profiles showing turbulence levels of $50 - 60\%$.

5.3.2 Description of Z_h Profile Data, $\beta = 90°$

The effects of orienting the internal coolant passage at 90° to the cooling hole axis are shown quite prominently in the charts of Z_h plane profile data. In the description that follows, the 'right' side of the diffuser is upstream relative to the internal coolant passage flow, and the 'left' side is downstream. The charts for an IVR of 0.4 in Fig. 5.13 quite clearly reveal a skewing of the velocity distribution to one side of the diffuser, as might be expected from the inlet configuration. At the hole inlet ($X_h/D = 0$), there is a moderate peak in velocity near the right wall, which by $X_h/D = 0.4$ has developed into a very narrow, strong peak at a value of $U/U_{j_{mean}} = 1.7$ compared with a value of 0.6 for the majority of the profile. At $X_h/D = 0.8$ the peak has reduced to $U/U_{j_{mean}} = 1.4$, is wider, and has moved toward the centreline of the hole. The velocity near the left wall has increased slightly and occupies about half the hole diameter. The next profile downstream shows a similar trend, but at $X_h/D = 1.4$ takes the form of a skewed 'M', with a velocity deficit distinguishable near the centreline. This double peak is still present 0.4D downstream (at $X_h/D = 1.8$), but has dispersed by $X_h/D = 2.2$. The location $X_h/D = 2.2$ is just before the start of the diffuser and the flow shows a small region of low velocity, uniform flow near the left wall before increasing quickly toward the right wall to a value of $U/U_{j_{mean}} = 1.4$. As the flow enters the diffuser, this profile shape continues, with high velocity fluid remaining near the right wall, reducing back to a uniform flow region in the left half of the hole. As with other cases, the area expansion of the diffuser results in a reduction of the mean velocity as the flow moves toward the hole exit, however the high velocity region near the right wall narrows slightly and maintains a peak value of about $U/U_{j_{mean}} = 1.1$ through to the end of the measurement domain.

Figure 5.14 shows the Z_h velocity and turbulence intensity profiles for an IVR of 1.0. The inlet profile at $X_h/D = 0$ again shows a region of high velocity fluid near the right

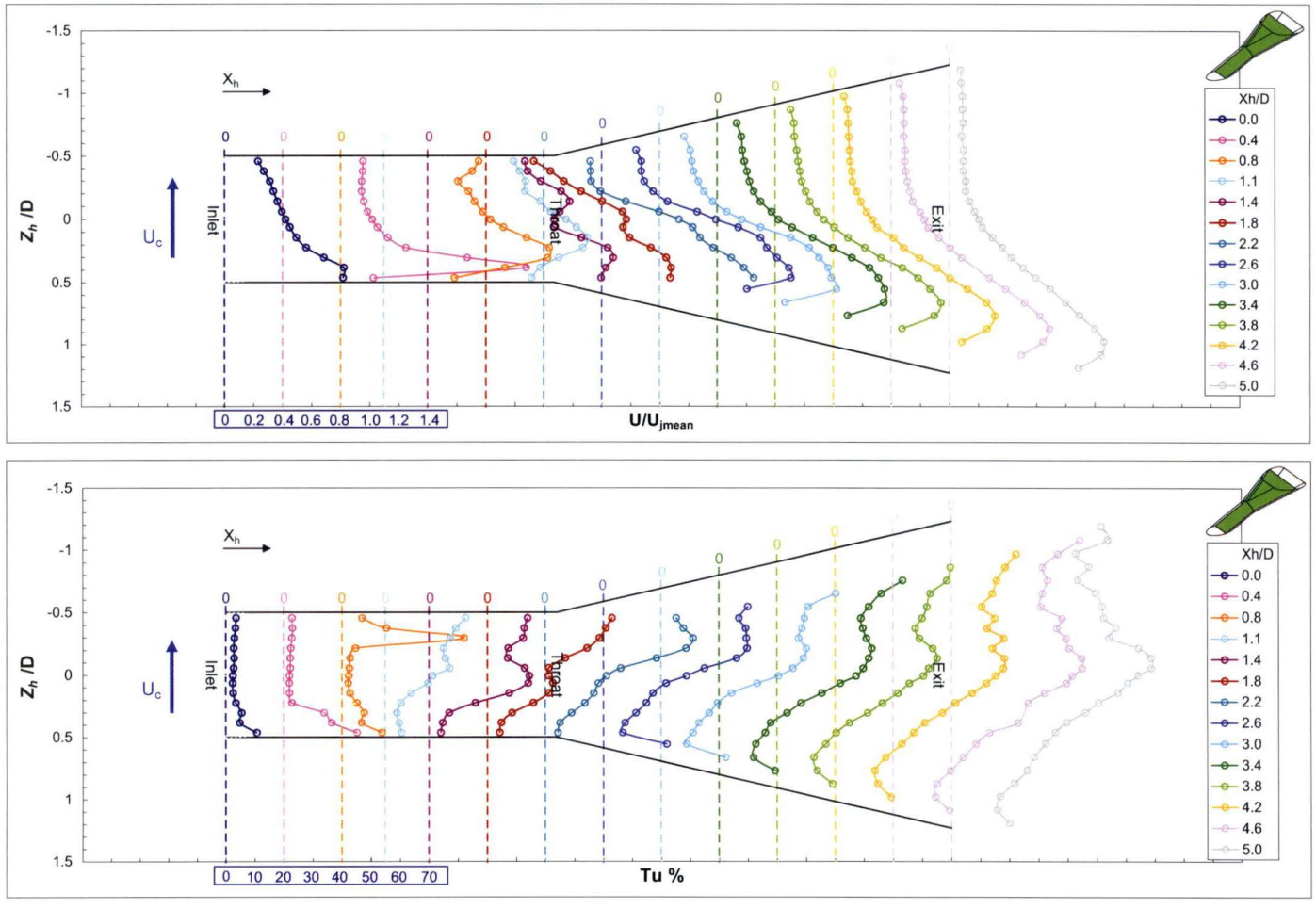

FIGURE 5.13: Z_h velocity and turbulence profiles for IVR = 0.4, $M = \infty$, $\beta = 90°$

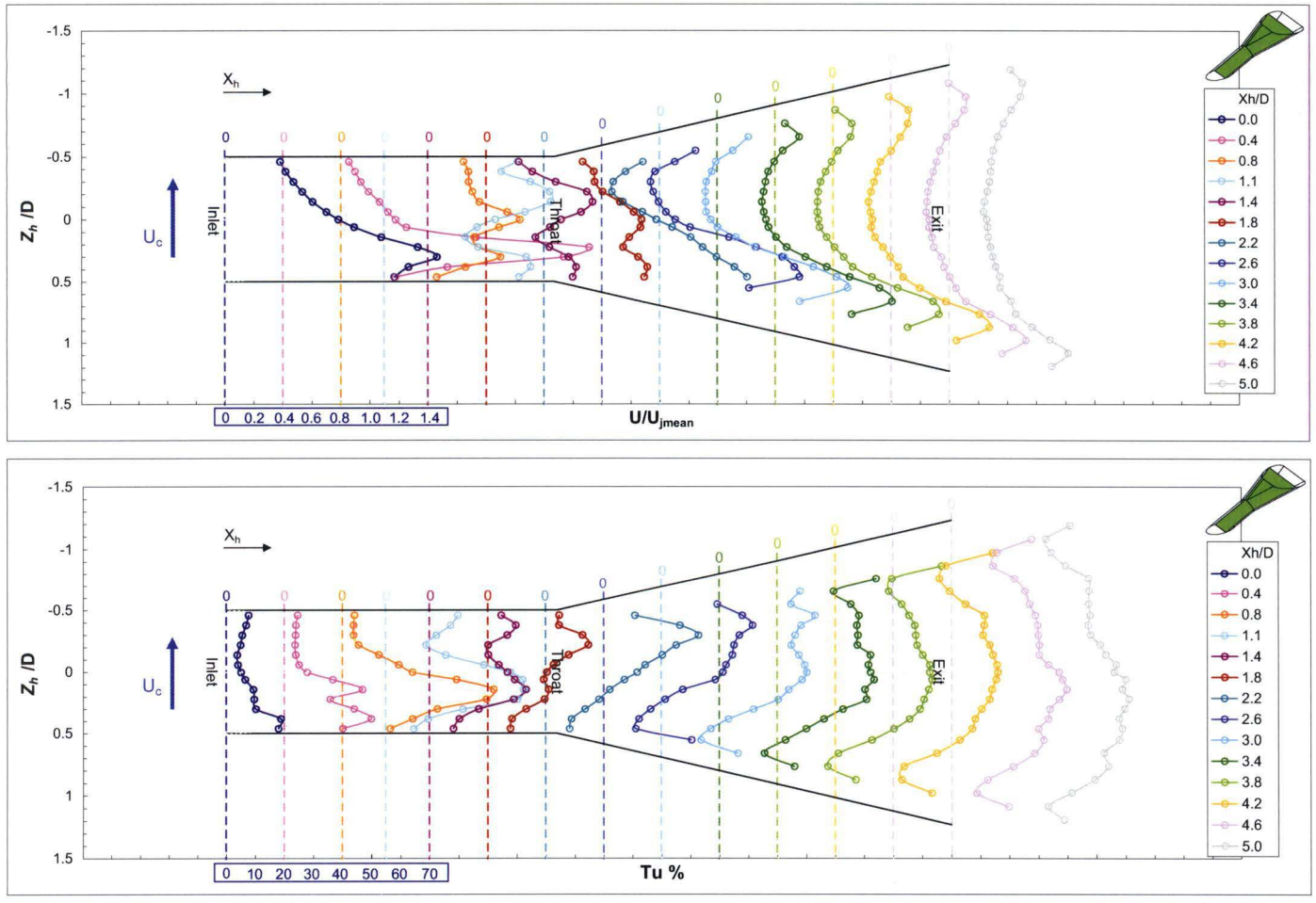

FIGURE 5.14: Z_h velocity and turbulence profiles for IVR = 1.0, $M = \infty$, $\beta = 90°$

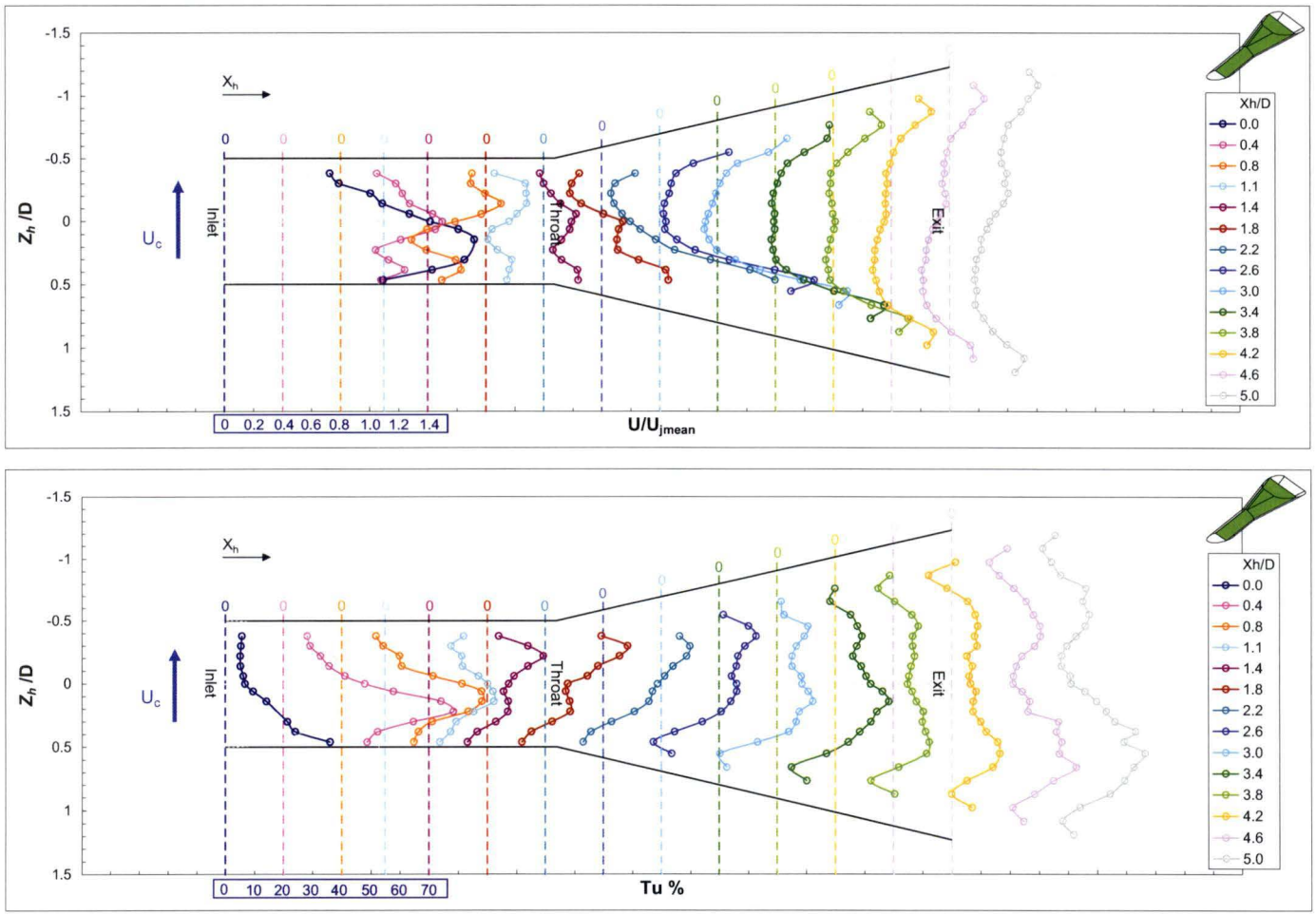

FIGURE 5.15: Z_h velocity and turbulence profiles for IVR = 1.6, $M = \infty$, $\beta = 90°$

wall of the hole, and the peak has moved toward the centreline when compared with the IVR = 0.4 case. The following profile at $X_h/D = 0.4$ shows a very high magnitude velocity peak at about $0.25D$ from the right wall, reaching a value of $U/U_{j_{mean}} = 2.1$, showing a similar shape to the equivalent profile in the IVR = 0.4 case. At $X_h/D = 0.8$ the 'M' shaped profile can be seen, with the central deficit sitting just below the centreline. Interestingly, the turbulence intensity profile here shows a single broad peak of 50% at the location of the velocity deficit, and reduces to lower values near the walls. This deficit is present in the next three velocity profiles and moves slightly toward the right wall. From $X_h/D = 2.6$ and downstream, the 'M' shaped profile is stretched to create a broad, shallow deficit in the middle region, and a peak in velocity at either side of the diffuser. There is a bias toward the right wall of higher velocity fluid as seen in the IVR = 0.4 case, but to a lesser extent.

At an IVR of 1.6, Fig. 5.15 shows a much broader and higher magnitude peak in velocity in the right half of the hole at the inlet. The turbulence level of this higher velocity fluid is also high at around 20-30%, compared to 5% in the left part of the hole where the velocity drops. The 'M' shaped profile seen in the lower IVR cases is present in the $X_h/D = 0.4$ profile and remains through to $X_h/D = 1.8$. Here, though, the location of the deficit minima moves from side to side, firstly toward the left wall, then back toward the right, before shifting again toward the left wall. In the diffuser, the profiles spread and flatten in the middle region, and in the last four profiles there is a small velocity peak toward the middle of the hole, suggesting a vortex tube on the left between this peak and the peak near the wall. The bias of higher velocity fluid toward the right wall is not as evident in the IVR = 1.6 case.

Interestingly, for all cases, the side of the diffuser to which the flow is skewed is opposite to that which might be assumed from the direction of the coolant passage cross-flow and earlier observations of the jetting effect for the $\beta = 0$ cases. This difference appears to be brought about by the cylindrical throat, oriented normal to the mean coolant flow direction, and inclined at 30°, inducing secondary flow rotation within the hole. Indeed, the velocity deficit present in profiles at $X_h/D = 0.8$ to 1.8 is a typical signature of a vortex core, supporting this secondary flow assumption. This rotation would be expected to be in a clockwise direction when looking along the hole axis from inlet to outlet.

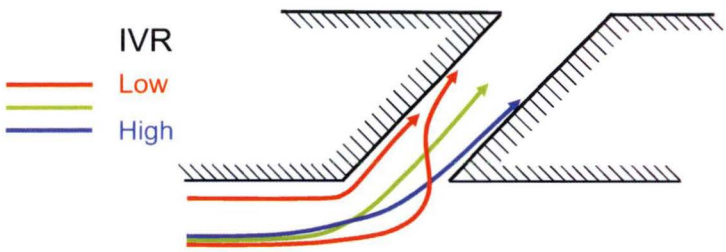

FIGURE 5.16: Depiction of inlet flow for low to high inlet velocity ratio

5.4 Influence of Inlet Velocity Ratio

5.4.1 Co-flow Configuration

The effects of variations in IVR have been discussed to some extent in the descriptions of internal flow distributions and are further described in this section. Measurements of both Y_h and Z_h velocity profile data are compiled in Figs. 5.17 and 5.18. An explanation of the flow pattern changes can be gained from examining the flow at the inlet to the cooling hole, as depicted in Fig. 5.16. At an IVR of 0.3 (low), the internal coolant passage mean flow velocity is much less than the cooling hole throat mean velocity, as given by the definition of the IVR. This requires passage fluid flowing into the cooling hole to turn and accelerate at the inlet to satisfy the volumetric flow required through the hole. The lower momentum coolant at the top of the passage allows this fluid to follow the upper wall and turn into the hole more easily. However, the volumetric flow requirements of the low IVR value demand more coolant than supplied from this region alone. Due to the 30° inclination of the hole axis, flow entering near the downstream inlet lip has to potentially turn 150° to enter the cooling hole. In testing, however, such extreme turning does not occur, with tuft investigations returning no evidence of reversed flow near the lip. Nevertheless, the internal Y_h velocity profiles clearly show that there is high velocity fluid near the lip at the first measurement location ($X_h/D = 0.8$), supporting a strong acceleration of fluid in this area. This highly accelerated fluid transfers to the upper wall within 0.4 diameters axially, splitting the hole flow into two parts - the high velocity core or jet at the upper wall, and a low velocity region along the lower wall. A strong shear layer between the upper and lower halves of the hole is thus established, highlighted by the peak in turbulence intensity values near the centreline as shown in Fig. 5.4. This phenomenon has been described by other workers (Leylek and Zerkle [13], Kohli and Thole [14, 55], Kissel et al. [59], and Saumweber and Schulz [27]) through CFD and assumptions from external flow measurements, as a 'jetting effect' where a core of high velocity fluid accelerates around the inlet lip and then separates from the lower wall to 'jet' along the upper wall.

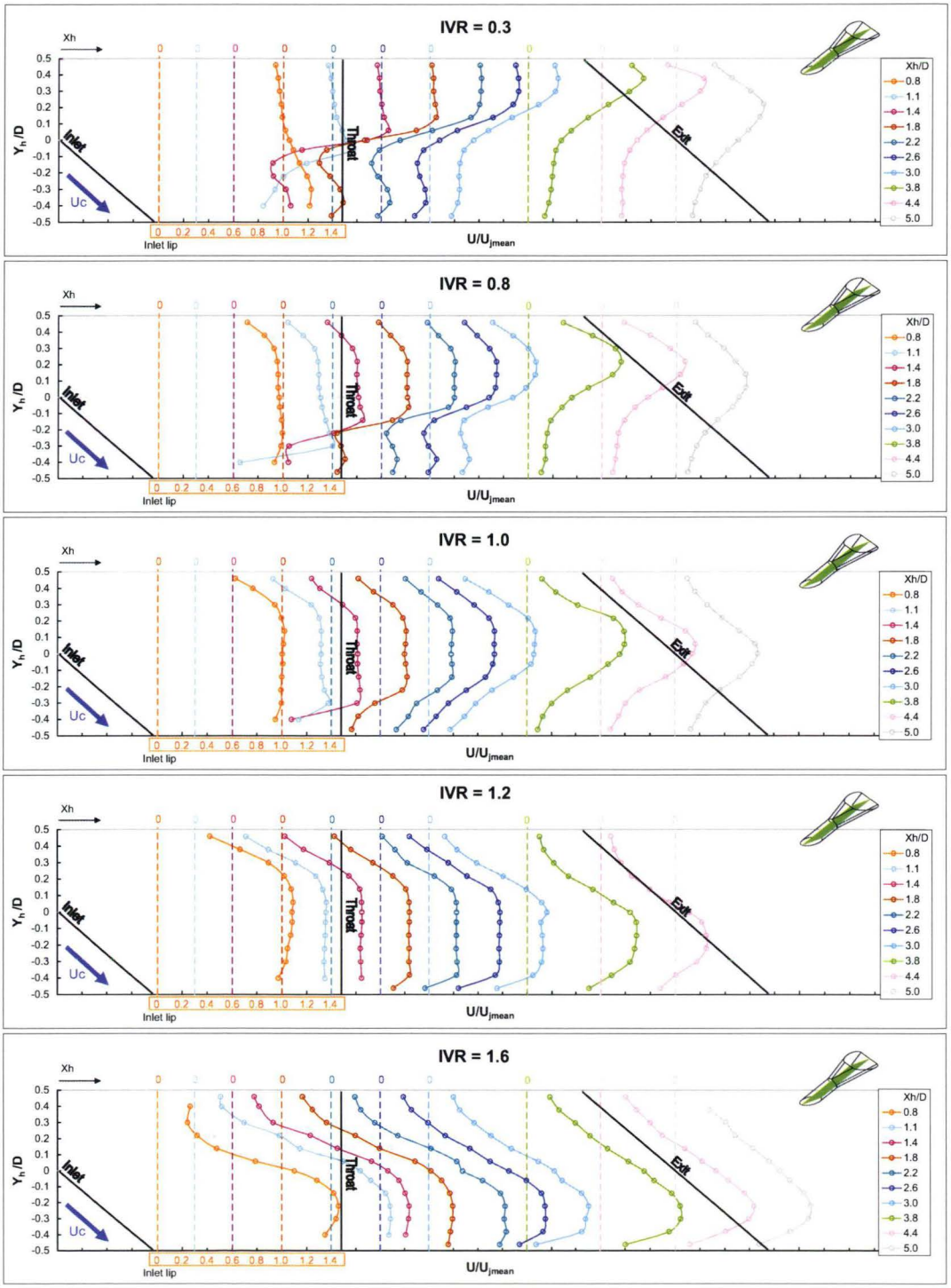

FIGURE 5.17: Change in internal Y_h velocity profiles with IVR, $M = \infty$, $\beta = 0$

At an IVR of 1.0, the coolant passage and throat mean velocities are equal, reducing the severity of any turning the incoming fluid has to endure. This in turn reduces the effect of any jetting or makes the extent of jetting nearly equivalent around the circumference of the inlet so that no particular edge separation dominates the internal flow. As a result, the main flow through the hole is near symmetric along the length of the hole, and fluid near the walls remains at a low velocity. The turbulence intensity is also significantly reduced compared to the higher and lower IVR cases, which has important implications for aerodynamic losses.

At an IVR of 1.6 (high) the coolant passage velocity is significantly faster than the mean throat velocity. As the flow reaches the inlet, the momentum of the fluid is too great to turn the 30° tightly and thus the flow jets towards the lower wall of the cooling hole. The 'smoother' entry to the hole results in higher fluid momentum and higher peak normalised velocity in the $Z_h = 0$ plane when compared to other IVR cases. This is clearly shown in Fig. 5.20 where profiles at several X_h/D locations from different IVR cases are presented together for comparison. These profiles are discussed further in Sec. 5.4.3.

Combining the results from both the Y_h and Z_h planes provides a more complete picture of the internal flow for different IVRs. The Z_h measurements are taken at the mid-height of the cooling hole passage, or $Y_h = 0$. The flow distribution in this plane, therefore, is determined by the height of the jet relative to $Y_h = 0$. For IVR = 0.3, the high velocity region is located above $Y_h = 0$. The Z_h plane measurements show that the high velocity region in the upper part of the hole also extends around the circumference of the hole. This indicates that there is a layer of high velocity fluid around the top and sides of the hole, surrounding a region of low velocity fluid in the centre of the diffuser.

At IVR = 1.0 the Y_h profiles show that the core fluid runs through the centre of the hole with a well developed turbulent pipe-flow profile. This is matched in the Z_h plane with the high velocity core flowing through the centre of the hole. The edge of this central core would be an oval shape, wider in the Z_h direction than in Y_h as indicated by the relevant widths of the central uniform flow regions. The jetting effect at high IVRs is not as strong as at low IVRs because the turning angle at the hole inlet is not as severe as before, meaning that here the $Y_h = 0$ plane cuts through the top of the jet, resulting in the sharper central peaks in the Z_h profiles.

In summary, for the $\beta = 0°$ configuration, there is a distinct progression of flow pattern as the IVR is increased from 0.3 to 1.6. At IVR values less than 1.0, a core region of higher velocity fluid is present near the upper wall of the hole, while at values higher than 1.0, the core fluid stays in the lower half of the hole. Very near to an IVR of 1.0, the

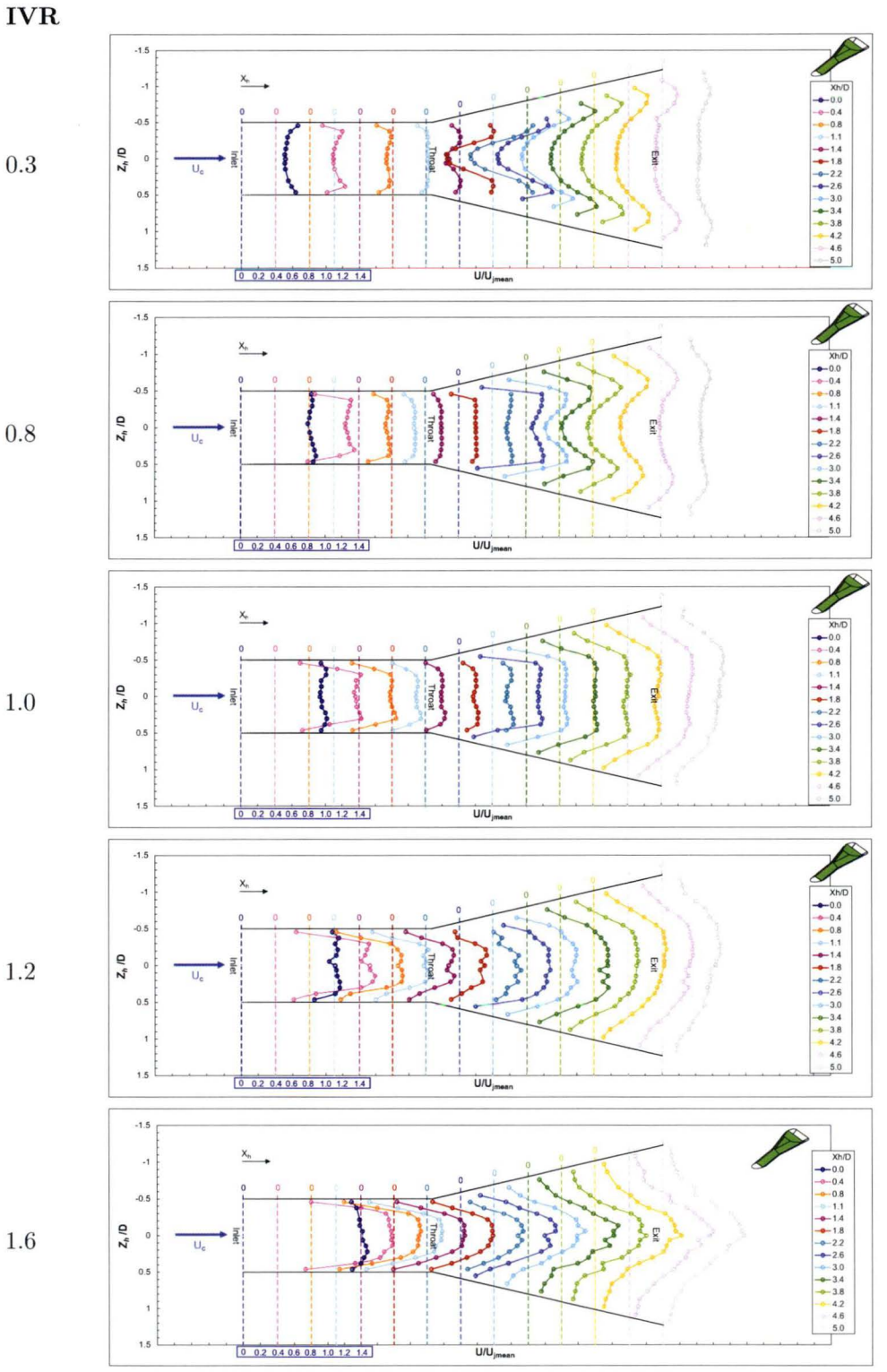

FIGURE 5.18: Change in internal Z_h velocity profiles with IVR, $M = \infty$, $\beta = 0$

flow is nearly symmetric along the length of the hole, with the core fluid region staying along the axial centreline of the hole.

5.4.2 Cross-flow Configuration

The trends seen for the co-flowing ($\beta = 0°$) coolant passage orientation in terms of inlet velocity ratio are not seen to the same extent for the cross-flow inlet case ($\beta = 90°$). The additional turning angle introduced by the cross-flowing coolant passage creates a more complex three-dimensional flow field, and the effects of changing IVR are not clear based alone on data from the two measurement planes presented in Figs. 5.10 - 5.15. There is still, however, a clear change in the internal flow pattern as the IVR is increased from 0.4 to 1.6, as shown in Fig. 5.19.

The most notable difference in Y_h profiles between the three IVR cases (Figs. 5.10 - 5.12) occurs at the first measurement location at $X_h/D = 0.8$. Here, the high velocity shifts from the lower, to the middle, and then to the upper wall as the IVR is increased. This is a similar trend to that for the ($\beta = 0°$) configuration, except the trend here is opposite. As identified earlier, the velocity deficit seen in both the Y_h and Z_h profiles is a typical signature of a vortex, with low velocity spiralling flow at the core inside a higher velocity outer tube. The Y_h profiles show this vortex core sitting near the lower wall and expanding with downstream distance. At the onset of the diffuser section, however, the profile shape quickly breaks down in the measurement plane to leave the broad, shallow deficit described in previous sections. The Z_h planes help to understand this marked change, suggesting that the vortex slows and expands to result in a much larger vortex across the majority of the diffuser.

In both the Y_h and Z_h profiles, as the IVR is increased, the vortex core is evident further upstream in the X_h - Z_h measurement plane, indicating that the location of the vortex within the cooling hole is shifting with changes in IVR. Also, the general development of profiles, particularly in the throat section, is shifted toward the inlet of the hole as the IVR is increased. This may be due to different rates of rotation within the hole caused by the different inlet conditions as the IVR is changed. Similarly, looking at the Y_h profiles for all three IVR cases, the high velocity region near the top wall reduces as the IVR is increased, and is only detectable closer to the inlet. From the Z_h profiles, there is a rise in the velocity magnitude near the right wall in the diffuser as the IVR is increased. These two observations further support the hypothesis that the IVR has a controlling influence on the degree of rotation of fluid within the cooling hole in the pure cross-flow configuration.

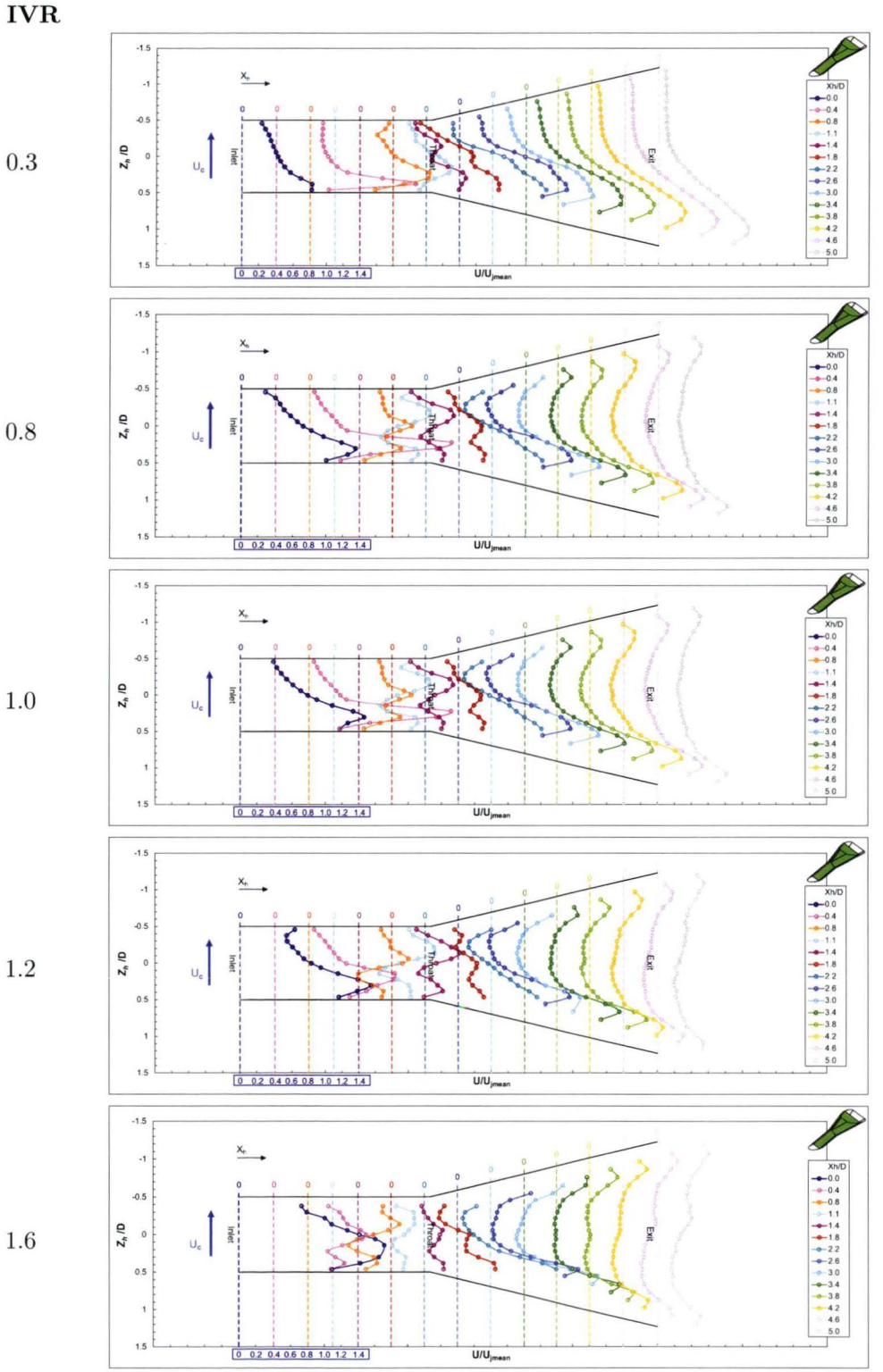

FIGURE 5.19: Change in internal Z_h velocity profiles with IVR, $M = \infty$, $\beta = 90$

Although the above interpretations of the measured data are insightful, the complex 3-dimensional flow field brought about by the large turning angles at the hole entry is difficult to understand from these profiles alone. Further insight can be gained by utilising computational models to provide a fuller picture of the flow behaviour. A more comprehensive explanation of the flow field and the effects of IVR for the $\beta = 90°$ configuration follows in Ch. 8.

5.4.3 Sensitivity of Flow Pattern to IVR

The marked difference in internal flow pattern between IVRs of 0.3, 1.0, and 1.6, motivated an investigation of the sensitivity of the flow pattern to variations in IVR. Measurements were made for the additional IVR values of 0.8 and 1.2 in the Y_h and Z_h planes for both the co-flow and cross-flow coolant passage configurations. These are presented in Figs. 5.17 - 5.18 alongside IVRs of 0.3, 1.0, and 1.6 for ease of comparison.

It is evident from the results presented thus far for the co-flowing coolant passage configuration, that an IVR of 1.0 creates an internal flow distribution that is near symmetric, uniform through the central region, and presents the lowest turbulence levels out of the tested cases. As discussed previously, moving either side of IVR = 1.0 creates a shift in the location of the core fluid region and distortions in both velocity and turbulence profiles within the hole. Looking at the Y_h profiles in Fig. 5.17, and comparing IVR 0.8 and 1.0, the shift of the core fluid jet towards the upper wall of the cooling hole is easily seen, and the velocity profile shape is very similar to that at an IVR of 0.3. This suggests that the top wall jet flow regime is dominant for all IVRs less than unity. Likewise for an IVR of 1.2, the internal Y_h velocity profiles are quite clearly shifted toward the lower wall when compared with the IVR = 1.0 case, indicating a tendency towards the flow pattern seen for IVR = 1.6.

Looking at the Z_h profiles in Fig. 5.18 for the same IVR cases, the change in profile shape as the IVR is either increased or decreased from a value of 1.0 can be clearly seen. The change in the internal flow distribution at IVR = 1.2 or 0.8 is consistent with the distribution observed at IVRs of 1.6 or 0.4 respectively, further confirming that there is a clear variation of the internal flow with IVR. Furthermore, the internal distribution is quite sensitive to changes in IVR, with the symmetric Y_h profiles only existing in a very narrow band of IVR values, in the order of IVR = 1.0 ± 0.1.

For the cross-flow ($\beta = 90°$) coolant passage configuration (Fig. 5.19), the change in flow pattern is more subtle as the IVR increases from 0.8 to 1.2. The most distinct change occurs around the hole inlet, where the first ($X_h/D = 0$) and second ($X_h/D = 0.4$) profiles show a change in the magnitude of peak velocity as the turning 'strength' of

flow into the hole decreases. This is reflected in the (less pronounced) shift in profiles at the hole exit with the peak values at either side becoming more equivalent.

A clearer comparison of profiles for different IVRs ($\beta = 0°$) can be seen in Fig. 5.20, where profiles taken at the same measurement location are directly compared. The progression of the peak velocity region from the upper to lower wall of the cooling hole as IVR increases is well demonstrated.

5.5 Influence of Coolant Passage Orientation

The measured data presented here for the co-flow and cross-flow inlet configurations permits a comparison of the internal flow fields to identify the influence of the coolant passage orientation. In general, the flow field for the $\beta = 90°$ case is markedly different to that for the $\beta = 0°$ case, due to the additional turning angle introduced by the 90° configuration. A comparison of the Y_h and Z_h profile measurements for each case shows that there is little similarity between the two coolant passage orientations. A discussion of the differences between the two configurations serves to clearly demonstrate the effect of the internal passage configuration on the flow development within the hole, and in turn on the interaction of the coolant and mainstream hot gas flows at the exit of the cooling hole.

The cross-flow configuration does not exhibit the type of strong jetting effect seen in the co-flowing configuration that dominates the internal flow field. This distinct change in internal flow patterns results in very different turbulence distributions between the two passage orientations. Turbulence intensity is generally lower at exit for the co-flow configuration, however, the turbulence distribution is not as uniform as it is in the cross-flow configuration, showing peak values near the walls in all IVR cases. Such a distribution may prove detrimental for interaction with the mainstream hot gas flow, encouraging mixing between the two streams and ultimately lowering cooling effectiveness.

The lack of strong secondary flow in the co-flow configuration appears to limit the influence of the diffuser on the internal flow field, in contrast to the cross-flow configuration where the distribution undergoes a significant transition between the cylindrical throat and the exit of the diffuser. The decelerating effect of the diffuser area expansion tends to reduce the severity of flow non-uniformity established at entry and in the throat section. The deceleration seems to even out the distributions of velocity and turbulence; however, the same deceleration of flow actually increases the relative turbulence level, contributing to the higher values seen in the exit area. This is evident in the cross-flow configuration, but less so for the co-flow configuration where the jetting fluid persists as a coherent core throughout the diffuser section and is dominant right to the exit

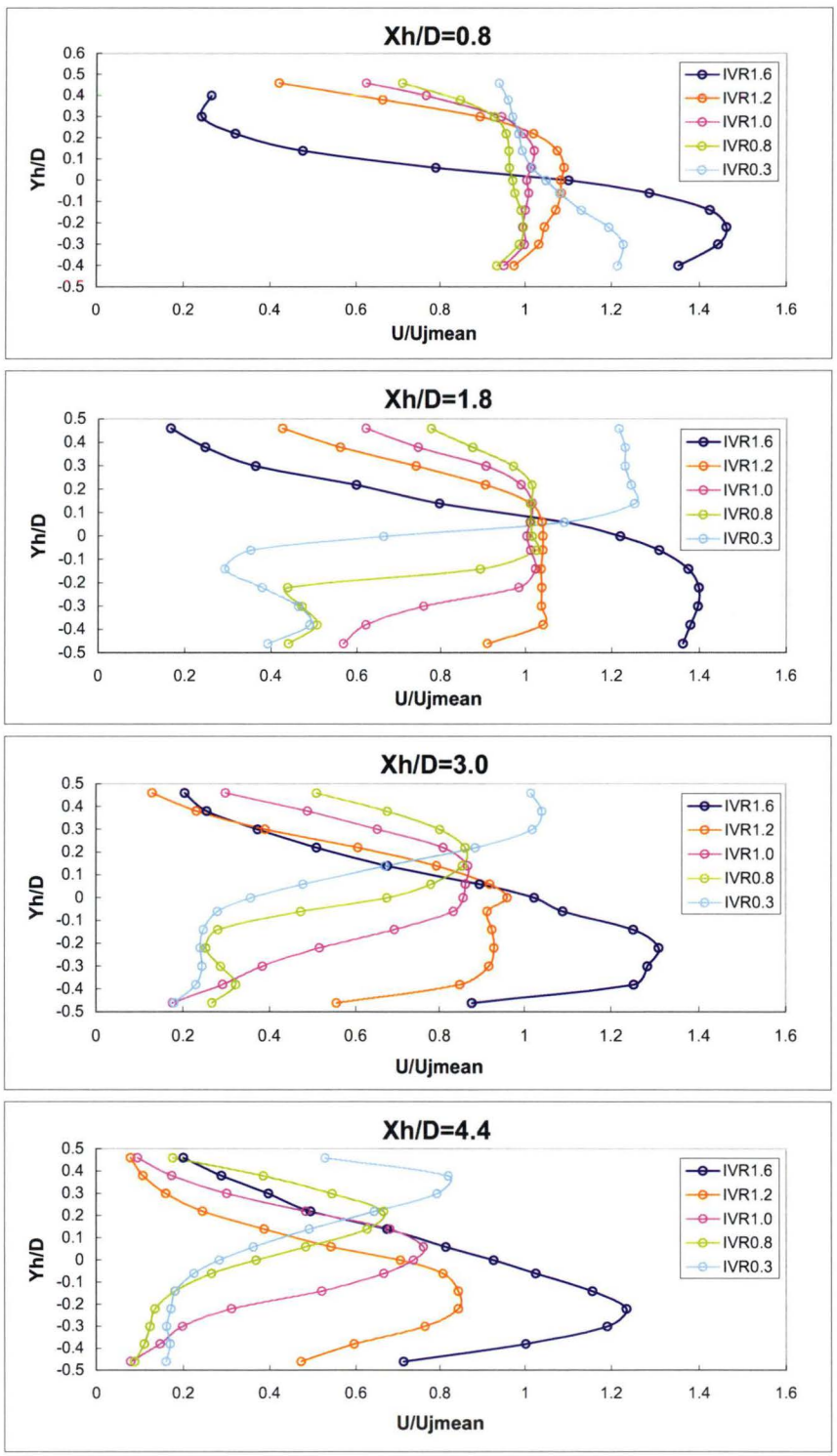

FIGURE 5.20: Comparison of internal Y_h velocity profiles at selected X_h/D locations, $M = \infty$, $\beta = 0°$

plane. Another prominent feature of the cross-flow configuration that is not evident in the co-flow configuration, is that of asymmetry of flow along the length of the hole. The secondary flow in the 90° coolant passage orientation case introduces a bias toward the right wall of the diffuser that is particularly evident for the IVR = 0.4 case.

An additional difference between the two configurations is in terms of aerodynamic loss. This will be investigated further in Ch. 7. However, it can be expected that the additional turning at inlet, secondary flow in the vortex structure, and higher turbulence levels caused by rotation of the coolant passage through 90° would result in higher aerodynamic losses through the cooling hole.

5.6 Influence of Exit Blowing Ratio

Two blowing ratios were tested for the full range of IVRs and both coolant passage configurations to determine the effect, if any, on the internal flow distribution at exit. The baseline case, already presented, had no external cross flow present, thereby eliminating any effects the external flow may have on the internal flow distribution. This case has a blowing ratio value of $M = \infty$ by definition. The comparison case was for a blowing ratio of $M = 1.3$; a value in the range of typical engine conditions. Figure 5.21 shows a comparison of the Y_h profiles between the two blowing ratio cases. The charts reveal that the presence of an external cross flow ($M = 1.3$) has no distinguishable effect on the flow within the cooling hole, except for the last 2 profiles in the measurement domain where, due to the 30° inclination angle of the hole, the Y_h profiles at $X_h/D = 4.4$ and 5.0 extend into the cross-flow above the cooling hole exit plane. The velocity and turbulence profiles here clearly show the exit cross-flow toward the upper wall, with elevated velocities and reduced turbulence intensities. These profiles also give an interesting insight into the interaction of the exit cross-flow and the cooling hole flow. The '0' dashed line for each of the exit profiles indicates how much of the exit flow is traversed; for the $X_h/D = 5.0$ profile, the upper half of the profile is entirely in the exit cross-flow.

Focussing on these two exit profiles, Fig. 5.22 reveals that the interaction between the ejected coolant and the oncoming exit cross-flow varies with IVR. The position of the jet at the exit plane of the hole, as determined by the inlet conditions, presents a different flow field to the oncoming exit cross-flow. At low IVR, the jet is near the upper wall and upon exiting the hole presents a strong blockage that pushes the oncoming flow away from the surface. This is evidenced by the lack of change to the $X_h/D = 4.4$ profile with $M = 1.3$, and a change to only the upper few points of the $X_h/D = 5.0$ profile as the measurement probe traverses into the edge of the cross-flow fluid. Compare this with the exit profiles for an IVR of 1.6 where the bulk of coolant exits near the lower

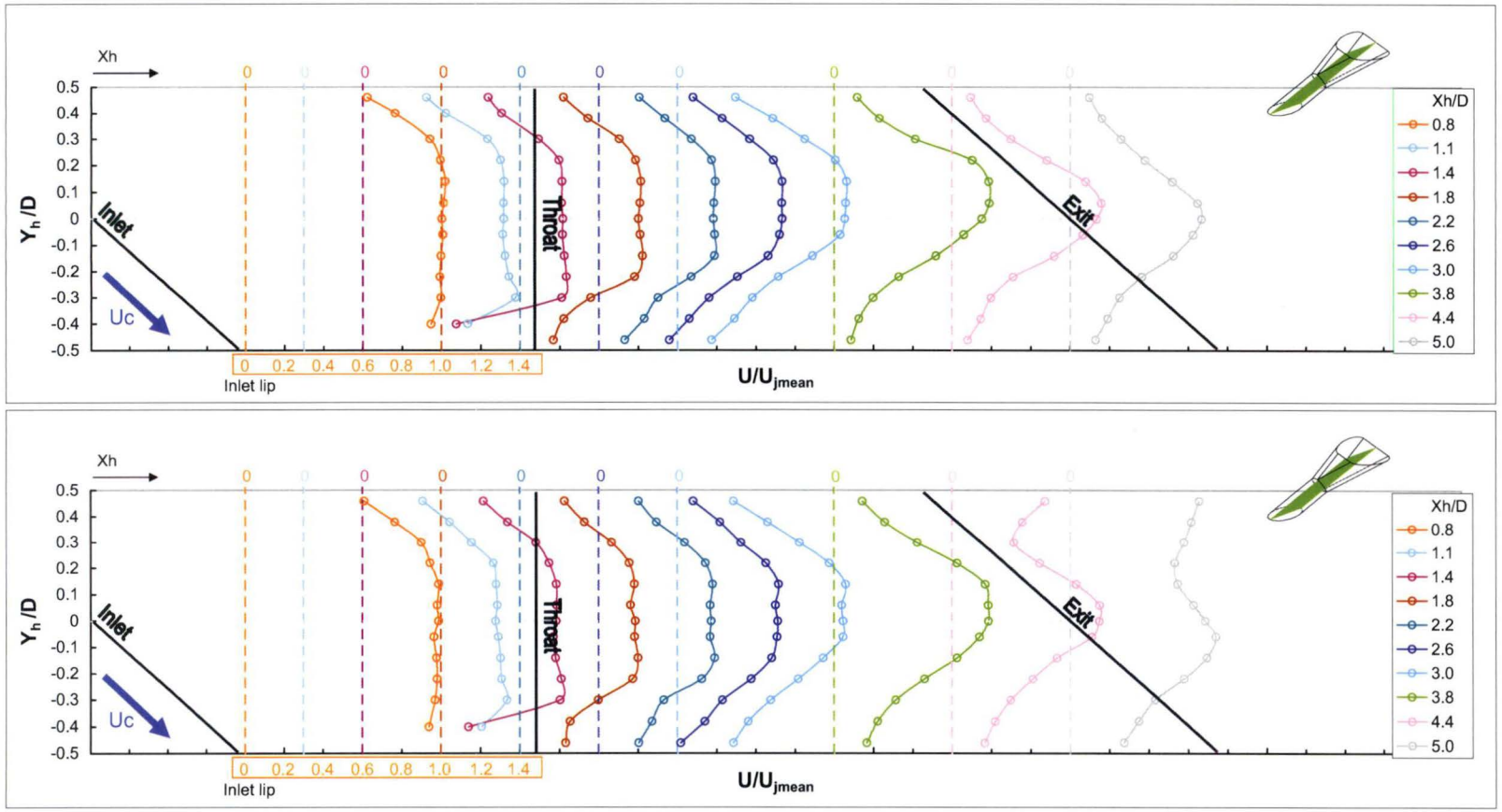

FIGURE 5.21: Effect of blowing ratio on Y_h velocity profiles for IVR = 1.0, $M = \infty$ (top), and M = 1.3 (bottom), $\beta = 0°$

wall, and the influence of the exit cross-flow can be seen near the upper wall and even slightly inside the hole at $X_h/D = 4.4$. At this higher IVR, the blockage presented by the exiting coolant is not seen by the exit cross-flow until almost half way across the hole, enabling this flow to stay near the surface. This is a combined effect, and has been described by others such as Andreopoulos and Rodi [10]. The oncoming cross-flow acts to 'squeeze' the coolant toward the lower, or downstream, wall. A shift in the location of the core jet fluid can be more clearly seen for the IVR = 1.0 case. The exit cross-flow provides increased velocity near the upstream wall of the hole, but when comparing to the $M = \infty$ case, the location of the peak velocity value has been pushed to the downstream wall as a direct result of the pressure field enforced by the approaching cross-flow.

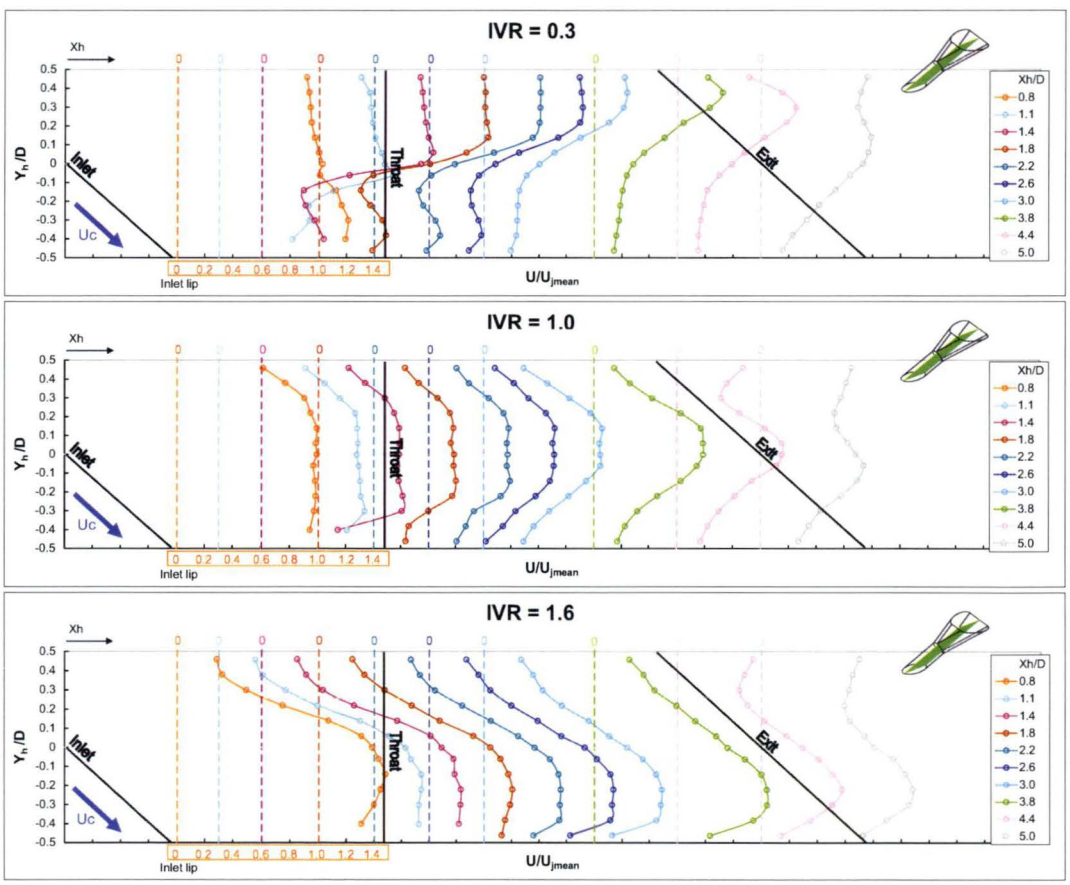

FIGURE 5.22: Change in internal Y_h velocity profiles with IVR, M = 1.3, $\beta = 0°$

The Z_h profile measurements (Fig. 5.23) show only a mild variation with the external cross-flow present for the $\beta = 0°$ cases. The profile at $X_h/D = 5.0$ shows slightly elevated velocity near the sidewalls of the diffuser and markedly reduced turbulence intensity. This change suggests that the external cross-flow is entering the hole at the sides where the blockage effect of the exiting coolant is weak. Such an occurrence has

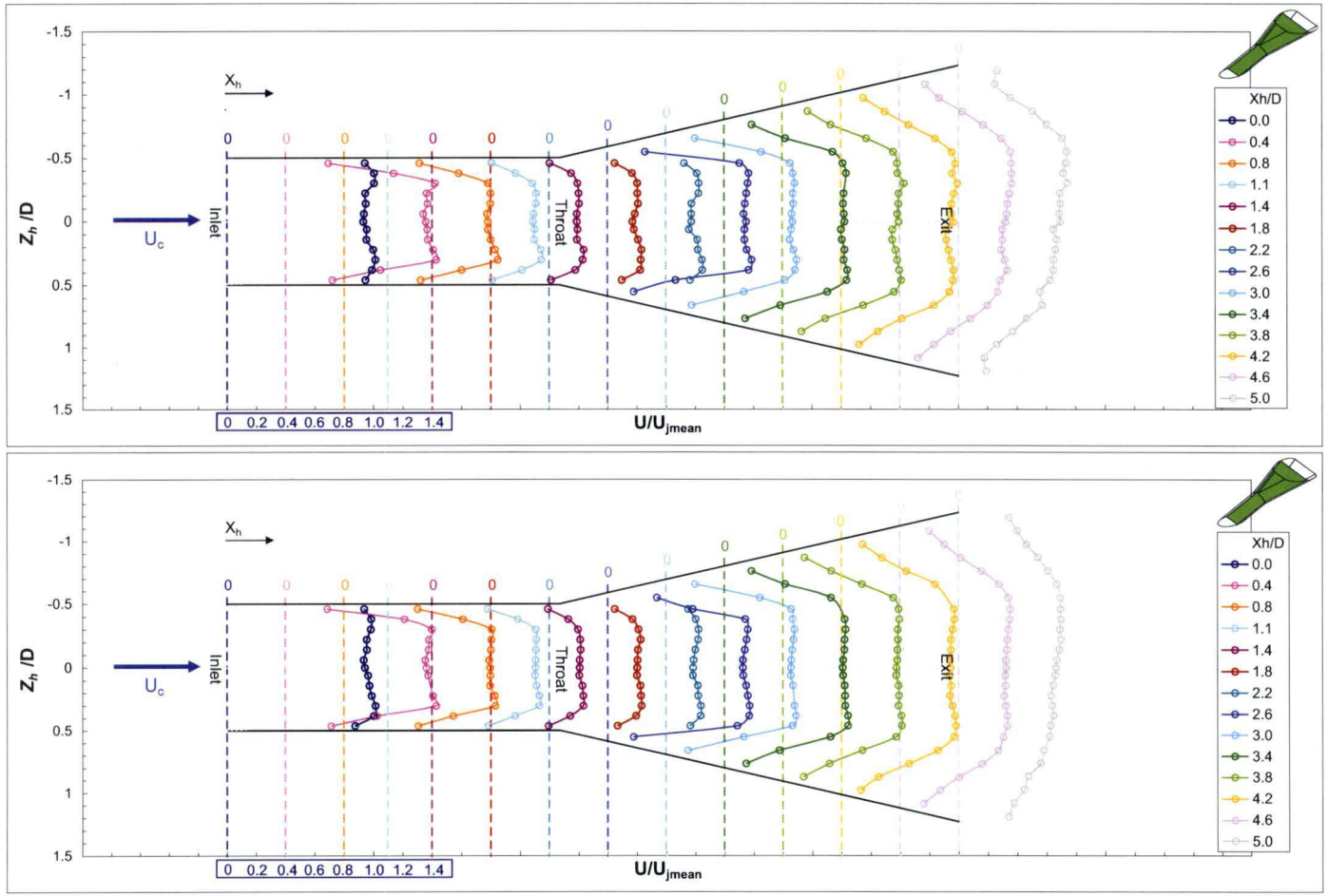

FIGURE 5.23: Effect of blowing ratio on Z_h velocity profiles for IVR = 1.0, $M = \infty$ (top), and M = 1.3 (bottom), $\beta = 0°$

serious implications for cooling performance, as any ingestion of hot gas fluid places higher thermal loads on the blade material.

5.7 Summary

A jetting effect within the hole has been identified from experimental measurements. The jetting is created by an inability of the incoming coolant flow to navigate the relatively sharp turn into the hole inlet. There is strong evidence that this jetting effect is governed by the IVR, and has implications on the flow distribution at exit of the hole. These results reinforce the need to include a full description of the flow configuration whenever results are being discussed, as it is clearly a combination of the coolant passage orientation, IVR, and blowing ratio that determines the coolant flow field at exit of the hole. For film cooling performance, this flow field determines how the two flows interact and progress downstream along the blade surface, and ultimately how beneficial the cooling effect is.

Chapter 6

Exit Flow Distribution

6.1 Overview

Data from measurements within the film cooling hole model presented in Ch. 5 revealed the significant impacts that inlet velocity ratio and internal coolant passage orientation have on the flow field development. When discussing film cooling performance, however, it would be remiss not to include investigations of flow development on the cooled surface downstream of the cooling hole exit, as it is this region to which the film cooling technique is directed. Thus, this chapter presents and analyses velocity and turbulence data measured in four lateral planes in the hole exit region.

6.1.1 Measurement Planes

Exit flow-field data were measured in the Y-Z plane at $X/D = -1, 0, 1$ and 2, with the measurement domain covering $Y/D = \pm 1.6$ and $Z/D = \pm 1.5$ (Fig. 6.1). The coordinate system here has its origin at the centre of the cooling hole exit plane, with X aligned axially with the working section, as shown in Fig. 4.12. Measurement planes were chosen to provide information on the progression of the coolant plume downstream of the cooling hole exit in the near-hole region. The hot-wire probe was traversed via an automated set-up, as described in Ch. 4. Figure 6.1 indicates the locations of the measurement planes relative to the cooling hole exit, with the measurement locations being at the intersection of the pink grid lines. The extents of the wind tunnel are shown to indicate the location of the measurement domain in relation to the hot gas volume. For easier interpretation of results, exit flow-field data is presented as a zoomed-in view of the near exit region for subsequent figures.

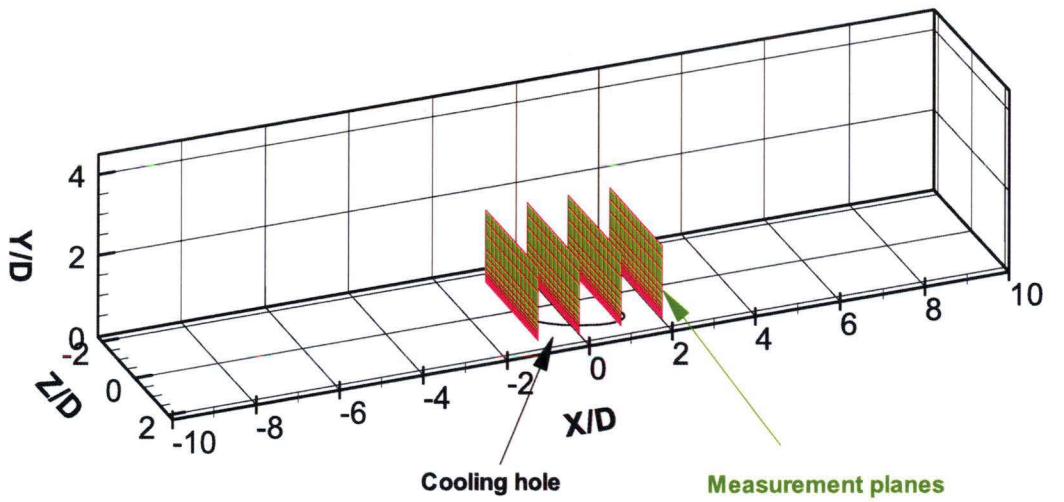

FIGURE 6.1: Exit flow-field measurement planes

6.2 Exit Flow Distribution for M = ∞, $\beta = 0°$

The exit cross-flow for $M = \infty$ cases is zero, as indicated by the large regions of $U/U_{j_{mean}} = 0$ in the contour plots upstream of the hole and around the coolant fluid. Turbulence plots for $M = \infty$ are confused by areas with zero or very close to zero velocity that create high patches of turbulence intensity in regions away from the exiting coolant. For consistency with other figures, the range of contour values used in the turbulence intensity plots has not been adjusted to resolve these uninformative areas and they appear as artificially high regions of stagnant fluid. Hence only those regions near to the surface, where velocity contours indicate the coolant exists, are useful in analysing the turbulence distribution.

Referring to Fig. 6.2 for an IVR of 0.3, the outline of coolant fluid shows a broad jet occupying the full exit width at $X/D = 0$. Moving downstream, the coolant continues to extend vertically, reaching 1 diameter above the surface by $X/D = 2$. The shape of the coolant outline, particularly at $X/D = 2$, suggests that the exiting jet is actually split into two core regions located at each side of the hole. There is a dip on the upper surface of the coolant profile at about $Z/D = 0$, denoting the separation of these two fluid cores. Such a distribution of velocity suggests a counter-rotating vortex pair issuing from the cooling hole, which has been identified by previous workers for a round cooling hole. The turbulence intensity profiles do not reveal a great deal, but do show high levels in the shear region at the edge of the emerging jet where the coolant and mainstream flows interact.

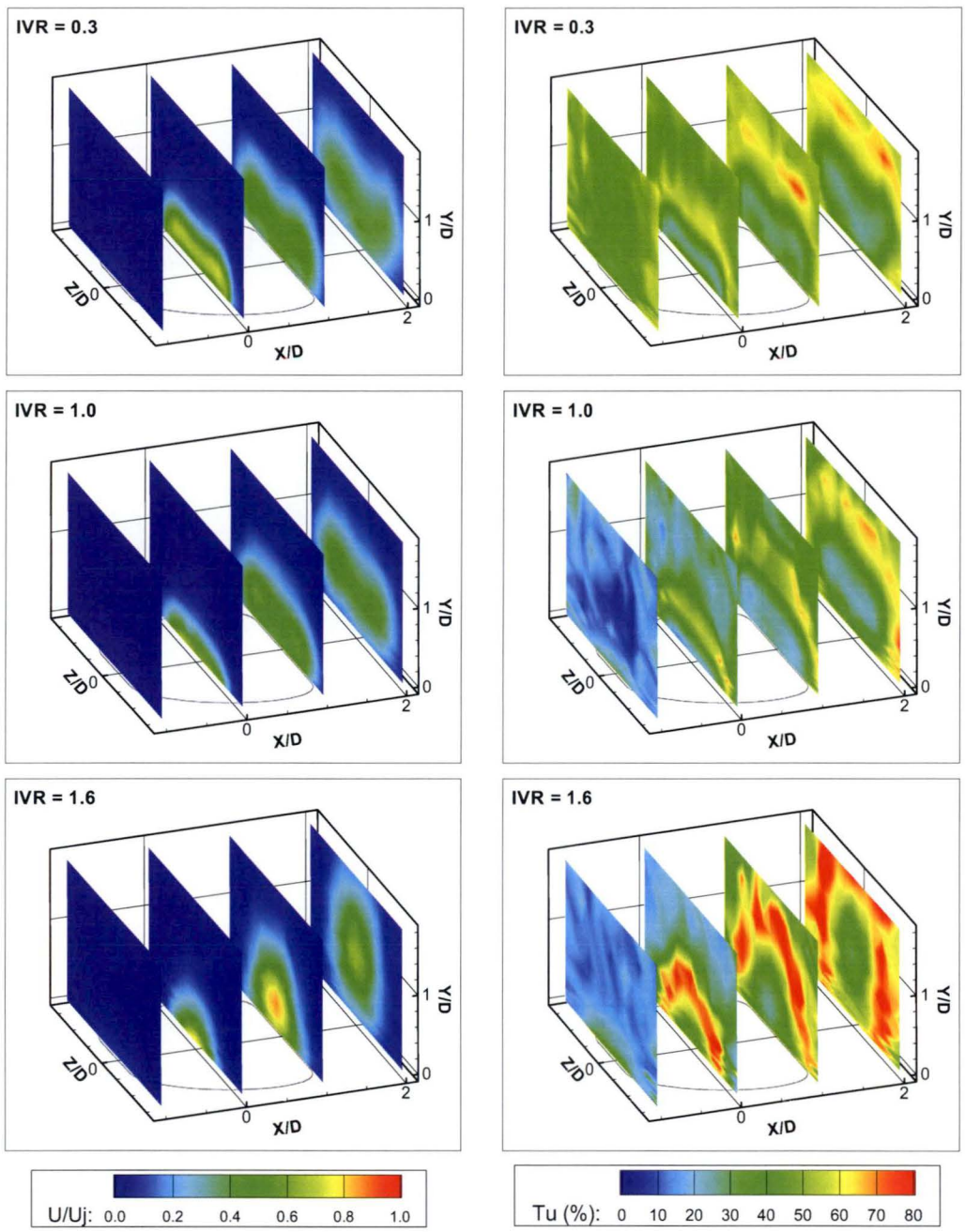

FIGURE 6.2: Contours of normalised velocity and turbulence intensity for IVR = 0.3, 1.0, and 1.6, $M = \infty$, $\beta = 0°$

At an IVR of 1.0 (Fig. 6.2) the flow distribution is very similar to that at 0.3, with the coolant fluid filling the exit width and rising and spreading with distance downstream. The bulk of the coolant fluid appears to have lifted away from the surface at $X/D = 2$, potentially leaving it exposed to hot-gas entrainment. There is some suggestion of a dual-core flow pattern (as for IVR = 0.3) at this location, though the effect is weak. Turbulence contours show spots of high intensity around the perimeter of the coolant fluid, but the overall level is reduced compared to the other tested IVRs.

At the highest IVR tested of 1.6 (Fig. 6.2), the coolant outline at the exit plane forms an almost perfect half circle, again lifting and spreading laterally as the coolant moves downstream. The flow pattern clearly shows a high-velocity core region decreasing in magnitude through a layer of shear to the stagnant hot-gas surrounding it. By $X/D = 2$, the jet spreading has reduced the central core velocity considerably, and the coolant is largely separated from the surface. Turbulence contours show very high levels around the perimeter of the jet, where a thick band of highly turbulent fluid indicates strong mixing between the coolant and hot-gas fluids.

6.3 Exit Flow Distribution for M = ∞, $\beta = 90°$

Contours of normalised velocity for an IVR of 0.4 are shown in Fig. 6.3. The direction of the coolant passage flow is shown in the lower left corner, and is the same for all $\beta = 90$ cases presented here. The figure clearly shows the bulk of coolant exiting from the right side of the cooling hole. Indeed, the contour plot at $X = 0$ shows the coolant exiting as a nearly round jet, with a central core of higher velocity fluid decreasing radially to $U/U_{jmean} = 0$. As the coolant fluid progresses downstream, the contours show a spreading both laterally and vertically of the jet and subsequent deceleration. The location of the core also tends to lift away from the surface, showing areas of mainstream flow drawn in under the coolant at $X/D = 2$. For the low IVR, turbulence intensity plots show moderate to high distributions, with the bulk of the cooling jet measured at between 20-25% Tu. The outline of the coolant can be clearly seen here, as it was for the velocity contours. Turbulence increases at the edges of the coolant jet, where a shear layer between the stagnant mainstream and the coolant exists.

As the IVR is increased to 1.0 (Fig. 6.3), a distinct change in the exit flow distribution is observed. At $X/D - 0$, coolant is exiting from both sides of the cooling hole, with flow on the left of the hole clearly penetrating vertically to a greater extent than that on the right. At the next measurement plane ($X/D = 1$), a higher velocity region close to the surface is visible at the right of the hole, and coolant now occupies the full width of the exit. This jet spreading leaves a thin layer of coolant near the surface. The vertical extent of the coolant distribution is again increased, particularly toward the left of the hole where the velocity is lower. At the end of the measurement domain, the coolant has dispersed further, maintaining an area of uniform velocity near the wall at the right side of the hole. On the left side of the hole, however, the coolant distribution extends to the top of the measurement plane and has a low velocity. Turbulence levels are around 20-25% in the regions of flow occupied by coolant. The tendency for the exiting coolant to stick to the right side of the hole and close to the surface generates lower turbulence levels in this region, although shear between the emerging jet and the exit

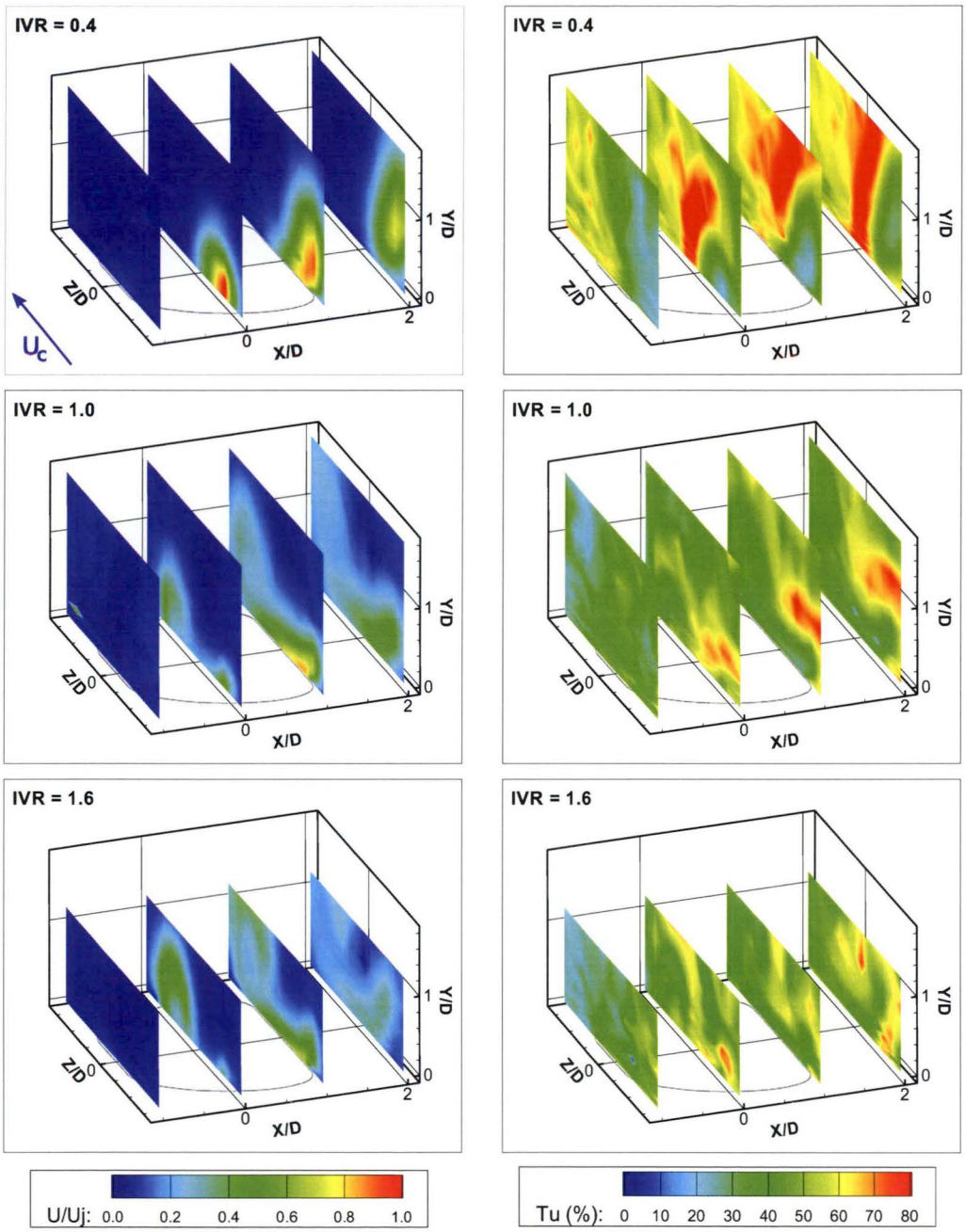

FIGURE 6.3: Contours of normalised velocity and turbulence intensity for IVR = 0.4, 1.0, and 1.6, $M = \infty$, $\beta = 90°$

fluid generates high turbulence above the coolant. At the left of the hole exit, however, moderate turbulence levels persist vertically suggesting that there is significant mixing between the coolant and mainstream in this lower velocity region.

At an IVR of 1.6 (Fig. 6.3), the flow pattern is almost the reverse of that seen in the low IVR case, with the bulk of the coolant flow now exiting from the left side of the cooling hole. The vertical spread of the coolant is evident at the $X/D = 0$ measurement plane

and downstream, though mostly on the left side of the hole. The contours here do not show a pronounced jet core as was seen for IVR = 0.4, with the velocity distribution of a lower magnitude and higher uniformity across the larger coolant area. At the next downstream measurement location ($X/D = 1$) the coolant has spread across the full exit width, much like IVR = 1.0 at the same location. The vertical dispersion of the coolant is significant on the left side of the hole, and the contours show a 'doughnut'-shaped velocity distribution, with low velocity fluid surrounded by faster flowing fluid. Such a distribution is characteristic of a vortex tube, as indicated by measurements in Ch. 5. By $X/D = 2$ the coolant has mixed out considerably, with a small region of low velocity fluid near the surface at the right of the hole. Areas of moderate turbulence intensity appear in a similar arrangement to that for IVR = 1.0. However, in the higher IVR case, the turbulence distribution is less congruant. The higher turbulence areas are again toward the left side of the hole, but are more dispersed. Indeed, at $X/D = 2$, the measurement plane shows an almost uniform (although high) turbulence intensity.

6.4 Influence of Inlet Velocity Ratio

6.4.1 Co-flow Configuration

The location of coolant fluid as it exits the cooling hole can be estimated with a good degree of certainty by looking for the thin shear layer between the coolant and hot-gas flows. Test data for the co-flow configuration in Fig. 6.2 shows that changes in IVR result in significantly different flow patterns at the exit and downstream. At high IVRs, the coolant fluid can clearly be identified as a round jet exiting the centre of the cooling hole. At an IVR of 1.0 the jet is more dispersed laterally (providing better coverage) and of lower velocity than the IVR = 1.6 case; at the lowest IVR tested of 0.3, the coolant jet is again spread laterally and is more uniform in its velocity distribution. This progression appears to be independent of the blowing ratio, with the internal flow dynamics dominating the coolant distribution at exit.

These observations can be directly attributed to the velocity profile at the cooling hole inlet as a result of the IVR. As established in Ch. 5, the internal flow pattern and distribution at exit of the cooling hole is strongly influenced by the IVR. The results presented here extend this finding to reveal significant changes in jet-mainstream interaction as the IVR is varied. It can be seen that the cases where the IVR is at a value of 1.0 show reduced levels of turbulence intensity when compared to higher or lower IVRs. This suggests reduced mixing with the mainstream hot-gas and potentially improved cooling effectiveness.

6.4.2 Cross-flow Configuration

The effect of IVR is also evident in the 90° cross-flow configuration from the contour plots presented in Fig. 6.3. As for the co-flowing cases, there is a progression from a cohesive, round jet with a defined core of high velocity, through to a more dispersed coolant distribution. With $\beta = 90°$, however, this progression is the reverse of the co-flowing cases, with the cohesive jet occurring at low IVRs, and the laterally dispersed coolant occurring at high IVRs. Clearly then, the IVR is having an equally substantial effect, but combined with a variation in internal cross-flow angle presents a very different exit distribution. Again this result is not unexpected, given the analysis of the internal flow dynamics presented in Ch.5. Besides the above effect of IVR, the contour plots reveal a shifting of the bulk of coolant from the right to the left side of the hole, at exit and downstream, which accompanies the general vertical and lateral spreading already described.

6.5 Influence of Coolant Passage Orientation

As identified in the previous sections, the most obvious change to the flow pattern (Fig. 6.4) for all IVRs and blowing ratios when the coolant passage orientation is varied, is the shifting of the location of the bulk coolant flow from being symmetric about the $Z/D = 0$ line, to having a bias toward one side or the other at exit. This change was identified in the internal flow field data and stems directly from the conditions at inlet to the hole. In addition, the rotation of the coolant passage to a 90° cross-flow creates a reversal in the flow pattern trends with IVR, with the higher velocity fluid moving from right to left at exit, as opposed to the left to right transition for $\beta = 0°$.

As well, the vertical penetration of the coolant is increased compared with the co-flowing configuration, for all IVRs. This vertical dispersion can be attributed to a larger velocity vector in the vertical direction as a result of swirling secondary flows within the hole. This vertical penetration comes at the expense of lateral coverage, with only a thin coolant layer present along the hole centreline. Secondary flows within the hole are also responsible for the slightly higher turbulence intensities for the cross-flow configuration.

6.6 Influence of Blowing Ratio

The influence of blowing ratio on the external flow distribution is significant (Fig. 6.5). Interactions between the two fluid regions are observed to generate notable differences whether the exit cross-flow is present or not. In both the co- and cross-flow coolant passage configurations local acceleration of the mainstream hot-gas occurs as it is deflected

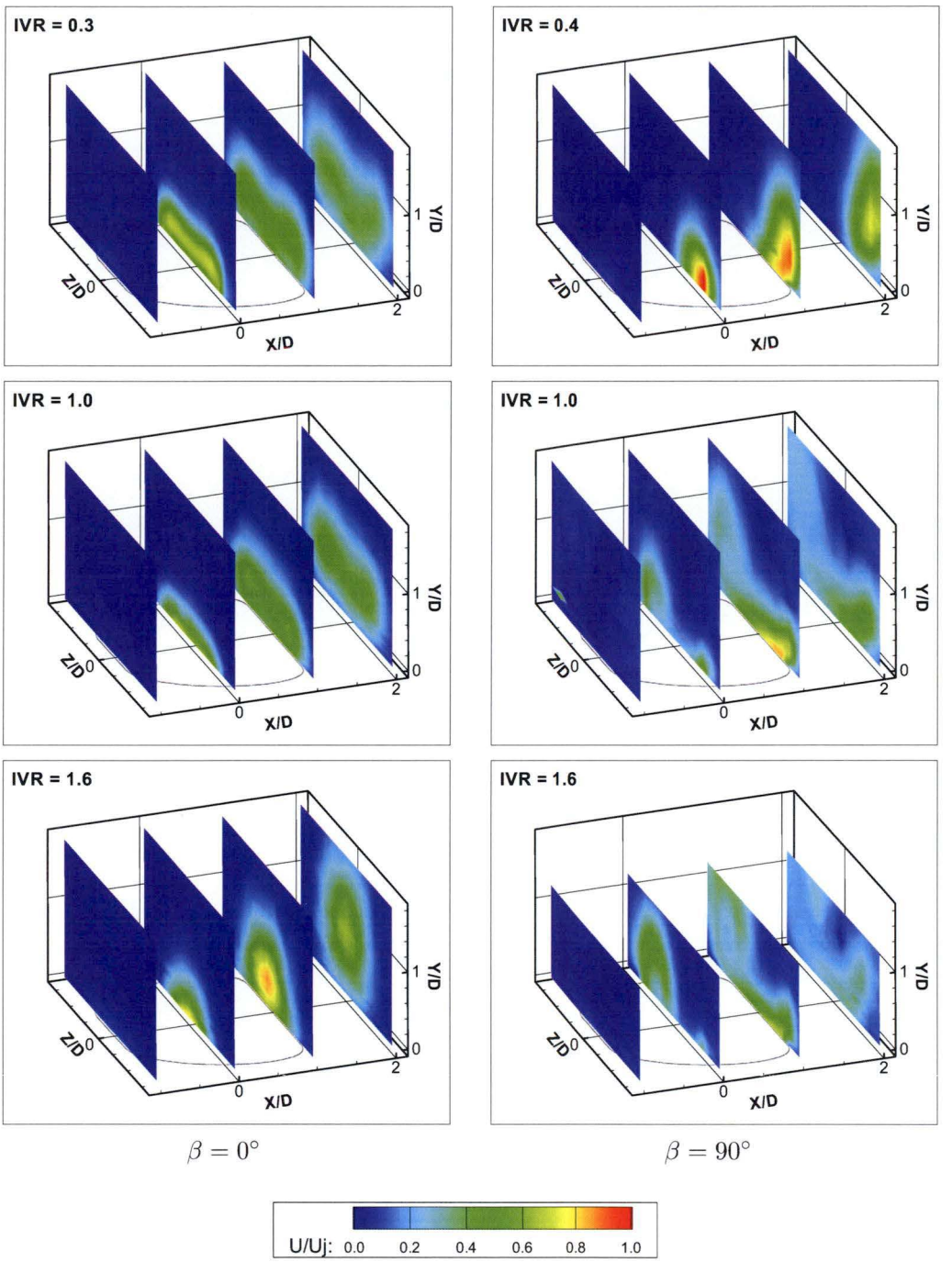

FIGURE 6.4: Effect of coolant passage orientation on the exit flow field for tested IVRs, $M = \infty$

from the surface by the incoming coolant jet. This effect, more evident in the $M = 1.3$ cases, is most clearly observed for IVR = 0.3, where the entire measurement domain above the exiting coolant fluid is accelerated, increasing the velocity markedly between X/D = -1 and X/D = 2. This effect is still observable at an IVR of 1.0, but at the highest IVR of 1.6, there is no distinguishable effect of the coolant jet on the mainstream

flow. The inverse of this mainstream lifting is that the presence of a cross-flow at exit acts to push the coolant fluid to the surface. This is good for film cooling as the coolant is forced to spread laterally, providing better surface coverage. In the cross-flow configuration and the lowest IVR, the suppressing effect of the mainstream hot-gas appears to force the strongly right-side coolant jet to flatten and spread across the full width of the hole, compared with the $M = 0$ case where the coolant stays firmly toward the right of the hole. The presence of an exit cross-flow also appears to reduce the overall levels of turbulence in the exit region of the hole.

6.7 Summary

Data presented in this chapter has revealed the nature of coolant and hot-gas flows in the exit region of the fan-shaped film cooling hole. The coolant distribution in the exit region is determined largely by internal flow dynamics of the hole, which are in turn heavily influenced by the inlet conditions to the hole. Variation of IVR over the range tested changes the exit flow pattern from a coherent, round jet, to a more dispersed coolant profile. The sense of IVR variation that causes this transition is dependent on the orientation of the coolant passage. The co-flowing configuration presents coolant distributions which are largely symmetric about the longitudinal hole axis, while the cross-flowing configuration generates a bulk coolant location that varies from one side of the hole to the other, depending on the value of IVR. Both of these trends persist downstream with or without the presence of an external cross-flow. Such a cross-flow plays a role in the dispersion of the exiting coolant, generally forcing the coolant to remain near the surface and to spread laterally, providing better coverage of the surface. The important point to note in all of these findings is that alterations to the internal flow conditions at the inlet of the cooling hole have lasting effects through the hole and onto the surface downstream, impacting significantly on film cooling performance. For the designer, this result emphasises the need to closely consider inlet geometry and flow conditions to optimise the performance of a film cooling scheme.

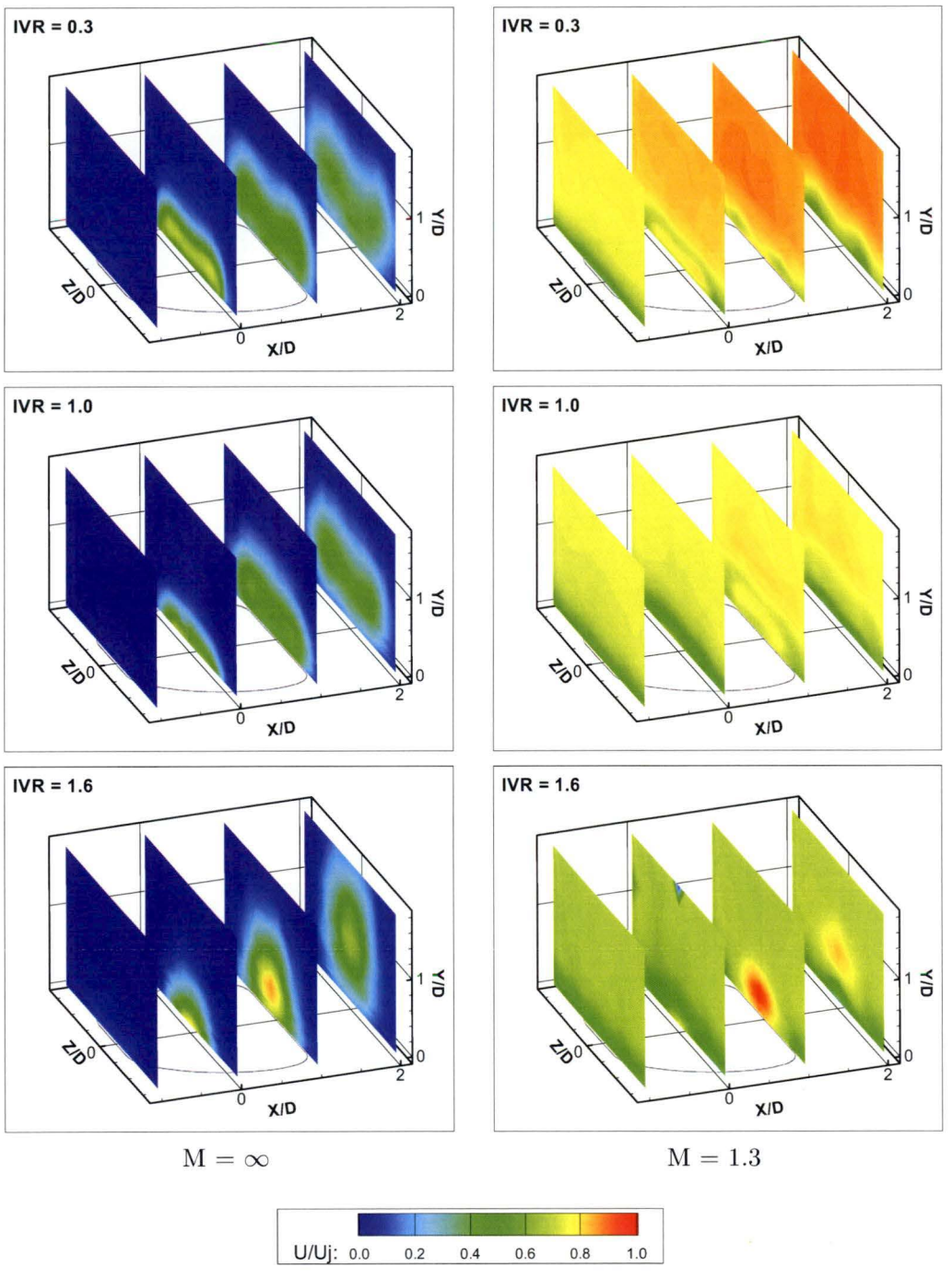

FIGURE 6.5: Effect of blowing ratio on the exit flow field for IVR = 0.3, 1.0, and 1.6, $\beta = 0°$

Chapter 7

Discharge Coefficients

7.1 Overview

The discharge coefficient, C_d, is used in cooling system design as a single parameter representation of the aerodynamic penalty associated with a particular geometric and fluid dynamic configuration. The coolant fluid can be as much as 5% or more of the total engine flow, and as this air is not heated in the combustor, it does less work through the turbine section and hence reduces the overall efficiency of the engine. It is essential, therefore, to keep the mass flow of coolant to the minimum amount that will achieve the required cooling performance. Flow to the coolant film is controlled through selection of cooling hole geometry and the total number of holes. This makes knowledge of the discharge coefficient for a wide range of geometries and flow conditions essential for design.

7.1.1 Measurement Technique

For large scale model testing, the actual cooling hole mass flow rate, $\dot{m}_{actual}$, was measured via a bell-mouth nozzle connected to the coolant supply loop, as detailed in Ch. 4. The ideal mass flow rate was calculated from measurement of the coolant total to mainstream static pressure ratio. The coolant total pressure was measured 2 hole diameters upstream of the cooling hole inlet with a total pressure tube inserted in the flow. The exit mainstream static pressure was measured via a wall static tapping on the main working section side-wall and at the same longitudinal position as the centre of the cooling hole exit plane. The ideal mass flow rate was then determined as

$$\dot{m}_{ideal} = A_t \sqrt{2\rho(P_{0c} - P_m)}$$

and the discharge coefficient as

$$C_d = \frac{\dot{m}_{actual}}{\dot{m}_{ideal}}$$

In addition to measurements of pressure drop across the hole, an 8 channel dynamic pressure measurement system, as detailed in Ch. 4, was used to record the axial pressure distribution along the side wall of the cooling hole model. A total of 7 wall tappings were spaced along the length of the hole at 1 diameter spacing. Due to access restrictions, the first four holes from the inlet were positioned on the upper wall, while the last three were on the lower wall. A tapping was positioned on both sides at the cross-over point between upper and lower wall. These pressures were recorded simultaneously via the data acquisition system at a sampling rate of 5kHz, and averaged over 5 seconds.

7.1.2 Measurement Matrix

Discharge coefficients were measured for a range of test cases as detailed in Tab. 7.1. These measurements were structured to cover IVRs from 0.3 to 3.5 in order to assess the influence of this parameter on C_d, given the significant alteration to the internal flow field with IVR already identified from measurements presented in Ch. 5. In addition, exit blowing ratios of M= 0.5 and 1.3 were tested along with the no external cross-flow condition ($M = \infty$).

$\beta°$	IVR	M
0	$0.3 - 3.5$	∞
		1.3
		0.5
90	$0.3 - 3.5$	∞
		1.3
		0.5

TABLE 7.1: Test cases for discharge coefficient measurements

7.2 Results

For low speed tests, the pressure ratio P_{0c}/P_m assumes values very close to 1, making it an inappropriate parameter to plot C_d data against when comparing with high speed results. A more useful parameter is the cooling hole Reynolds number based on throat diameter and mean throat velocity, $Re_{j,D}$, which varies with pressure ratio and in this study is matched to engine conditions. Discharge coefficient results are presented in Fig. 7.1 for all tested configurations, plotted against $Re_{j,D}$. At low $Re_{j,D}$, all configurations show similarly low values of C_d. As $Re_{j,D}$ increases, C_d rises quite sharply, and at about $Re_{j,D} = 5000$ the curves diverge, with data for the cross-flowing inlet starting to flatten out. At higher $Re_{j,D}$, the marked difference between the two inlet orientation cases can be seen. In general, the variation of C_d for the fan-shaped hole is characterised

by a sharp increase at low $Re_{j,D}$ (to a peak value for the co-flowing orientation), before trending towards a constant value at higher $Re_{j,D}$. This plateau region appears to occur for $Re_{j,D} > 25,000$ for the current geometry. For the co-flowing configuration, there is a peak value of C_d at about $Re_{j,D} = 10,000$, and beyond this C_d decreases with increasing $Re_{j,D}$. This trend was also found by Rowbury [5] and may be explained by increased flow separation within the diffuser leading to a decrease in diffuser efficiency. The effect of blowing ratio appears to be a slight reduction in C_d for blowing ratios less than $M = 1$, and no notable difference at higher blowing ratios. In these low speed cases, the discharge coefficient can reach values in excess of unity; an occurrence that is discussed further in Sec. 7.4.1.

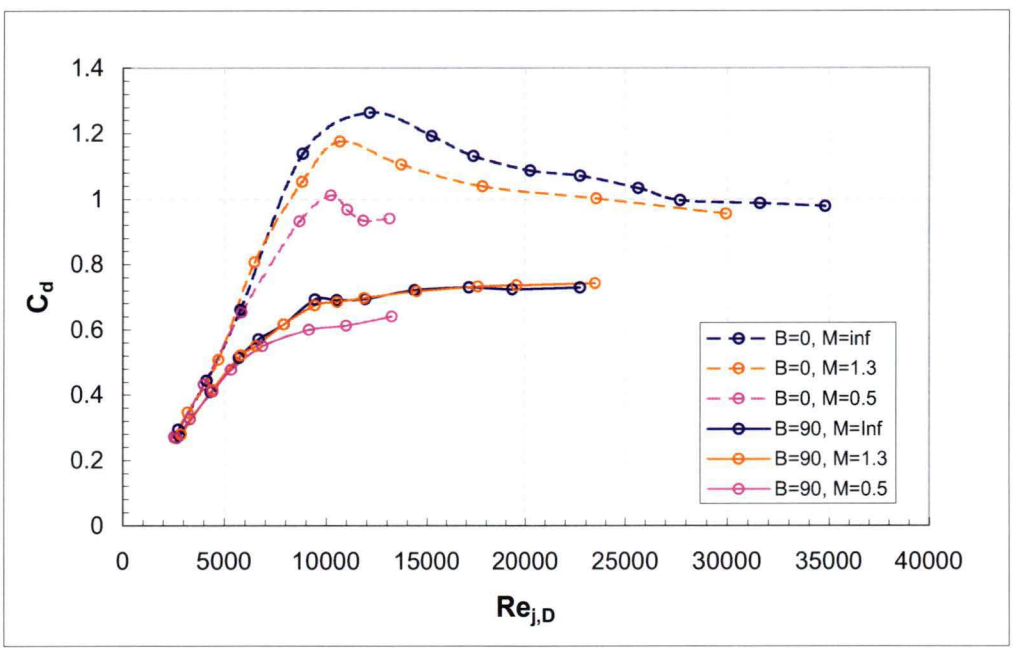

FIGURE 7.1: Variation of discharge coefficient with hole Reynolds number

7.2.1 Influence of IVR

The data presented in Fig. 7.2 shows the variation of C_d with IVR. The general trend is a decrease in C_d as IVR is increased, with all tested configurations collapsing toward a common low value of $C_d = 0.3$ at an IVR of 3.5.

Looking first at the data for the co-flowing coolant passage ($\beta = 0°$), there is a marked peak to $C_d = 1.3$ at an IVR close to 0.8, before reducing markedly to $C_d = 0.7$ at an IVR of 1.4. At IVR values from $0.3 - 0.8$, C_d increases from $0.9 - 1.3$. Comparing this observation with those made from the internal flow measurements presented in Ch. 5, an inference can be made about the loss mechanisms at work. The most prominent internal flow feature identified for the co-flowing case is the jetting effect at the hole

inlet. The peak in C_d at an IVR of 0.8 corresponds to the jet being positioned slightly toward the upper wall of the cooling hole, with little flow separation at the inlet lip. At lower IVRs, the coolant has to turn through a large angle at the downstream inlet lip, separating within the hole and generating significant secondary flow patterns. The elevated turbulence levels seen at the inlet in Fig. 5.4 for the IVR = 0.3 case and Fig. 5.6 for the IVR=1.6 case contribute to the higher loss through the cooling hole and hence lower values of C_d. As the IVR increases through 0.8, the level of turbulence at the hole inlet reduces and becomes uniform across the diameter, corresponding to the lowest amount of pressure loss and hence the highest C_d. Similarly, at IVRs greater than 0.8, the jetting region shifts toward the lower wall and again strong secondary flows and high turbulence intensities can be seen as a result of inlet and diffuser separation. Correspondingly, C_d decreases at these higher IVRs.

In line with these observations, it is interesting to note that the flow angle at an IVR of 0.8 is $\arccos(0.8) = 37°$. The inclination angle of the cooling hole, α, is 30°. The discharge coefficient results suggest, therefore, that minimum entry losses occur (and hence maximum mass flows) for a co-flowing configuration when the angle of flow at the inlet is equivalent to the inclination angle of the hole. For the current geometry, this suggests an 'optimum' IVR of $\cos(30) = 0.87$ to achieve maximum C_d.

For the cross-flowing coolant passage ($\beta = 90°$), an increase in IVR results in a decrease in C_d over the whole range tested, with no peak value observed. From IVR = $0.4 - 1.0$, the decrease in C_d is mild, changing from about 0.75 to 0.7. At IVR values greater than 1.0, the rate of C_d decline increases, falling to low values of about 0.3 over the range tested.

7.2.2 Influence of Orientation Angle

The differences between C_d results for the two tested passage orientations is easily identifiable from Figs. 7.1 and 7.2. Across the mid range of IVRs, from $0.4 - 1.5$, the cross-flowing configuration results in significantly lower discharge coefficients compared to the co-flowing configuration. At higher IVRs, the two sets of curves merge, decreasing towards a value of $C_d = 0.3$ at an IVR of 3.5. This consistently low C_d value suggests that a similar degree of loss is occurring for both orientations at high IVR. It can be inferred that higher IVRs produce significant inlet separation and secondary flow that is almost independent of the cooling passage orientation. This disturbance at the inlet generates high levels of turbulence, as seen in Fig. 5.6. Hence, the losses are almost equally high for the two orientations, and the discharge coefficients correspondingly low. Clearly, the peak in C_d seen in the $\beta = 0°$ configuration is suppressed for $\beta = 90°$. This can be largely attributed to the strong secondary flow and high turbulence at the hole

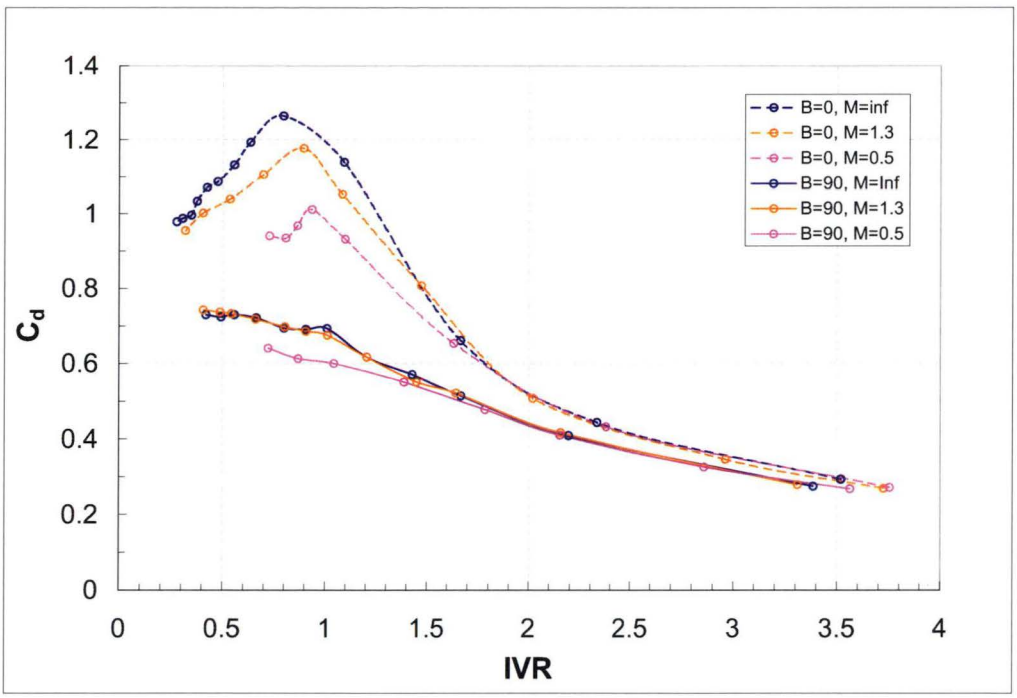

FIGURE 7.2: Variation of discharge coefficient with inlet velocity ratio

entry as a result of the 90° turning of the flow from the coolant passage; there is no 'optimum' IVR for which inlet separation is minimised.

7.2.3 Influence of Blowing Ratio

The effect of blowing ratio on C_d was investigated for three values of $M = 0.5$, 1.3, and ∞ at an IVR of 1.0, and measured results are shown in Fig. 7.3. The chart shows a marked rise in C_d with blowing ratio from 0.5 to 1.3, but beyond this, for both coolant passage orientations, the effect of blowing ratio is minimal. This demonstrates that there is a narrow band of low blowing ratio where the flow dynamics at exit are sensitive to changes in M. At low blowing ratios, the exit region flow is dominated by the external cross-flow. At blowing ratios greater than about 1.0, however, the coolant jet is influenced less by the external cross-flow, and the jet conditions at exit then control the pressure field.

Rowbury [5], conducted large scale measurements of static pressure distribution around the exit of a cylindrical cooling hole. The data revealed that the average exit pressure was lower than the expected pressure determined from the distribution around the cylindrical leading edge model without film cooling. As a result, C_d showed an increase in the presence of an external cross-flow. The data presented here, and indeed other fan-shaped hole studies such as Gritsch et al. [62] and Hay and Lampard [51], show the opposite trend, with an external cross-flow causing a reduced value of C_d. The reduction in exiting

coolant velocity due to the area expansion of the diffuser results in less penetration of the coolant into the mainstream when compared to a cylindrical geometry at the same mass flow rate. This effect presents the oncoming mainstream flow with a reduced blockage for the fan-shaped hole, which does not accelerate as strongly as it is turned around the exiting jet. The local pressure reduction is not significant, and the configuration results in a reduction in C_d.

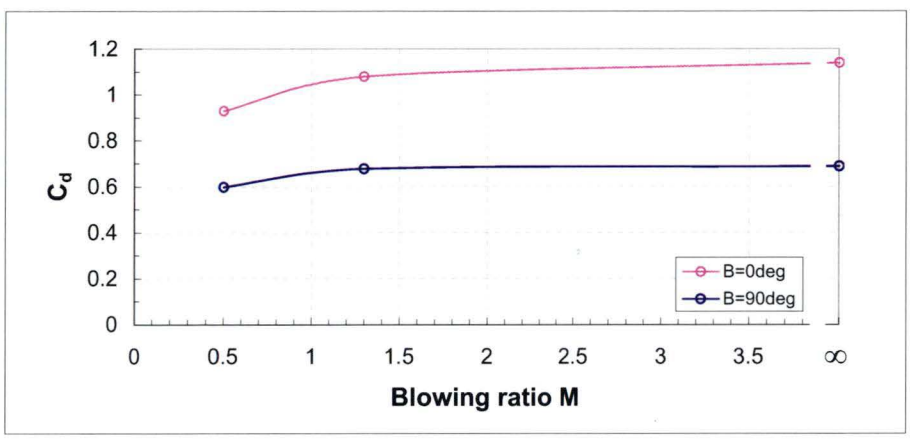

FIGURE 7.3: Variation of discharge coefficient with blowing ratio, IVR = 1.0

7.3 Axial Pressure Profiles

To investigate the main sources of loss for each configuration, static pressure taps were installed along the top and bottom walls of the cooling hole in the centreline plane. Pressure measurements from these taps for different IVRs help to identify the locations at which pressure is lost or recovered, and hence locate critical regions of the configuration. Figure 7.4 shows the axial pressure profiles in the $\beta = 0°$ configuration and no external cross-flow for a range of IVRs, and Fig. 7.5 shows the $\beta = 90°$ configuration. Here the static pressures are presented as a pressure coefficient, $C_p = \frac{P_{stat} - P_{c_{tot}}}{P_{j_{dyn}}}$, where $P_{j_{dyn}}$ is the jet dynamic pressure, calculated from the mean jet velocity.

The variation of static pressure coefficient along the length of the hole shows some commonality between the two coolant passage orientations in terms of a loss just downstream of the inlet, and some pressure recovery through the diffuser. Within the results for each configuration, the pressure profiles are nearly the same for IVR < 1. At higher IVRs, however, the pressure coefficients are much lower, corresponding to the low values of C_d seen in Fig. 7.2. Pressure recovery through the diffuser for the two configurations is similarly poor at high IVRs. However, at IVRs < 1, the $\beta = 0°$ configuration shows significant pressure recovery,compared to the negligible recovery shown in the $\beta = 90°$ configuration. This suggests that the internal flow resulting from the inlet cross-flow is

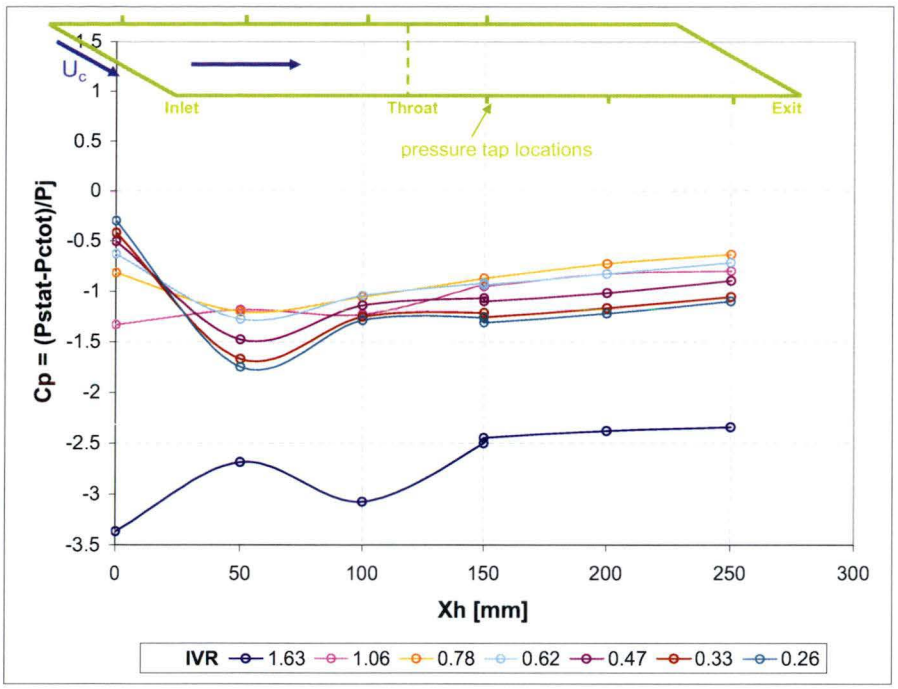

FIGURE 7.4: Static wall pressure distribution along hole axis for M = ∞, $\beta = 0°$

stalling the diffuser, likely induced by the secondary flow rotation generated from strong flow turning at the hole inlet.

For the co-flowing configuration, an IVR very close to unity (1.06) clearly shows the least amount of variation in static pressure at the inlet, representing minimal losses as the flow enters the hole without significant separation from the inlet lip. However, the flow dynamics in the diffuser section for this IVR appear to limit the pressure recovery somewhat. In fact, it is the slightly lower case where IVR = 0.78 that demonstrates the greatest pressure recovery, in line with the peak C_d value of 1.3 measured at an IVR of 0.8 in Fig. 7.2.

Reducing the blowing ratio to $M = 0.5$ appears to have little effect on the axial pressure profiles for IVR < 1 in the cross-flow case, as shown in Fig. 7.6. For higher IVRs, however, the presence of a cross-flow at exit results in a greater overall recovery through the diffuser, albeit that the discharge coefficients are still very low.

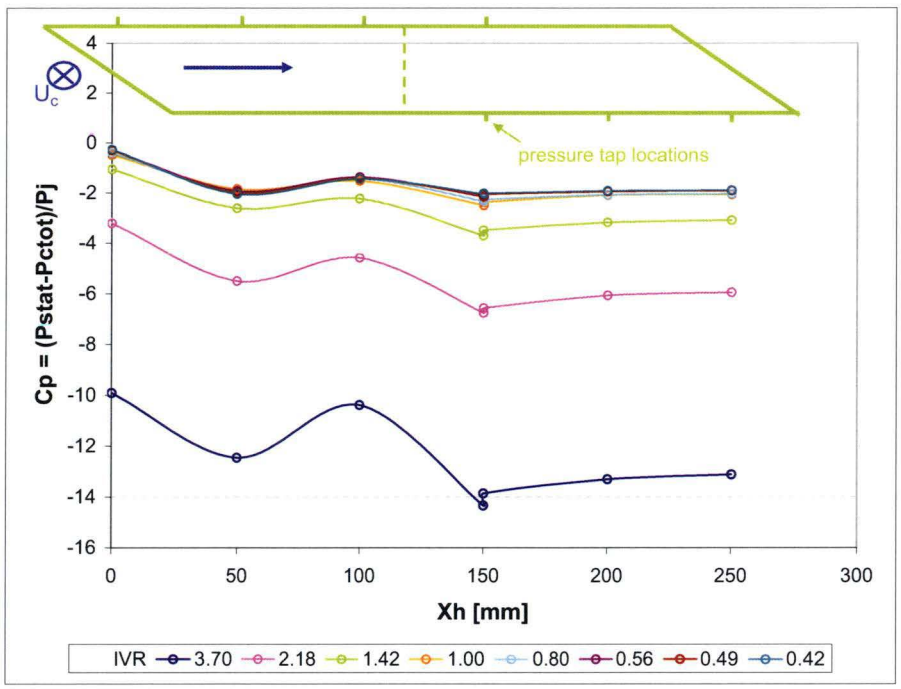

FIGURE 7.5: Static wall pressure distribution along hole axis for M = ∞, $\beta = 90°$

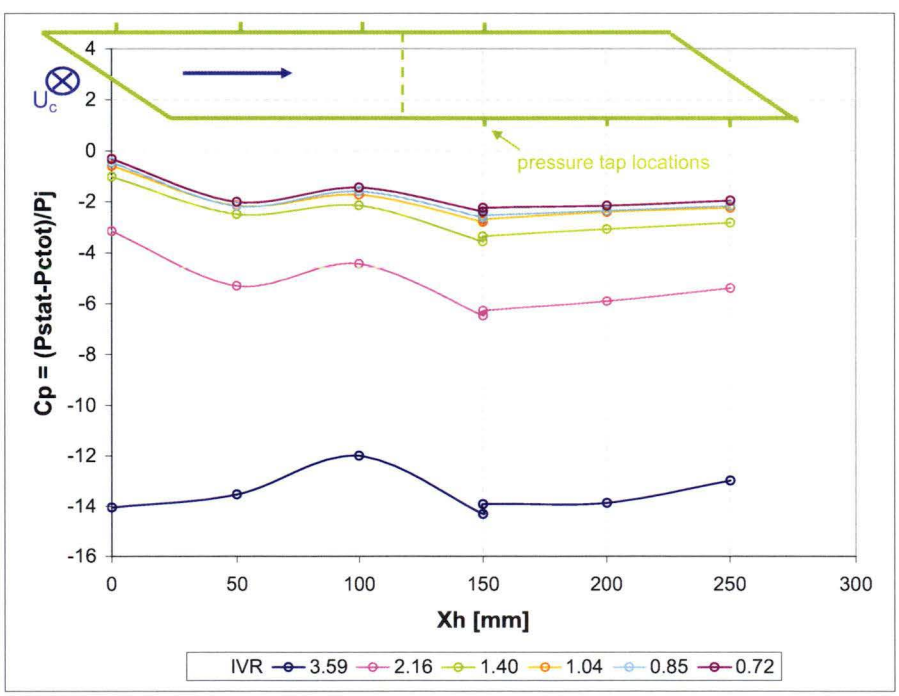

FIGURE 7.6: Static wall pressure distribution along hole axis for M = 0.5, $\beta = 90°$

7.4 Fluid Compressibility and the Impact on C_d

Although somewhat outside the scope of experimental measurements for the current study, the influence of compressible flow effects on the in hole flow and discharge coefficients will be discussed here.

7.4.1 Low Speed Flow

From the results of discharge coefficients presented for the large scale cooling hole model, it is clear that the overall C_d values are much higher than those presented by other workers from high-speed experiments. Indeed, low-speed measurements indicate C_d well above unity, in contrast to high speed results which demonstrate a typical maximum of $C_d = 0.8$. From this, the question was raised as to what the driving mechanism for this difference was, and if there was a correlation between low and high speed results.

In determining C_d for fan-shaped cooling holes, common practice is to use the ideal mass flow rate through a cylindrical hole having the same diameter as the inlet section of the shaped hole [62]. This enables direct comparison of results to cylindrical holes, but has implications on calculation of absolute values, particularly at low speed. Figure 7.7 is a two-dimensional depiction of a typical diffuser. Supply pressure $P1$ feeds the diffuser which has a cross-sectional area $A2$ and pressure $P2$. The diffuser expands to area $A3$ and an exit pressure of $P3$. Assuming an ideal nozzle under incompressible flow conditions, where frictional and separation losses are neglected, the ideal flow rate is given by

$$Q_i = A2\sqrt{\frac{2(P2 - P1)}{\rho(1 - m^2)}}$$

where $m = A2/A1$. In terms of the actual inlet and exit pressures, we can write

$$Q_i' = C_{d_i}.A2\sqrt{\frac{2(P3 - P1)}{\rho(1 - m^2)}}$$

Equating Q_i and Q_i' gives

$$C_{d_i} = \sqrt{\frac{P2 - P1}{P3 - P1}}$$

From continuity and Bernoulli and rearranging we arrive at

$$C_{d_i} = \sqrt{\frac{1 - (A1/A2)^2}{1 - (A1/A3)^2}}$$

If, as in the current study, the total pressure at inlet $P_{0c,1}$ is used in place of the static pressure, the ideal discharge coefficient reduces to

$$C_{d_i} = \frac{A3}{A2}$$

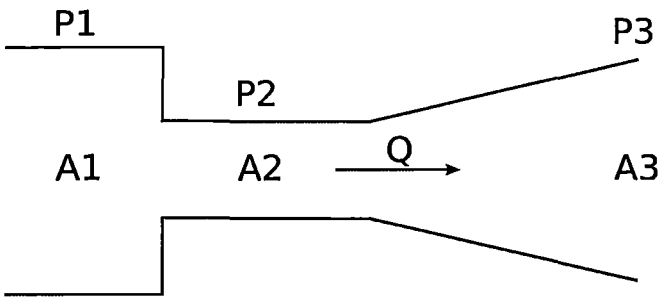

FIGURE 7.7: Schematic of two-dimensional diffuser

which shows that the ideal discharge coefficient is dependent only on the nozzle area ratio. Therefore, three possible cases for the ideal discharge coefficient exist:

$$\begin{aligned} A2 < A3 &\rightarrow C_{d_i} > 1 \\ A2 = A3 &\rightarrow C_{d_i} = 1 \\ A2 > A3 &\rightarrow C_{d_i} < 1 \end{aligned}$$

For the current geometry, $A2 < A3$ so C_{d_i} will be greater than unity. Indeed, $C_{d_i} = A3/A2 = 2.86$. This simple calculation demonstrates that for incompressible, ideal flow, the maximum discharge coefficient possible is 2.86; well in excess of the maximum of 1.0 for a nozzle venturi meter. Such a result explains the C_d values obtained from the low-speed measurements in the UTas film cooling rig, where for the co-flowing coolant passage C_d is greater than unity for low to medium IVRs. The fan-shaped portion of the hole acts as a diffuser, recovering pressure as the flow decelerates in the expanding area, and enabling a lower pressure at the throat for a given pressure ratio. The upstream total-to-throat static pressure ratio is therefore higher for the fan-shaped hole, leading to greater velocities and an enhanced mass flow [5]. This result does not mean that the discharge coefficients are artificially inflated, but that when compared to a cylindrical geometry of equivalent inlet section diameter, the fan-shaped hole demonstrates superior aerodynamic performance in most configurations. This may not be the case, however, under conditions that promote stall in the diffuser, as discussed in the following sections.

7.4.2 High Speed Flow

Rowbury [5] uses a non-dimensional mass flow parameter to conveniently describe the ideal mass flow rate:

$$\frac{\dot{m}_{ideal}\sqrt{RT_{0c}}}{AP_{0c}}$$

For incompressible flow, this parameter varies with the coolant total pressure and exit mainstream static pressure as

$$\frac{\dot{m}_{ideal}\sqrt{RT_{0c}}}{AP_{0c}} = \sqrt{2\left(1-\frac{P_m}{P_{0c}}\right)}$$

while for compressible, unchoked flow the dependence is defined by

$$\frac{\dot{m}_{ideal}\sqrt{RT_{0c}}}{AP_{0c}} = \left(\frac{P_m}{P_{0c}}\right)^{\frac{1}{\gamma}}\sqrt{\frac{2\gamma}{\gamma-1}\left[1-\left(\frac{P_m}{P_{0c}}\right)^{\frac{\gamma-1}{\gamma}}\right]}$$

and for compressible choked flow

$$\frac{\dot{m}_{ideal}\sqrt{RT_{0c}}}{AP_{0c}} = \sqrt{\gamma}\left(\frac{2}{\gamma+1}\right)^{\frac{\gamma+1}{2(\gamma-1)}}$$

Choked flow occurs when the velocity in the throat of the diffuser reaches a Mach number of 1. The upstream total to downstream static pressure ratio at which this occurs is called the critical pressure ratio. Further reductions in the downstream or exit static pressure will not result in further increases in mass flow, as changes in the exit conditions can only propagate upstream at the speed of sound. Hence there is a theoretical limiting value of discharge coefficient that is independent of pressure ratio once the critical pressure ratio is exceeded.

It is evident from results of Hay and Lampard [51] and Gritsch et al. [62] that choking of the flow, and the resultant plateauing of C_d, occurs at a pressure ratio considerably higher than the theoretical critical value for that geometry as predicted from quasi 1-D compressible flow theory. Jackson [79] concluded that 'thick' plate orifices have a curved velocity profile, implying that the velocity at all radii will not be sonic at the critical pressure ratio. Subsequently, it is expected that C_d will not be constant at pressure ratios higher than the critical pressure ratio, but will tend towards some constant value. This helps to explain why the high speed results from workers such as Gritsch et al. [62] do not show a plateau in C_d until pressure ratios above the critical pressure ratio are reached.

In an ideal convergent-divergent nozzle, which the diffused cooling hole approximates, further reductions in exit pressure once the critical pressure ratio has been reached create normal shock waves in the diffuser section. This shock moves toward the exit plane as the exit back pressure is reduced further. The occurrence of shock waves at any location within the hole is detrimental to film cooling in two ways. First, the shock results in a loss of energy thus requiring more energy to eject the coolant, and second, the shock wave causes a rise in temperature which effectively reduces the cooling potential of the film. If P3 is sufficiently low the flow in the diffuser will be isentropic, and the

static pressure will fall continuously from the throat to the exit. Then $P3 < P1$ for compressible flow, leading to lower values for C_{d_t} than in subsonic flow where $P3 > P1$ under ideal conditions.

7.5 C_d Results from Previous Studies

A series of papers by Gritsch et al. [22, 62] measured discharge coefficients for fan-shaped holes with a co-flowing and cross-flowing internal coolant passage. The authors investigated various combinations of coolant passage and mainstream Mach numbers up to Ma = 0.6, and compared round, type B laterally expanded (28°), and type A forward-laterally expanded geometries. In the co-flowing configuration, C_d values for the type B fan-shaped hole showed a sharp rise at low pressure ratios, reaching a peak value before tending towards a lower value at higher pressure ratios. Interestingly the peak value was at a C_d greater than unity, indicating that the fan-shaped expansion is able to recover significant pressure at low pressure ratios. This trend is matched by measurements from Rowbury [5] made on a scale model of a complete nozzle guide vane with rows of fan-shaped cooling holes. For the cross-flowing configuration, the measurements by Gritsch et al. [22], reproduced in Fig. 7.8, do not show this peak, but rather increase sharply at low pressure ratios before reaching a plateau at higher pressure ratios. This plateau value is lower than that for the co-flowing cases.

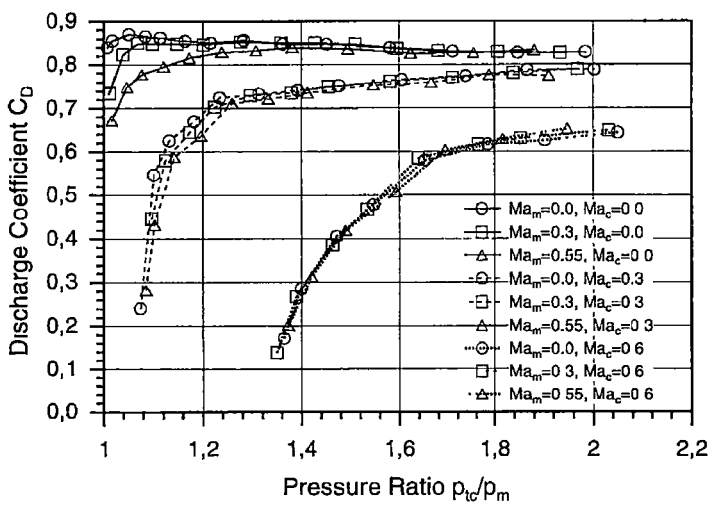

FIGURE 7.8: Fan-shaped hole C_d measurements, from Gritsch et al. [22]

Comparing these C_d trends with those of the current study reveals a distinct similarity. The plots of C_d variation with cooling hole Reynolds number shown in Fig. 7.1 show the characteristic peak at low $Re_{j,D}$ then a decrease toward a constant value at higher $Re_{j,D}$. The change in trend when the internal passage is rotated to 90° also matches the

high-speed results of Gritsch et al. [22], with C_d values now rising and rolling off toward a constant, but lower value at higher $Re_{j,D}$. Rowbury presents C_d data versus hole Reynolds number, as shown in Fig. 7.9, and again the similarity to the current results is evident. There is some difference in the location of the peak value, with Rowbury's data peaking at $Re_h = 5,000$ compared with Re_h $(Re_{j,D}) = 10,000$ in the current study. The inlet conditions for the Rowbury work are those which would typically occur in a cooled vane, where large cavities feed the cooling hole rows; this configuration presents inlet conditions more consistent with a co-flowing coolant passage rather than a cross-flowing configuration, and as such, it is not surprising that the C_d trend is in line with results from the co-flowing configuration of both the current work and that of Gritsch et al. [62].

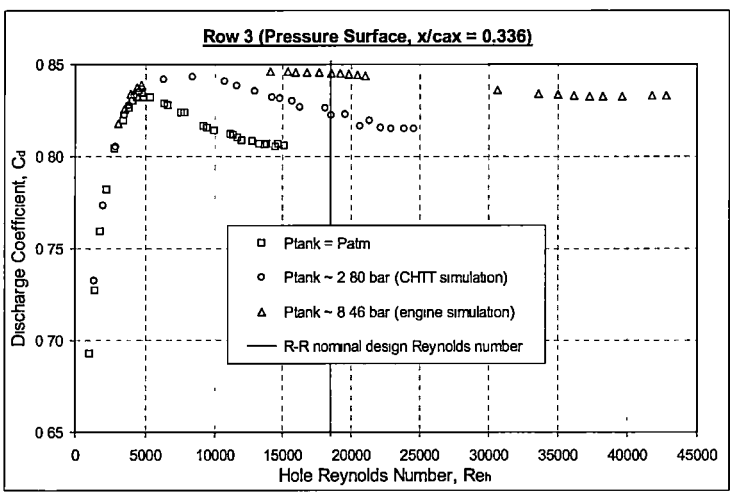

FIGURE 7.9: Fan-shaped hole C_d measurements, from Rowbury [5]

The similarity in trends between the high and low speed test results indicates that compressibility is not the dominant factor in determining discharge coefficients for fan-shaped holes. This is particularly true at design pressure ratios, which are generally at the lower end of those tested in research facilities. The onset of sonic flow in the throat due to the effects of the vena-contracta and boundary layer growth is therefore unlikely to be seen at engine operating conditions. Furthermore, high speed C_d results do not appear to demonstrate any identifiable effects from the occurrence of shock waves in the diffuser section as the pressure ratio is increased.

7.6 Summary

Discharge coefficients play an important role in the design process for film cooling schemes. Knowledge of the aerodynamic penalty associated with using a particular

cooling hole configuration under specific operating conditions (as indicated by a discharge coefficient value) is essential for generating optimum performance. This chapter has presented discharge coefficient data for the fan-shaped hole geometry over a range of IVRs and for co- and cross-flowing coolant passages at inlet. The losses associated with large turning angles and inlet separation result in the cross-flow configuration having lower values of C_d across all tested IVRs than the co-flowing configuration, decreasing continuously as the IVR is increased. In contrast, the co-flowing cases show a peak in C_d near an IVR of 0.8 where inlet losses are minimised. The results suggest that minimum inlet losses occur when the cosine of the IVR is equivalent to the inclination angle of the hole. Static pressure profiles along the hole centreline reveal the extent of inlet losses for all cases as well as the difference in diffuser performance for pressure recovery. Importantly, an analysis of the current low-speed results with those from high-speed facilities by other workers has revealed close similarity in C_d trends.

Chapter 8

Computational Flow Simulations

8.1 Overview

Computational fluid dynamics (CFD) is a numerical approach to solving and analysing the governing equations of fluid dynamics using the processing power of computers. Techniques for solving a fluid dynamics problem in this way have been paced by developments in computer technology, growing in complexity and efficacy of modelling with time. As computing power becomes more widely available and less expensive, the capabilities of CFD are being made available to a much wider community. In addition, freeware, private, and commercial software has continued to evolve with and capitalise on these advancements, and there are now many packages that provide a convenient graphical user interface for fluid dynamics problem set-up, solving, and analysis of results.

Despite these advances in computational power and numerical methodology, CFD solutions on even the most sophisticated machines can only provide approximations to the actual flow. Resolving all the scales of turbulent motion continues to pose a significant challenge, although capability is improving with development of large eddy simulations (LES) and more recently direct numerical simulations (DNS) where all of the relevant length scales can be resolved. The resource requirements for running LES and DNS remain high, however, and these approaches are largely not viable in industry. A Reynolds-Averaged Navier-Stokes (RANS) simulation is more commonly used as it greatly reduces the computational effort compared to direct numerical simulation. The equations solved represent the mean flow quantities only, while all scales of turbulence are modelled.

The ease with which CFD can now be implemented is a boon for small research institutes, and the insight into a flow problem gained from three-dimensional post-processing graphics is highly valuable. As a design tool, CFD is utilised across a broad range of

disciplines, enabling a wider variety of designs to be analysed in a shorter period of time. As such, parametric studies and 'optimisation' of designs can be achieved with relatively little cost. With all these improvements in the capabilities of CFD, however, there still exists a need to validate the solutions against real-world data, thus providing a degree of confidence in parametric variations. The demand for experimental results will, therefore, continue into the foreseeable future, with the direction of experiment increasingly driven by the validation requirements of CFD.

The computational results presented in this chapter represent the use of CFD technology in guiding the analysis of experimental results. Contour plots of velocity and turbulence distributions are extracted from the numerical solution and compared alongside those of the experimental measurements taken in the UTas film cooling facility. The degree of similarity enables a judgement on the solution accuracy in other areas of the domain. The cases presented here demonstrate a good match to experiment and subsequently provide a means of visualising the flow field in three-dimensions. These findings build on those from preceding chapters in analysing the effect that variations in inlet conditions have on the coolant flow path and downstream behaviour.

8.2 Computational Methodology

8.2.1 Boundary Conditions

Experimental velocity profiles were applied at the inlet boundaries for both the mainstream exit cross-flow and the coolant passage. Turbulence intensity was set at 1% for the exit cross-flow and 5% for the coolant passage. A mass flow rate boundary condition at the oulet of the coolant passage enabled control of the mass flow through the cooling hole, and a pressure outlet was set for the exit cross-flow.

8.2.2 Solution Method

For the current investigation, the CFD package used was ANSYS CFX version 11.0, for which a number of research licences were held within the School of Engineering. ANSYS CFX is a general purpose CFD software suite that combines an advanced solver with powerful pre- and post-processing capabilities [80]. ANSYS workbench integrates the conventional CFX applications with other applications to enable additional functionality such as geometry creation, meshing, multi-physics analysis, as well as design optimisation.

In this study, the Shear Stress Transport (SST) turbulence model was used for turbulent closure as it is regarded as one of the better two-equation turbulence models at predicting separation in an adverse pressure gradient [80]. The ω-based SST model combines the advantages of the k-ϵ and k-ω models, and includes turbulent shear stress transport into the formulation of the eddy-viscosity. The model is designed to give highly accurate predictions of the onset and the amount of flow separation under adverse pressure gradients and is recommended for high accuracy boundary layer simulations. The superior performance of this model has been demonstrated in a large number of validation studies [81], and to benefit from this model, a resolution of the boundary layer of more than 10 points is required.

The near wall flow was modelled using 'automatic' wall functions, which automatically switch between a low Reynolds number approach and scalable wall functions, depending on local conditions and the wall normal element spacing [80]. The working fluid properties were modelled using air as an ideal gas at 20° C. A second-order accurate 'high resolution' (blend factor of 1.0) advection scheme was used. The six equations solved were u, v and w-momentum, and conservation of mass, turbulent kinetic energy (k) and turbulent frequency (ω). A convergence criterion for maximum RMS residuals of 10^{-5} was set, which is one order of magnitude below the default level used by the solver [80].

8.2.3 Hardware

The solution times for a steady state simulation were generally around 3 hours using 10 processors of an SGI ALTIX 4700 system (64-bit Itanium 2, 1.6 GHz). Convergence was typically achieved within 75 - 100 iterations.

8.2.4 Mesh

The mesh or grid used in a computational simulation often has a significant impact on the quality and accuracy of the results. An understanding of the key areas of flow, the advective scheme and turbulence model to be used, is critical in creating a mesh that allows these components to operate effectively and produce realistic results.

For the current investigation, the computational domain was divided into 7 regions to allow independent mesh controls to be applied to each. The CFX Mesh package, incorporated in ANSYS Workbench, was used to generate the grid. All regions were meshed using a hybrid method consisting of tetrahedral elements in the far wall flow and inflated prismatic elements in the near wall flow to improve boundary layer modelling. The total number of elements was approximately 3.4×10^6. A mesh independence study revealed no significant change in the solution using a mesh with 1.5 times as many

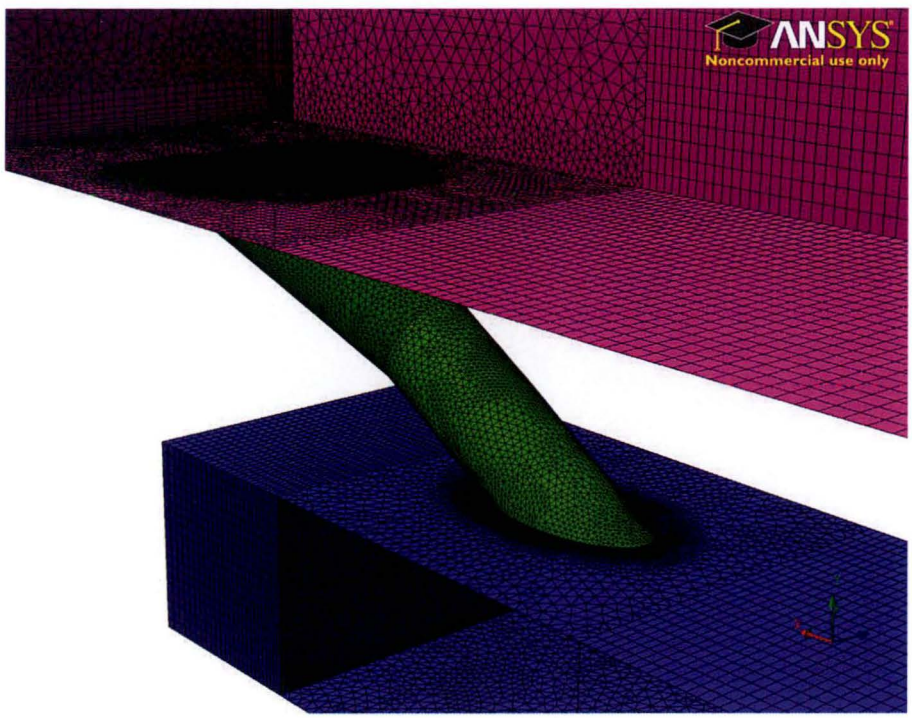

FIGURE 8.1: Computational Mesh

elements, but some variation with half as many elements. Hence, the current mesh was chosen to balance mesh independence with computational load. The mesh can be seen in Fig. 8.1. The y^+ value of the mesh element adjacent to the wall varied between 10 - 50 in all cases. Post-processing showed that the boundary layer was resolved by around 10 elements, as recommended in the software documentation for CFX 11.0 [80].

8.3 Experimental Validation of Computed Flow Field

As mentioned in Sec. 8.1, computational solutions of the governing fluid dynamics equations for the film cooling facility need to be validated against experimentally measured data to establish confidence in the simulated result. The aim in this section is to compare contour plots of velocity and turbulence in two measurement planes for the selected flow cases presented in this chapter.

8.3.1 Co-flow Configuration

A comparison of normalised velocity contours in Fig. 8.2 and 8.3 shows good qualitative agreement between the experimental measurements and computed flow field. The shape of the flow field is remarkably similar for the same IVR, although not showing exactly the same distribution in terms of absolute values of $U/U_{j_{mean}}$. The agreement is not as

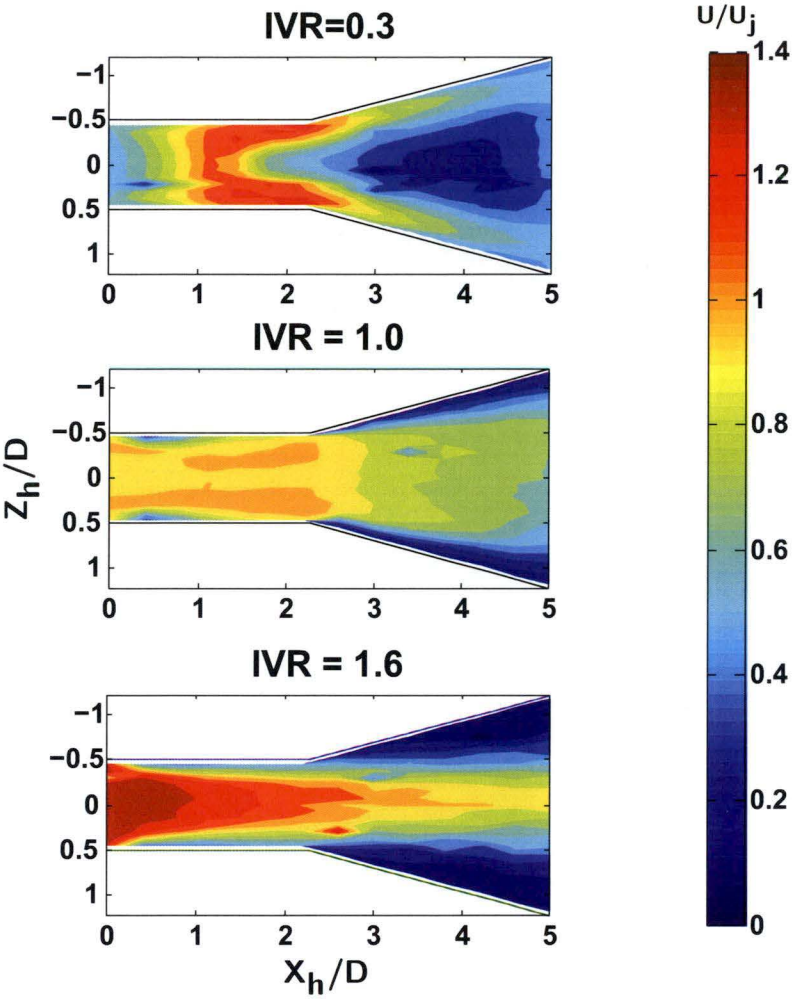

FIGURE 8.2: Contours of normalised mean velocity on plane $Y_h = 0$, for M = 1.3, $\beta = 0°$ (experiment)

good where CFD predicts a region of low velocity in the centre of the diffuser, similar in distribution to the IVR = 0.3 case. This suggests that the flow pattern for an IVR of 1.0 occurs only over a narrow band of IVRs, and that inaccuracies in the modelling have generated a flow field more like that for low IVRs. The velocity gradient in a direction normal to the plane is high. This means that slight differences in flow patterns can cause large differences in the distribution captured by the $Y_h = 0$ cut plane, and such sensitivity is a likely source of some of the differences between the experimental and computational results shown here. Nevertheless, the variation of flow pattern with changes in IVR is well matched by the computational results.

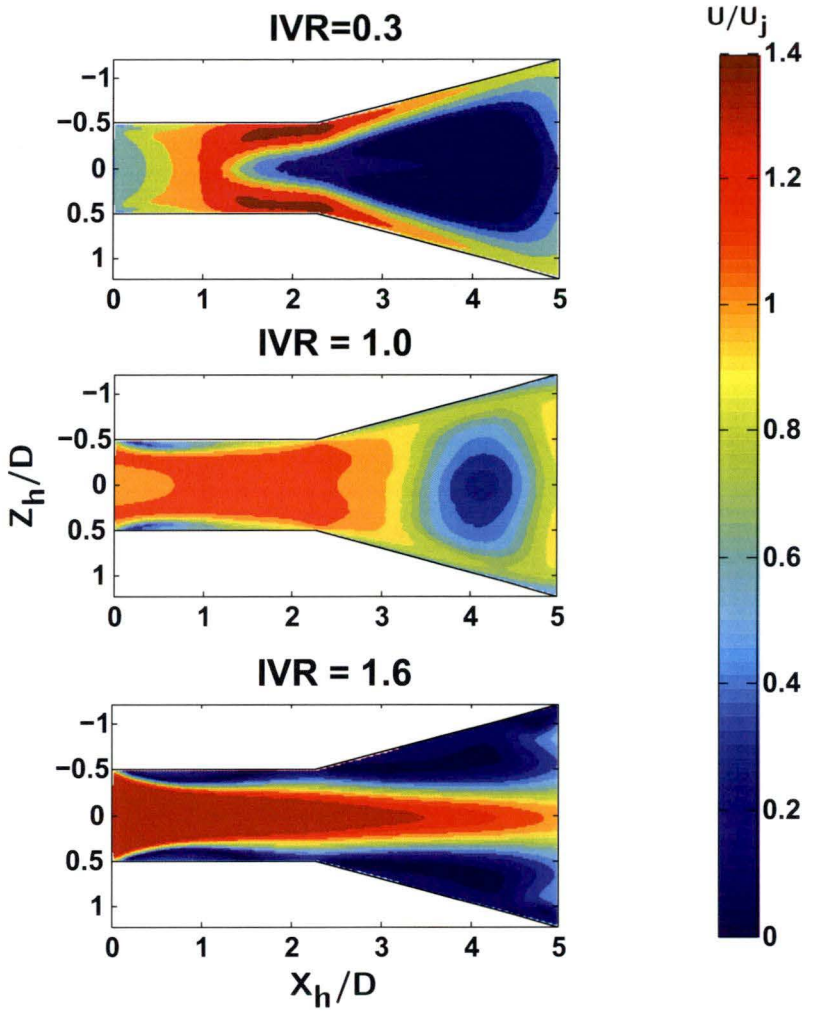

FIGURE 8.3: Contours of normalised mean velocity on plane $Y_h = 0$, for M = 1.3, $\beta = 0°$ (CFD)

8.3.2 Cross-flow Configuration

For the cross-flow coolant passage configuration ($\beta = 90°$) the similarities between experiment and CFD are not as strong as for the co-flowing passage. Solution convergence was satisfactory, but demonstrated oscillatory behaviour. The point in solution time at which the results file was generated may not, therefore, be truly representative of the average flow field recorded in the experimental measurements. Nevertheless, plots presented in Fig. 8.4 and 8.5 show that the simulation is still capturing the main flow patterns for the $\beta = 90°$ configuration, and importantly, the variation with IVR.

The similarities identified between the mid-height contours of normalised velocity indicate that the computational simulation is representing the actual flow field well; in particular the flow field changes as the blowing ratio is increased from 0.3 to 1.6 are

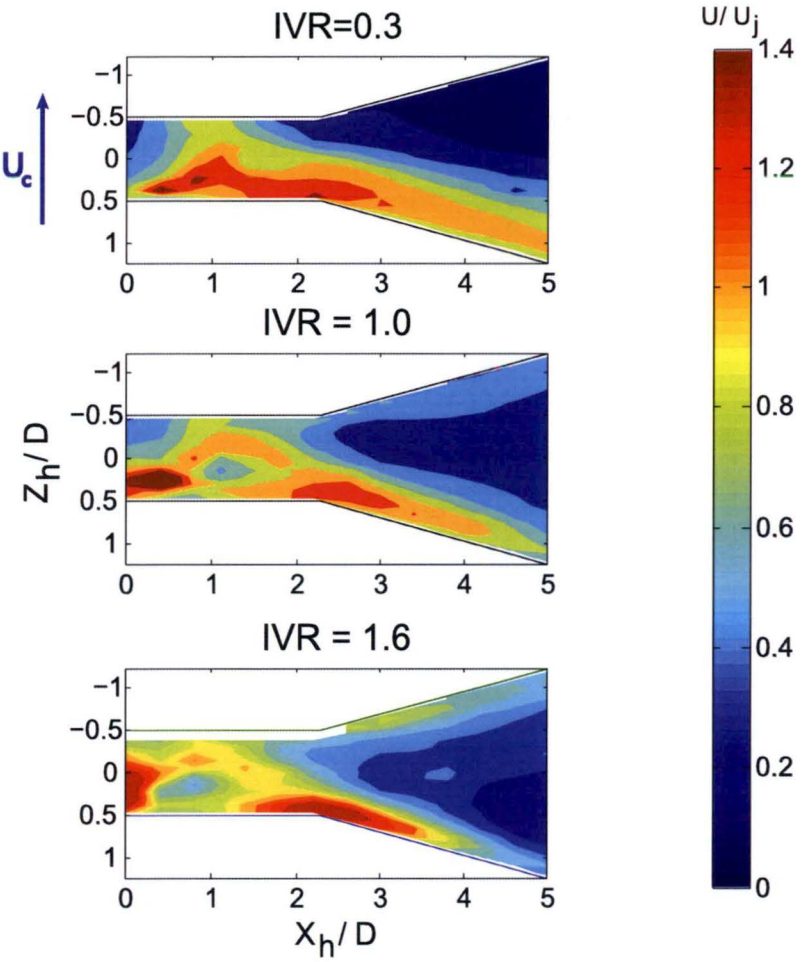

FIGURE 8.4: Contours of normalised mean velocity on plane $Y_h = 0$, for M = 1.3, $\beta = 90°$ (experiment)

seen to a very similar extent in the experimental solution. The similarities are such that the computational solution for the remainder of the domain can be expected to provide a realistic picture of the flow in the wind tunnel, and assist in understanding the experimental measurements.

8.4 Simulated Flow Field for M = 1.3, $\beta = 0°$

The flexibility of CFD allows several views of the flow field to be constructed to assist in visualisation. The following paragraphs describe the distribution of coolant and the development of the coolant flow from four unique views, which together provide a thorough display of the computed domain.

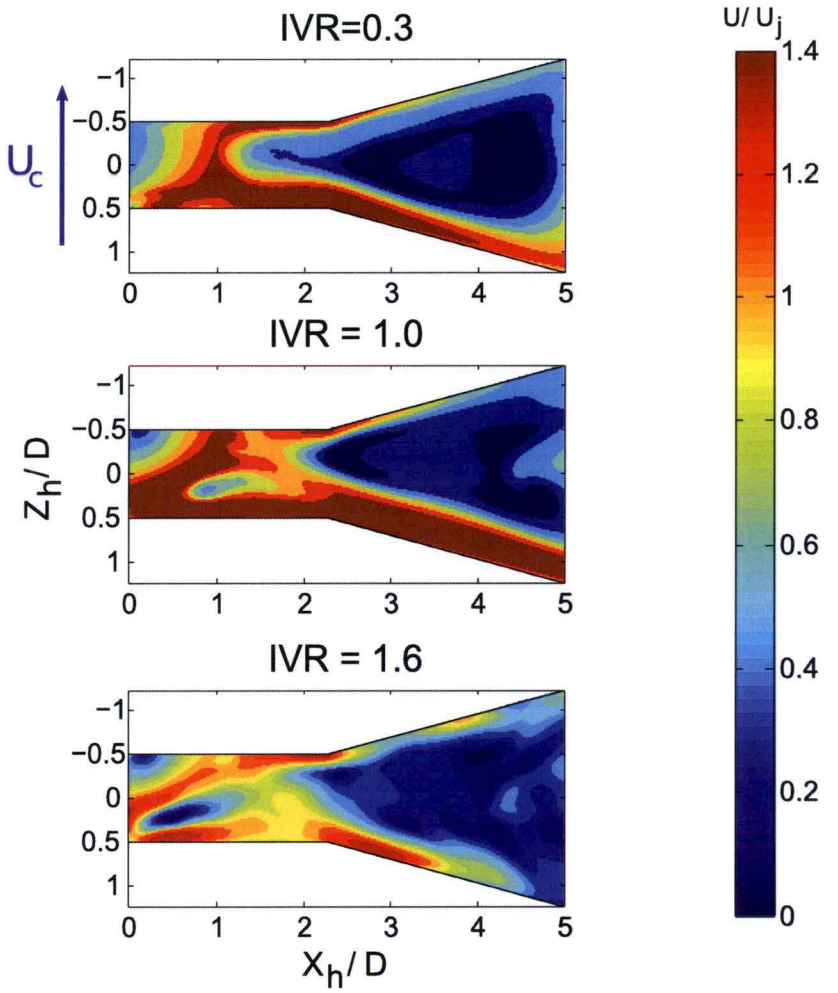

FIGURE 8.5: Contours of normalised mean velocity on plane $Y_h = 0$, for M = 1.3, $\beta = 90°$ (CFD)

8.4.1 In-hole Velocity Contours and Streamlines

Figure 8.6 shows a view from behind and slightly below the cooling hole. Contours of normalised velocity $U/U_{j_{mean}}$ are plotted on Y_h -Z_h planes at five locations along the hole axis. In all cases 30 evenly spaced streamlines were released from a plane at $X_h/D = 3.5$ and calculated upstream and downstream. and streamlines through the hole are also shown, coloured by $U/U_{j_{mean}}$. The bulk flow direction is into the page, away from the viewer. The same quantities are shown in Fig. 8.7, but looking from the side and upstream of the hole such that the bulk flow direction is from left to right; contours of $U/U_{j_{mean}}$ are plotted on planes normal to the cooling hole axis. The three IVR test cases of 0.3, 1.0, and 1.6 are shown for comparison.

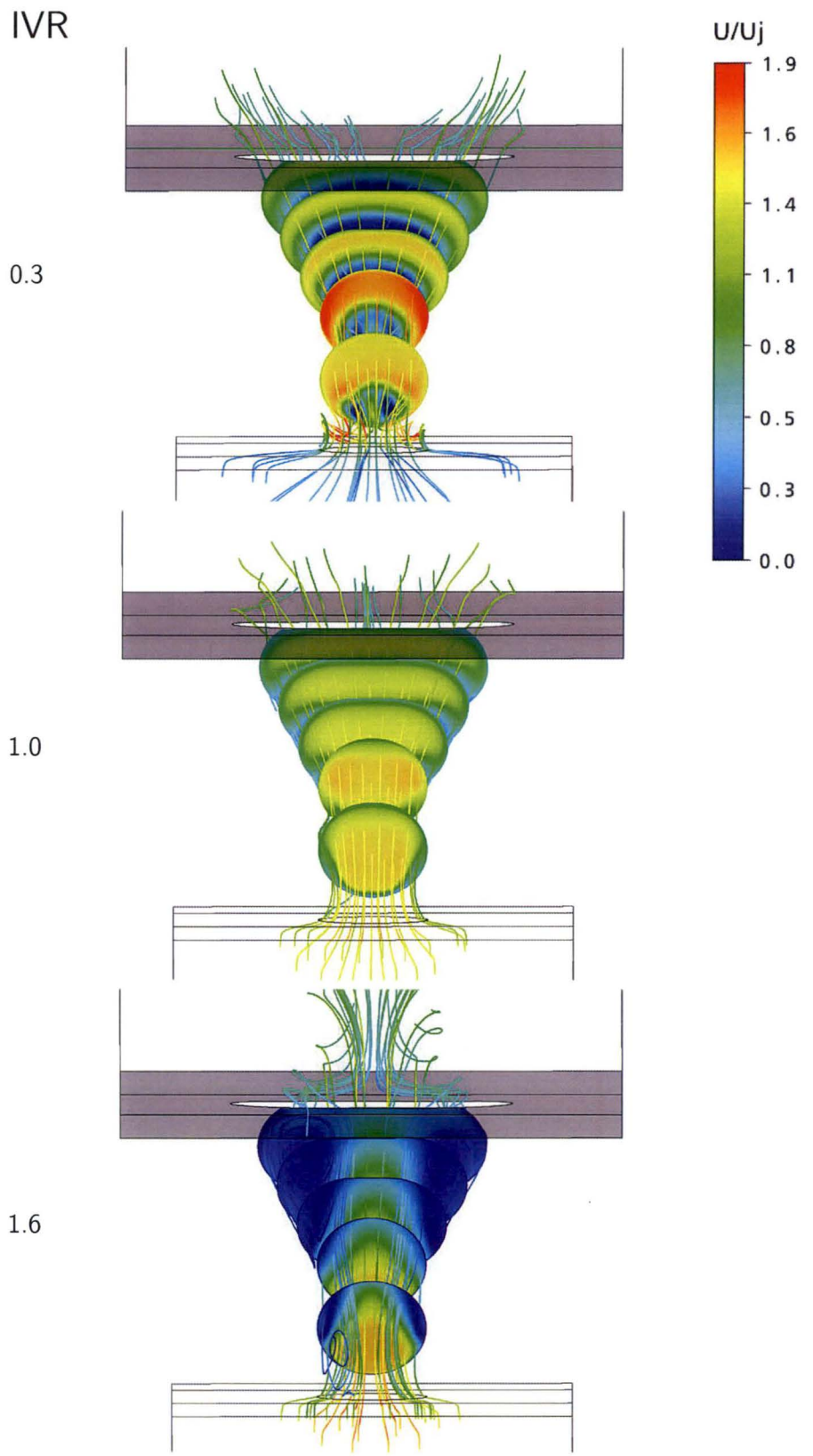

FIGURE 8.6: Comparison of computed flow fields for IVR = 0.3, 1.0, and 1.6, $\beta = 0°$

8.4.1.1 Velocity Contours

For an IVR of 0.3 (Fig. 8.6) the contour plot closest to the inlet shows faster moving coolant occupying the upper portion of the throat. In the lower portion, lower velocity fluid is present with two distinct and nearly symmetrical spots of very low velocity either side of the cooling hole centre-plane. Further downstream, the low velocity region expands, reducing the flow area for faster moving coolant and accelerating it in the process. As the flow moves into and through the diffuser section of the hole, the adverse pressure gradient retards the flow and encourages the low velocity region to expand further. This results in a thin band of higher velocity coolant around the upper wall of the hole that is present right to the hole exit.

Looking again at Fig. 8.6, a higher IVR of 1.0 presents a flow distribution at the contour plane closest to the inlet that is quite different to that at an IVR of 0.3. The velocity is nearly uniform across the entire diameter for the higher IVR, reducing to lower values near the wall; in this case, disturbing effects at the inlet are minimal. Near the start of the diffuser a region of very low velocity begins to form on the lower wall, more clearly shown in Fig. 8.7. This region grows in the diffuser to occupy half the hole height by the final contour plane. This aspect of the flow field does not appear to be representative of the experimental measurements presented in Ch. 5 for an IVR of 1.0. In the experimental case, the Y_h velocity profiles show a symmetric distribution across the height of the hole and the bulk flow moves through the centre of the hole. As discussed in Sec. 8.3, and supported by IVR sensitivity investigations in Ch. 5, the band of IVRs for which the 'transitional' flow pattern between low and high IVRs occurs is quite narrow. Thus, inaccuracies in the modelling approach may have in effect generated a flow pattern more characteristic of an IVR slightly less than 1.0.

Increasing the IVR to 1.6, velocity contours again reveal a very different flow pattern. The first contour in the cooling hole throat shows two low velocity regions at the upper sides of the hole, split either side of a triangular shaped region of higher velocity coolant. Further downstream the distribution appears similar, with higher velocity coolant remaining in the centre of the hole right throughout the diffuser. The two low velocity regions increase in size as the flow moves out of the throat and into the diffuser.

8.4.1.2 Streamlines

Three-dimensional streamlines superimposed in Fig. 8.6 provide an additional level of insight into the cooling hole flow and its variation with IVR. Looking first at the IVR = 0.3 case, the streamlines at hole entry clearly show two vortices roll up at either side of the inlet lip, and quickly develop into two adjacent cores of opposing rotation. These are

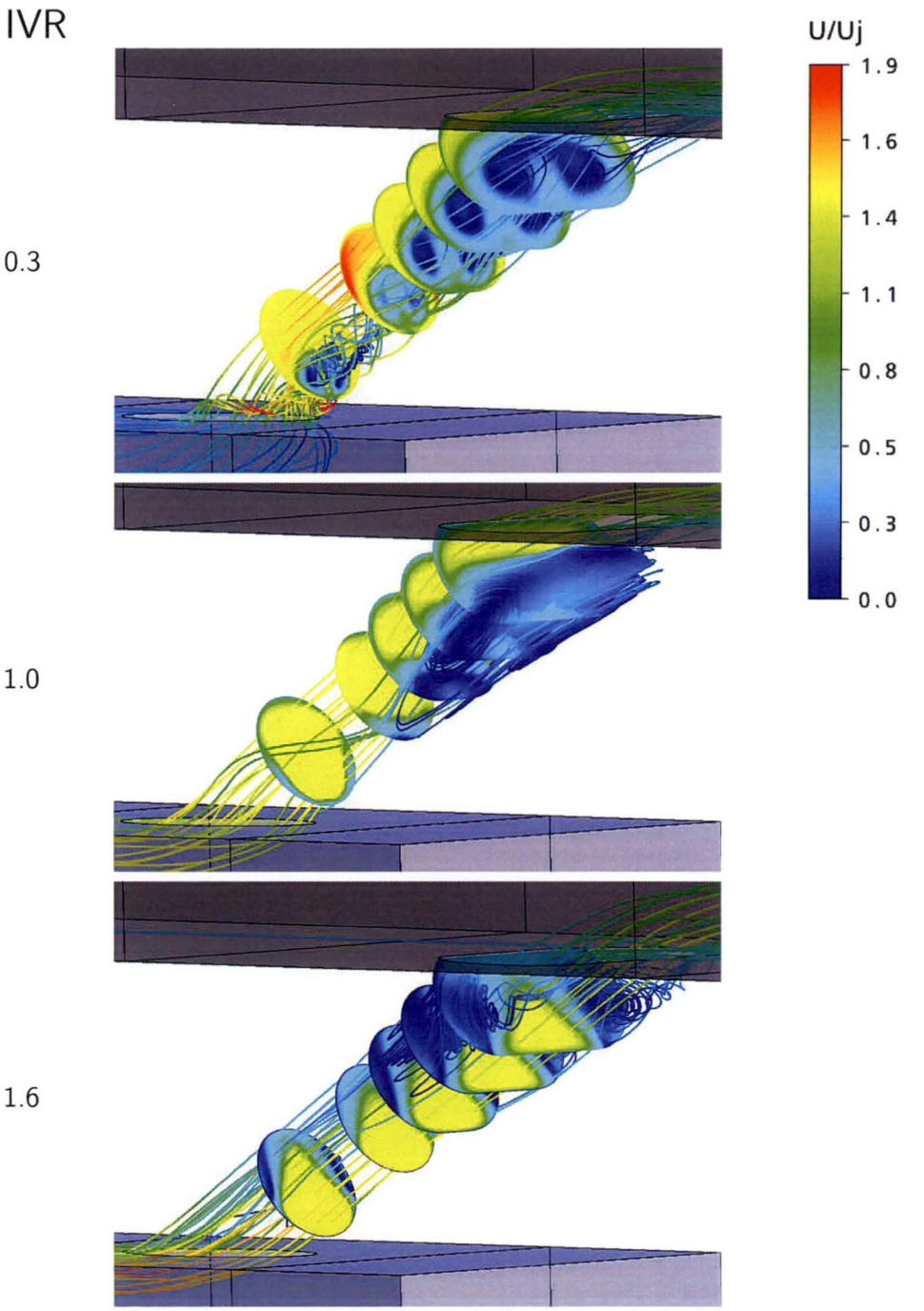

FIGURE 8.7: Comparison of computed flow fields for IVR = 0.3, 1.0, and 1.6, $\beta = 0°$

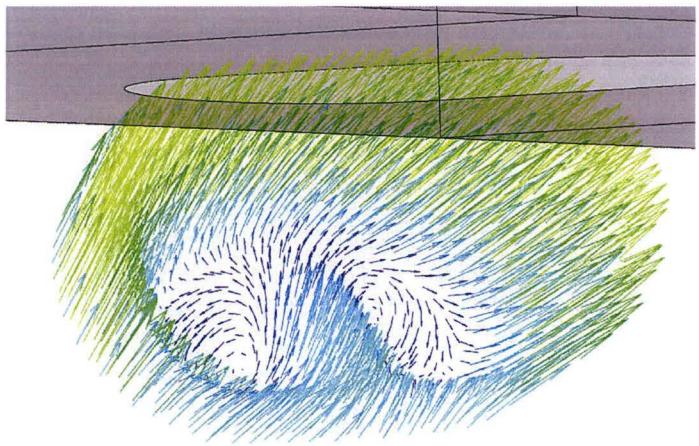

FIGURE 8.8: Velocity vectors showing flow pattern near diffuser exit for IVR = 0.3, $\beta = 0°$

more clearly seen in Fig. 8.7 between the first two contours. The vorticity of the right side vortex is positive, while that of the left is negative about the cooling hole axis. This flow pattern is typical of the counter-rotating vortex pair commonly seen in the exit flow distributions for inclined round jets, and reported by many previous workers. For the fan-shaped hole, it appears that these vortices persist and spread through the diffuser, where their strength diminishes somewhat. The streamlines at exit show the coolant separating away from the centreline to form two 'arms' on the surface downstream. This is in contrast to the flow behaviour upon exit for the typical counter-rotating vortex pair, where the above-mentioned vorticity tends to draw exit cross-flow hot-gas down and under the ejecting coolant jet toward the surface.

The vector plot shown in Fig. 8.8 helps to explain this behaviour. The faster flowing coolant is at the upper wall of the hole, and consequently is only influenced by the upper half of the vortices. As the faster fluid progresses toward the hole exit, it picks up a component of velocity toward the outer wall of the hole, in the direction of the top side of the vortex. This velocity component is sufficient to direct the faster flowing fluid laterally outward once it has left the hole.

For an IVR of 1.0, streamlines at the hole inlet show a much weaker roll up at the lip, and no notable signs of continued vortex behaviour through the hole. At exit, the streamlines show much less variation in direction from a purely axial flow, however, fluid near the sidewalls of the diffuser exhibits a stronger lateral velocity component and ejects at an angle not dissimilar to that of the diffuser wall before being straightened by the exit cross-flow.

Streamlines for an IVR of 1.6 show no signs of inlet lip roll-up, and instead show fluid being drawn straight into the hole from upstream. The fast flowing fluid in the coolant

passage carries significant momentum and does not turn sharply into the cooling hole throat. This results in separation of the flow in the throat just downstream of the inlet, as evidenced by recirculation of a streamline at the upper left of the inlet. As shown in Fig. 8.7, there are large recirculating regions of flow in each side of the diffuser which appear to be rotating from the central high velocity region out toward the side walls, likely due to drag from the shear layer of the coolant jet. At the exit, this rotation influences the path of the higher velocity coolant, with a strong secondary flow imposed that acts to sweep fluid from the sides of the exit firstly outward, and then back under the higher velocity core towards the centreline of the hole downstream. Although not obvious in the figure, the high IVR case shows some signs of mainstream flow ingestion at the sides of the diffuser at exit. This is undesirable from a cooling perspective, potentially imposing severe temperature gradients on the more fragile exit lip.

8.4.2 Inlet and Exit Flow Pattern

Referring to Fig. 8.6 and comparing the exit streamlines for all three IVRs, there is a trend as IVR is increased for the streamlines to tend towards the centreline. At IVR = 0.3 the streamlines are split to each side of the cooling hole centreline; at IVR = 1.0 they are more evenly distributed; at IVR = 1.6 the streamlines are concentrated towards the centreline. Similarly, the height of the ejected coolant 'jet' increases with IVR. Figure 8.9 shows the coolant streamlines from above, looking towards $-Y$. The effect of IVR is again obvious, showing further the extent to which the spread of the coolant streamlines varies at exit. Particularly for the IVR = 1.6 case, the strong secondary flow rotation once the coolant exits the hole is clearly visible in this view, and points to the potential for mainstream flow ingestion at the sides of the hole.

8.4.3 Symmetry Plane Vectors

Figure 8.10 shows velocity vectors in the ($Z = 0$) plane of symmetry through the hole for the three test case IVRs. These images further show the prominent jetting of coolant fluid originating from the downstream lip of the hole inlet for low IVR. This jetting effect has been shown by previous numerical simulations such as those of Kohli and Thole [14] and Leedom and Acharya [15]. These workers found the effect to be most prominent for plenum inlet or low coolant passage velocity cases, which correspond to low IVR values. Figure 8.10 demonstrates that the strength of the jetting region decreases as the IVR approaches 1.0, but then slightly separates from the upstream lip as the IVR is further increased. The velocity vectors for the IVR = 1.0 case shows signs of recirculating flow in the low velocity region below the coolant jet. However, this recirculation is not

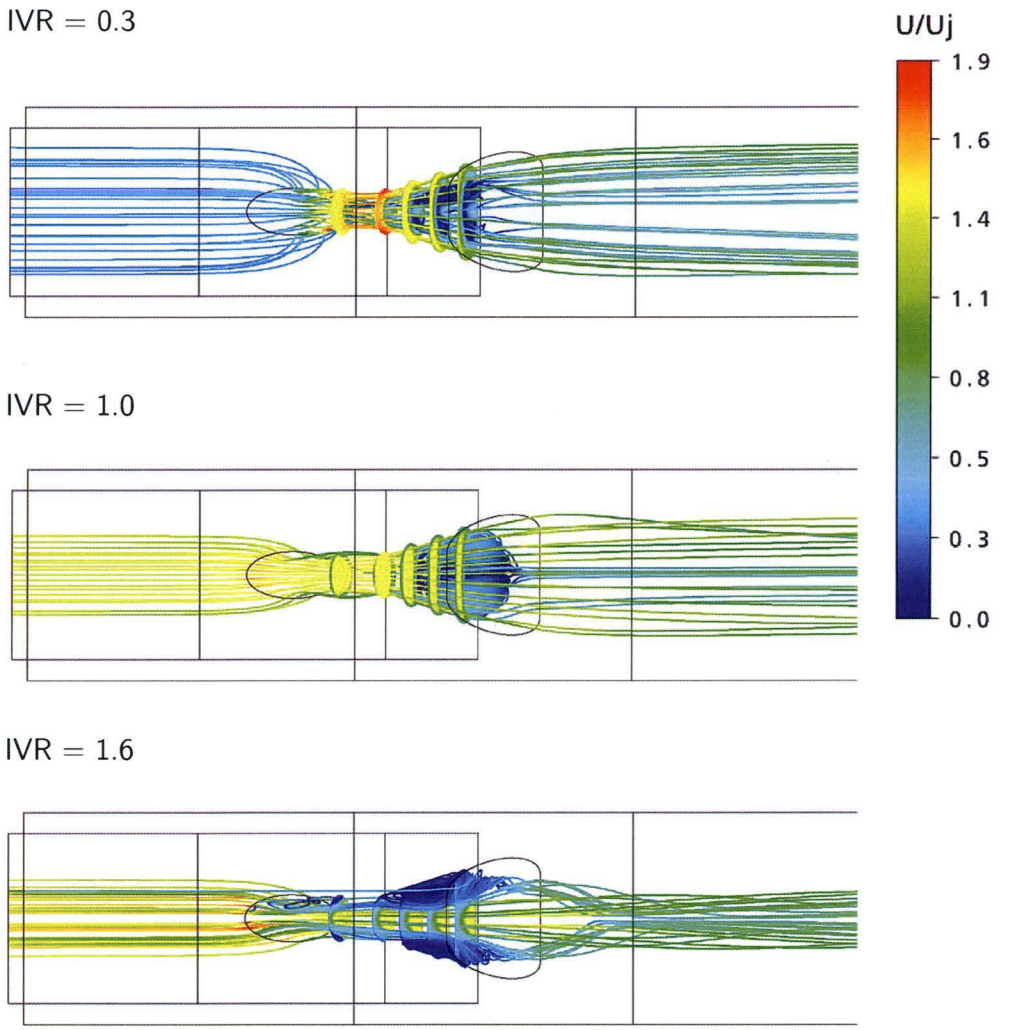

FIGURE 8.9: Comparison of computed flow field streamlines for IVR = 0.3, 1.0, and 1.6, $\beta = 0°$

evident in the experimental results, indicating inaccuracies in the numerical modelling as indicated in Sec. 8.3.1.

8.5 Simulated Flow Field for M = 1.3, $\beta = 90°$

8.5.1 In-hole Velocity Contours and Streamlines

As with the $\beta = 0°$ case, Fig. 8.11 shows a view from behind the cooling hole and slightly down, but here the coolant passage flow is from right to left, rather than into the page. Contours of normalised velocity $U/U_{j_{mean}}$ are plotted on Y_h -Z_h planes at five locations along the hole axis, and streamlines through the hole are also shown, coloured by $U/U_{j_{mean}}$.

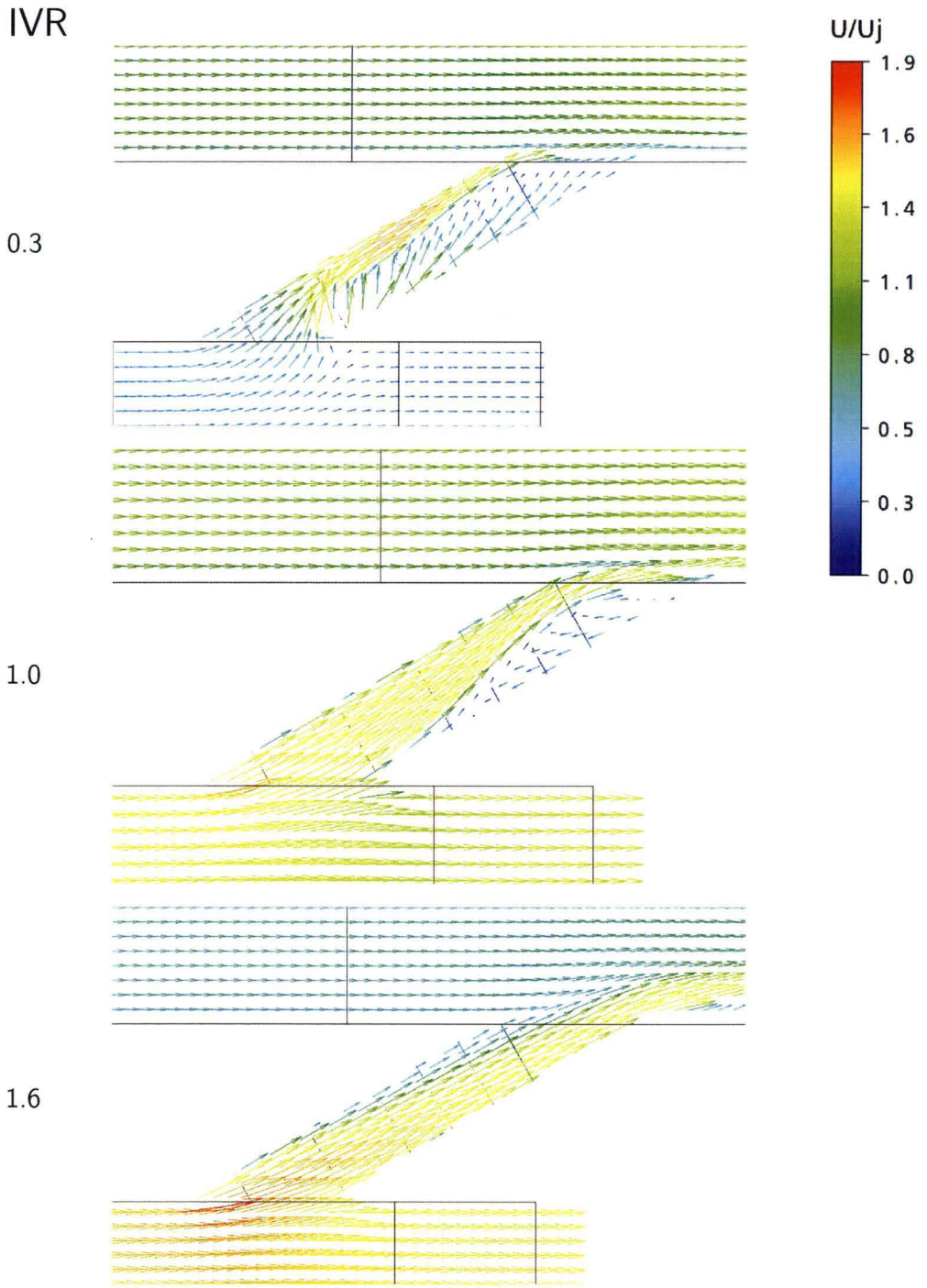

FIGURE 8.10: Comparison of symmetry plane ($Y_h = 0$) mean velocity vectors for M = 1.3, $\beta = 0°$

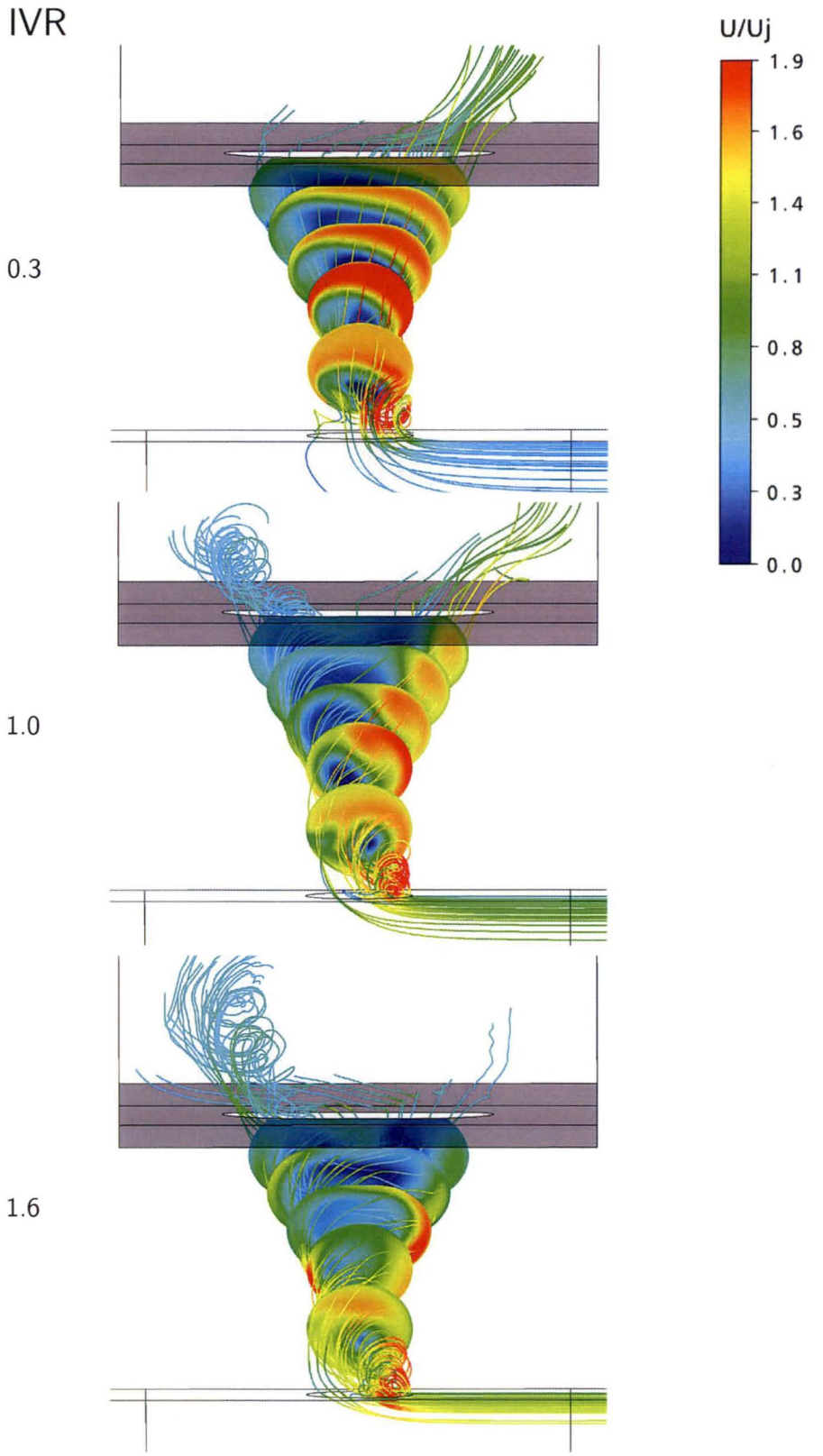

FIGURE 8.11: Comparison (view 1) of computed flow field for IVR = 0.3, 1.0, and 1.6, $\beta = 90°$

8.5.1.1 Velocity Contours

At an IVR of 0.3, contours of U/U_{Jmean} near the inlet show a region of low velocity fluid surrounded by an area of evenly distributed higher velocity fluid. By the second contour plane, the high velocity region has contracted and intensified in strength to be 1.5 times the mean throat velocity in this upper region. The lower velocity region has expanded, and shows a nucleus of very low velocity increasing radially. This flow progression continues right to the exit, by which point the area expansion of the diffuser has allowed the lower velocity region to expand. As well, the high velocity fluid is limited to a small region in the upper right corner and across the top of the hole.

At an IVR of 1.0, the distribution of U/U_{Jmean} at the inlet again shows a spot of very low velocity, surrounded across the top and right sides by faster moving fluid. The growth of this lower velocity region forces the area of higher velocity to contract and accelerate, as shown by the second contour plane. Just inside the diffuser, the contours show a much larger region of low velocity fluid with the high velocity region very much confined to the right corner of the plane. This distribution persists to the exit, with the low velocity region expanding to fill the bulk of the diffuser.

At still a higher IVR, the first contour plot shows a reduced area of high velocity fluid toward the top of the hole, and also a lower velocity magnitude. The spot of very low velocity fluid still exists just right of the hole centre, but the velocity magnitude surrounding it is higher than for the other two IVR cases. The next contour plane downstream shows that the high velocity region has rotated clockwise to now lie against the side wall of the hole, and the low velocity spot has shifted to the left side of the hole. Local acceleration of fluid near to the left wall gives very high velocity in this small region. Further downstream again, the low velocity region expands in the adverse pressure gradient imposed by the diffuser, forcing the high velocity fluid near the right wall to accelerate, before slowing by the next contour plane as the effects of the increasing pressure retard the flow.

8.5.1.2 Streamlines

Streamlines through the hole reveal much about the strong secondary flows that originate at the hole inlet. As the coolant enters the hole it must turn through a compounded angle of 90° and 30° from the coolant passage. This turning results in the generation of a strong vortex in the upstream (relative to the coolant passage flow) half of the inlet area. The strength of the vortex, which has a positive vorticity, is highlighted by streamline colouration with values of $U/U_{Jmean} = 0.5$, showing that the vortex roll-up significantly accelerates entrained fluid. In the downstream half of the inlet, coolant from the passage

turns and accelerates, but this turning is less severe as the fluid stays near the upper wall of the hole and flows smoothly into the throat. Shortly downstream within the hole, the acceleration of this fluid is balanced by a deceleration in the lower part of the hole. This is manifested in a dissipation of the inlet lip vortex velocity, although strong secondary flows are still present throughout the hole. This vortex spreads and transforms into a large body of recirculating fluid in the diffuser, as can be seen in Fig. 8.12. There is evidence of a similar, yet much weaker, vortex forming on the downstream side of the inlet lip, which likely contributes to the highly turbulent recirculating region in the diffuser.

At a higher IVR of 1.0, the fluid entering the hole does not need to accelerate as the velocities of the passage and throat are matched. However, the turning into the hole again generates a strong vortex on the upstream lip. Flow in the downstream half of the inlet turns and is picked up by the rotating vortex to be pushed to the upper right corner of the contour planes where it remains right through to exit, eventually issuing into the exit cross-flow. The inlet lip vortex remains intact, and the strong secondary flow persists right through the diffuser, reducing in velocity, but growing in physical size. At exit, Fig. 8.11 clearly shows the vortex tube leaving the hole on the left side.

At IVR = 1.6, the flow pattern is similar, but the inlet vortex is again enlarged when compared to the IVR = 1.0 case, due to the volume of fluid required to turn into the hole being reduced. Streamlines at the hole inlet in Fig. 8.11 show the vortex roll-up at the inlet lip, with fluid strongly accelerated as it is turned. There are also several streamlines toward the left of the hole indicating that the flow path of coolant does not form part of the vortex, sweeping into the hole and following a larger radius rotation, before turning over and around to the right of the hole in the same sense of direction as the lip vortex. This fluid forms the bulk of the high velocity regions identified in the contour plots. The lip vortex expands and dominates the flow through the diffuser, dragging more of the high velocity fluid into the rotation. This is shown by the strong bias of the exit flow towards the left of the hole and the vortex tube.

8.5.2 Inlet and Exit Flow Pattern

The view of coolant flow shown in Fig. 8.13 reveals more about the inlet and exit flow patterns for the three IVR test cases at 90° coolant passage orientation. At the inlet, the growth with IVR of the upstream lip vortex is evident, as is the transition of this vortex as it enters the diffuser for all cases. For the lowest IVR, axially aligned vorticity is reduced as the vortex reaches the higher pressure in the diffuser, slowing the mean velocity and generating a recirculating region with vorticity largely aligned at right angles to the main flow direction. This fluid appears to circulate until it is picked up

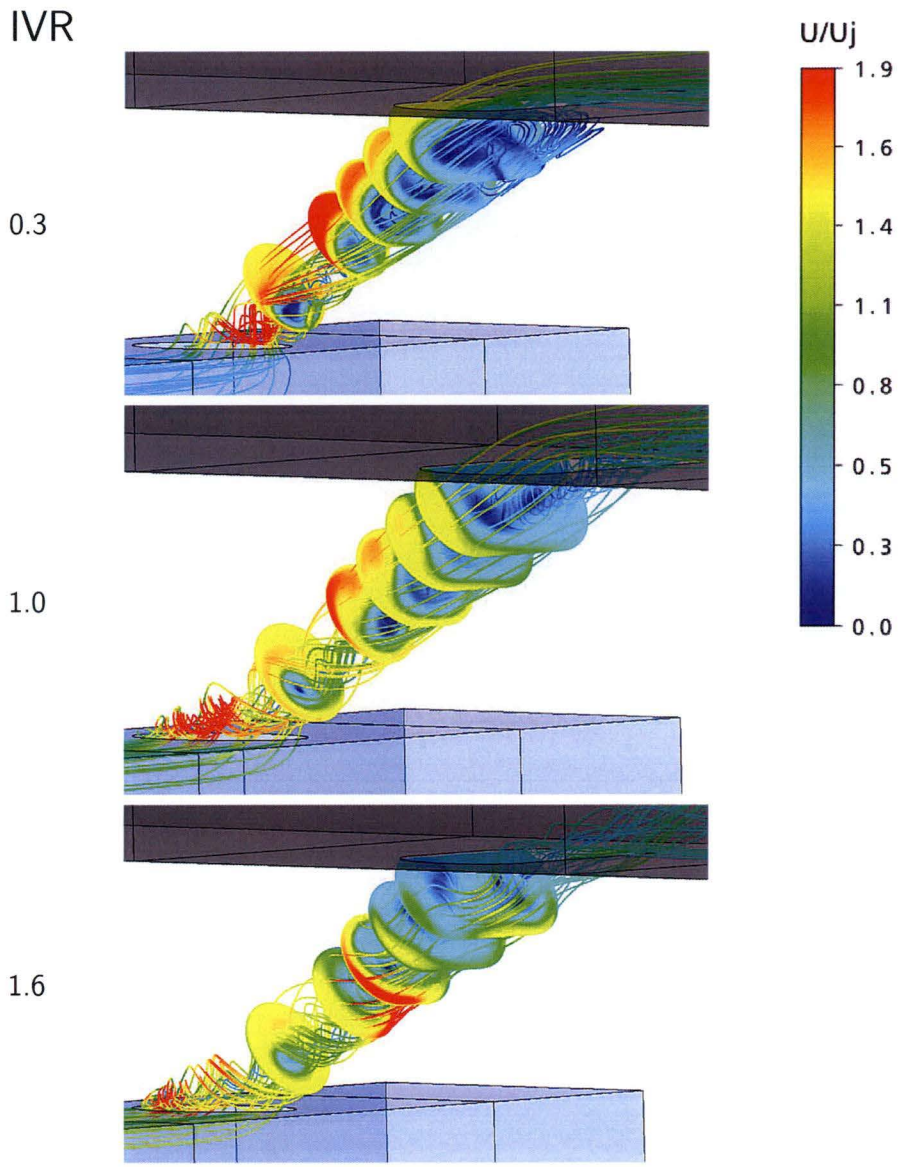

FIGURE 8.12: Comparison (view 2) of computed flow field for IVR = 0.3, 1.0, and 1.6, $\beta = 90°$

in the faster moving jet at the right of the hole and carried to exit, giving the largely right-side biased exit flow distribution.

An IVR of 1.0 does not require the coolant passage fluid to turn as sharply into the hole, as the stagnation point has moved upstream compared with an IVR of 0.3. The less severe turning into the hole achieves two main things: the vortex is not squeezed by the bulk of the turning fluid (enabling it to fill more of the inlet area); and the vortex tube is able to continue through the diffuser, maintaining enough momentum to exit the cooling hole. In the diffuser, some vortex fluid is picked up by the faster moving fluid and is carried through to exit at the right side of the hole, similar to that for IVR = 0.3.

At exit, there is a vortex tube of strong secondary flow issuing from the left side of the hole, and a jet of fast moving fluid at the right side.

This flow pattern is seen again in the IVR = 1.6 case, but here the vortex tube is more dominant, producing a larger region of slower moving fluid at the left of the hole, and a smaller jet of faster flowing fluid at the right of the hole. The reduction in the faster flowing fluid is such that at exit there is no obvious flow cohesion into a jet type flow. In fact, only the fluid closest to the right wall of the diffuser remains to issue from the hole on this side. The streamlines in Fig. 8.13 shows that there is a significant velocity component of the exiting coolant towards the vortex tube. Interestingly, the streamlines for the high IVR case show more coolant fluid staying near the downstream surface than for either of the lower IVRs tested.

8.6 Influence of Inlet Velocity Ratio

8.6.1 Co-flow Configuration

The effects of IVR on the co-flowing configuration discussed in previous chapters are confirmed here with the simulated results. Increasing the IVR moves the stagnation point of the coolant further upstream, which determines where the bulk flow of coolant is positioned within the hole. Additionally, vortices on each side of the hole are generated at the inlet lip for the low IVR case which grow with downstream distance and force the higher velocity fluid toward the top and sides of the hole, producing a laterally dispersed distribution at exit. These vortices are no longer detectable at an IVR of 1.0, where the inlet flow is smooth and the bulk flow through the throat is positioned at the centre of the hole. Despite the diffuser flow not accurately representing that from the experimental measurements, the flow at exit from simulation compares well with exit distributions presented in Ch. 6, showing a uniform region of flow covering the full width of the exit. At the highest IVR tested, 1.6, the relatively faster moving and higher momentum coolant in the passage cannot turn sharply into the hole, and is carried to the downstream lip of the inlet where it flows along the lower wall of the hole. A consequence of this more shallow turning is the creation of two vortices in the separated flow region at the upstream side of the inlet. These vortices grow in size as the flow progresses into the diffuser to result in a pair of vortices, one either side of a central high velocity core. The resulting exit distribution is biased toward the centre of the hole, with a prominent jet of coolant issuing from the hole.

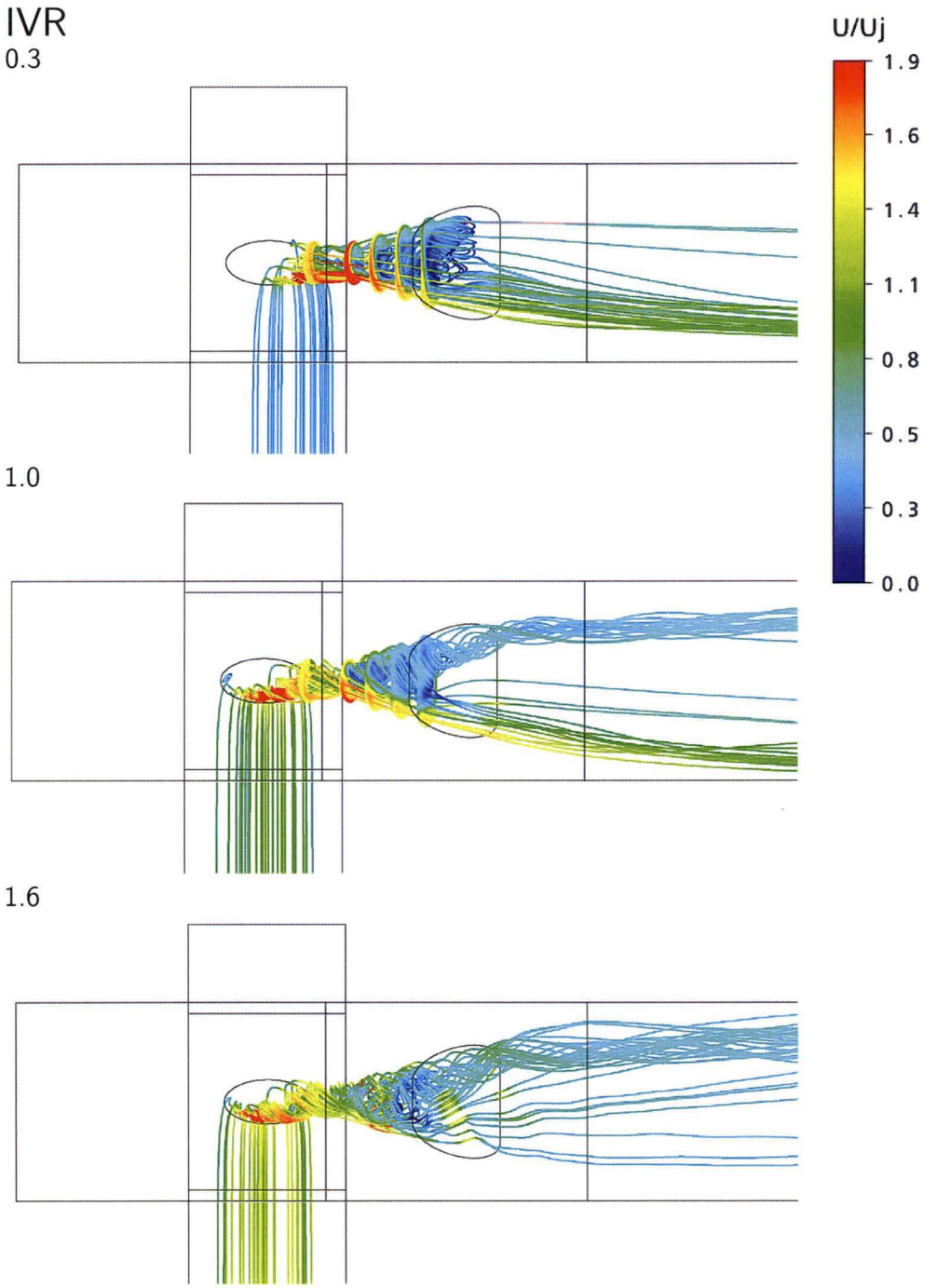

FIGURE 8.13: Comparison of computed flow field streamlines for IVR = 0.3, 1.0, and 1.6, $\beta = 90°$

8.6.2 Cross-flow Configuration

For the cross-flow configuration, the predominant difference in flow pattern as the IVR is varied is a change in the size and strength of the inlet lip vortex, generated as a consequence of the large turning angle into the hole from the coolant passage. The relative velocities of the passage and throat govern how much the coolant is accelerated as it enters the hole, and subsequently how the flow develops through the hole. The acceleration of fluid into the hole, required by the low IVR, draws more coolant into the hole. As this acceleration reduces at higher IVRs, the area of high velocity fluid reduces, and the upstream lip vortex is able to increase in strength. Streamlines shown in Fig. 8.13 further demonstrate the effects of IVR on the inlet lip vortex. At low IVRs, the vortex is contained to the upstream lip near the lower wall of the hole. At an IVR of 1.0, the vortex is generated by roll-up along almost the full length of the upstream lip, and at higher IVRs the vortex is larger again. The corresponding variation in exit flow from the hole is equally striking, with the vortex tube not evident at low IVRs, but becoming more dominant as the IVR is increased, to be the prevailing structure at exit for IVR = 1.6. This vortex tube occurs for IVRs of 1.0 and higher in the current study, although the IVR cross-over point at which the vortex becomes evident at exit could be as low as IVR = 0.8, based on internal flow measurements from Fig. 5.18.

8.7 Influence of Coolant Passage Orientation

The change in flow distribution with coolant passage orientation is quite evident from the figures presented in this chapter and discussions thus far. Introduction of the 90° cross-flow at inlet creates an asymmetry of flow that is characterised by an inlet lip vortex that carries strong secondary flow through the hole. Accordingly, the faster moving coolant occupies a relatively narrow region of flow area toward the side of the diffuser, producing an exit distribution with a jet of higher velocity coolant from the right of the hole, and a highly turbulent vortex tube from the left. This is in contrast to the 0° cross-flow (ie co-flowing) where symmetry about the centre-plane is maintained right through the cooling hole. The internal flow pattern shows much greater variation with IVR for the co-flowing case as the jetting effect at the inlet lip is more pronounced.

8.8 Summary

Computational fluid dynamics simulations have been run in order to provide greater insight into the three-dimensional flow field through a shaped film cooling hole. When used appropriately, CFD provides an excellent analysis tool, and in the present case has

enabled more confident interpretation of the experimental flow field measurements. In turn, the experimental data was used to validate the computational solution, with very good agreement for the co-flowing coolant passage configuration. Streamlines together with contour and vector plots of normalised mean velocity clearly show the significant effects of IVR on the flow distribution. In all cases, the simulated results have shown that vorticity is a defining characteristic which has a significant impact on aerodynamic loss, and on the distribution of velocity at the hole exit.

Chapter 9

Discussion

The experimental and computational data presented in this thesis provides a unique insight into the complex three-dimensional flow field through a fan-shaped film cooling hole. The following pages serve to consolidate this information in a description of the key flow characteristics, the influence of inlet velocity ratio and coolant passage orientation, aerodynamic loss, and the opportunities for film cooling system design.

9.1 Flow Pattern for the Co-flow Coolant Passage

The co-flowing coolant passage ($\beta = 0°$) occurs in numerous film cooling situations, particularly around the leading edge of a turbine blade, and within guide vane passages. In this configuration, the IVR has a controlling role over the flow behaviour at the inlet by determining the amount of internal flow separation that occurs. This separation is brought about by movement of the stagnation point of the coolant flow as it turns to enter the hole, moving further upstream with increasing IVR.

9.1.1 Inlet Flow

At low IVRs, the coolant passage mean velocity is considerably less than that in the throat of the cooling hole. Coolant near the top wall of the passage turns smoothly into the hole and is accelerated. However, the volume of coolant passing through the hole requires more fluid than can be supplied by the passage flow directly upstream of the inlet. Accordingly, coolant fluid is drawn in from the sides of the hole and, importantly for the internal flow development, from the downstream inlet lip.

With the stagnation point just downstream of the inlet, and the hole inclined at 30°, this potentially creates a 150° turn for the downstream lip flow to navigate. Such a large angle is too great for the flow to turn smoothly, and inlet lip separation occurs inside the hole on the lower wall of the throat. The streamlines from the computational simulation

clearly show this effect, revealing a broad spread of flow in the passage converging both laterally and vertically to enter the cooling hole. The effects of inlet lip separation are also evident from the experimental profiles on the lower wall showing high turbulence levels just inside the hole inlet.

An additional effect of the lateral ingestion of coolant into the hole at low IVRs is the roll-up of fluid at either side of the inlet. These lip vortices come together shortly downstream near the lower wall of the throat to establish a pair of counter-rotating vortices, much like those seen by other workers ([10], [8]) in the exit region of a round cooling hole.

As the IVR is increased, the stagnation point at inlet moves upstream so that extreme turning at the downstream inlet lip is reduced. Results presented in the current study suggest that inlet lip separation is almost entirely eliminated at an IVR of between 0.8 and 1.0, where the cosine of the IVR is close to the 30° inclination angle of the hole. Experimental measurements and CFD both indicate that for this case the velocity distribution just inside the hole becomes approximately axi-symmetric, and has a broad region of almost uniform velocity at the centre. The velocity decreases towards the wall, closely resembling a typical pipe flow. Inlet lip vortex roll-up is suppressed and no secondary flow patterns emerge within the throat, maintaining low turbulence levels in the bulk coolant flow.

At still higher IVRs, the flow pattern continues to transition as the stagnation point moves further upstream. At the highest tested IVR of 1.6, the volumetric flow rate through the hole is a small percentage of the coolant passage flow, meaning that the hole fluid is drawn from a thin region near the upper wall of the coolant passage. The inlet flow is such that the fast moving passage fluid turns a shallow angle into the hole, jetting across to the lower cooling hole wall and separating from the upstream lip. This generates a region of very low velocity fluid at either side of the upper portion of the hole, which eventually extends right through the diffuser. Streamlines indicate that these low velocity regions contain some axially aligned vorticity, induced by inlet lip roll-up and wall curvature.

The overall flow progression, therefore, involves movement of the stagnation point and a transitioning of inlet lip separation from the downstream lip to the upstream lip as the IVR is increased from 0.3 to 1.6. A narrow range of IVR values exist between IVR = 0.8-1.0 where no inlet lip separation is detected and the coolant flows smoothly into the hole. For this case, internal flow uniformity is high and turbulence levels low.

9.1.2 Internal Flow

Once in the hole, the amount of flow separation from the inlet combined with the adverse pressure gradient in the diffuser determines the internal flow pattern. At low IVRs, the inlet separation at the downstream lip causes fluid to jet towards the upper wall of the hole, while the pair of counter-rotating vortices continue to occupy the lower portion of the hole. The adverse pressure gradient imposed by the diffuser creates a tendency for the flow to separate, but in the low IVR case the flow is already split due to separation at the inlet. The adverse pressure gradient then acts to disperse the vortices, forcing the jetting fluid to remain near the upstream side of the hole, but also to deflect laterally around the separated fluid where it remains attached to the diffuser side walls.

Increasing the IVR to near 1.0, a smoother flow path into the hole enables the flow to remain radially symmetric right throughout the cooling hole. The overall effect of the diffuser is to retard the flow, reducing the peak velocity in the centre of the hole as the flow spreads to fill the increasing cross-sectional area. Velocities near the wall remain low, and the distribution at exit has a broad area of uniform flow across the central portion. This configuration clearly has the least secondary flow patterns within the hole.

At the highest tested IVR of 1.6, the upstream lip separation at either side of the hole and the strong core of high velocity fluid continue into the diffuser where the adverse pressure gradient brings about the typical wall separation observed at the entrance of a two-dimensional diffuser with a large area ratio. This 'jet flow' regime of stall, as described by Kline [78], consists of a central jet of higher velocity fluid accompanied on either side by regions of nearly steady recirculating flow.

9.1.3 Exit Flow

The impact of different inlet and internal flow patterns, as determined by the IVR, manifests in a variation of coolant distribution at the exit and downstream of the cooling hole. At the lowest IVR, coolant leaves the hole with a significant lateral velocity component, such that the higher velocity flow spreads beyond the lateral extents of the hole downstream. As the faster flowing coolant has been forced to the upper wall of the hole, the bulk of coolant exits more toward the upstream edge of the exit and maintains some vertical penetration into the cross-flow at exit. The dominance of the counter-rotating vortex pair within the hole is reflected in the downstream distribution with the outline of the coolant jet revealing two 'arms' at either side.

Measurements of velocity in the exit region show the coolant distribution for IVR = 1.0 to be evenly spread across the whole width of the exit. The coolant emerges as a broad 'bubble' with a smooth curve across the top and around the sides of the flow. The distribution is also quite uniform laterally, in line with the velocity profiles in the Y Z plane within the hole at exit. Turbulence levels are also low, particularly in the central region, reflecting the smooth flow path from the inlet and through the hole.

For the higher IVR of 1.6, the jet flow seen within the diffuser persists downstream of the hole, with the flow continuing to demonstrate a core of high velocity fluid along the hole centreline. This coolant jet has the highest penetration into the exit cross-flow of all tested IVRs in the co-flowing configuration, lifting and spreading with distance downstream.

9.2 Flow Pattern for the Cross-flow Coolant Passage

With the coolant passage rotated to flow at 90° to the cooling hole axis, the effects of IVR at inlet are not as obvious as they are for the co-flowing passage configuration. The variation of IVR still creates a shift in the stagnation point in much the same fashion as for the co-flowing case, but the situation is complicated by the additional turning angle introduced by the passage orientation combined with the cooling hole inclination angle.

9.2.1 Inlet Flow

A significant characteristic of the inlet distribution is fluid roll-up on the upstream inlet lip and generation of a vortex tube. This is the result of the sharp 90° turning angle of the cross-flow passage configuration, and the inability of the flow to navigate such a sudden change in direction. At low IVRs, the cooling hole fluid is drawn from a relatively large volume of the cooling passage, bringing fluid in laterally and even from slightly downstream of the inlet. The acceleration of the coolant into the hole creates a strong axial velocity component that largely overrides the component in the direction of the passage flow. This fluid turns into the hole and shortly after flows axially through the throat.

At the lowest experimental IVR in the cross-flow configuration of 0.4, a vortex tube originates in the lower right quadrant of the hole inlet plane when viewed from behind the cooling hole. Fluid in this region is highly accelerated due to strong, mostly axially aligned, positive vorticity, but quickly slows as the vortex expands to occupy the lower half of the hole downstream. The extent of vortex roll-up is constrained by the amount of fluid turning into the hole to achieve the volumetric flow rate required by the IVR.

At a higher IVR, the inlet lip vortex is larger and has stronger vorticity. The stagnation point is now further upstream and the coolant entering the hole flows further toward the downstream side of the inlet before turning. At still higher IVRs, this effect is further intensified, producing an inlet flow that is almost entirely spiralling with positive vorticity. In this case, the vortex tube occupies almost half the inlet area and is surrounded by higher velocity fluid with slower secondary flow rotation.

9.2.2 Internal Flow

The internal flow pattern follows directly from that at inlet, showing a distinct change with IVR. In all cases, a shear layer exists between the vortex and the region of higher velocity fluid along the top of the throat. This layer of shear acts to transfer energy between the fluid streams, imparting rotational motion to the higher velocity fluid in addition to that created by the wall curvature. The shear layer also enables a degree of rotational 'slippage' between the two flows, which reduces as the IVR increases. In the low IVR case, the high velocity fluid that occupies over half the inlet area is contracted as the vortex expands downstream, jetting toward the top wall of the throat but also spiralling around clockwise toward the right wall. Some of this higher velocity fluid continues to spiral right through the diffuser, arriving on the bottom wall at exit.

The adverse pressure gradient of the diffuser retards the higher velocity fluid somewhat, but acts to a greater extent to disperse the inlet lip vortex. This significantly reduces the axially aligned vorticity, which is overcome by the strong shear layer at the edge of the high velocity region, and transitions into a large area of recirculating fluid in the diffuser. This sort of flow pattern is similar to a regime of stall seen in two-dimensional diffusers with wide angles of expansion, where the fluid jets along one side wall and the remainder of the diffuser is filled with a large recirculating region,as described by Kline [78].

As the IVR is increased, the internal flow pattern tends toward a more persistent inlet lip vortex and a reduction in the magnitude and flow area of the high velocity region. The stronger turning of the vortex draws more energy through the shear layer and causes the high velocity region to rotate further around the walls of the hole. At an IVR of 1.0, the high velocity fluid is sufficiently turned to be fully located in the right side of the hole at exit. At an IVR of 1.6, the strength of the vortex is such that the high velocity region is all but eliminated, decreasing in magnitude substantially downstream, and rotating around the hole to be on the lower left wall at the hole exit. At these higher IVRs, the vorticity generated at the inlet persists through the diffuser and the vortex tube remains intact. Indeed, the spiralling vortex tube clearly dominates the internal flow at higher IVRs.

9.2.3 Exit Flow

At the exit of the cooling hole, the changes of flow pattern with IVR are more evident than at the inlet. The strong jet of coolant along the right wall of the diffuser dominates the exit flow at low IVRs. Coolant leaves the hole as a well formed jet with a definite core of high velocity fluid that initially flows close to the downstream surface. A short distance downstream, however, the jet core lifts away from the surface, decelerating and spreading laterally somewhat. Further downstream, the bulk coolant flow occupies at most half of the exit width of the cooling hole. The large recirculating region restrains the coolant from exiting on the left of the hole, with only a small amount of fluid leaving the hole from this area.

At an IVR of 1.0, the strength of the inlet lip vortex carries through to the exit where coolant fluid ejects from the hole as a vortex tube. The exit flow in this case is split, with the jet of high velocity fluid at the right of the hole, and the vortex tube at the left of the hole. The secondary flow of the vortex tube, and a significant vertical velocity component, encourages mixing with the exit cross-flow. The vortex quickly spreads downstream, being almost fully dispersed just two diameters from the hole centre. The strength of the jet flow is reduced compared to the low IVR case and consequently remains closer to the surface. Mutual spreading of the vortex and jet flows, together with some centrally ejected coolant, provides a region of coverage on the surface along the centreline.

For the highest IVRs, the dominance of the vortex tube flow at exit is increased such that the majority of coolant exits from the left side of the hole. Stronger rotation within the hole draws the high velocity jet around and under the vortex to reinforce this left-biased distribution. The vorticity of the flow again encourages mixing with the exit cross-flow and the coolant is quickly dispersed, being almost fully mixed-out just two diameters downstream. Remnants of the jet flow remain toward the right side of the hole and help provide some coverage on the surface downstream.

9.3 Influence of IVR and Passage Orientation

Clearly, for both inlet passage configurations the influence of inlet flow variations on the flow development within the hole and downstream is significant. The IVR primarily influences the location of the stagnation point in the coolant passage, shifting further upstream as the IVR is increased. This, in combination with the passage orientation, manifests in a consistent progression of internal and exit flow patterns with IVR. The location and extent of inlet lip separation is closely tied to movement of the stagnation

point. For the co-flowing case, this presents a shifting of separation from the downstream to the upstream inlet lip, with an intermediate inlet flow showing no separation at an IVR close to 1.0. The corresponding changes at exit are a shifting of coolant from exiting at either side of the hole, to being distributed across the entire exit width, to issuing mostly along the centreline at higher IVRs.

In the cross-flow passage orientation ($\beta = 90°$), the variation with IVR is again evident. However, the effect of stagnation point variation is different due to the added turning angle in the flow path. Separation occurs on the upstream lip for all IVRs; a variation in IVR affects the severity of turning into the hole, and consequently the extent and intensity of the upstream inlet lip vortex. At low IVRs, the vortex is small and is quickly dissipated downstream where it transitions into a large region of recirculating fluid. At higher IVRs, the intensity of the vortex increases such that it becomes the dominant flow feature within the hole and at exit. In all cross-flow cases a jet of higher velocity fluid exists at the inlet as the coolant accelerates into the hole. This jet remains strong through the hole at low IVRs, but is progressively weakened as the IVR is increased and the vortical flow strengthens. This flow progression is reflected at exit, where the bulk flow moves from a strong jet at the right side of the hole, to a dispersed, higher turbulence vortex tube at the left of the hole.

Clearly then, the primary difference between the co- and cross-flow configuration is the creation of an upstream inlet lip vortex due to the large turning angle into the hole in the $\beta = 90°$ case. The presence of this vortex generates an asymmetric internal flow distribution and a similarly asymmetric exit flow. In both configurations, the internal and exit flow distributions are governed by the IVR: for the co-flowing case it determines the location of the inlet lip stagnation point and the position of the bulk coolant within the hole; for the cross-flowing case it determines the stagnation point location, but more importantly the extent and strength of the inlet lip vortex. For the cross-flow configuration, the trend with IVR is a progressive one, with the flow pattern undergoing a definite transition from low to high IVRs; there is no 'mid-point' IVR as there is in the co-flowing configuration where an IVR of 1.0 creates a smooth flow entry to the hole.

Interestingly, the different configurations result in a reversal in the trend with IVR of the type of flow that emerges from the hole. For the co-flowing configuration, an increase in IVR transitions the flow from a dispersed exit flow to one that is very much a jet type flow. Conversely, for the cross-flow configuration, an increase in IVR shifts from a strong jet flow to a more dispersed exit distribution as the dominance of the vortex tube increases.

9.4 Influence of Blowing Ratio M

The introduction of a cross-flow at the hole exit has been shown to have an effect on the coolant distribution downstream of the hole. However, the coolant flow path prior to exit remains unvaried irrespective of the blowing ratio set. In the tested configurations, the primary effect of the exit cross-flow is to push the coolant toward the surface, reducing vertical penetration, and slightly improving lateral spreading. In most cases, this would bring about an increase in laterally averaged cooling effectiveness; but the extent of mixing between the two flows due to high levels of turbulence may trend effectiveness in the other direction.

An effect of blowing ratio on discharge coefficients was highlighted in Ch. 7. At blowing ratios less than about M = 1.5, discharge coefficients are reduced for both coolant passage configurations, although the trend with IVR remains. The relative strengths of the two fluid streams at exit determine the pressure field at the exit plane. At low M, the exit cross-flow creates a greater blockage for the exiting coolant, forcing it to exit more from the downstream edge of the hole. The static pressure in the mid-plane of the exit is reduced by the increased velocity of the mainstream, but the blockage to the coolant is increased which limits the flow of coolant. Beyond the 'critical' value of about $M = 1.5$, the cooling hole flow has enough momentum to deflect the mainstream away from the exit and can more freely flow from the hole. In the current study, increases in M beyond this value had no effect on the discharge coefficient.

In light of the minimal influence of blowing ratio in this study, an important point to note is that experiments conducted by increasing the blowing ratio for a fixed exit flow and fluid density must produce associated changes in the IVR. The results obtained in this manner depend on the combined effects of blowing ratio and IVR, and it is therefore incorrect to attribute the observed changes to the influence of blowing ratio alone. There are many cases in literature, as identified in Ch. 2, where the IVR has been varied inadvertently between test cases. The author hopes that any future work will acknowledge the important role the IVR has to play in defining the coolant flow field in addition to the traditional parameters such as exit blowing ratio.

9.5 Aerodynamic Losses

Discharge coefficients are an important measure of aerodynamic performance for the cooling system designer, and being able to predict the value of C_d for a particular configuration is highly valuable. While no predictive correlation for discharge coefficients

is provided in this study, analysis of the internal flow in combination with a measure of C_d gives a sense of the implications of inlet conditions on aerodynamic performance.

From the extensive description of internal flow features and measured axial pressure profiles presented in this study, areas within the flow where pressure is lost or recovered can be identified. For the co-flowing configuration, C_d follows a distinct variation with IVR. At low IVRs, the discharge coefficient is also low, with significant pressure losses at entry due to separation from the downstream inlet lip, and the counter-rotating vortices partially stalling the diffuser and limiting pressure recovery. C_d then increases steadily toward a peak value of almost 1.3 for the $M = \infty$ case at an IVR close to 0.8. The smooth inlet flow and good performance of the diffuser contribute to these high values. With IVR increased to 1.6 and higher the diffuser stalls, pressure recovery is significantly reduced, and the discharge coefficient decreases continually. The upstream lip separation, strong jetting within the hole, and large regions of recirculating fluid within the diffuser combine to produce the high aerodynamic losses.

In all cases, the discharge coefficients for the cross-flowing configuration are significantly less than those for the co-flowing coolant passage. The cross-flow configuration introduces additional mechanisms for aerodynamic loss and inhibits the performance of the diffuser to such an extent that pressure recovery through this portion is almost negligible. Very strong secondary flows and associated high turbulence levels dissipate flow energy and contribute to a loss of pressure through the hole. Lower IVR cases, where the inlet lip vortex roll-up is less intense, show lower losses at the inlet than at higher IVRs. The pressure recovery through the remainder of the hole is similar for all IVRs, but does little to overcome the initial loss. Consequently, as IVR is increased, the discharge coefficient decreases quite rapidly.

From a design point of view, the co-flowing configuration and an IVR of close to 0.8 provides the highest discharge coefficients, while for the cross-flow configuration a range of IVRs less than 1.0 provide reasonably good performance, with C_d values of about 0.7. At IVRs greater than about 2.5, the aerodynamic performance of both configurations is similarly poor.

9.6 Relevance to Film Cooling Design

Experimental research is about the discovery and exploration of phenomena, and gaining a level of understanding greater than that which was available previously. The most desirable outcome of engineering research, however, is its integration into a design of a product or process. Some conclusions are therefore drawn here on the benefits for film

cooling design that control of inlet velocity ratio and coolant passage orientation can elicit.

The IVR and coolant passage orientation are clearly parameters which have a definite and substantial effect on the strength and distribution of the emerging coolant jet. This has implications for both aerodynamic loss and downstream cooling effectiveness that present additional challenges for the designer. As the main focus of the current study was to investigate the internal flow field of the fan-shaped cooling hole, the influence of IVR and passage orientation on flow downstream of the exit has been limited to lateral contour planes and computational simulations. The influence on the thermal performance of the coolant film downstream of the hole can therefore only be inferred. However, examination of cooling effectiveness contours from other workers using similar configurations provides a guide for interpretation.

The variation of C_d indicates that the least amount of aerodynamic loss, and hence the highest coolant mass flow for a given pressure ratio, occurs for the co-flowing passage and an IVR such that the resultant flow angle at inlet matches the inclination angle of the hole. For the current geometry of $\alpha = 30°$, the 'optimum' IVR is then 0.87. The resulting uniformity of flow at the exit produces the most even distribution of coolant near the surface downstream. Turbulence levels through the bulk of the coolant are also low, reducing the amount of mixing with the exit cross-flow. It is expected that this configuration will provide the highest laterally averaged cooling performance out of all the configurations tested. Although the exit distribution for the low IVR case is similar, turbulence levels within the flow are approximately twice as high; this would tend to encourage mixing with the mainstream.

The cross-flow coolant passage demonstrates comparatively lower performance for all tested configurations, in line with findings from Saumweber and Schulz [27]. Additional turning at the inlet, strong secondary flows, an asymmetry of the flow at exit, and higher turbulence levels culminate in higher losses and sparse coverage downstream. As with the co-flowing configuration, however, a 'best' case configuration would be for an IVR close to 1.0, where C_d is reasonable (at least no worse than the the other tested IVRs) and the exit distribution demonstrates coverage across the width of the hole at exit, albeit with high turbulence intensity throughout.

Although not directly investigated in this study, analysis of the inlet flow for the cross-flow configuration suggests that internal geometric parameters will still have an impact on the flow distribution at exit. Assuming that the degree of swirl velocity generated at the inlet remains constant for a given IVR, the length of the throat, and indeed the total length of the hole, will play a significant role in the exit distribution by potentially changing where the jet of high velocity fluid leaves the hole. Undoubtedly though, the

variation of IVR will continue to control this distribution via changes in stagnation point location and inlet lip separation. The inlet flow will also likely be affected by variations in the inclination angle of the hole and inlet lip shaping, while the merging of adjacent cooling hole flows downstream of the exit may improve the overall performance of the asymmetric cross-flow passage exit distributions.

For the turbine blade designer, the dominant theme from this research is that the effects of inlet conditions to the hole, and in particular inlet velocity ratio and coolant passage orientation, have a controlling effect on the coolant distribution on the surface downstream of the hole. Achieving the best possible performance for a given cooling hole geometry thus requires all these parameters to be considered, and where possible an IVR of $\cos(\alpha)$ and a co-flowing coolant passage should be sought.

Chapter 10

Conclusions and Recommendations

Film cooling of turbine components continues to be one of the most important contributors to overall gas turbine engine efficiency, enabling higher turbine entry temperatures well above normal component operating temperatures. Although there is a large amount of experimental data pertaining to film cooling, motivation for the present research stemmed from the identification of a gap in literature regarding the inlet conditions of film cooling holes. In addition, the vast majority of previous studies have reported values of cooling effectiveness and heat transfer coefficient, with relatively few studies investigating the internal aerodynamic flow field. This is particularly so for fan-shaped film cooling holes, despite widespread use of this type of geometry in industry. The principal goal of this thesis was thus to provide a unique examination of the internal flow field of a fan-shaped cooling hole and the effects of flow conditions at the cooling hole inlet.

Experimental measurements were made on the custom-built large scale film cooling rig at the University of Tasmania Aerodynamics Laboratory. The design of the facility, construction, instrumentation and control, and commissioning were undertaken by the author as an integral part of the research programme. The cooling hole model geometries are at a scale of 50:1 as compared with typical film cooling holes in aero-engine applications. Detailed flow measurements can be made within the hole and in the exit region using a three-axis traverse system. The completed facility enables the acquisition of high-quality flow field data for the detailed examination of film cooling configurations.

The configurations tested in this study focussed on the variation of the inlet velocity ratio (IVR), coolant passage orientation angle (β), and exit blowing ratio (M). Measurements revealed that the IVR has a strong influence on not only the inlet flow, but also the subsequent flow development through the cooling hole and at exit. This is true for both tested coolant passage orientations ($\beta = 0°$ and $90°$) though the effect manifests

in different ways. All flow configurations are dominated by inlet lip separations which establish a definite flow pattern within the hole. Results indicate that an IVR of close to 1.0 presents a coolant distribution at exit that offers the best lateral coverage and persistence downstream. In addition, this value of IVR also returns the highest discharge coefficient, with a peak value in excess of $C_d = 1.2$ for the co-flowing ($\beta = 0°$) coolant passage. Importantly, the performance of the co-flow configuration is always higher than that of the cross-flow ($\beta = 90°$) configuration. The author hopes that any future work will acknowledge the important role the IVR has to play in defining the coolant flow field in addition to the traditional parameters such as exit blowing ratio.

Computational simulations of selected test configurations provided guidance on the three-dimensional flow field through the cooling hole, showing the extent of inlet lip separations, large regions of stall within the diffuser, and the flow distribution downstream of the exit. The simulations were particularly useful in interpreting the experimental measurements in the inlet region for a cross-flow configuration, where the complexities of the dual turning angle create significant swirl and the establishment of a vortex tube. Simulated results were compared to experimental data in selected regions to provide a good level of validation of the calculated flow physics. Importantly, the computed results clearly demonstrated the shift in flow pattern with IVR for both passage orientations.

For the cooling system designer, the findings in this study highlight the need for consideration of the cooling hole inlet conditions. Clearly, the distribution of coolant at exit is heavily influenced by the flow characteristics at inlet, and neglect of parameters such as IVR and passage orientation can result in cooling performance far from expectations. Results in this study suggest that the co-flowing passage provides the best performance, both in terms of aerodynamic efficiency and surface coverage. Minimum loss occurs with IVR approximately 1.0 when there is no identifiable separation at the hole inlet, and discharge coefficients are maximised. The cross-flow coolant passage introduces an asymmetry to the internal and exit flows that reduces surface coverage and efficiency. However, an IVR of 1.0 still provides a 'best case' performance in this configuration.

The scope for future work in this area is broad, and a number of recommendations for future work can be made:

- Further measurements of the internal flow field for other hole geometries, such as the inclusion of an inlet flare to model 'as constructed' holes. Other factors such as hole roughness, throat length, and inclination angle could also be investigated;
- Experimental and/or computational investigations to identify the dependence of observed flow affects on cooling hole Reynolds number;

- Extension of the experimental unsteady flow field work presented in App. A to the cross-flow coolant passage configuration to reveal more about the periodic nature of the diffuser flow;
- Greater utilisation of the advantages of CFD simulations. Modelling and comparison of different geometries and the influence of flow parameters could be straightforward in a dedicated computational investigation. In particular, a comparison with a cylindrical hole may reveal whether internal or external effects are dominant in the flow distribution at the hole exit;
- Analysis of other flow quantities, such as vorticity and wall shear stress distributions to further understand the internal flow patterns. Validation of wall pressure data in addition to velocity distributions;
- Performing unsteady simulations of the cooling hole flow to identify time-dependent features;
- Further investigations into the comparative heat transfer performance within and on the external surface of the blade for different IVR values and geometries.

There is considerable scope here for investigation via computational simulations due to the flexibility it provides. However, there remains a need for validation using experimental data which should not be neglected. Analysing the effects of hole geometry and flow parameter variations with an awareness of the influence of IVR and passage orientation may reveal further trends that can add to the overall understanding of the inter-relationships between parameters. Building on the current study will augment the utility of these results in design, and progress the state-of-the-art of film cooling toward higher turbine temperatures and even greater efficiencies.

Appendix A

Unsteady Flow Investigation

A.1 Overview

For some time, workers within the film cooling area have discussed the possible occurrence of oscillatory behaviour in the diffuser section of a fan-shaped film cooling hole. This stems from the fact that the area enlargement and associated expansion angle of the diffuser is in excess of that typically accepted as the limit for preventing flow separation. Work by Kline et al. [78] on the behaviour of diffusers sets limits for flow stability and established regimes of operation for which the flow pattern assumes a particular characteristic behaviour. Some workers, in conversation, have said to have established this phenomenon with some manner of flow manipulation, such as the temporary covering of one half of the hole to force the flow to exit from the exposed side only, before removing the cover in order to incite oscillations or 'flapping' of the flow from one side of the diffuser to the other.

This type of flow feature is possibly explained by a separated flow zone in one side of the hole (caused by the large diffuser angle) creating the roll-up of a large eddy that is fed by a shear layer between the main attached jet and the separated lower velocity fluid. This eddy is then shed from the side wall creating an area of low pressure that acts to draw the jetting fluid away from the previously attached wall towards the opposing side of the diffuser. In the same process, a separated region is established on the side of the previously attached wall and another large eddy created. This type of flow dynamic would then perpetuate to create the previously described diffuser 'flapping'. It can be assumed that this flapping phenomenon only occurs within a small range of flow conditions for a particular geometry. To examine this hypothesis of oscillatory flow behaviour in the diffuser, a series of experimental measurements were made using the large scale facility and two single axis hot-wire probes.

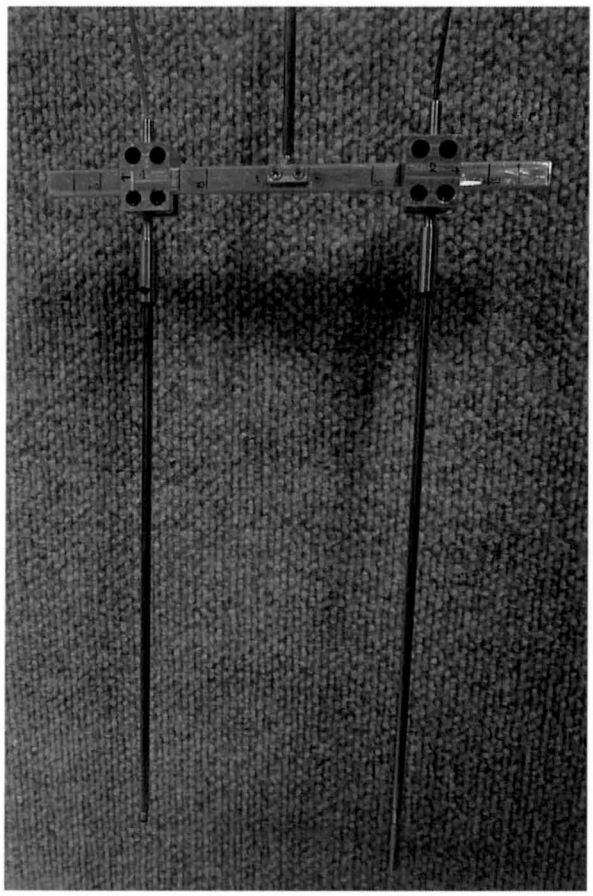

FIGURE A.1: Custom manufactured dual probe support stem

A.2 Experimental Set-up

A special probe holder (Fig. A.1) was designed by the author and manufactured to enable two probes to be positioned and traversed simultaneously. The spacing between probes can be easily varied by using the marked scale on the cross-bar and adjusting the clamps. Two single axis hot-wire probes were positioned on the lateral centreline of the cooling hole exit at (X,Y) = (0,0).

A.2.1 Flow Conditions and Measurement Parameters

Tests were made at six values of hole Reynolds number, spanning from $Re_{j,D} = 2-4.3\times 10^4$. To isolate the effects of $Re_{j,D}$ the IVR and exit blowing ratio were held constant for all tests. This required simultaneous adjustment of the coolant passage and exit cross-flows. Signals from the hot-wire sensors were recorded for a duration of 1 second at 25kHz after passing a 10kHz low-pass analogue filter.

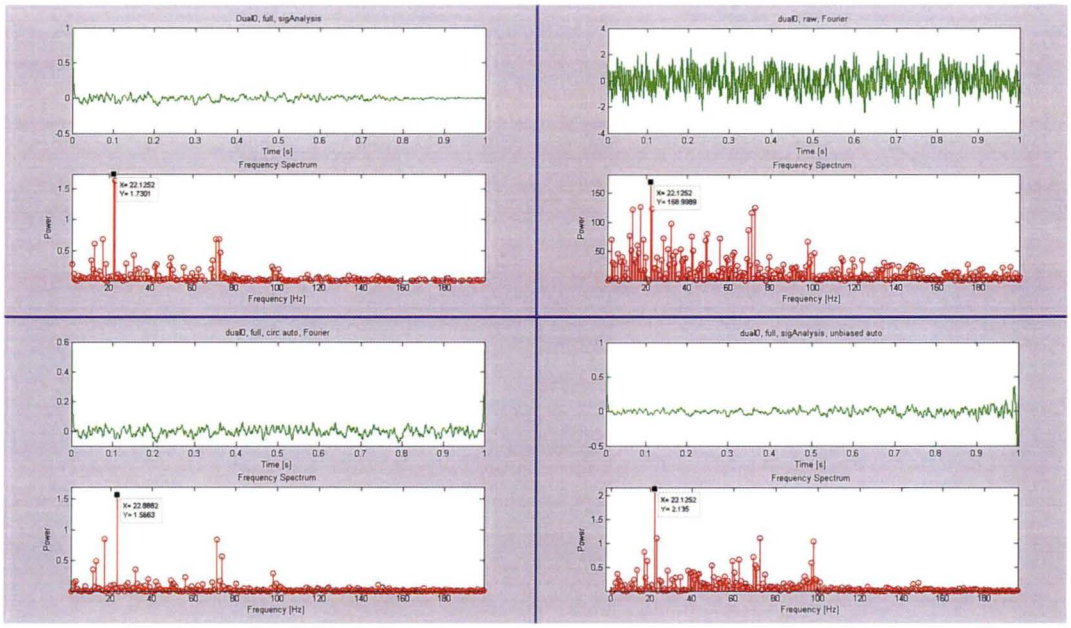

FIGURE A.2: Effect of autocorrelation as a noise reduction technique

A.3 Signal Analysis Techniques

Customised MATLAB code was written to generate the required correlations and power spectrums for analysis of the raw signals. The signal analysis methods used were validated against demonstration code provided by Shilling and Harris [82]. The production of identical results to this code gave confidence in the processing methodology and implementation. Data was auto-correlated to de-noise the signals after removing the time-mean, then passed through a fast Fourier transform (FFT) to determine the frequency components.

The effect of auto-correlation is to average out or reduce the noise. Not only is the circular auto-correlation less sensitive to noise, but the circular auto-correlation of a periodic signal is itself periodic with the same period. Using MATLAB for data analysis, a linear auto-correlation is easily implemented and provides similar benefits in terms of reducing signal noise while preserving the dominant frequency components of the signal. To confirm this, Fig. A.2 shows a comparison of the two methods of auto-correlation and the associated power spectrum. Clearly the dominant peaks at 22Hz and 73Hz are identified by both methods.

A.3.1 Effect of Signal Length

Preliminary data analysis has revealed some variation in the output of a Fourier transform directly related to the length of the analysed signal. It is a basic concept of the

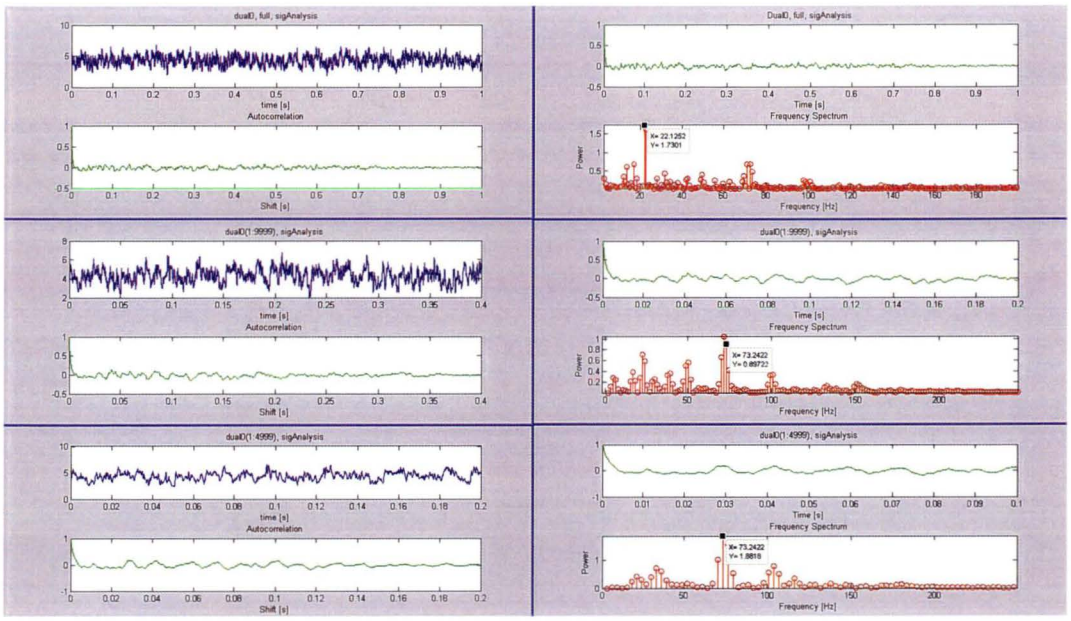

FIGURE A.3: Influence of sample length on calculated frequency spectrum

Fourier transform that when transforming from the time to the frequency domain, the frequency resolution is governed by the length of the signal in time as $F = f_s/N = 1/T$. Therefore, a longer sample time will produce a higher frequency resolution. In addition, the sampling time has implications on the frequency components able to be measured. If the sampling time is too short, lower frequency (longer period) fluctuations will not be seen within the sampled 'window', or at least the relative power of that frequency component will be significantly reduced. To avoid this, the sampling time must be long enough to ensure that the lowest frequencies of interest are captured. Figure A.3 shows how the calculated frequency spectrum changes as the sample length is reduced.

A.3.2 Repeatability

Fourier analysis of a time-resolved signal is enlightening only if the signal is representative of a persistent flow phenomenon that has a periodic nature. To establish the persistence of the measured cooling hole exit flow field fluctuations, three independent measurements were made for two different $Re_{j,D}$ cases. In addition, extended time traces of 2 seconds duration were made for each of these cases. In general, the repeatability tests revealed the largely random nature of the measured turbulent flow field with spectrums from repeated cases indicating different peak power frequencies.

The measurements made by the hot-wire sensor at $Z/D = 1$ for the first case did, however, reveal a consistent peak power at around 28Hz, as shown in Fig. A.4. Although

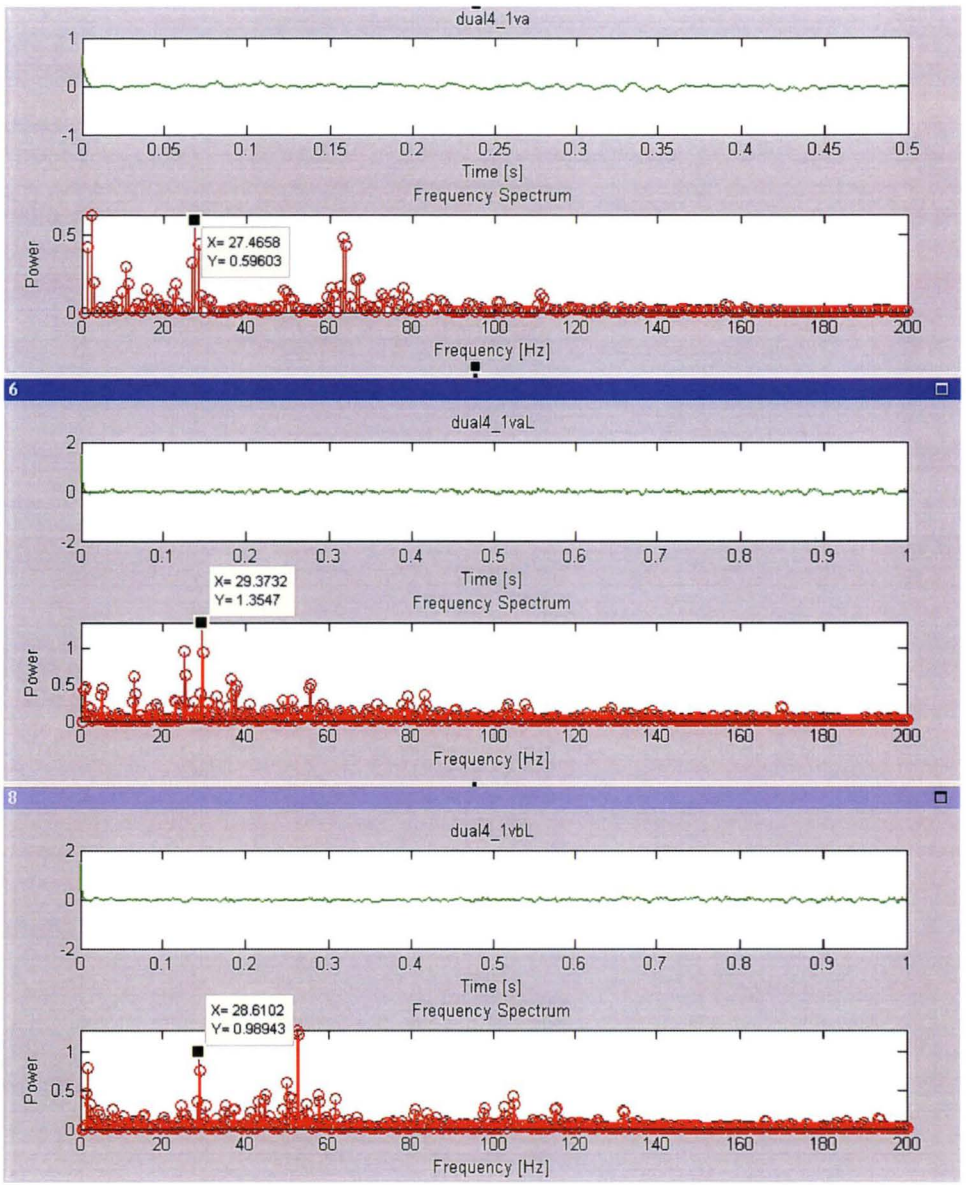

FIGURE A.4: Repeatability of measured frequency spectrum

the spectrums do not compare well across the entire frequency range, this 28Hz peak is clearly evident across all three signals.

A.3.3 Signal Processing Validation

To provide an increased level of confidence in the data acquisition and processing techniques employed for hot-wire measurements, an in-situ testing procedure was set-up in the working section mainstream. A small, 1.3mm diameter tube was positioned in the $Y - Z$-plane upstream of the single axis hot-wire probe to develop a periodic Karman

Component	Resonant Frequency (Hz)
Main wind tunnel	28
Coolant passage Helmholtz	19
Coolant supply loop	47
Cooling hole	686
Probe support	274
Probe support vortex shedding ($U = 19\text{ms}^{-1}$)	950

TABLE A.1: Resonant frequencies for facility components

vortex street. NACA report 1191 [83] provides guidance on behaviour of vortex generation behind cylinders, and from empirical data suggests a Reynolds number range of $40 < Re_d < 150$ for a stable vortex street. A freestream velocity of 1.5 ms$^-$1, near the lower limit of the wind tunnel, sets $Re_d = 132$ for the 1.3 mm tube. Working from the empirical curve fit for the above Re_d range, the Strouhal number, relating shedding frequency to velocity, can be given by

$$St = fd/U = 0.212 \times (1 - \frac{21.2}{Re_d}) \tag{A.1}$$

where f is the shedding frequency, d the cylinder diameter, and U the velocity past the cylinder. For the above values of Re_d, U, and d, this suggests a frequency of 205.3Hz. Data acquired from the hot-wire and processed by the custom MATLAB code returned a dominant frequency at approximately 201Hz, providing confidence in the acquisition system.

A.3.4 Resonant Frequencies

In order to oscillations of interest from those of the apparatus, a number of calculations were made to determine the resonant frequencies of the main passages, and the natural frequencies of the probe supports. The various calculated frequencies are shown in Tab. A.1.

A.4 Results

As highlighted in the resonant frequency assessment of the wind tunnel components, 28Hz is a possible acoustic resonance frequency of the main wind tunnel. If this frequency component of the signal was due to the acoustic resonance of the main wind tunnel, it would be expected to be identified in the traces of both hot-wires. The spectrums from the $Z/D = -1$ hot-wire sensor shown in Fig. A.6 do not, in general, show a strong peak at or near 28Hz, except for case 3.

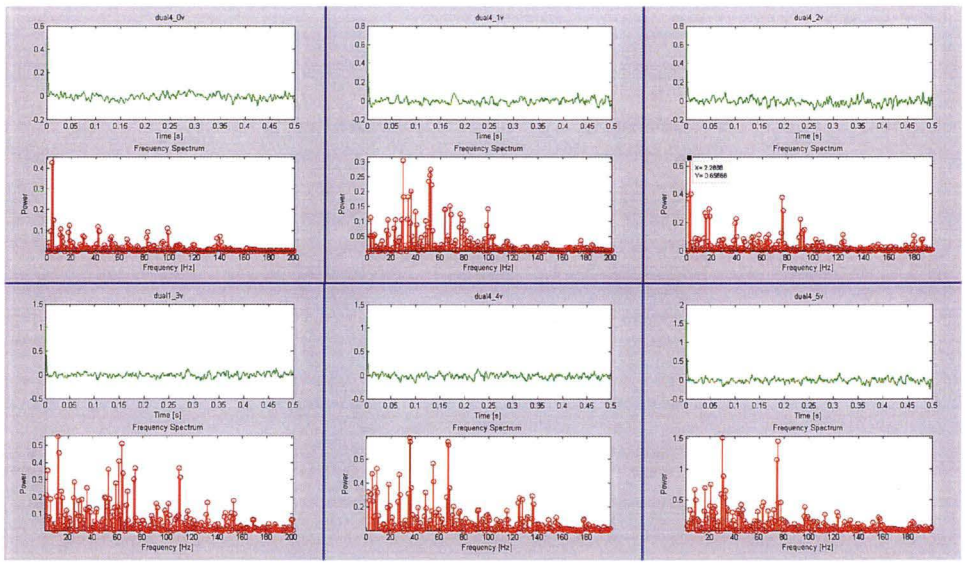

FIGURE A.5: Variation of frequency spectrum with $Re_{j,D}$ (wire A)

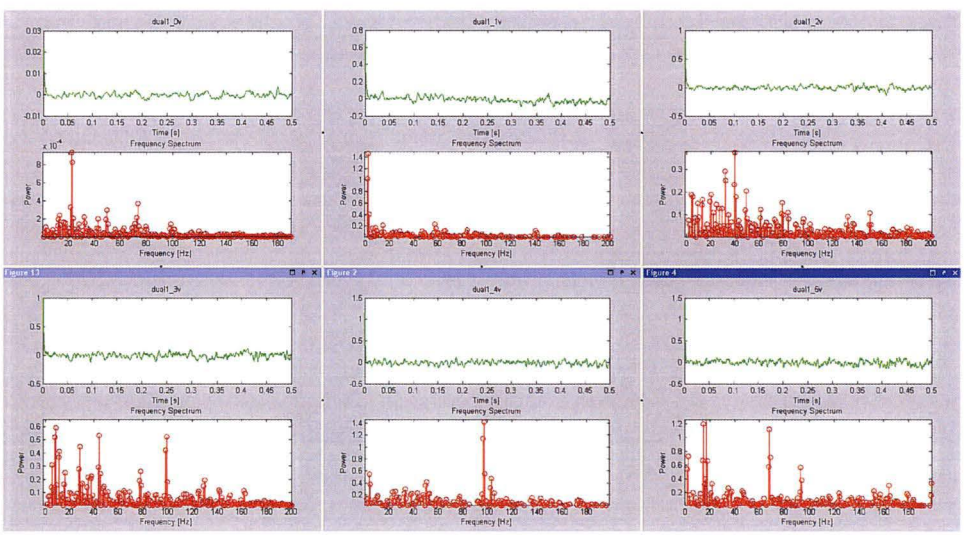

FIGURE A.6: Variation of frequency spectrum with $Re_{j,D}$ (wire B)

The frequency components of each hot-wire signal were plotted and compared to identify any immediately obvious trends with increasing $Re_{j,D}$. As shown in Fig. A.5, the dominant frequency components from sensor A shift around as $Re_{j,D}$ is varied with no discernible pattern. The results are similar for sensor B (Fig. A.6), with the dominant higher-power frequencies changing between cases.

Comparing between sensor A and B, however, there seems to be little correspondence between the frequency spectrums at each $Re_{j,D}$. In all cases, the signals from both sensors show very little signal power at frequencies above about 100Hz and the spectrum is essentially flat beyond 200Hz. This suggests that the period of any fluctuating flow

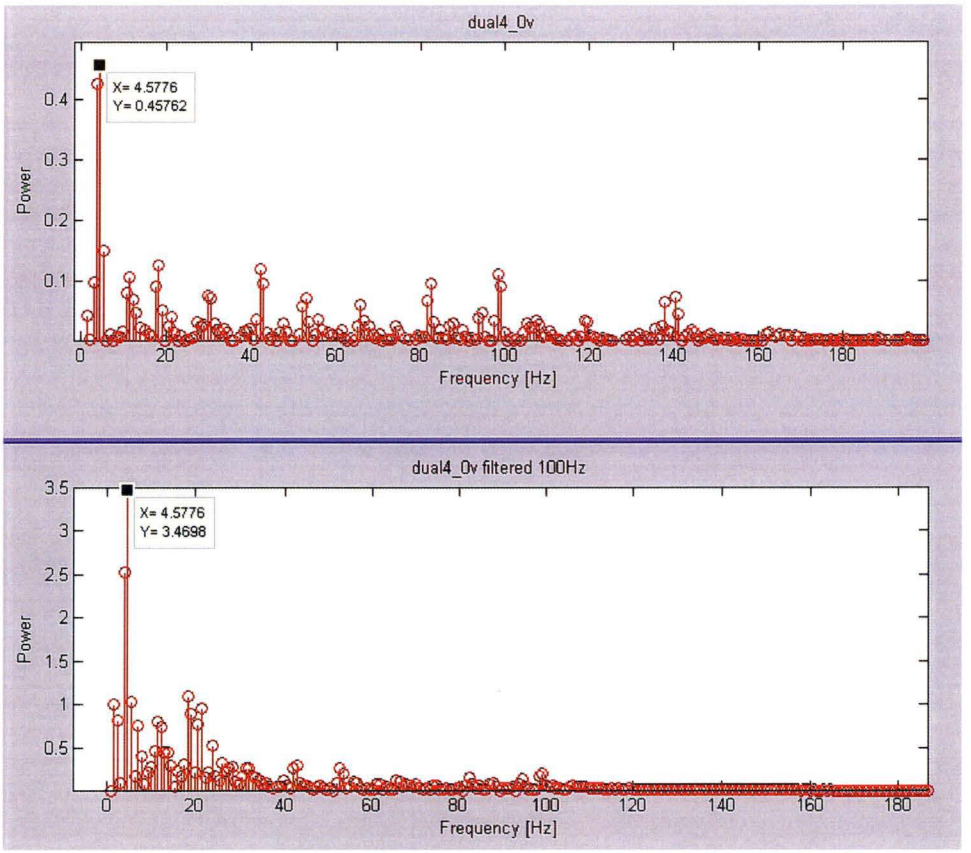

FIGURE A.7: Effect of signal filtering on frequency spectrum

component (less than 100Hz) is at least 10ms, which at a typical flow speed of 4 $ms^{-}1$ equates to a flow-through length of over 8 diameters, or 1.6 hole lengths. Since such a scale is large compared to the diameter of the hole, we can assume that the observed higher power frequencies are not due to eddy passing fluctuations, but are the result of some other occurrence in the flow dynamics.

The 'flapping' flow phenomenon is hypothesised to occur at lower frequencies. As most of the frequency plots showed a fairly cluttered spectrum below 100Hz, a low-pass digital filter was applied to the signals and the power spectrum re-calculated to determine the effect on the power distribution at low frequencies after removing the higher frequency noise. This operation re-distributed the signal power to lower frequencies enabling those lower frequencies to become more dominant in the spectrum, as shown in Fig. A.7.

A.4.1 Cross-correlations

Further comparison of the signal pairs was obtained by running a linear cross-correlation and observing the power spectrum of the correlation to identify any significant frequencies. Figure A.8 shows the two input signals and the resulting cross-correlation.

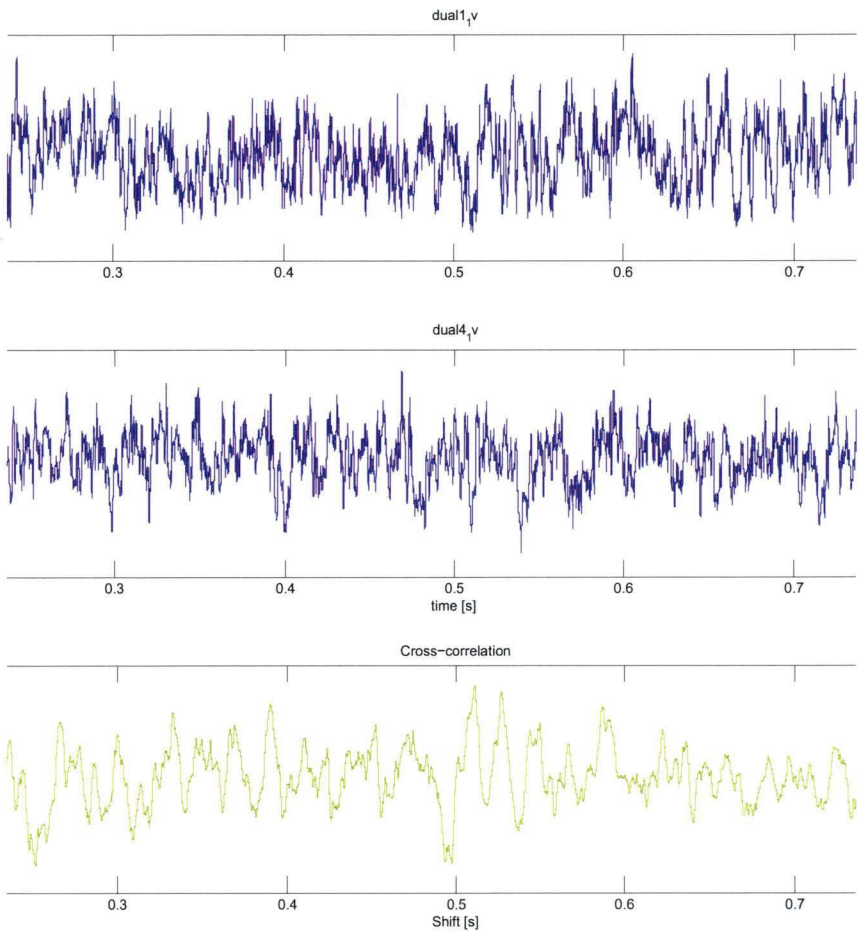

FIGURE A.8: Cross correlation of two simultaneously sampled hot-wire signals

This brief investigation of correlation between simultaneously sampled signals did not reveal any significant trends. At this point in the unsteady flow investigation, a decision was made that the time available would be better spent concentrating on recording flow field measurements for a range of cases, rather than pursuing a clear demonstration of oscillatory behaviour.

A.5 Summary

Additional data (not presented here) did not provide any dominant flow frequencies or any identifiable patterns that suggested oscillatory behaviour. It may be that conditions conducive to oscillating flow were not established for the series of tests performed. Such conditions may only occur across a narrow band of cooling hole Reynolds numbers for a particular geometry, and, given the findings from this research regarding inlet velocity ratio, require a particular value of IVR to generate large scale instabilities. In addition, the tests performed here were for a co-flowing coolant passage only, where the flow pattern appears to remain symmetric about the cooling hole centre-plane. Flow field results from within the hole, presented in Ch. 5, suggest that the 'flapping' phenomenon may be more likely to occur for the pure cross-flow ($\beta = 90°$) configuration, where the bulk flow is already biased to one side of the diffuser due to turning effects at the hole entrance. An investigation more focused on unsteady flow effects would determine the extent of this.

Appendix B

Component Specifications

Furness Controls

FCO12/14

Pressure and Flow Measurements

MICROMANOMETERS

FCO12/14

FCO12 2 Range Digital Micromanometer

A high quality differential pressure micromanometer with digital display and two ranges giving a total resolution of 1:20,000.

Currently, over 10,000 Furness Controls micromanometers are used in universities and research establishments around the world, measuring pressures in fan testing, heat exchanger design and aeronautics.

The FCO12 and FCO14 instruments feature automatic zero, allowing the instrument to be used accurately, immediately after switch-on. A function switch introduces a square root extractor converting the instrument to an anemometer, measuring velocity in metres/sec. A small pitot static tube is provided for this purpose, together with a length of twin-core plastic tubing and all housed in a leather carrying case. A variable response control allows the reading of fluctuating pressure and the output signal of 0-5 Vdc can be fed to data capture systems.

The micromanometers are based on a capacitance differential pressure transducer of unique design which measures differential pressures from .001 Pascal. Each instrument includes a differential pressure transducer, rechargeable battery pack, a readout meter (analogue or digital), a range switch and equalising valve. Additional features are: automatic zero, variable response control and a centre zero function switch.

Where a multiple of pressure input exists, Furness Controls can supply Scanning Boxes for use in conjunction with micromanometers. Please request leaflet FC091 for further information.

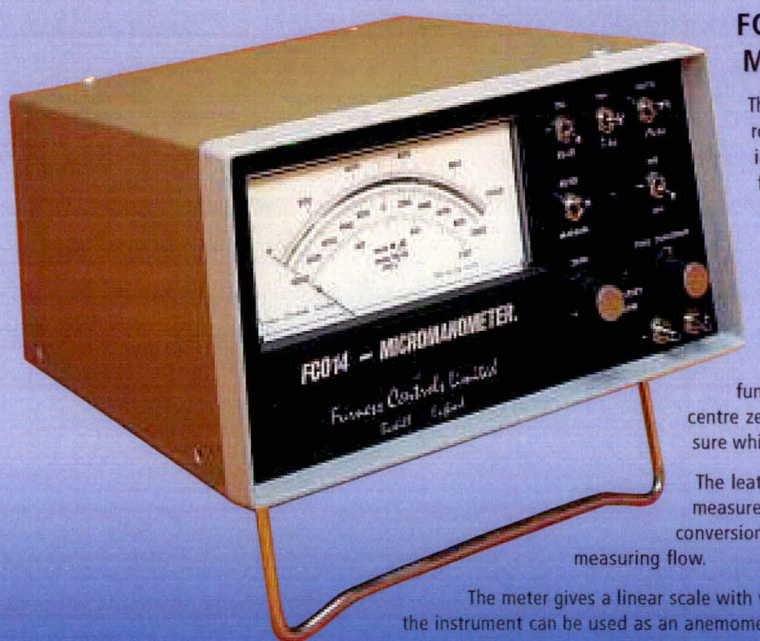

FCO14 3 Range Analogue Micromanometer

The analogue version features a large mirror-scale meter with 100 graduations, each individually calibrated and marked in our factory for the highest resolution and accuracy.

In addition to automatic zero, the instruments all use 4, 'D' size rechargeable batteries, and a separate ac charger unit making the instrument highly versatile.

On the FCO14 analogue instrument, a function switch converts the instrument to a centre zero scaling for measuring differential pressure which vary positive and negative around zero.

The leather case includes a pitot tube for velocity measurements and the instruction manual giving conversion tables for temperature correction when measuring flow.

The meter gives a linear scale with velocity when the m/s switch is selected so the instrument can be used as an anemometer.

FCO12/14

Furness Controls

FCO12/14

Pressure and Flow Measurements
MICROMANOMETERS

FCO12/14

MODELS

FCO12	10%	100%	metres/sec
Model 1	±1.999 Pascals	±19.99 Pascals	0-5.6 m/s
Model 2	±19.99 Pascals	±199.9 Pascals	0-18 m/s
Model 3	±199.9 Pascals	±1999 Pascals	0-56 m/s
Model 4	±1.999 kPascals	±19.99 kPascals	0-180 m/s

FCO14	1%	10%	100%	metres/sec
Model 1	±0.1 Pascals	±1 Pascals	±10 Pascals	0-4 m/s
Model 2	±1 Pascals	±10 Pascals	±100 Pascals	0-12 m/s
Model 3	±10 Pascals	±100 Pascals	±1000 Pascals	0-40 m/s
Model 4	±100 Pascals	±1000 Pascals	±10000 Pascals	0-120 m/s
Model 5	±200 Pascals	±2000 Pascals	±20000 Pascals	0-180 m/s

GENERAL SPECIFICATION

Accuracy	±0.5% FS (±1 digit FCO12), (FCO14 display 1% FSD)
Resolution FCO12 FCO14	1 part in 2,000 each range 1 part in 100 each range
Temperature effect on range	±0.5% per 10°C
Temperature effect on zero (manual setting)	±0.04%, 100% range per 10°C
Zero stability on automatic	Drift is less than the readout resolution
Response	Variable damping 20 ms to 10 seconds
Overload	10 x max DP
Static	±1 bar gauge pressure
Output	±5 V each pressure range; 0-5 V flow range
Supply	Four 'D' size cells, Ni-Cad fitted give 14 hourse use on 40 hours on FCO14, 200-240 ac or 100-120 ac power unit supplied recharges internal cells in 15 hours.

Agent's Stamp:

UKAS CALIBRATION 0500

ELECTRICAL EQUIPMENT CERTIFICATION SERVICE BS EN ISO 9002

UKAS QUALITY MANAGEMENT 020

Furness Controls has a NAMAS certified laboratory which offers pressure calibration from 0 to 40 kPa

Furness Controls Limited

Beeching Road, Bexhill, East Sussex, UK. TN39 3LJ
Tel: +44 1424 730316 Fax: +44 1424 730317
E-mail: sales@furness-controls.com
Web site: http//www.furness-controls.com

BR56414.06.01

Mixvent Series - Mixed-Flow Fans - TD-800/200 Hi

Location

Designation

Project

Notes

FEATURES

The Mixvent Series is a very compact design of mixed-flow fans that is part of a very flexible system designed specifically for use in homes, hotels and apartments etc., as well as for hot and cold air transfer from one room to another.

Construction
Casings of the 1300/250 and 2000/315 models are of epoxy coated steel; other sizes are of reinforced injection moulded polypropelene plastic. All units are provided with an integral mounting foot.
Impellers are of injection moulded plastic and of mixed-flow design.

Motors
Type - 2-speed. Models 250-350 are shaded pole; 500 and above are squirrel cage induction motor.
Electricity supply - 220-240V, single-phase, 50Hz.
Bearings - sleeve up to size 350/125 and ball for all other models.
Speed-controllable using VA type speed controller in high speed only.

Internal Thermal Protection
By fuse to size 350/125 and for all other models manual-reset thermal overload protection device in accordance with mandatory requirement for in-duct fans AS/NZS60335-2-80:2004

Testing
Air flow to BS848:Part 1, 1980
Noise to BS848:Part 2, 1985
Special Note
Avoid the use of spring-loaded backdraft dampers, extensive lengths of duct and air valves with the TD-250/100 and TD-350/125 models.

Special Features
The fans can be removed without disturbing the connecting ductwork via specially designed support brackets.
Fitted with plug and lead, wired in high speed.
Multi-stage fans
In addition to being used as single-stage fans the Mixvent range can be arranged in parallel, in series or in both parallel and series. Such flexibility enables higher air flow and pressure demands to be met.

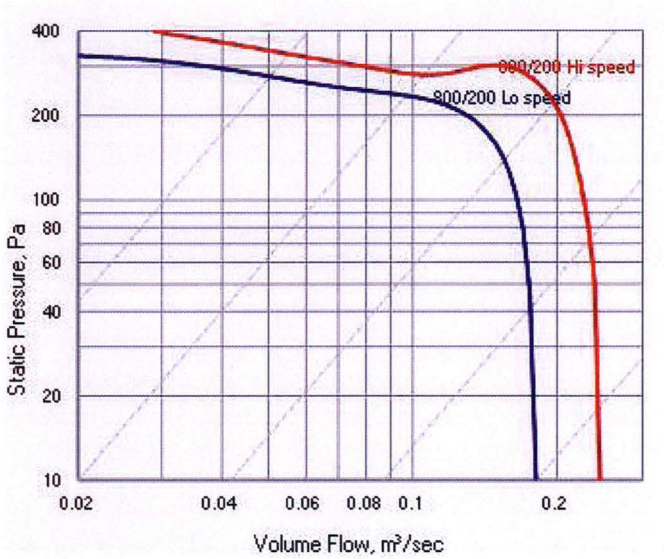

Technical Data				
Fan Speed	**Avg. dBA**	**kWatts**	**Amps**	**Max. °C**
42	53	0.120	0.60	

In-duct Sound Power Levels L_wdB re 1pW							
63	**125**	**250**	**500**	**1k**	**2k**	**4k**	**8k**
	60	64	73	66	67	62	55

Mixvent Series - Mixed-Flow Fans - TD-800/200 Hi

SUGGESTED SPECIFICATION

The In-line fans shall be of the Mixvent Series as supplied by Fantech Pty. Ltd.

Impellers shall be of mixed flow design and driven by 2-speed single-phase motors with integral thermal protection.

All fans shall be fully tested to BS848:Part, 1980 for air flow and BS848:Part 2, 1985 for noise.

WIRING DIAGRAM - TD-800/200 Hi

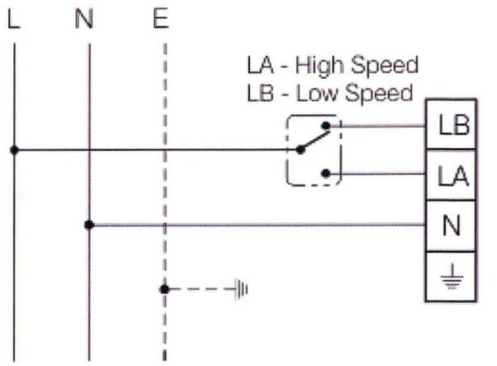

For Special Motors, Contact Fantech for Details.

Dimensions, mm

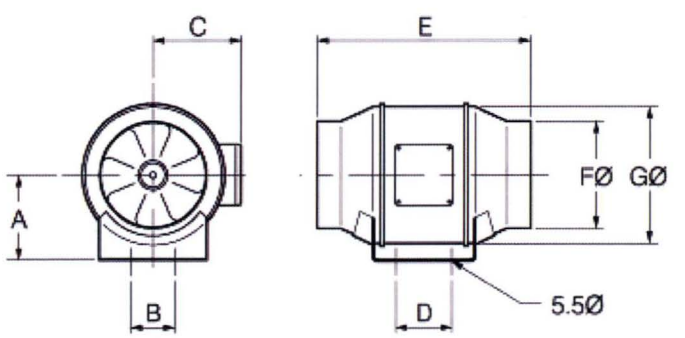

A	B	C	D	E	F	G
124	94	141	100	302	198	217

FANTECH

OFFICES & AGENTS

Victoria
Fantech Pty. Ltd.
Tel:+61 (03) 9554-7845
The Ventilation Warehouse Pty. Ltd.
Tel:+61 (03) 9696-3044

New South Wales
Fantech Pty. Ltd.
Tel:+61 (02) 8811-0400

Uniair Distributors Pty. Ltd.
Tel:+61 (02) 4961-6088
Refrigeration and Air Supplies
Tel:+61 (02) 4226-5133
Airovent
Tel:+61 (02) 9153-6005
The Ventilation Warehouse Pty. Ltd.
Tel:+61 (02) 9698-8130
Ideal Rayson
Tel:+61 (02) 6025-1866

South Australia
Fantech Pty. Ltd.
Tel:+61 (08) 8294-0530

Queensland
Air Design Pty. Ltd.
Tel:+61 (07) 3299-9888

Capricorn Air Conditioning
Tel:+61 (07) 4775-5222

Northern Territory
Fantech Pty. Ltd.
Tel:+61 (07) 8947-0447

Western Australia
Systemaire Pty. Ltd.
Tel:+61 (08) 9209-4999

Tasmania
Major Air Pty. Ltd.
Tel:+61 (03) 6344-6888

ACT
Ideal Rayson
Tel:+61 (02) 6280-5511

Auckland
Fantech (NZ) Ltd.
Tel:+64 (09) 444-6266

Christchurch
Fantech (NZ) Ltd.
Tel:+64 (03) 379-8622

Wellington
Fantech (NZ) Ltd.
Tel:+64 (04) 566-0532

No. 2 "RICHARDSON" V.B. FAN CAPACITY TABLE

Volume Cu. Ft./Min.		STATIC PRESSURE — INCHES OF WATER								
		2	3	4	5	6	7	8	10	12
100	R.P.M.	1800	2120	2430						
	H.P.	.05	.08	.11						
150	R.P.M.	1820	2180	2500	2770	3000	3240			
	H.P.	.08	.11	.15	.19	.24	.29			
200	R.P.M.	1930	1940	2560	2830	3050	3300	3500	3900	4250
	H.P.	.10	.16	.20	.25	.30	.36	.40	.53	.65
250	R.P.M.	2080	2380	2680	2920	3120	3350	3580	3950	4300
	H.P.	.15	.19	.25	.31	.37	.43	.49	.63	.77
300	R.P.M.	2200	2500	2780	3000	3210	3450	3620	4010	4350
	H.P.	.20	.26	.32	.38	.45	.52	.59	.74	.90
350	R.P.M.	2440	2690	2910	3120	3350	3540	3730	4100	4420
	H.P.	.28	.34	.41	.48	.55	.62	.7	.86	1.03
400	R.P.M.	2620	2850	3060	3300	3480	3680	3880	4210	4540
	H.P.	.36	.44	.51	.60	.68	.75	.83	1.02	1.18
450	R.P.M.		3050	3250	3440	3620	3820	4000	4320	
	H.P.		.55	.65	.73	.82	.90	1.00	1.16	
500	R.P.M.		3260	3440	3620	3800	3970	4140	4460	
	H.P.		.72	.81	.88	.97	1.08	1.16	1.36	
550	R.P.M.			3690	3830	4000	4150	4320		
	H.P.			.94	1.08	1.18	1.26	1.40		
600	R.P.M.			3880	4030	4200	4320	4480		
	H.P.			1.16	1.27	1.42	1.50	1.60		
650	R.P.M.				4250	4400	4500			
	H.P.				1.56	1.61	1.80			

No. 2½ "RICHARDSON" V.B. FAN CAPACITY TABLE

Volume Cu. Ft./Min.		STATIC PRESSURE — INCHES OF WATER								
		4	5	6	7	8	10	12	14	16
200	R.P.M.	2000	2200	2400	2600	2780				
	H.P.	.21	.27	.33	.39	.46				
300	R.P.M.	2050	2240	2440	2630	2790	3100	3400	3680	3920
	H.P.	.30	.38	.45	.54	.62	.79	1.00	1.18	1.35
400	R.P.M.	2150	2340	2520	2700	2850	3150	3440	3690	3930
	H.P.	.40	.49	.59	.69	.79	1.00	1.22	1.45	1.65
500	R.P.M.	2300	2460	2640	2790	2940	3240	3510	3750	4000
	H.P.	.55	.66	.76	.87	.98	1.23	1.47	1.72	2.00
600	R.P.M.	2440	2600	2770	2910	3080	3350	3600	3840	
	H.P.	.74	.86	.98	1.10	1.22	1.50	1.77	2.07	
700	R.P.M.	2610	2750	2900	3050	3190	3460	3710	3950	
	H.P.	1.03	1.13	1.25	1.40	1.55	1.80	2.14	2.44	
800	R.P.M.	2800	2950	3090	3200	3340	3600	3830		
	H.P.	1.36	1.47	1.64	1.73	1.90	2.21	2.51		
900	R.P.M.	3040	3160	3280	3410	3520	3750	3970		
	H.P.	1.72	1.92	2.01	2.20	2.31	2.68	3.02		
1000	R.P.M.		3400	3500	3610	3710	3920			
	H.P.		2.38	2.62	2.69	2.86	3.21			
1100	R.P.M.				3800	3900				
	H.P.				3.38	3.46				

Appendix C

Publications Arising from Thesis

Design and Construction of a Facility for Film Cooling Research

16th Australasian Fluid Mechanics Conference
Crown Plaza, Gold Coast, Australia
2-7 December 2007

Design and Calibration of a Facility for Film Cooling Research

J.S. Porter J.E. Sargison A.D. Henderson

School of Engineering
University of Tasmania, Hobart, Tasmania, 7005 AUSTRALIA

Abstract

An existing open circuit wind tunnel has been modified to incorporate a secondary supply loop to provide controlled flow conditions at the inlet to a film cooling hole model. The primary or crossflow fluid enters from atmosphere through a smooth two dimensional contraction before entering the working section. The newly constructed supply loop has a single inlet from a high pressure source, in-line blower, and a 600mm long rectangular passage working section. Various film cooling geometries can be installed to connect the supply loop passage to the main wind tunnel working section. The installation of the supply loop enables variation of cooling hole inlet conditions, including crossflow velocity, mass flow rate, and flow direction. Detailed flow measurements were made to establish uniformity of flow in the supply passage and accurate control of coolant mass flow. A range of operating conditions have been established and calibrated for use in subsequent research.

Nomenclature

D	cooling hole diameter
ρ	air density (kg/m^3)
U_∞	mainstream velocity (m/s)
U_j	coolant jet velocity (m/s)
r	velocity ratio = U_j/U_∞
M	mass flux (blowing) ratio = $\rho_j U_j/\rho_\infty U_\infty$
I	momentum flux ratio = $\rho_j U_j^2/\rho_\infty U_\infty^2$
Tu	turbulence intensity (%)

Introduction

The use of film cooling techniques to control the operating temperature of gas turbine components continues to be one of the most important contributors to the overall performance of a gas turbine jet engine. It can be shown that even small increases in turbine entry temperature (TET) result in large increases in engine thrust and overall engine efficiency. These elevated temperatures have been made possible partly by improvements in materials technology, including surface coatings, but to a greater extent through improved aerodynamics and film cooling design [1]. Film cooling involves bleeding a small percentage of cooler air from the high pressure compressor and passing it around the combustion chamber to be fed to the turbine vanes and blades internally. This cool air then moves through the inside of the blade, providing convective cooling, before being ejected through discrete rows of holes in the blade surface. These discrete 'jets' of coolant fluid optimally coalesce to form an insulating film of air between the hot mainstream gases (from the combustor), and the blade material. Cooling hole design is a constant trade-off between maximum cooling performance and aerodynamic efficiency

The aerodynamic component of cooling hole performance is often seen as secondary in importance to that of the heat transfer and cooling effectiveness. Indeed, preventing the blade from thermally induced failure is a primary aim, and thus concentration on thermal performance is understandable. However, as indicated above, the important value of overall engine efficiency has a strong dependence on the performance of the turbine section. This means that optimising the coolant flow path to reduce aerodynamic entropy generation is a very worthwhile exercise. Figure 1 shows a typical coolant flow path through the internal passages of a high pressure turbine blade. Coolant is fed from the root of the blade along a series of passages and bends, where high levels of turbulence are induced by transverse ridges. These are designed to increase the wetted area of the internal blade material and thus provide increased levels of convective cooling. Film cooling holes are drilled either by laser or electro-discharge machining at particular locations to create a surface pattern that provides the best film coverage. Typically, these holes are either cylindrical (round) or fan-shaped, with an expanded exit. The angles of the hole axis relative to the passage and external hot-gas flows are varied, and depend on the location of the hole both internally and on the blade surface. In addition, the surface outline of the hole will also vary with hole angle, and with the hole geometry. The transverse ribs, sharp 180 degree bends, mixing of the coolant and mainstream flows, and in-hole turbulence all contribute to entropy production. Numerous parameters need to be examined to determine the combinations of hole size, shape, angle, mass flow etc to identify and reduce these sources of entropy production and improve turbine and thus overall engine efficiency.

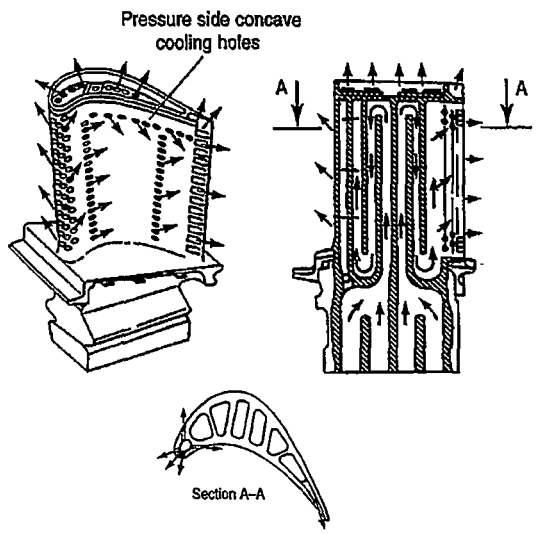

Figure 1. Internal coolant flow path in a high pressure turbine blade [2]

Research currently in progress by the Authors, using the wind tunnel design presented in this paper, is focussed on the fundamental fluid dynamic processes involved in a single coolant jet ejection into a crossflow. The project aim is to make high resolution measurements of the flow field in and around 50-times scale models of typical film cooling hole geometries. A solid understanding of the dynamic mechanisms of the jet-crossflow interaction for shaped cooling holes is still lacking, as the

extensive body of findings pertain overwhelmingly towards cooling performance results. The coolant flow path within an actual turbine blade or vane is quite complex. There is significant variation of internal and external flow direction in relation to hole orientation for different hole locations around a blade. Also, the pressure difference across a hole is strongly effected by the location of that hole in the coolant and mainstream flows. It has been shown through studies such as [3], [4], and [5] that the inlet conditions for a cooling hole have an important effect on the flow within the hole, which in turn affects the discharge coefficient and cooling effectiveness for that configuration. Thus, trying to replicate the flow conditions both internally and externally in a film cooling model is important.

A number of ratios help define the operating characteristics of a cooling hole or series of holes. These include the velocity ratio, r, temperature ratio, TR, density ratio, DR, mass flux (blowing) ratio, M, and momentum flux ratio, I. The values of these ratios are frequently used in research to try and match the conditions in an actual engine, and many previous studies have revealed the effect of changing these parameters on film cooling performance, and to an extent, on discharge coefficients. Direct engine modelling covering all parameters is unfeasible for most investigations, and thus the parameters considered vital in reproducing aspects of the flow that are critical to the phenomenon under examination must be identified. Having a low speed tunnel means that Mach numbers cannot be reproduced. However, velocities are set, in conjunction with the hole diameter, to achieve Reynolds numbers in the range of typical values in actual blades. Table 1 below lists a number of quantities and their typical values in an operating engine, and those selected in the current research investigation.

Parameter	Engine value	Test value
D (hole diameter)	0.7 - 1.2 mm	50 mm
α (inclination angle)	20 – 60°	30°
L/D	3 – 6	5
Fan expansion angle	14 – 32°	30°
DR	1.5 – 2	1
r (velocity ratio)	0.5 – 2	0.5 – 1.5
M	0.8 – 4	0.5 – 1.5
I	0.9 – 2	0.25 – 2.25
Re_{Di}	$1 - 3 \times 10^4$	$1 - 5 \times 10^4$

Table 1. Comparison of actual and experimental parameters.

Description of the facility

The existing wind tunnel selected for modification was an open circuit design using an axial flow fan to draw air through the working section. A previous modification created a meter long working section 225x225 mm in cross-section, preceded by a smooth two-dimensional contraction [6]. This resulted in mainstream turbulence intensity of 0.6%, flow direction uniform to within ±0.5°, and velocity uniform to within ±2%. Maximum mainstream velocity was 20 m/s. These features of the tunnel remain in the new design. The existing tunnel enabled a complete side of the working section, with integrated cooling hole model, to be removed and replaced with different hole geometries. A round and a fan-shaped hole model could be fitted to the working section. Inlet to the hole was via a bellmouth tube to measure the cooling flow, preceding a plenum chamber mounted normal to the hole axis (see figure 2). Velocity (and mass flux) ratios of up to 0.76 could be achieved in the existing configuration.

Required specifications

Table 1 lists a range of values that the current research aims to employ in evaluating the flow. The existing set-up was unsuitable to achieve these values for several reasons. The mainstream hot-gas flow and coolant passage flow in an actual blade are generally in parallel planes, as shown in figure 3. When compared with the existing configuration, we can see that the important hole inlet conditions are not being well replicated by the plenum feed and perpendicular entry. The maximum velocity through the metering section was limited by the achievable pressure difference across the hole, created by the drop in static pressure of the mainstream flow. In addition, no variation of internal crossflow direction was possible due to the plenum at inlet. The existing cooling hole geometries were not suitable due to the perpendicular inlet, and the 28° expansion angle of the existing model was increased to 30°, as the current research intends to examine the unsteady flow features within the overexpanded exit of fan-shaped holes. This is still representative of holes used in actual blade designs, based on data supplied by Rolls-Royce Plc [7].

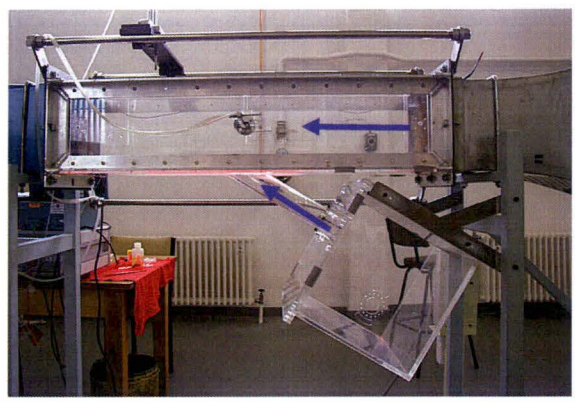

Figure 2. Existing working section with plenum and perpendicular hole inlet.

It should be noted that although the supply loop air is referred to as 'coolant', the work here is not reproducing engine like temperature ratios between the two flows. This is due to the difficulties in cooling the large volumes of air required, and also the undesirable thermal effects on hot-wire measurements in the mixing region of the coolant and mainstream flows if they were at different temperatures. Hence 'coolant' refers to the air passing through the supply loop and cooling hole model. There is scope, however, for experiments with different density ratios in future work, by using a foreign gas with appropriate density as the coolant.

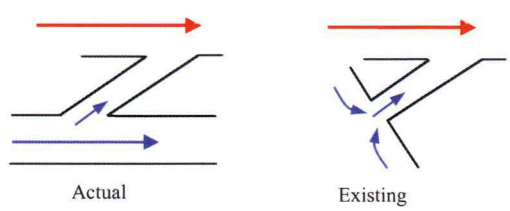

Figure 3. Comparison of actual blade internal coolant flow with the existing coolant supply configuration.

Supply loop design

Extensive measurements of the existing framework and components enabled a 3D CAD model of the wind tunnel assembly to be constructed. A significant design challenge was to incorporate the supply loop within the confines of this framework. Combining three-dimensional computer models of the current and new components, allowed proposed supply loop designs to be examined in all required positions prior to construction, and major misfitting problems rectified. The design evolution resulted in a recirculating loop with a rectangular clear

acrylic supply passage, large 180° bends, a fan, and an inlet from a controlled air supply. Several transitional pieces, designed to prevent flow separation, connect the rectangular passage to round cross-section bends of 150 mm internal diameter. These 90 degree bends were sourced from stormwater supplies and have a radius of curvature of ~250 mm to minimise turning losses. Two bends were joined together and fitted with mounting flanges to connect with the transitional pieces. All joins were sealed with a silicone gasket and tape where required. The blower is a 0.14 kW in-line mixed flow single phase fan made by Fantech, commonly used in air-conditioning applications, capable of delivering a 200 Pa pressure rise at a flow rate of 0.2 m^3/s. A Powerform Controls variable voltage controller was coupled to the fan to adjust speed remotely.

The supply loop components are supported by a stand-alone mobile framework. to enable easy manoeuvring. This facilitates varying internal crossflow directions, through repositioning of the loop at almost any angle relative to the mainstream flow direction of the wind tunnel. A three dimensional drawing of the supply loop is shown in figure 4.

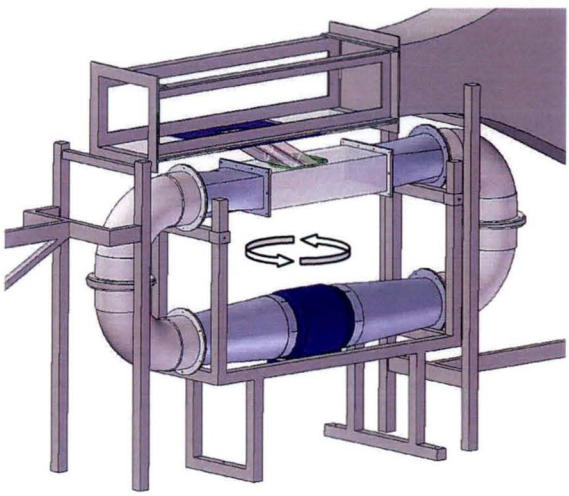

Figure 4. CAD model of supply loop design positioned within existing framework. Arrows indicate direction of supply loop rotation.

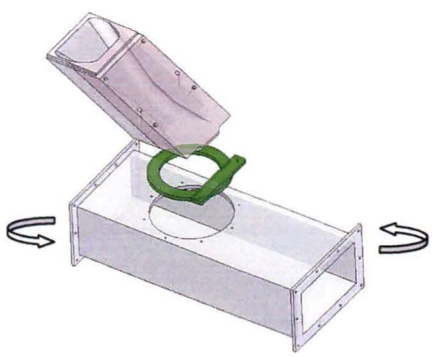

Figure 5. Exploded view of hole connection to passage and mainstream. Arrows indicate rotation of supply passage in relation to cooling hole model.

Supply passage

The supply passage dimensions were guided by the passage Reynolds number required to be representative of engine conditions, having a range of $7000<Re_h<90{,}000$ [3]. The passage dimensions were chosen at a height of 100 mm (2D) and width of 180 mm (3.4D), with 6 diameters of passage upstream and 4 diameters downstream of the hole centre. A novel component of this design is the ability to easily rotate the supply loop relative to the hole axis, and allow straightforward interchanging of hole geometries. A large 160mm diameter hole in the top of the passage allows a custom flange for each cooling hole geometry to be inserted. The round hole permits rotation of the supply loop about the hole inlet centre, as shown in figure 5.

Figure 6. Completed supply loop installed. Flow from right to left.

Cooling hole model

The variation of coolant flow path within a turbine blade or vane gives rise to a need for different hole geometries to improve cooling performance. The major development in cooling hole design over the last 30 years has been the progression from cylindrical holes to holes with flared or fan-shaped exits. Fan-shaped holes offer advantages such as superior coolant spread across the blade surface, and reduced detachment from the cooled surface at higher blowing ratios. In modern turbine components, fan-shaped holes often have an expansion angle near 30 degrees. This generally results in an over-expansion of the cooling hole flow and the rapid diffusion results in large scale flow separations and associated unsteadiness. In line with the research aim of investigating the sources of entropy production in the coolant flow path, the investigation will make measurements of the pressure field in the inlet region, within the hole itself, and in the near field exit region where the coolant fluid interacts with the mainstream. This should provide a greater understanding of the actual flow mechanisms within a highly diffused hole, and provide quantitative data for comparison with computational fluid dynamics results. The cooling hole model geometries are at large 50:1 scale to permit detailed flow field measurements.

Two different models have been constructed, and both have a laterally expanded exit with an included angle of 30 degrees. The throat or metering section diameter of the holes was selected based on the maximum achievable mainstream velocity, and matching the hole Reynolds number to engine like values, in the order of $Re_{Dj} = 3 \times 10^4$. Both geometries were based around typical designs used in Rolls-Royce turbine blades [7]. The hole models differ in that one has a short flared inlet in addition to the flared outlet, reflecting the actual manufactured hole shape due to machining processes. The second hole geometry has a cylindrical throat before expansion. Both hole models were machined from clear acrylic as it is non-conducting and optically clear. Schematics of the geometries are presented in figure 7, and a finished manufactured hole is shown in figure 8.

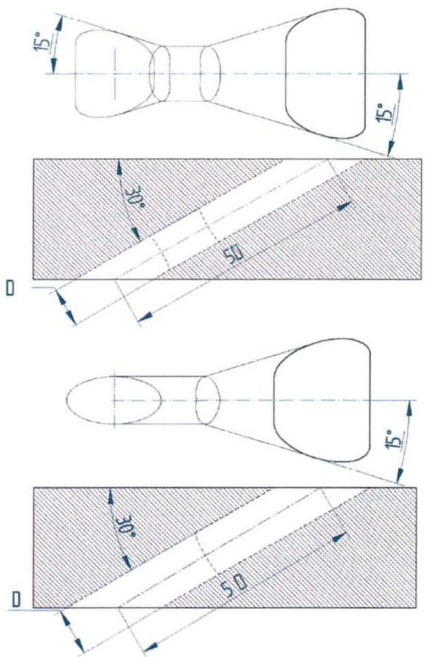

Figure 7. Cooling hole model geometries

Figure 8. Cooling hole model machined from clear acrylic

Coolant air metering

One of the main independent variables in this investigation is the velocity ratio between the cooling hole and mainstream flows. With a density ratio of unity, this is also equivalent to the mass flux or blowing ratio. In order to calculate the velocity of coolant through the metering section of the cooling hole geometries, the mass flow rate of the coolant needs to be known. The design of the supply loop means that the air entering the loop is equivalent to that leaving the loop through the cooling hole. Accurate measurement of the mass flow through the cooling hole is thus essential to calculate the velocity through the metering section of the hole geometries. This is achieved by a design that takes direction from the facility at the University of Karlsruhe as described in [8]. The supply loop is closed apart from one inlet, connected to a metered compressed air source, and one exit, the film cooling hole. In this way, at steady state, the mass flow of air that enters the supply loop is equivalent to the mass flow exiting through the cooling hole. A mass flow metering system is installed at the compressed air wall outlet. This consists of a pressure regulator, needle valve, digital flow rate meter, pressure transducer, and thermocouple (figure 9). A flexible hose connects the metering system to the supply loop inlet port, as can be seen in figure 6. The compressed air line is driven by a screw-type compressor, capable of delivering 4.3 m^3/min at 75 bar, which equates to approximately 0.6 kg/s of air. This is well above the 0.072 kg/s required to achieve a blowing ratio of 1.5. The pressure regulator and needle valve are manually set to achieve the desired mass flow rate. A pressure transducer monitors the static pressure immediately upstream of the flow meter, and a thermocouple monitors the temperature. Knowing the volumetric flow rate from the meter, together with the pressure and temperature of the air, enables the mass flow rate to be calculated. In addition, the supply loop blower allows the internal crossflow velocity to be varied independently of the blowing ratio.

Figure 9. Coolant air metering components R-L: pressure regulator, needle valve, pressure transducer, flow-rate meter, thermocouple.

Measurement uncertainty analysis

Uncertainty analysis is an important component of the presentation of measured data. A comprehensive review of error sources and the propagation of those errors through the measurement system and subsequent data reduction allows a defined level of confidence to be established in the reported values. Instrumentation of the wind tunnel included calibration and uncertainty estimation for the various measurement devices in use. The procedure followed was based on the approach of Moffat [9] and similarly from Dunn [10]. All combined uncertainties are expressed at 95% confidence and result from appropriate propagation of uncertainties through the measurement and data reduction system.

Coolant air supply calibration

The coolant air supply system was calibrated against a standard orifice plate. The plate was fitted within a length of pipe that had appropriate connections to the flexible piping from the metering equipment. The mass flow rate from the system was set to a range of values that created a calibration curve for the flow measurement system. Figure 9 shows the resulting plot and fitted polynomial regression. The combined uncertainty in mass flow values is less than 2% of a reading.

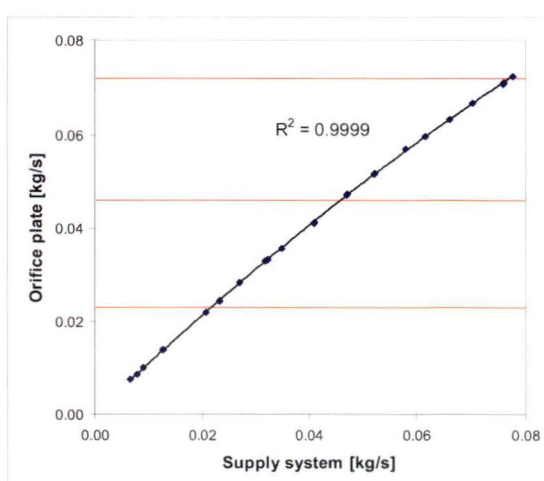

Figure 9. Calibration curve for coolant supply measurement system. Horizontal lines indicate desired operating points.

Supply passage profiles

Mean velocity

Measurements of flow velocity, direction, and turbulence were made in the coolant supply passage upstream of the cooling hole inlet. Probe insertion points were created on the supply passage mid-planes to allow both a vertical and horizontal traverse, as indicated in figure 10. A 4 mm Airflow Developments Ltd. Pitot-static tube was used to make time-averaged velocity measurements in each traverse direction to determine the uniformity of flow in the passage. Initially, no flow conditioning was installed in the supply loop between the blower and supply passage. The vertical Pitot traverse revealed significant non-uniformity in the flow due to a combination of flow turning through the bends, and a residual effect of the fan. Progressive levels of conditioning, consisting of 2 mm square nylon mesh screens, were inserted into the loop at flanged connections between the transitions and 180 degree bends upstream of the passage. The process was incremental, starting with a single layer of mesh at the upper flange, and adding up to two layers of non-aligned mesh at the upper and lower flanges. A 5 cell diameter long section of honeycomb straightener was also positioned in the round-rectangular transition just upstream of the passage start.

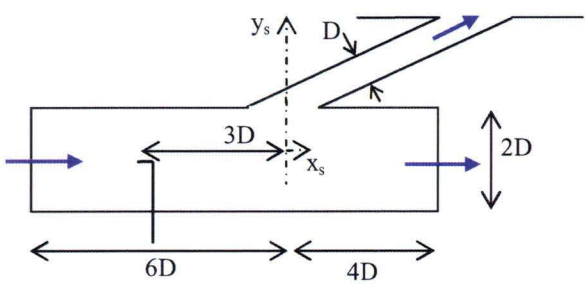

Figure 10. Coolant supply passage coordinate system and probe positioning.

The resulting profiles from various configurations of mesh are shown in figure 11. It is interesting to compare the vertical profiles with those from a horizontal traverse, as shown in Figure 12. Immediately it can be seen that the horizontal profiles exhibit far less variation than their vertical profile counterparts. This led to the conclusion that the large peaks in the vertical profiles near the walls and significant variation through the interior could not be due to the blower, as some radial consistency in the profiles would be expected. Attention was subsequently drawn to the positioning of the honeycomb in the end of the round-rectangular transition. It was possible, due to the convergent angle of the transition upper and lower walls, that some coolant may have been ejected from around the honeycomb at an angle to the passage axis. This fluid would also be slightly accelerated as it passed through the reducing flow area between the angled wall and axially aligned honeycomb exterior, and would not be subjected to pressure losses from entering and passing through the honeycomb cells. This would explain the regions of higher velocity fluid near the walls. As a result, it was decided to move the honeycomb into the rectangular supply passage to try and eliminate this feature.

Placing a layer of nylon mesh across the downstream end of the honeycomb had a significant impact on the uniformity of the velocity profile in the supply passage. This is due to the smaller mesh cell size breaking up the wakes from the honeycomb cells and thus reducing the length scale of the turbulent eddies. Smaller eddies take less downstream distance to dissipate and create a more uniform flow more quickly. There is still some variation across the passage, however the profile is quite flat through the central region with flow uniformity to within ±1.5%.

It should be noted that in an actual turbine blade passage, the flow would be expected to be somewhat non-uniform due to the presence of turbulating ribs, passage bends, and flow effects from preceding holes. So although we wish to have a consistent and defined velocity profile upstream of the hole inlet, the creation of a typical profile for fully developed flow is not essential.

	Mesh at bend start	Mesh at bend end	Honeycomb	Mesh over honeycomb
A				
B		X		
C	X	X	X	
D	X	X	X	X

Table 2. Flow conditioning configurations for supply loop.

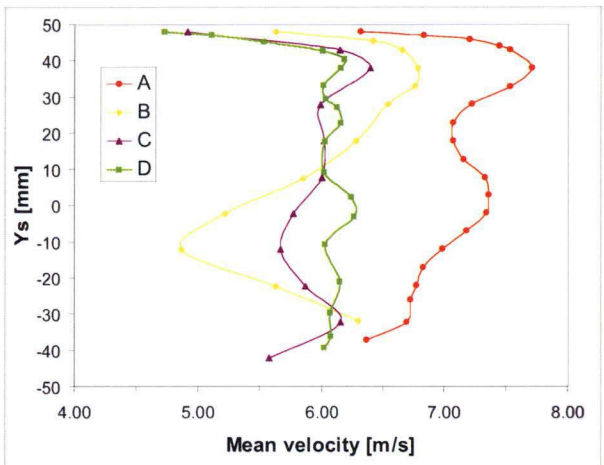

Figure 11. Vertical centreline mean velocity profiles for different conditioning configurations – see table 2.

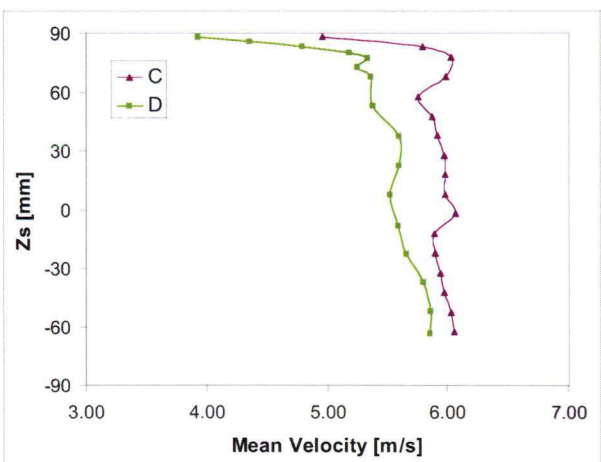

Figure 12. Horizontal centreline mean velocity profiles for different conditioning configurations – see table 2.

Flow direction

A 3-hole wedge probe was used to assess the flow direction in the mid planes of the supply passage. The results, shown in figure 11, indicate that the honeycomb flow straightener works well. Flow direction is parallel to the passage walls to within ±1°.

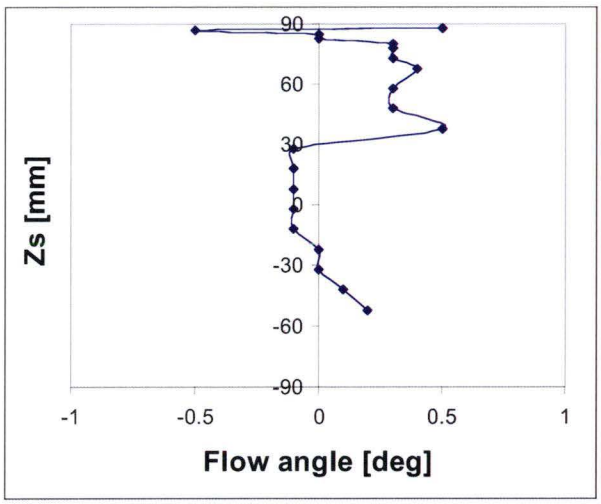

Figure 13. Coolant supply passage flow direction in centreline vertical (x_s-y_s) plane.

Turbulence intensity

A single axis hot-wire probe provided measurements of average velocity and turbulence intensity in the supply passage. Measurements revealed good agreement with velocity profiles from the Pitot-static traverse. Turbulence intensity values of about 2% were measured through the central region of the passage flow. The effect of the mesh on the downstream side of the honeycomb flow straightener can be seen in the uniformity of the turbulence intensity through this central region in both figure 15 and 17.

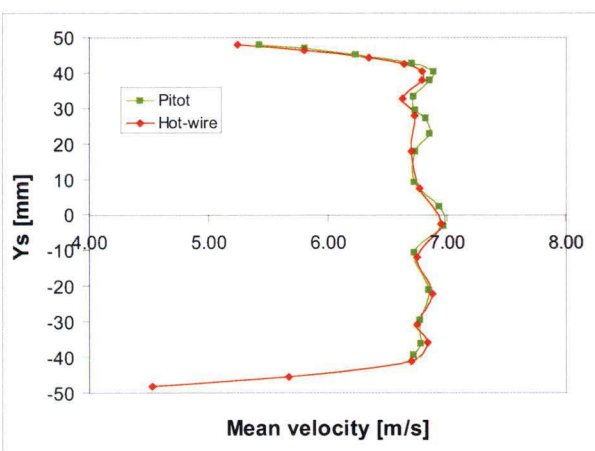

Figure 14. Supply passage mean velocity profiles from hot-wire and Pitot traverses in the centreline vertical (x_s-y_s) plane. Configuration D – see table 2.

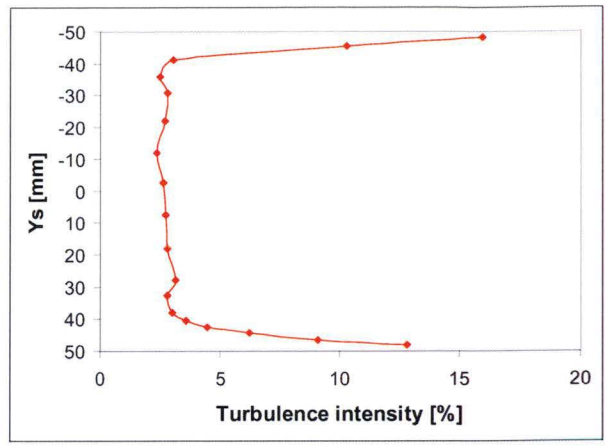

Figure 15. Turbulence intensity profile in the centreline vertical (x_s-y_s) plane. Configuration D – see table 2.

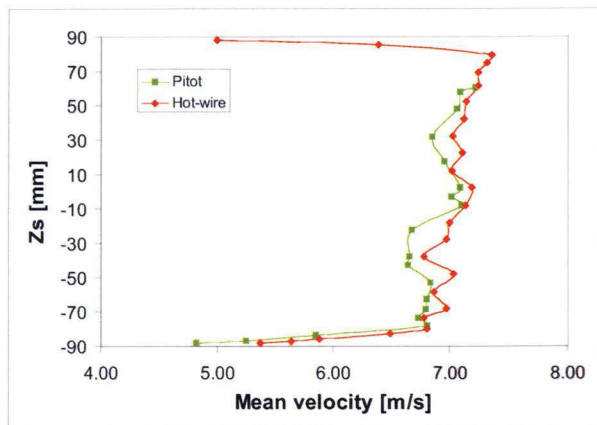

Figure 16. Supply passage mean velocity profile in centreline horizontal (x_s-z_s) plane. Configuration D – see table 2.

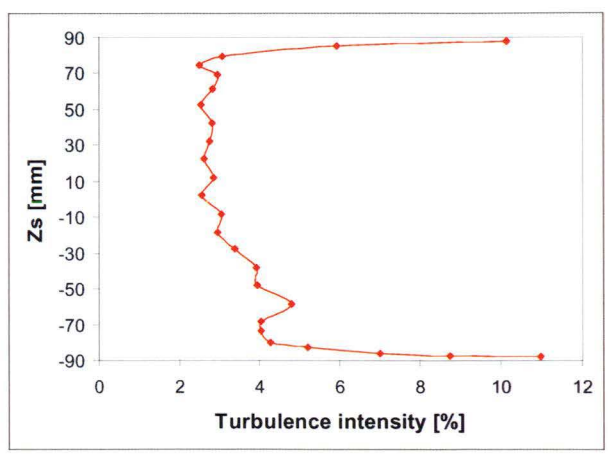

Figure 17. Supply passage turbulence intensity profile in centreline horizontal (x_s-z_s) plane. Configuration D – see table 2.

Conclusions

A new wind tunnel design for detailed flow field measurements in film cooling flows has been presented. The coolant supply system enables variation of the coolant flow through the hole geometry independent of the internal crossflow velocity. Measurements of the coolant supply passage flow and refinement of the flow conditioning methods resulted in a straight, and near uniform velocity profile in the passage upstream of the hole inlet.

Turbulence intensity values in the passage freestream are 2%. The large, 50:1 scale of the cooling hole model makes this design novel, and capable of generating highly detailed flow field measurements. These measurements will enable sources of entropy production to be established, and assist in the design of more aerodynamically efficient cooling holes.

Acknowledgments

The authors wish to acknowledge Rolls-Royce Plc Derby for providing funding for this research project, in addition to ongoing support and guidance. The Author acknowledges support through receipt of an Australian Postgraduate Award.

References

[1] Gostelow, J.P. 1984, *Cascade Aerodynamics*, Thermodynamics and Fluid Mechanics, Pergamon Press, Sydney.

[2] Cohan, H., Rogers, G. and Saravanamuttoo, H. 1996, *Gas Turbine Theory*, 4th edn, Longman Group Limited, Harlow, England.

[3] Kohli, A. and Thole, K.A. 1997, "A CFD investigation on the effects of entrance crossflow directions to film-cooling holes", paper presented to American Society of Mechanical Engineers, Heat Transfer Division, (Publication) HTD, 223-32.

[4] Gritsch, M., Schulz, A. and Wittig, S. 2003, "Effect of internal coolant crossflow on the effectiveness of shaped film-cooling holes", *ASME J Turbomachinery*, vol. 125, no. 3, pp. 547-54.

[5] Gritsch, M., Saumweber, C., Schulz, A., Wittig, S. and Sharp, E. 2000, "Effect of internal coolant crossflow orientation on the discharge coefficient of shaped film-cooling holes", *Journal of Turbomachinery*, vol. 122, no. 1, pp. 146-52.

[6] Sargison, J.E., Walker, G.E. and Rossi, R. 2004, "Design and calibration of a wind tunnel with a two dimensional contraction", paper presented to 15th Australasian Fluid Mechanics Conference, University of Sydney, 13th-17th December,

[7] Rolls-Royce Plc, *Film cooling data,* Personal communication to JS Porter, June 2006.

[8] Wittig, S., Schulz, A., Gritsch, M. and Thole, K.A. 1996, "Transonic film-cooling investigations: effects of hole shapes and orientations", paper presented to American Society of Mechanical Engineers,

[9] Moffat, R.J. 1988, "DESCRIBING THE UNCERTAINTIES IN EXPERIMENTAL RESULTS." *Experimental Thermal and Fluid Science*, vol. 1, no. 1, pp. 3-17.

[10] Dunn, P.F. 2005, *Measurement and Data Analysis for Engineering and Science*, McGraw-Hill Series in Mechanical Engineering, McGraw-Hill, New York.

Influence of Inlet Velocity Ratio on the Outlet Flow Uniformity of a Fan-Shaped Film Cooling Hole

Porter, J. S., Henderson, A. D., Walker, G. J., Influence of inlet velocity ratio on the outlet flow uniformity of a fan-shaped film cooling hole, Proceedings of the ASME Turbo Expo 2009: Power for lands sea, and air, Volume 7: Turbomachinery, Parts A and B., Orlando, Florida, USA., June 8–12, 2009. pp. 1639-1650. ASME. https://doi.org/10.1115/GT2009-59581

Appendix D

Database of Flow Measurements

Experimental data collected during the course of this study are presented for reference on the attached DVD.

Bibliography

[1] Cohen, H., Rogers, G., and Saravanamuttoo, H., 1996. *Gas Turbine Theory*, 4th ed. Longman Group Limited, Harlow, England.

[2] Aainsqatsi, K., 2008. *Schematic diagram illustrating the operation of a low-bypass turbofan engine.* http://commons.wikimedia.org/wiki/File:Turbofan_operation_lbp.svg.

[3] Gostelow, J. P., 1984. *Cascade Aerodynamics.* Thermodynamics and Fluid Mechanics. Pergamon Press, Sydney.

[4] Bunker, R. S., 2005. "A review of shaped hole turbine film-cooling technology". *Journal of Heat Transfer,* **127**(4), pp. 441–453.

[5] Rowbury, D. A., 1998. "Discharge coefficients of nozzle guide vane film cooling holes". PhD thesis, University of Oxford.

[6] Peterson, S., 2003. "Structural features of jets-in-crossflows for film-cooling applications". In Proc. 41st Aerospace Sciences Meeting and Exhibit, AIAA2003-303, AIAA.

[7] Kelso, R. M., Lim, T. T., and Perry, A. E., 1996. "An experimental study of round jets in cross-flow". *Journal of Fluid Mechanics,* **306**, pp. 111–144.

[8] Haven, B., and Kurosaka, M., 1997. "Kidney and anti-kidney vortices in crossflow jets". *Journal of Fluid Mechanics,* **352**, pp. 27–64.

[9] Smith, S., and Mungal, M., 1998. "Mixing, structure and scaling of the jet in crossflow". *Journal of Fluid Mechanics,* **357**, pp. 83–122.

[10] Andreopoulos, J., and Rodi, W., 1984. "Experimental investigation of jets in a crossflow". *Journal of Fluid Mechanics,* **138**, pp. 93–127.

[11] Fric, T., and Roshko, A., 1994. "Vortical structure in the wake of a transverse jet". *Journal of Fluid Mechanics,* **279**, pp. 1–47.

[12] Moussa, Z., Trischka, J. W., and Eskinazi, S., 1977. "Near field in the mixing of a round jet with a cross-stream.". *Journal of Fluid Mechanics,* **80**(1), pp. 49–80.

[13] Leylek, J., and Zerkle, R., 1994. "Discrete-jet film cooling: a comparison of computational results with experiments". *ASME Journal of Turbomachinery,* **116**(3), pp. 358–368.

[14] Kohli, A., and Thole, K., 1997. "A CFD investigation on the effects of entrance crossflow directions to film-cooling holes". In Proc. ASME 32nd National Heat Transfer Conference, August, Baltimore, USA, Vol. 12, pp. 223–232.

[15] Leedom, D. H., and Acharya, S., 2008. "Large eddy simulations of film cooling flow fields from cylindrical and shaped holes". In Proc. ASME Turbo Expo 2008, GT2008-51009, June, Berlin, Germany.

[16] Hale, C., Plesniak, M., and Ramadhyani, S., 2000. "Film cooling effectiveness for short film cooling holes fed by a narrow plenum". *ASME Journal of Turbomachinery,* **122**(3), pp. 553–557.

[17] Hale, C. A., Plesniak, M. W., and Ramadhyani, S., 2000. "Structural features and surface heat transfer associated with a row of short-hole jets in crossflow". *International Journal of Heat and Fluid Flow,* **21**(5), pp. 542–553.

[18] Sinha, A. K., Bogard, D. G., and Crawford, M. E., 1991. "Film-cooling effectiveness downstream of a single row of holes with variable density ratio". *ASME Journal of Turbomachinery,* **113**(3), pp. 442–449.

[19] Goldstein, R., Eckert, E., and Burggraf, F., 1974. "Effects of hole geometry and density on three-dimensional film cooling". *International Journal of Heat and Mass Transfer,* **17**, pp. 595–607.

[20] Gritsch, M., Schulz, A., and Wittig, S., 1998. "Adiabatic wall effectiveness measurements of film-cooling holes with expanded exits". *ASME Journal of Turbomachinery,* **120**(3), pp. 549–556.

[21] Dittmar, J., Schulz, A., and Wittig, S., 2002. "Assessment of various film cooling configurations including shaped and compound angle holes based on large scale experiments". In Proc. ASME Turbo Expo 2002, GT2002-30176, June, Amsterdam, The Netherlands.

[22] Gritsch, M., Saumweber, C., Schulz, A., Wittig, S., and Sharp, E., 2000. "Effect of internal coolant crossflow orientation on the discharge coefficient of shaped film-cooling holes". *ASME Journal of Turbomachinery,* **122**(1), pp. 146–152.

[23] Lutum, E., Von Wolfersdorf, J., Weigand, B., and Semmler, K., 2000. "Film cooling on a convex surface with zero pressure gradient flow". *International Journal of Heat and Mass Transfer,* **43**(16), pp. 2973–2987.

[24] Kohli, A., and Bogard, D., 1999. "Effects of hole shape on film cooling with large angle injection". In Proc. ASME Turbo Expo 1999, 99-GT-165, June, Indianapolis, USA.

[25] Reiss, H., and Boelcs, A., 2000. "Experimental study of showerhead cooling on a cylinder comparing several configurations using cylindrical and shaped holes". *ASME Journal of Turbomachinery,* **122**(1), pp. 161–70.

[26] Colban, W., and Thole, K., 2007. "Influence of hole shape on the performance of a turbine vane endwall film-cooling scheme". *International Journal of Heat and Fluid Flow,* **28**(3), pp. 341–356.

[27] Saumweber, C., and Schulz, A., 2008. "Comparison of the cooling performance of cylindrical and fan-shaped cooling holes with special emphasis on the effect of internal coolant cross-flow". In Proc. ASME Turbo Expo 2008, GT2008-51036, June, Berlin, Germany.

[28] Saumweber, C., and Schulz, A., 2008. "Effect of geometry variations on the cooling performance of fan-shaped cooling holes". In Proc. ASME Turbo Expo 2008, GT2008-51038, June, Berlin, Germany.

[29] Saumweber, C., and Schulz, A., 2008. "Free-stream effects on the cooling performance of cylindrical and fan-shaped cooling holes". In Proc. ASME Turbo Expo 2008, GT2008-51030, June, Berlin, Germany.

[30] Gritsch, M., Colban, W., Schär, H., and Döbbeling, K., 2005. "Effect of hole geometry on the thermal performance of fan-shaped film cooling holes". *ASME Journal of Turbomachinery,* **127**(4), pp. 718–725.

[31] Nakamata, C., Okita, Y., Fukuyama, Y., and Yoshida, T., 2007. "Recent progress in the research on advanced cooling technologies for a next-generation aero-engine". In Proc. ISABE.

[32] Sargison, J. E., Guo, S. M., Oldfield, M. L. G., Lock, G. D., and Rawlinson, A. J., 2002. "A converging slot-hole film-cooling geometry-part 1: Low-speed flat-plate heat transfer and loss". *ASME Journal of Turbomachinery,* **124**(3), pp. 453–460.

[33] Sargison, J. E., Guo, S. M., Oldfield, M. L. G., Lock, G. D., and Rawlinson, A. J., 2002. "A converging slot-hole film-cooling geometry-part 2: Transonic nozzle guide vane heat transfer and loss". *ASME Journal of Turbomachinery,* **124**(3), pp. 461–471.

[34] Thole, K., Gritsch, M., Schulz, A., and Wittig, S., 1998. "Flowfield measurements for film-cooling holes with expanded exits". *ASME Journal of Turbomachinery,* **120**(2), pp. 327–336.

[35] Haven, B. A., Yamagata, D. K., Kurosaka, M., Yamawaki, S., and Maya, T., 1997. "Anti-kidney pair of vortices in shaped holes and their influence on film cooling effectiveness". In Proc. ASME Turbo Expo 1997, 97-GT-45, June, Orlando, USA.

[36] Bunker, R. S., 2008. "The effects of manufacturing tolerances on gas turbine cooling". In Proc. ASME Turbo Expo 2008, GT2008-50124, June, Berlin, Germany, Vol. 4, pp. 81–96.

[37] Crabb, D., Durao, D. F. G., and Whitelaw, J. H., 1981. "A round jet normal to a crossflow". *ASME Journal of Fluids Engineering,* **103**, pp. 1006–1012.

[38] Burd, S., Kaszeta, R., and Simon, T., 1998. "Measurements in film cooling flows: Hole l/d and turbulence intensity effects". *ASME Journal of Turbomachinery,* **120**, pp. 791–798.

[39] Lutum, E., and Johnson, B., 1999. "Influence of the hole length-to-diameter ratio on film cooling with cylindrical holes". *ASME Journal of Turbomachinery,* **121**(2), pp. 209–216.

[40] Zuniga, H., Krishnan, V., Ling, J., and Kapat, J., 2007. "Trends in film cooling effectiveness caused by increasing angle of diffusion through a row of conical holes". In Proc. ASME Turbo Expo 2007, GT2007-28287, May, Montreal, Canada, Vol. 4, pp. 949–961.

[41] Sargison, J. E., Guo, S. M., Oldfield, M. L. G., and Rawlinson, A. J., 2001. "The variation of heat transfer coefficient, adiabatic effectiveness, and aerodynamic loss with film cooling hole shape". *Annals of the New York Acadamy of Sciences,* **934**, pp. 361–368.

[42] Pietrzyk, J., Bogard, D., and Crawford, M., 1990. "Effects of density ratio on the hydrodynamics of film cooling". *ASME Journal of Turbomachinery,* **112**(3), pp. 437–443.

[43] Kohli, A., and Bogard, D. G., 1998. "Effects of very high free-stream turbulence on the jet-mainstream interaction in a film cooling flow". *ASME Journal of Turbomachinery,* **120**, pp. 785–790.

[44] Saumweber, C., Schulz, A., and Wittig, S., 2002. "Free-stream turbulence effects on film cooling with shaped holes". In Proc. ASME Turbo Expo 2002, GT2002-30170, June, Amsterdam, Netherlands.

[45] Rohde, J., Richard, R., and Metger, G., 1969. Discharge coefficients for thick plate orifices with approach flow perpendicular and inclined to orifice axis. Tech. Rep. TND-5467, NASA.

[46] Hay, N., Lampard, D., and Benmansour, S., 1983. "Effect of crossflows on the discharge coefficient of film cooling holes". *Journal of Engineering for Power,* **105**(2), pp. 243–248.

[47] Thole, K., Gritsch, M., Schulz, A., and Wittig, S., 1997. "Effect of a crossflow at the entrance to a film-cooling hole". *ASME Journal of Fluids Engineering,* **119**(3), pp. 533–540.

[48] Miller, D., 1990. *Internal Flow Systems,* 2nd ed. BHRA (Information Services).

[49] Hay, N., and Lampard, D., 1998. "Discharge coefficient of turbine cooling holes: A review". *ASME Journal of Turbomachinery,* **120**(2), pp. 314–319.

[50] Gritsch, M., Schulz, A., and Wittig, S., 1998. "Method for correlating discharge coefficients of film-cooling holes". *AIAA Journal,* **36**(6), pp. 976–980.

[51] Hay, N., and Lampard, D., 1995. "The discharge coefficient of flared film cooling holes". In Proc. ASME Turbo Expo 1995, 95-GT-15, June, Houston, USA.

[52] Lloyd, S., and Brown, A., 1986. "Velocity and turbulence fields in pipe entrance regions in the presence of cross flows". *ASME Journal of Engineering for Gas Turbines and Power,* **108**(3), pp. 498–503.

[53] Byerley, A., 1989. "Heat transfer near the entrance to a film cooling hole in a gas turbine blade". PhD thesis, University of Oxford.

[54] Gillespie, D., Byerley, A., Ireland, P., Wang, Z., Jones, T., and Kohler, S., 1996. "Detailed measurements of local heat transfer coefficient in the entrance to normal and inclined film cooling holes". *ASME Journal of Turbomachinery,* **118**(1), pp. 285–90.

[55] Kohli, A., and Thole, K., 1998. "Entrance effects on diffused film-cooling holes". In Proc. ASME Turbo Expo 1998, 98-GT-402, June, Stockholm, Sweden.

[56] Gritsch, M., Schulz, A., and Wittig, S., 2001. "Effect of crossflows on the discharge coefficient of film cooling holes with varying angles of inclination and orientation". *ASME Journal of Turbomachinery,* **123**(4), pp. 781–787.

[57] Gritsch, M., Schulz, A., and Wittig, S., 2003. "Effect of internal coolant crossflow on the effectiveness of shaped film-cooling holes". *ASME Journal of Turbomachinery,* **125**(3), pp. 547–554.

[58] Adami, P., Martelli, F., Montomoli, F., and Saumweber, C., 2002. "Numerical investigation of internal crossflow film cooling". In Proc. ASME Turbo Expo 2002, GT2002-30171, June, Amsterdam, The Netherlands.

[59] Kissel, H., Weigand, B., Von Wolfersdorf, J., Neumann, S., and Ungewickell, A., 2007. "An experimental and numerical investigation of the effect of cooling channel crossflow on film cooling performance". In Proc. ASME Turbo Expo 2007, GT2007-27102, May, Montreal, Canada, Vol. 4, pp. 147–158.

[60] Pietrzyk, J., Bogard, D., and Crawford, M., 1989. "Hydrodynamic measurements of jets in crossflow for gas turbine film cooling applications". *ASME Journal of Turbomachinery,* **111**(2), pp. 139–145.

[61] Brandner, P., and Walker, G., 2007. "An experimental investigation into the performance of a flush water-jet inlet". *Journal of Ship Research,* **51**(1), pp. 1–21.

[62] Gritsch, M., Schulz, A., and Wittig, S., 1998. "Discharge coefficient measurements of film-cooling holes with expanded exits". *ASME Journal of Turbomachinery,* **120**(3), pp. 557–563.

[63] Hyams, D., and Leylek, J., 2000. "Detailed analysis of film cooling physics: Part III - streamwise injection with shaped holes". *ASME Journal of Turbomachinery,* **122**(1), pp. 122–132.

[64] Vennard, J. K., and Street, R. L., 1982. *Elementary Fluid Mechanics*, 6 ed. John Wiley & Sons, New York.

[65] Han, J., 1984. "Heat transfer and friction in channels with two opposite rib-roughened walls.". *Journal of Heat Transfer,* **106**(4), pp. 774–781.

[66] Porter, J., Sargison, J. E., Walker, G., and Henderson, A., 2008. "A comparative investigation of round and fan-shaped cooling hole near flow fields". *ASME Journal of Turbomachinery,* **130**.

[67] Sargison, J., Walker, G., and Rossi, R., 2004. "Design and calibration of a wind tunnel with a two dimensional contraction". In Proc. 15th Australasian Fluid Mechanics Conference, December, Sydney, Australia.

[68] Rossi, R., 2004. Blade-cooling mechanism: Calibration of the open circuit wind tunnel. Tech. rep., University of Tasmania/ Ecole Polytechnique Nantes, France.

[69] Wittig, S., Schulz, A., Gritsch, M., and Thole, K., 1996. "Transonic film-cooling investigations: effects of hole shapes and orientations". In Proc. ASME Turbo Expo 1996, 96-GT-222, June, Birmingham, UK.

[70] Rolls-Royce, 2006. Film cooling data. internal communication.

[71] Jorgensen, F. E., 2002. *How to measure turbulence with hot-wire anemometers - a practical guide.* DANTEC Dynamics, Skovlunde, Denmark.

[72] TSI, 1993. IFA100 instruction manual.

[73] Miller, R., and Hodson, H., 2005. Advanced experimental methods. Tech. rep., Whittle Laboratory, Cambridge University.

[74] Bruun, H. H., 1995. *Hot-wire anemometry: principles and signal analysis.* Oxford University Press, NewYork.

[75] Moffat, R. J., 1988. "Describing the uncertainties in experimental results.". *Experimental Thermal and Fluid Science,* **1**(1), pp. 3–17.

[76] Dunn, P. F., 2005. *Measurement and Data Analysis for Engineering and Science.* McGraw-Hill Series in Mechanical Engineering. McGraw-Hill, New York.

[77] Arts, T., Boerrigter, H., Carbonaro, M., Charbonnier, J.-M., Degrez, G., Olivari, D., Riethmuller, M., and Van den Braembussche, R., 1994. *Measurement Techniques in Fluid Dynamics*, 2nd ed. von Karman Institute.

[78] Kline, S. J., 1959. "On the nature of stall". *ASME Journal of Basic Engineering,* **81**, pp. 305–320.

[79] Jackson, R., 1963. "The compressible discharge of air through small thick plate orifices". *Applied Scientific Research,* **A13**, pp. 241–248.

[80] ANSYS, 2008. CFX 11 users guide.

[81] Bardina, J., Huang, P., and Caokley, T., 1997. "Turbulence modeling validation". In Proc. AIAA 28th Fluid Dynamics Conference, AIAA-1997-2121, June, Colorado, USA.

[82] Schilling, R. J., and Harris, S. L., 2005. *Fundamentals of Digital Signal Processing using MATLAB.* Nelson, USA.

[83] Roshko, A., 1915. On the development of turbulent wakes from vortex streets. Tech. Rep. 1191, NACA.